Quantum Analogues of Two-Dimensional Classical Turbulence

Matthew Thomas Reeves

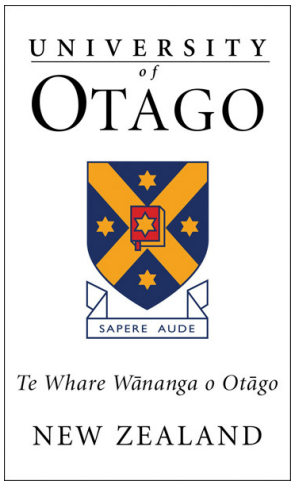

A thesis submitted for the degree of

Doctor of Philosophy

at the University of Otago, Dunedin,
New Zealand

Abstract

Turbulence, the irregular motion of fluids, is a challenging problem in physics. Yet some properties of turbulence appear to be universal, independent of the underlying host fluid supporting the motion. Recent studies have found that turbulence in superfluid helium, a quantum fluid, exhibits two of the most fundamental laws of classical fluid turbulence: the Kolmogorov $-5/3$ law, and the dissipation anomaly. These laws appear despite the fluid being highly constrained by quantum mechanical effects, and completely lacking kinematic viscosity. Such findings suggest further insight into the universal features of turbulent phenomena can be gained by studying analogies between classical and quantum turbulence.

Atomic Bose-Einstein condensates (BECs) offer a new platform for the study of quantum turbulence; the geometric control available in BEC experiments offers the possibility of studying quantum turbulence in effectively two-dimensional fluids. As two-dimensional turbulence exhibits dramatically different features from its 3D counterpart, BEC systems allow for further study of the analogies between classical and quantum turbulence. In this thesis we numerically and theoretically study 2D quantum turbulence in BECs within the framework of the Gross-Pitaevskii model. We focus on analogies with classical 2D turbulence, with the aim of identifying common or universal features.

First we investigate coherent vortex structures in negative temperature equilibria via an experimentally accessible flow-field measure. Coherent vortices are shown to produce a clear signal in this measure that is independent of the confinement geometry, and we demonstrate that it can be observed in dynamical simulations.

Second, studying a quantum analogue of the two-dimensional cylinder wake, we investigate the phenomenon of Strouhal oscillations. We find that the Strouhal number obeys a universal relation, similar to the classical form, upon introducing a modified superfluid Reynolds number that accounts for the critical velocity for vortex nucleation. Like the classical Reynolds number, the superfluid Reynolds number is found to govern the transition from laminar to turbulent behaviour in the quantum fluid.

Finally, simulating decaying 2D quantum turbulence for very large vortex numbers, we show that quantum fluids are capable of supporting the direct enstrophy cascade, a fundamental feature of two-dimensional turbulent flows. The quantum fluid manifests key features of the classical cascade, including Batchelor's -3 law of the inertial range, scaling of the inertial range against the superfluid Reynolds number, and the value of the Kraichnan-Batchelor constant.

The findings from this work thus provide some new insight into the universality of fundamental turbulence concepts, and their applicability to quantum fluids.

Acknowledgements

There are a number of people without whom this PhD would have been both impossible and considerably less enjoyable.

First and foremost, I'm very grateful to my supervisor Dr. Ashton Bradley. For the most part I thoroughly enjoyed this PhD, and Ashton I believe you are one of the main reasons. Thank you for so many fun and stimulating discussions, for offering me advice whenever I've needed it, and for giving me encouragement when I couldn't tell I had interesting results and felt like giving up. Thank you also for giving me so many opportunities to attend conferences and to travel overseas both to visit Brian Anderson in Arizona and attend NEQFLUIDS in France. Thank you Ashton for all the work you have put into both this research and into me as your student. I am lucky enough to say that my PhD supervisor has also become one of my closest friends, which is probably not something every PhD student can say. It has been a pleasure to work with you and learn from you, and I honestly believe I could not have asked for a better supervisor.

A very big thank you must go to Dr. Tom Billam, who, for all intents and purposes, has served as a terrific additional supervisor for the last couple of years. Working with Tom has been great fun, and I've learned a lot from him, especially about programming! A lot of this work would have taken me much longer without having Tom's guidance through finicky details of calculations, or feedback on general ideas.

Many thanks to those who have made the Quantum Theory room a great work environment, in particular Dr. Xiaoquan Yu, Lewis Williamson, Dr. Sam Rooney, and Dr. Danny Baillie. Thank you all for many amusing chats and interesting discussions, and for being a constant reminder that I am not nearly half as clever as I would like to be. Thanks also to Gavin King, Bianca Sawyer, and Michael Cawte, for your friendship over the years, for putting up with all my grumbling, and for making life in general more enjoyable.

Thank you to Kahla, for your love and emotional support, keeping me calm during meltdowns, letting me complain (at length) about thesis writing, and especially for your company during many stressful late nights when we both had to finish our theses at the same time! Finally, a big thank you to Mum and Dad, for being a lifeline throughout my studies, and for your unconditional love and encouragement.

Contents

Chapter 1

Introduction

1.1 Turbulence

Turbulence, the irregular motion of fluids, is a ubiquitous phenomenon that occurs in the vast majority of both natural and man-made flows [1–4]. It appears in systems in which the key basic ingredient of fluid motion, namely, advective nonlinearity, is the dominant mechanism. As such, turbulent processes, in one form or another, are important in a diverse range of physical systems. "Ordinary" hydrodynamic turbulence is relevant in the atmosphere and oceans, and its understanding is therefore crucial to informing climate and weather predictions [5], and the distribution of pollutants or microorganisms such as plankton [6, 7]. It is problematic in pipelines, where it hinders transport and increases mechanical vibrations [8], yet highly desirable in combustion engines where (compressible) turbulent mixing greatly enhances efficiency [9]. Furthermore, as many manifestations of turbulence often exhibit similar properties, concepts from hydrodynamic turbulence theory often apply to other turbulent phenomena. Examples include magnetohydrodynamic turbulence, important in the solar wind [10], the earth's core [11] and fusion plasmas [12, 13], or wave turbulence, occurring in ocean waves and optical fibres [14]. More broadly, turbulence is inherently a problem of strong nonlinearity and large fluctuations, a general property shared by many condensed matter systems. In addition to its physical importance, turbulence is also a subject of fundamental mathematical interest: the notions of chaos, scale invariance, and statistical predictability have origins rooted in the study of turbulence [15]. The smoothness problem of the Navier-Stokes equations, the governing equations of turbulence, is one of the remaining unsolved Millennium Prize problems put forward by the Clay Mathematics Institute. These are but a few examples.

Turbulence is largely considered an unsolved problem. Although the governing equations have been known since Stokes and Navier, turbulence is unsolved in the sense that we are not yet able to infer the properties of the flow from first principles, even for the simplest imaginable scenarios [16]. In fact, despite several centuries of investigation, turbulence does not even have a formal definition. Many texts actually refuse to give one (e.g. [17, 18]) since it is widely believed that the problem is not sufficiently well-understood, and we cannot define something we do not understand all that well. Nonetheless, turbulence does have a list of well-agreed upon characteristics that are common to most texts (e.g, [1–3, 17, 19]):

- Intrinsic spatiotemporal randomness, irregularity. Turbulence is chaos (but not necessarily vice versa); its intrinsic property is self-stochastization.
- Loss of deterministic predictability; statistically predictable.
- A very large number of strongly interacting degrees of freedom (thus excluding chaotic systems with only a handful of degrees of freedom).
- A wide range of relevant length and time scales, implying that certain characteristic dimensionless numbers (e.g. Reynolds number) are much larger than unity.
- Enhanced mixing properties, giving highly efficient transport of momentum (implying enhanced drag), energy, and passive tracers (chemicals, heat).
- Strongly non-linear and non-equilibrium, non-integrable, non-local, non-Gaussian, and non-Markovian (i.e. not memoryless).
- A complex interplay of order and disorder.
- Turbulent flows contain vorticity, i.e., the curl of the fluid velocity field $\boldsymbol{\omega} = \nabla \times \mathbf{u}$ is non-zero.[1]

1.2 Two-Dimensional Turbulence

The study of two-dimensional (2D) turbulence was not initially motivated by situations of direct physical interest [16, 20]. Rather, its study was considered as a

[1]The term "turbulence" is usually understood as synonymous with "hydrodynamic turbulence", i.e., Navier-Stokes turbulence or similar (Secs. 2.1 and 2.6). Some forms of turbulence, for example weak-wave turbulence (Ref. [14] and Sec. 3.6.1) do not contain vorticity.

reduced problem which could help to understand the more practical but very challenging problem of three-dimensional turbulence.[2] Two-dimensional flows are generally more analytically tractable, and significantly less demanding to simulate numerically. However, it was soon realized that 2D turbulence could have a practical importance of its own. Although purely 2D flows do not truly exist, there are a number of examples in geophysics and astrophysics where the transverse scales are much larger than the vertical ones, such that quasi-2D turbulence is a good approximation. Examples include planetary atmospheres [21, 22], and plasmas constrained by strong magnetic fields [13]. It was thus realised that understanding two-dimensional turbulence could be the first step to a complete understanding of these systems. Furthermore, controlled study of two-dimensional turbulence is no longer limited to simulation; experimental developments in, e.g., soap films [23–27], have now made it possible to study two-dimensional turbulence in the laboratory.

Yet it was also found that two-dimensional turbulence demonstrates a number of unique behaviours that have since come to broaden the understanding of what turbulence is, and how it can behave. Most notably, in marked contrast to 3D turbulence, highly turbulent 2D flows are characterised by vanishing energy dissipation, such that under free evolution they evolve towards non-trivial equilibrium distributions that happen to be characterized by *negative* absolute temperatures. This curious behaviour ultimately stems from a preferential transport of energy to large scales, rather than small scales where viscosity acts most efficiently. This large-scale energy transport causes coherent structures — long lived, strong regions of vorticity — to play a far more important role than in three dimensions. Possibly the most striking example is Jupiter's Great Red Spot, which has been observed to persist for at least several centuries (Fig. 1.1). Properties of the storm can be described within a quasi two-dimensional framework [28–30].

1.3 Quantum Turbulence

Quantum fluids, such as superfluid helium (Helium II) [31], ultracold Fermi gases [32] and Bose-Einstein condensates (BECs) [33], exhibit a unique form of turbulence [34]. These fluids, constrained by quantum mechanical effects, can only support vorticity in the form of thin quantum vortex filaments, whose strengths are constrained to single

[2]Some authors argue turbulent flows are strictly *three-dimensional*. Inevitably this leads to semantic arguments over whether or not two-dimensional flows are "actually" turbulent. It can nonetheless be agreed that two-dimensional flows can exhibit many characteristics of turbulence.

Figure 1.1: False colour image, showing turbulence in Jupiter's atmosphere, as observed by NASA's Voyager 1 spacecraft. The Great Red Spot, a coherent vortex structure, is a storm several times the size of earth, that has been observed to persist for several centuries. In the image one can clearly see a complex interplay of order and disorder

quanta of $\pm h/m$, where h is Planck's constant and m is the mass of a constituent particle. These quantized vortices are stable, topological objects with a well-defined vortex core scale ξ ($\sim$ 1Å in superfluid helium), and produce a highly constrained velocity field. Consequently, turbulence in these fluids is referred to as *quantum turbulence*.

Quantum turbulence is important in its own right: it is crucial to informing the application of superfluid helium as a coolant in infrared astronomy devices, and large scale superconducting devices such as those in particle accelerators and fusion experiments (see [35] for a review). Here superfluid helium is the coolant of choice due to its remarkable thermal properties; in superfluid helium temperature travels as a *wave* (called "second sound") rather than diffusively, giving it a far larger thermal conductivity than any other known material [31]. However, large heat fluxes cause turbulence to form, which in turn limits the superfluid's ability to transport heat efficiently through the second sound mechanism [35]. Quantum turbulence is also believed to play a role in pulsar glitches — a potential source for further detection of gravitational waves [36, 37].

Although much younger than its classical counterpart, quantum turbulence is still a well-established field, having been studied in superfluid helium for some 60 years [31, 38–42]. Early experiments focussed on the unusual two-fluid nature of quantum turbulence, arising due to the interpenetrating viscous (normal) fluid and inviscid (superfluid) components, and particular attention was paid to turbulence generated by the mechanism of thermal counterflow. This unique kind of turbulence became of considerable interest due to the aforementioned practical applications, but, being quite distinct to other forms of turbulence, its interest initially lay primarily with the low temperature physics community [43]. However, in the last two decades, studies of turbulence generated by more conventional means, like propellors or towed grids, began to uncover surprising similarities between quantum turbulence and classical turbulence, and there has been considerable interest in investigating how far these analogies go. In particular, despite its completely different small-scale structure, quantum turbulence has been found to exhibit two of the most fundamental laws of classical hydrodynamic turbulence: the Kolmogorov $-5/3$ law [44–47], and the dissipation anomaly [47–50]. These similarities are now known to persist even at very low temperatures, where the normal fluid component is negligible and viscosity is totally absent. Other close analogies, such as the von-Karman vortex street [51, 52] and superfluid boundary layers [53], have been discovered only in the last few years. Such nontrivial similarities suggest that, as with two-dimensional turbulence, a deeper

understanding of quantum turbulence can also contribute to a broader understanding of the very diverse phenomenon of turbulence as a whole, and, in particular, a more complete understanding of the universal features of turbulent phenomena.

1.4 Quantum Turbulence in Atomic Gases

Within the last five years or so it was demonstrated that quantum turbulence could be feasibly realised in ultracold atomic gases, specifically atomic Bose-Einstein condensates (BECs) [54–56]. These trapped dilute gases, confined by magnetic and optical fields, are clouds typically spanning tens to hundreds of microns, containing $\sim 10^4$–10^7 atoms cooled to temperatures of a few hundred nano Kelvin. They are most commonly comprised of alkali atoms, usually ^{87}Rb or ^{23}Na, which have become the workhorse species since Bose-Einstein condensation was first achieved using them in 1995 [57, 58].

An appealing aspect of atomic gases is their relative simplicity. Although one might argue quantum turbulence to be simpler due to the discrete vorticity enforced by quantum mechanical constraints [59–63], in some respects the problem, even in pure superfluid helium, is arguably worse than classical turbulence: not only is the problem not well-defined, but neither are the governing equations of motion. Whereas it is widely accepted that the Navier-Stokes equations (probably) contain classical turbulence in its entirety [2], a quantitatively accurate microscopic model still does not exist for superfluid helium despite extensive study for nearly a century. This is largely owing to the complexity arising from the strong interactions present in the system. Turbulence in superfluid helium is therefore typically studied phenomenologically, with vortex filament models [38], semi-classical two-fluid models [64] or the Gross-Pitaevskii equation [65] and its modifications [66]. In contrast, atomic Bose-Einstein condensates, being weakly interacting boson gases near zero temperature, are extremely well-described by the Gross-Pitaevskii model, allowing for the possibility of a very rigorous comparison between theory, numerical simulations, and experiments.

Furthermore, having now developed as a field of study for over 20 years, the experimental technology in the field of atomic gases field has reached a certain level of maturity, such that experiments now have exquisite control over many fundamental properties of these systems. Condensates can now be produced with tuneable atomic interaction strengths [67–69], in essentially arbitrary confining potentials [70, 71], and in effectively one- or two-dimensional geometries [69, 71]. If desired, additional complexity such as disordered potentials [72], or long range (dipolar) interactions [73], can

also be introduced, piece by piece. Furthermore, the vortex core scale in these dilute gases is much larger ($\xi \sim 1\mu$m), and in principle tuneable through the interactions, such that probing the smaller scales of turbulence may be simpler than in superfluid helium. Although methods do exist in helium to measure the magnitude of the vorticity using trapped ions [31], image vortex lines with hydrogen tracer particles [74], or the measure vortex line-length through second sound attenuation [75], measuring the whole velocity or vorticity field across all scales, and in particular down to the small scales, still poses an experimental challenge [40, 45, 47, 76]. In atomic gases, it should be possible to directly measure the entire vorticity field via optical means [77]. Harnessing this control could allow for certain aspects of quantum turbulence to be probed in a level of detail that would be otherwise difficult or impossible.

1.5 Two-Dimensional Quantum Turbulence

The degree of geometric control available in atomic gases allows strong axial confinement to be enforced, suppressing vortex dynamics along one direction. This offers the unique possibility of extending the study of quantum turbulence into the two-dimensional realm. This *two-dimensional quantum turbulence* (2DQT) is arguably a minimally complex manifestation of purely quantum turbulence, comprised of a definite number of degrees of freedom, in the form of straight-line, quantum vortex filaments.

Being a phenomenon that contains many degrees of freedom (vortices), and a large range of relevant length scales, quantum turbulence is still likely to be challenging to study in atomic gases. In particular the larger vortex core scale does place atomic gases at somewhat of a disadvantage in terms of the range of dynamically-available length scales in which turbulence can develop. Two-dimensional quantum turbulence should be much less challenging than its three-dimensional counterpart in this regard, since much spatially larger condensates should be possible given condensates containing the same number of atoms. Additionally, in highly oblate geometries, where vortices are effectively simple point-like objects of unit charge, optically probing the vorticity field is dramatically simplified [77, 78], since the dynamics can be oriented to remain orthogonal to a chosen optical imaging axis. Furthermore, just as with two-dimensional turbulence, numerical simulation is significantly less demanding, thereby allowing for more detailed numerical studies than would otherwise be possible.

1.6 Recent Experimental Developments

To date, the majority of studies in the 2DQT field (and QT in atomic gases in general) have been numerical. However, within the last three years experimental developments have rapidly made some considerable ground, and experiments have now conducted measurements of some quantities of basic interest. Due to the simpler nature of vortex imaging in 2D, measurements of thermal friction coefficients [79], vortex number decay [78, 80], and detailed observations of vortex annihilation events have already been demonstrated (see Fig. 1.2). A number of studies have also shown viable stirring protocols for controlled generation of vortex distributions and turbulence [52, 78, 81–85] (see also Fig. 1.3). Hard-wall trapping potentials, producing large, uniform density condensates have been demonstrated in two [71, 86] and three [70] dimensions. While there is still progress to be made before detailed studies of turbulence can be conducted, observations of more fundamental interest have also been demonstrated within the last few months: the first evidence of a von-Karman vortex street and the transition to turbulence have been observed in the wake of a stirring obstacle [52]. Furthermore, crucially, vortex sign detection has been recently demonstrated using Bragg spectroscopy [87], such that the entire vorticity field can now be measured. While vortex imaging in 3D quantum turbulence presently provides comparatively limited information, clear signatures of (classical) wave turbulence have been recently observed in a 3D uniform BEC [88].

1.7 The Purpose of This Thesis

Examples such as thermal counterflow clearly demonstrate that the study of quantum turbulence should not necessarily be limited only to classical analogies. However, given the wealth of knowledge available on classical turbulence, and our present relative ignorance about 2D quantum turbulence, focussing on classical analogies seems like a sensible place to start. The focus of this thesis is therefore the numerical and theoretical study of two-dimensional quantum turbulence, and specifically its analogies with two-dimensional classical turbulence. The overarching questions are:

- Can standard fundamental measures of turbulence, or simple modifications of them, be readily applied to 2DQT systems? Do seemingly universal aspects of 2D turbulence also apply to the quantum scenario?

- By studying well-understood classical analogues, can we determine what kinds

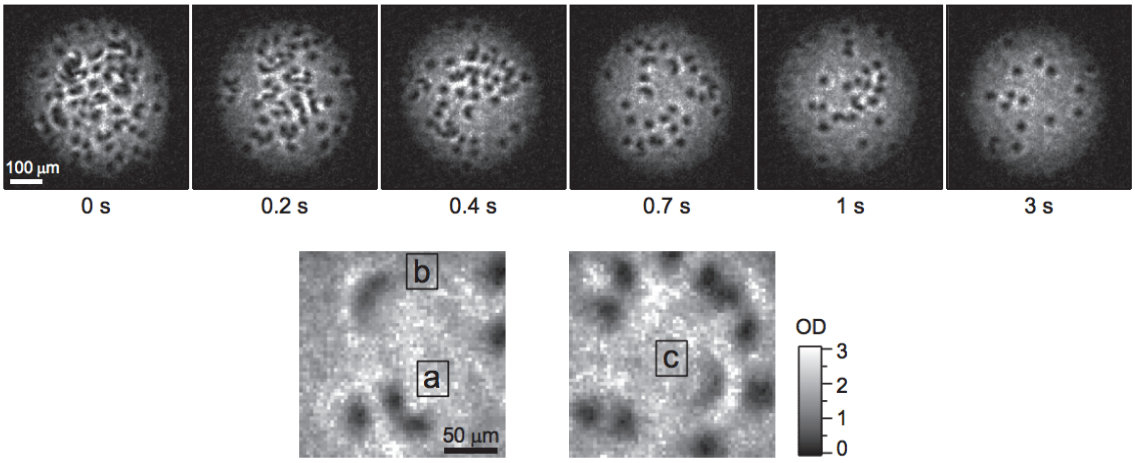

Figure 1.2: Images adapted from Kwon *et al.* (2014), Ref. [78]. Atomic density absorption image sequence showing decay of 2D quantum turbulence in a harmonically confined, quasi-two-dimensional Bose-Einstein condensate of sodium atoms. The small density holes within the cloud are individual quantum vortices. Close-up images show vortex-antivortex annihilation events, in which vortices merge and form crescent-shaped density waves.

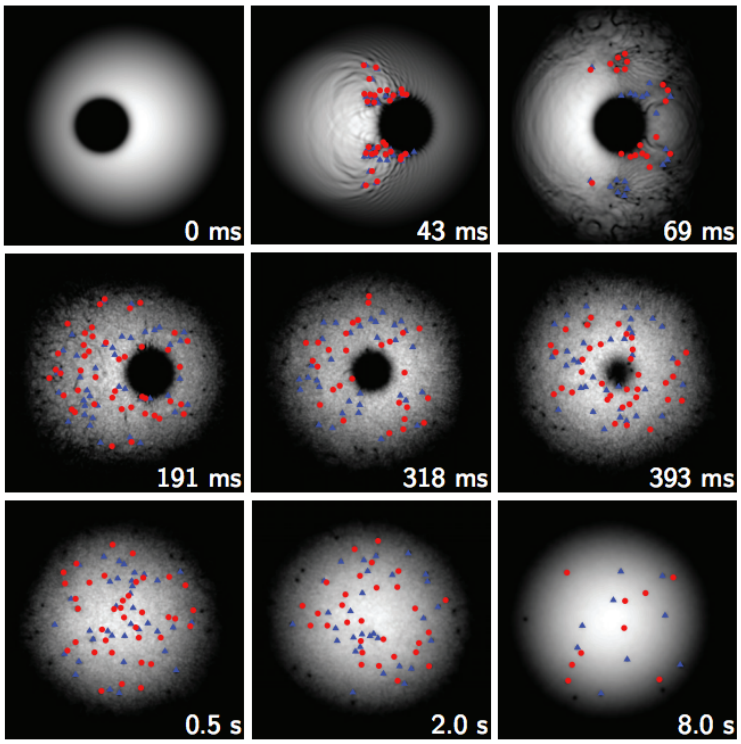

Figure 1.3: Images adapted from Stagg *et al.*, (2014) Ref. [89]. Simulation of the initial forcing cycle of the experiment shown in Fig 1.2. Turbulence is generated via stirring with a large, repulsive potential, which, in the experiment, is supplied by a blue-detuned laser beam. The beam is then ramped down such that the turbulence may freely decay.

of conditions are going to be needed for 2DQT to be seriously studied in atomic gases, in such a way that significant contributions can be made to broadening the understanding of turbulent phenomena?

- Can we identify measures that are easily accessible experimentally, both to aid as an experimental diagnostic, and to allow for theoretical speculation to be more readily confronted by experiment?

Due to the nature of these goals, the focus of this work has not been to model experimental scenarios in a highly realistic manner. Rather, owing to the difficulty in directly simulating turbulent flows, the approach here is more aligned with the approach often taken in classical turbulence, namely, on understanding the fundamental underlying processes in turbulent flows of the governing equations, through minimally complicated systems (extensive use of periodic boundary conditions is made).

1.8 Overview

The remainder of this thesis is structured as follows. Chapters 2 and 3 are essentially reviews of the relevant background. Chapter 2 provides the essential background on classical turbulence: the basic properties of the cylinder wake, cascades in fully-developed turbulence, and coherent vortex equilibrium distributions, which are relevant to the quantum analogues studied in this thesis, are presented in some detail. Our primary focus is 2D turbulence, but where deemed necessary or useful, 3D turbulence is discussed as a point of contrast and comparison. Chapter 3 introduces the relevant quantum fluids and quantum turbulence background. While 2D quantum turbulence itself is a relatively new field, much of the relevant underlying physics of quantum vortices has been well studied, and some of the knowledge about 3D quantum turbulence in superfluid helium provides useful guidance. Towards the end of the chapter, the recent developments in the studies of wakes, cascades and equilibrium states are reviewed, to provide motivational context for the original work presented in the subsequent chapters. It is our aim that the information collected and summarized in Chapters 2 and 3 will provide a useful resource for others who become interested in the subject in the future. Chapters 4, 5, and 6 then present original work, which, broadly speaking, focusses on coherent structure equilibria, the cylinder wake, and cascade phenomena respectively. Chapter 7 presents concluding remarks and future outlook.

1.9 Peer-Reviewed Publications

The original work presented in this thesis is the work for which I was the primary author. The work presented in Chapter 4 was published in Physical Review A [90]. The work of Chapter 5 was highlighted as an Editors' Suggestion in Physical Review Letters [91]. The work presented in Chapter 6 is currently under preparation for submission.

[90] M. T. Reeves, T. P. Billam, B. P. Anderson, and A. S. Bradley, *Signatures of Coherent Vortex Structures in a Disordered 2D Quantum Fluid*, Phys. Rev. A **89**, 053631 (2014).

[91] M. T. Reeves, T. P. Billam, B. P. Anderson, and A. S. Bradley, *Identifying a Superfluid Reynolds Number via Dynamical Similarity*, Phys. Rev. Lett. **114**, 155302 (2015). Highlighted as an Editors' Suggestion.

A number of collaborative works (which I coauthored) were published over the duration of this PhD: Ref. [92] was published in Physical Review Letters; Ref. [93], which laid some of the groundwork for the study presented in Chapter 6, was highlighted as an Editors' Suggestion in Physical Review A; Ref. [94] was published in Physical Review A.

[92] T. P. Billam, M. T. Reeves, B. P. Anderson, A. S. Bradley, *Onsager-Kraichnan Condensation in Decaying Two-Dimensional Quantum Turbulence*, Phys. Rev. Lett. **112**, 145301 (2014).

[93] T. P. Billam, M. T. Reeves, and A. S. Bradley, *Spectral Energy Transport in Two-Dimensional Quantum Vortex Dynamics*, Phys. Rev. A **91**, 023615 (2015). Highlighted as an Editors' Suggestion.

[94] X. Yu, T. P. Billam, J. Nian, M. T. Reeves, and A. S. Bradley, *Theory of the vortex-clustering transition in a confined two-dimensional quantum fluid*, Phys. Rev. A. **94**, 023602, (2016).

Chapter 2

Classical Hydrodynamic Turbulence

This chapter provides the essential background on classical fluid turbulence. The basic properties of the cylinder wake, cascades in fully-developed turbulence, and coherent vortex equilibrium distributions, which are relevant to the quantum analogues studied in this thesis, are presented in some detail. Our primary focus is 2D turbulence, but where deemed necessary or useful, 3D turbulence is discussed as a point of contrast and comparison.

2.1 The Navier-Stokes Equations

Hydrodynamic turbulence, normally referred to as simply "turbulence", is a phenomenon that is believed to be entirely described by the Navier-Stokes equations for an incompressible Newtonian fluid. These equations govern the evolution of the velocity field, $\mathbf{u}(\mathbf{x}, t)$

$$\frac{\partial \mathbf{u}}{\partial t} + (\mathbf{u} \cdot \nabla)\mathbf{u} = -\frac{\nabla p}{\rho} + \nu \nabla^2 \mathbf{u} + \mathbf{f}. \tag{2.1}$$

Here ρ is the density of the fluid, $p(\mathbf{x}, t)$ is the pressure field, ν is the kinematic viscosity ($\nu = \mu/\rho$, where μ is the molecular viscosity), and $\mathbf{f}(\mathbf{x}, t)$ embodies any external forcing mechanisms, such as gravity or external stirring. Once supplemented by the incompressibility condition

$$\nabla \cdot \mathbf{u} = 0 \tag{2.2}$$

and the boundary conditions, (often the no-slip condition $\mathbf{u} = \mathbf{0}$ at the boundary), the problem is completely specified. It appears that we are missing an equation for the pressure to close the system of equations, but this is in fact provided by the incompressibility condition. Taking the divergence of Eq. (2.1) gives the Poisson equation

$$\frac{\nabla^2 p}{\rho} = -\nabla \cdot [(\mathbf{u} \cdot \nabla)\mathbf{u}]. \tag{2.3}$$

The solutions to this equation are *non-local*, so changes in the velocity field are instantaneously communicated to the rest of the fluid through the pressure. Obviously, this arises from assuming the fluid is perfectly incompressible.

Although Eq. (2.1) looks complicated, it is nothing more than Newton's second law, expressed in terms of the velocity field rather than the position of a fluid parcel, since the former happens to be more convenient for a continuum. The two terms on the left correspond to acceleration in time and space, respectively. The nonlinear $(\mathbf{u} \cdot \nabla)\mathbf{u}$ term, which corresponds to *advection*, is ultimately the source of the difficulty of the equations. The viscosity manifests itself through a diffusion term $\nu\nabla^2\mathbf{u}$, which acts to "smooth out" the velocity field. The viscosity arises from assuming the fluid is *Newtonian*, such that the shear components of the stress tensor are linearly proportional to the velocity gradients

$$\sigma_{ij} = p_{ij} + \tau_{ij} = -p\delta_{ij} + \mu\left(\frac{\partial u_i}{\partial x_j} + \frac{\partial u_j}{\partial x_i}\right). \tag{2.4}$$

Taking the divergence of the stress $\sum_j \partial\sigma_{ij}/\partial x_j$ then yields the pressure and the viscous diffusion terms in Eq. (2.1) for an incompressible fluid. Equation (2.2), the incompressibility condition, is nothing more than the law of mass conservation

$$\frac{\partial \rho}{\partial t} + \nabla \cdot (\rho\mathbf{u}) = 0 \tag{2.5}$$

under the constraint of constant density. This is a valid assumption provided the velocities involved are much less than the speed of sound in the fluid. For sufficiently large velocities, density fluctuations begin to become important (see Sec. 3.2.5). It should also be stressed that the incompressibility does not necessarily imply that the density is constant, although this is usually true for hydrodynamic turbulence, and this gives us the benefit of a kinematic viscosity that is not spatially dependent. This condition is satisfied in laboratory experiments, as well as the smaller scales of the atmosphere [1]. However, such density variations are important, for example, in the

ocean, where the flow is incompressible, but the density variations must be taken into account in some way, e.g., through the Boussinesq approximation [95].

2.2 The Reynolds number

Something rather illuminating can be revealed from the Navier-Stokes equations simply by expressing them in a dimensionless form. Suppose we have a given flow geometry and we are able to identify a characteristic velocity U and characteristic length scale L. It does not matter precisely what these scales are, as long as we define them consistently for a particular problem. Then we may express the following quantities in terms of dimensionless variables (denoted by tildes):

$$x = L\tilde{x} \qquad \mathbf{u} = U\tilde{\mathbf{u}} \qquad \frac{\partial}{\partial t} = \left(\frac{U}{L}\right)\frac{\partial}{\partial \tilde{t}} \qquad p = \rho U^2 \tilde{p}, \qquad \nabla = \frac{1}{L}\tilde{\nabla}, \tag{2.6}$$

and with the above definitions, Eq. (2.1) becomes

$$\frac{\partial \tilde{\mathbf{u}}}{\partial \tilde{t}} + (\tilde{\mathbf{u}} \cdot \tilde{\nabla})\tilde{\mathbf{u}} = -\tilde{\nabla}\tilde{p} + \left(\frac{\nu}{UL}\right)\tilde{\nabla}^2\tilde{\mathbf{u}}. \tag{2.7}$$

The quantity in the parentheses is the inverse of the Reynolds number

$$\boxed{\mathrm{Re} = \frac{UL}{\nu}} \tag{2.8}$$

which is the only remaining adjustable parameter in the equations. Furthermore, since all quantities are now dimensionless, our specification of the boundary condition is now reduced to the specification of the boundary *geometry*. Flows with the same boundary geometry and Reynolds number are said to be *dynamically similar*; flows with any combination of L, U, and ν that yield the same Reynolds number will be identical under an appropriate rescaling of space and time.[1,2] In many situations the

[1]The reason why this works is because the Navier-Stokes equations are *scale invariant*. If we apply a scaling transformation of the form

$$\{\mathbf{r}, \mathbf{u}, t\} \to \{\lambda\mathbf{r}, \lambda^h\mathbf{u}, \lambda^{1-h}t\} \quad \lambda \in \mathbb{R}_+, h \in \mathbb{R} \tag{2.9}$$

we find that all terms are scaled by λ^{2h-1}, except for the viscous term which is scaled by λ^{h-2}. The only solution is $h = -1$, which leaves the Reynolds number unchanged.

[2]Dynamical similarity is the reason why scale models can be used to inform the design of technical machinery, e.g., aircraft.

Reynolds number is the sole control parameter of the problem, and, combined with the details of the boundary geometry, completely determines the properties of the flow. As such, it is one of the most important quantities in turbulence theory. It is equally valid to think of the Reynolds number as a quantity that measures the ratio of inertial and viscous forces in a flow. Dimensional analysis of the ratio of the inertial and viscous terms gives

$$\frac{|\mathbf{u}\cdot\nabla\mathbf{u}|}{|\nu\nabla^2\mathbf{u}|}\sim\frac{U^2/L}{\nu U/L^2}=\frac{UL}{\nu}. \tag{2.10}$$

Turbulence hence arises through the interplay between these two competing forces; at low Reynolds numbers, viscosity can stabilise perturbations, but at high Reynolds numbers, inertial forces dominate to amplify them. The onset of turbulence depends on the particular geometry, but usually occurs for $\mathrm{Re}\sim 10^2$–10^3. It should be that noted while the Reynolds number characterises the degree of turbulence, it is incredibly difficult to pin down a "critical" value, since this can be highly sensitive to imperfections in the boundaries, or residual turbulence upstream [96]. The limit $\mathrm{Re}\to\infty$ defines a theoretically idealised form of turbulence, in which the turbulence is free to evolve unconstrained by boundaries or the influence of viscosity. It is referred to as the zero viscosity limit, or *fully developed* turbulence.

2.3 The Cylinder Wake

To see how turbulence develops in a system as the Reynolds number is increased, it is useful to consider a basic example. The wake produced by a circular cylinder embedded in a uniform flow is perhaps one of the simplest systems we can imagine, and serves as a paradigmatic example for the transition to turbulence in fluids. It will also serve as a useful reference for later chapters, where we will study the superfluid analogue of this system.

Fig. 2.1 shows the development of the flow past a cylinder with increasing Reynolds number. Here, turbulence essentially develops in the system through a series of broken symmetries.[3] At low Reynolds number, in the Stokes flow regime Fig.2.1(a), the flow exhibits a high degree of symmetry; one can barely tell that the flow is from left to right. However, as the Reynolds number is increased, this symmetry is broken, and a steady recirculation zone forms behind the obstacle [Fig 2.1(b)]. The length

[3]For a detailed discussion on this "broken symmetries" view of the transition to turbulence, see the text by Frisch [2].

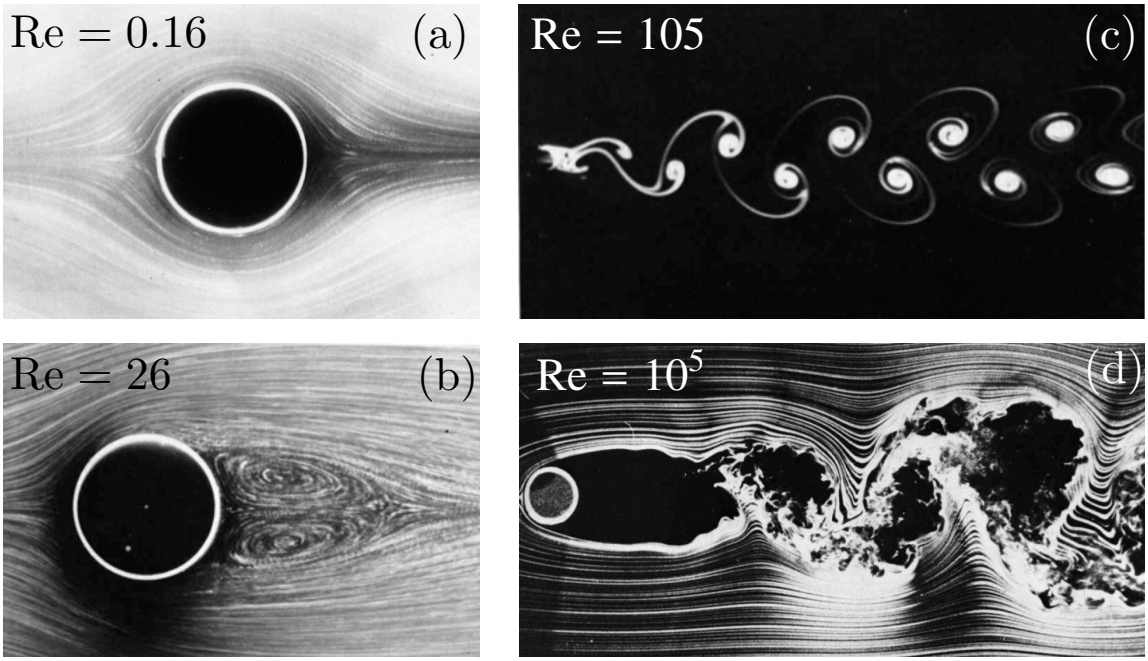

Figure 2.1: Examples of different qualitative flow regimes and their corresponding Reynolds numbers for a cylinder embedded in a uniform flow. Flows are visualised via aluminium dust in water (a,b), electrolytic precipitation in water (c), or smoke in air (d). Images reproduced from Van Dyke's *"An Album of Fluid Motion"* [97].

of the recirculation zone grows with increasing Reynolds number, until it eventually becomes unstable, at Re $\approx$ 40. The time invariance symmetry in the flow is then broken; periodic shedding of alternate-sign vortices occurs, leading to the formation of a *von-Karman vortex street* [Fig. 2.1(c)]. At about Re = 200, the flow starts to become unstable, and becomes increasingly irregular thereafter [Fig. 2.1(d)]. Notice that at higher Reynolds numbers, the periodic shedding persists and can still be clearly seen in Fig. 2.1(d), despite the highly irregular nature of the wake.

2.3.1 Strouhal Oscillations

The oscillatory vortex shedding that occurs at the onset of vortex street formation, and persists into the irregular flow regime is an intriguing phenomenon that is in fact common to the wakes of all bluff (i.e., not streamlined) bodies. An early investigator of this phenomenon was Strouhal [98], who became interested in the problem upon noticing that telegraph wires would "whistle" on windy days. Performing an experiment with wires and rigid rods, he found that the frequency of the shedding f depended only on the diameter of the cylinder D and the free-stream velocity of the

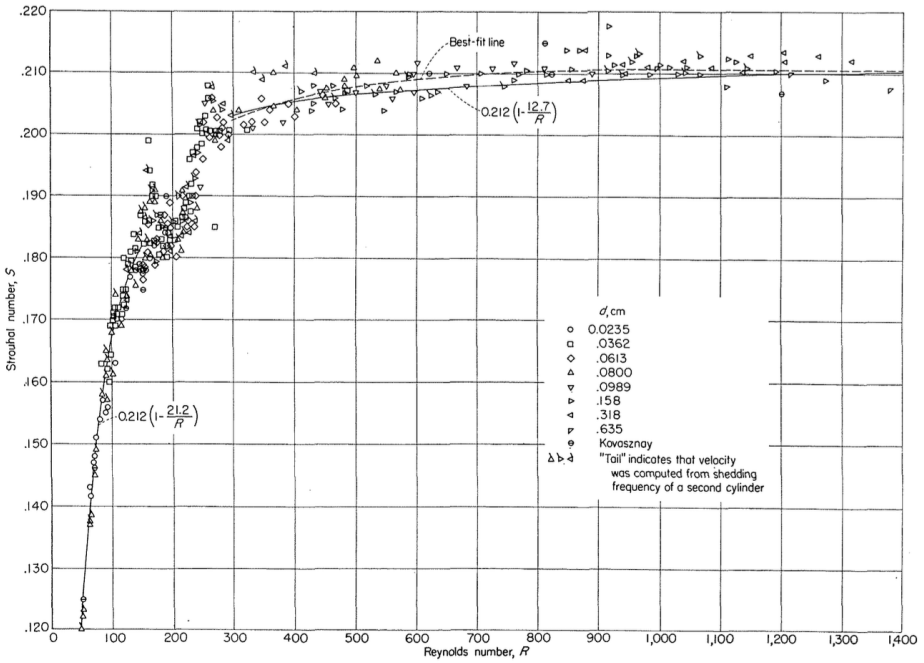

Figure 2.2: A graph of Strouhal number vs. Reynolds number for a cylinder in a uniform flow, obtained in the seminal wind tunnel experiments by Roshko [99].

flow u. Furthermore, he found that these quantities were always related through the expression

$$fD/u \approx 0.2. \tag{2.11}$$

This quantity is now known as the Strouhal number

$$\mathrm{St} = \frac{fD}{u}, \tag{2.12}$$

which, similar to the Reynolds number, can be considered as a dimensionless measure of the ratio of unsteady and steady inertial terms: $(\partial\mathbf{u}/\partial t)/(\mathbf{u}\cdot\nabla\mathbf{u}) \sim fD/u$. The apparent universal value of this quantity discovered by Strouhal is in fact a consequence of dynamical similarity — since the Strouhal number is a *dimensionless* quantity, it can be expressed as a universal function that depends only on the Reynolds number: $\mathrm{St} = \mathrm{St}(\mathrm{Re})$.[4] The universal nature of the Strouhal-Reynolds number relation is demonstrated in Fig. 2.2, which shows experimental wind tunnel data obtained by Roshko [99] for a wide range of cylinder sizes. The qualitative changes in the flow are readily seen in the St-Re relation: the steeply rising part of the curve corresponds to

[4]This is only true when the boundary is stationary. If the boundary is driven at some oscillation frequency, the Strouhal number becomes an independent control parameter.

the laminar von-Karman street, and the plateau corresponds to irregular shedding, and a turbulent wake. The two regions are separated by an instability region.[5] These qualitative regions exist for practically all obstacle shapes, although the precise form of the curve is different in each case. Notice in Fig. 2.2 that the St-Re curve is well-described by the empirical formula

$$\mathrm{St} = \mathrm{St}_\infty \left(1 - \frac{A}{\mathrm{Re}}\right), \tag{2.13}$$

where the asymptotic value $\mathrm{St}_\infty = 0.212$ agrees with the value originally discovered by Strouhal. The empirical St-Re relation is remarkably useful; if one of the flow parameters is difficult to measure, it can be accurately determined from the Strouhal number if the other quantities are known. An example of this application is in soap-film experiments — these films play a central role in experimental studies of two dimensional turbulence, yet their viscosity is difficult to measure. In Ref. [26], the St-Re relation was used to determine a relation between soap film thickness and its viscosity.

2.4 Statistical Description of Turbulent Flows

A key feature of turbulent flows is their random nature. Despite being governed by a deterministic system of equations, independent measurement sequences of a turbulent flow (for example two different time series measuring the drag force on a cylinder) will be completely different, even under seemingly identical conditions. In fact, owing to the chaotic nature of the flow, we might have anticipated that a fully deterministic description is futile, since we cannot know the boundary conditions exactly under any real situation.

However, it has been long established that the *statistical* properties of turbulent flows are reproducible. If one conducts a large number of independent experiments N to form a statistical ensemble, and takes the average of the measurements obtained, all the statistical properties such as the mean, variance, etc. will be practically identical to a seperate ensemble, provided the ensembles are large enough to obtain reliable statistical data. Similarly, in the steady cylinder flow problem, if one constructs histograms from the two time series, the statistical properties will be identical provided that time series are long enough.

[5] This region corresponds to the development of three-dimensional instabilities, and is absent in 2D flows like soap films [27].

It is therefore necessary to discuss how we describe turbulent flows statistically. The discussion presented here is essentially a condensed version of that presented in Batchelor [1], and we refer the reader there, or to Frisch [2], or Pope [3] for a more detailed discussion. The statistical properties of the turbulent velocity field at n points $\mathbf{u}_1 = \mathbf{u}(\mathbf{x}_1)$ etc. is determined by the joint probability distribution $P(\mathbf{u}_1, \mathbf{u}_2, \ldots \mathbf{u}_n)$. The probability average of a function $F(\mathbf{u}_1, \mathbf{u}_2, \ldots, \mathbf{u}_n)$ is

$$\langle F \rangle = \int F P(\mathbf{u}_1, \mathbf{u}_2, \ldots, \mathbf{u}_n) d\mathbf{u}_1 d\mathbf{u}_2 \ldots d\mathbf{u}_n \tag{2.14}$$

$$= \lim_{N\to\infty} \frac{1}{N} \sum_{i=1}^{N} F\left(\mathbf{u}_1^{(i)}, \mathbf{u}_2^{(i)}, \ldots, \mathbf{u}_n^{(i)}\right), \tag{2.15}$$

where (i) denotes the measurements made in the ith independent experiment used to form a statistical ensemble of N experiments. If P and hence all averaged values are independent of position, the velocity field is called a "stationary" function of $\mathbf{x}$. In such a case, we may replace the probability average with the spatial average

$$\langle F \rangle_x = \lim_{V\to\infty} \frac{1}{V} \int F(\mathbf{u}_1, \mathbf{u}_2, \ldots, \mathbf{u}_n) d\mathbf{y} \tag{2.16}$$

for a *single* realisation of $\mathbf{u}$, and here $\mathbf{u}_1$ etc. should be understood as $\mathbf{u}(\mathbf{x}_1 + \mathbf{y})$. Similarly if the turbulence is a stationary function of time, then

$$\langle F \rangle_t = \lim_{T\to\infty} \frac{1}{T} \int F(\mathbf{u}_1, \mathbf{u}_2, \ldots, \mathbf{u}_n, t) dt \tag{2.17}$$

may be used interchangeably with Eq. (2.15). Naturally we must ask how we may go about characterising the probability distribution, through quantities that can be readily measured. First considering the statistics at a single point $P(\mathbf{u})$, the answer lies in the Fourier transform of $P(\mathbf{u})$, the *characteristic function*

$$\phi(\boldsymbol{\alpha}) = \int e^{i\boldsymbol{\alpha}\cdot\mathbf{u}} P(\mathbf{u}) d\mathbf{u} = \sum_{p=0}^{\infty} \frac{i^p}{p!} \langle (\boldsymbol{\alpha}\cdot\mathbf{u})^p \rangle. \tag{2.18}$$

From Eq. (2.18), we thus find that the complete probability distribution for the velocity field at a single point can be characterised by the set of moments formed from the tensor products of the velocity, written in index notation as

$$Q_{ij\ldots p} = \langle u_i(\mathbf{x}) u_j(\mathbf{x}) \ldots u_p(\mathbf{x}) \rangle, \tag{2.19}$$

and $P(\mathbf{u})$ can be recovered through the inverse Fourier transform. Generalising this

argument to any number of points, we find that the statistical properties of a turbulent flow can therefore be completely characterised by the infinite set of tensors formed by the m-order product of the velocity components at n different points ($n \leq m$), i.e., in terms of the "m-order n-point product mean values" [1]

$$Q^{(m)}_{ij\ldots p}(\mathbf{r}) = \langle u_i(\mathbf{x}_1, t) u_j(\mathbf{x}_2, t) \ldots u_p(\mathbf{x}_m, t) \rangle \tag{2.20}$$

where the shorthand $\mathbf{r}$ defines a $d \times n$ dimensional vector (for d dimensions), comprised of the n different vectors contained in the set $\{\mathbf{x}_1, \mathbf{x}_2, \ldots, \mathbf{x}_m\}$. It is sometimes more convenient to work with the Fourier-space representation of such quantities, and we hence define the Fourier transform

$$\chi^{(m)}_{ij\ldots p}(\mathbf{k}) = \left(\frac{1}{2\pi}\right)^{dn} \int e^{-i\mathbf{k}\cdot\mathbf{r}} Q^{(m)}_{ij\ldots p}(\mathbf{r}) d\mathbf{r} \tag{2.21}$$

and its inverse

$$Q^{(m)}_{ij\ldots p}(\mathbf{r}) = \int e^{i\mathbf{k}\cdot\mathbf{r}} \chi^{(m)}_{ij\ldots p}(\mathbf{k}) d\mathbf{k}. \tag{2.22}$$

Although there are infinitely many quantities like Eq. (2.20), we can in principle consider as many as we desire, to obtain a description of the statistical properties as accurate as required. However, the higher order terms contain information about the "wings" of the probability distribution, and thus contain information about events that are rarer and are hence contribute less to the statistical description. They are also more difficult to measure reliably, since larger data sets are required to obtain reliable information about rarer events. As such, the lower order terms are the most important. The two-point correlation tensor

$$R_{ij}(\mathbf{x}, \mathbf{r}) = \langle u_i(\mathbf{x}) u_j(\mathbf{x} + \mathbf{r}) \rangle \tag{2.23}$$

and three-point correlation tensor

$$R_{ijk}(\mathbf{x}, \mathbf{r}, \mathbf{r}') = \langle u_i(\mathbf{x}) u_j(\mathbf{x} + \mathbf{r}) u_k(\mathbf{x} + \mathbf{r}') \rangle \tag{2.24}$$

along with their Fourier transforms are the most commonly considered quantities.

2.5 Homogeneous and Isotropic Turbulence

A seemingly simple system like the cylinder wake in fact turns out to exhibit an incredibly rich structure and significant complexity. In particular, the spatial inhomogeneity of this system, introduced by the no-slip boundary condition, makes the system difficult to analyse analytically — both the average flow properties and the turbulent fluctuations depend on their position in space, and the direction relative to the boundary. Such difficulties motivate the consideration of an idealised form of turbulence of minimal complexity, without the presence of *any* boundaries. Such an assumption is a valid description of turbulence in regions within the bulk of the fluid, far from any boundaries which are the original driving source of the turbulent flow. This assumption allows the consideration of *homogeneous* turbulence, in which properties of the flow are independent of their spatial position, e.g.,

$$\langle \mathbf{u}(\mathbf{x}) \rangle = \langle \mathbf{u}(\mathbf{x} + \mathbf{r}) \rangle \tag{2.25}$$

from which it follows $\langle \mathbf{u} \rangle = \text{const.}$, and can always be chosen to be zero by the Galilean invariance and momentum conservation of the Navier-Stokes equations. The simplification of the problem can be taken even further, by assuming the statistics of the turbulence is *isotropic*, being independent of rotations and reflections of the coordinate axes. Under the assumption of isotropy (which also requires homogeneity), the two-point correlation tensor becomes dramatically simplified (see Ref. [1] for a detailed explanation)

$$R_{ij}(\mathbf{x}, \mathbf{r}) = R_{ij}(\mathbf{r}) = R_{ij}(r) \propto R_{ii}(r), \tag{2.26}$$

i.e., the two-point correlations can be expressed in terms of a single scalar function with one scalar argument. In practice it turns out that homogeneous and isotropic turbulence can be readily generated experimentally, by for example passing a uniform flow through a periodic structure which has no directional preference, such as a grid of bars or a wire mesh. This *grid turbulence* can also decay sufficiently slowly with downstream distance that the flow can be well approximated as homogeneous and isotropic. It also happens that, at sufficiently large Reynolds numbers, the smaller scales of the turbulent flow can become fully-developed, and treated as isotropic and homogeneous to a reasonable degree.

In the idealised studies of homogeneous and isotropic turbulence, the interest lies in a class of asymptotic statistical states that are (partially) independent of a wide

class of initial states, rather than specific solutions to any particular problem. These states are usually steady in time, or only evolve in time in some simple manner, and quite often involve scale-invariant solutions such as power laws. Such an approach happens to be valid because, rather conveniently, nonlinear dynamical systems with many strongly coupled degrees of freedom have a tendency to exhibit emergent, self-organising behaviour [1, 17].

2.6 Conservation and Balance Laws

The most convenient (and common) way to mathematically impose homogeneity is to assume periodic boundary conditions

$$u_i(x, y, z) = u_i(x + lL, y + mL, z + nL);\ l, m, n \in \mathbb{Z}, \tag{2.27}$$

because the periodicity enforces the flow to have zero or constant mean flow, and there is no physical boundary to introduce inhomogeneity. The quantity

$$\boldsymbol{\omega} = \nabla \times \mathbf{u} \tag{2.28}$$

is the vorticity. Flows that satisfy $\boldsymbol{\omega} = \mathbf{0}$ are said to be irrotational, whereas turbulent flows all contain vorticity. Under periodic boundary conditions, the total vorticity is $\int \omega \, d\mathbf{x} = 0$ and is conserved, since it cannot be introduced or removed without a boundary. The line integral of the velocity around a closed contour (or by Stokes' theorem, the area integral of the vorticity within the contour)

$$\Gamma = \oint \mathbf{u} \cdot d\mathbf{l} = \int \boldsymbol{\omega} \cdot d\mathbf{a} \tag{2.29}$$

is called the *circulation*. In an *inviscid* ($\nu = 0$) incompressible fluid,[6] the circulation is conserved for a contour that follows the flow: $\partial\Gamma/\partial t + \mathbf{u} \cdot \nabla\Gamma = 0$ (this is known as Kelvin's Theorem). In general, the vorticity equation is

$$\frac{\partial \boldsymbol{\omega}}{\partial t} + (\mathbf{u} \cdot \nabla)\boldsymbol{\omega} = (\boldsymbol{\omega} \cdot \nabla)\mathbf{u} + \nu\nabla^2\boldsymbol{\omega}. \tag{2.30}$$

The first term on the right hand side is a source term, and corresponds to *vortex stretching* due to velocity gradients. Now, if a fluid flow is constrained to be two-dimensional ($\mathbf{u} = (u_x, u_y, 0)$), the vorticity has only a z component $\boldsymbol{\omega} = (0, 0, \omega(x, y))$,

[6] Or a barotropic compressible fluid for which $p = p(\rho)$ only.

and this has a dramatic consequence: the vortex stretching term vanishes, yielding

$$\frac{\partial \omega}{\partial t} + \mathbf{u} \cdot \nabla \omega = \nu \nabla^2 \omega, \tag{2.31}$$

such that, in the zero viscosity limit, the vorticity is conserved along the flow trajectory. It follows that, in contrast to three-dimensional flows, in the inviscid limit two dimensional flows possess additional conserved quantities, the (infinite) set of the vorticity moments

$$\Omega_n = \int \omega^n d^2\mathbf{x}. \tag{2.32}$$

Of these quantities, the square vorticity or *enstrophy*

$$\Omega_2 = \Omega = \frac{1}{L^2} \int |\omega|^2 d^2\mathbf{x} \tag{2.33}$$

is of particular significance, because of its relation to the energy of the flow. The kinetic energy per unit mass is

$$E = \frac{1}{2L^2} \int |\mathbf{u}(\mathbf{x})|^2 d^2\mathbf{x} \tag{2.34}$$

and in the absence of boundaries and external forcing it obeys the balance equation

$$\frac{dE}{dt} = -\nu\Omega. \tag{2.35}$$

The importance of the enstrophy is clear: it governs the dissipation of energy. Meanwhile, the enstrophy obeys a balance equation, where its decay is governed by vorticity gradients

$$\frac{d\Omega}{dt} = -\nu |\nabla \omega|^2. \tag{2.36}$$

In unforced 2D flows, the energy and enstrophy are therefore monotonically decaying quantities, *bounded by their initial values*. It is this feature that primarily distinguishes 2D and 3D turbulent flows. Because the enstrophy is bounded from above in 2D, the energy is conserved in the zero viscosity limit

$$\lim_{\nu \to 0} \frac{dE}{dt} = 0, \tag{2.37}$$

such that freely evolving high Reynolds number flows have approximately constant energy. In contrast, one of the fundamental experimental laws of three-dimensional turbulence is the *dissipation anomaly*: the energy dissipation is *finite* as the viscosity

tends to zero

$$\lim_{\nu \to 0} \frac{dE}{dt} = \epsilon \neq 0. \tag{2.38}$$

The source of this strange behaviour is, of course, the vortex stretching term. It adds a source term to the enstrophy balance equation that allows it to grow indefinitely, in such a way that it compensates for the diminishing viscosity. Through their haphazard motion, in three dimensions vortices may lengthen, and, by the circulation theorem and continuity, they must then radially contract, and amplify their vorticity (see, e.g. [100]). For this reason, in both steady forced turbulence, and the early stages of the decaying turbulence, and regardless of the details of the forcing mechanism, the energy dissipation happens to obey an extremely useful empirical relation [1, 2]

$$\epsilon = \frac{AU^3}{L}, \tag{2.39}$$

which has the rather odd and remarkable property that it is *independent of the viscosity* ν. Here U and L are again the characteristic velocity and length of the flow. The dimensionless parameter A is nearly constant; it varies slightly in different situations, but is always of order unity.

2.7 Spectral Representation

Fourier analysis is an indispensable tool for the analysis of homogeneous and isotropic turbulence, because it provides a means by which to formally define the motion at different *scales*. We will also see that Fourier analysis allows us to define an effective number of *degrees of freedom* for a given turbulent flow. We start with the Navier-Stokes equations for an incompressible fluid (neglecting the forcing term), in index notation for convenience,

$$\frac{\partial u_i(\mathbf{r})}{\partial t} + u_j(\mathbf{r}) \partial_j u_i(\mathbf{r}) = -\frac{\partial_i p(\mathbf{r})}{\rho} + \nu \, \partial_j \partial_j \, u_i(\mathbf{r}), \tag{2.40}$$

accompanied by the incompressibility condition

$$\partial_j u_j(\mathbf{r}) = 0, \tag{2.41}$$

where $\partial_j \equiv \partial / \partial x_j$ and we are using the Einstein summation convention over repeated indices. Now confining our attention to the two-dimensional case, let us assume

periodic boundary conditions in a square box of length L:

$$u_i(x, y) = u_i(x + mL, y + nL);\ m, n \in \mathbb{Z}. \tag{2.42}$$

The velocity field can be written as a Fourier series

$$u_i(\mathbf{r}) = \sum_{\mathbf{k}} \hat{u}_i(\mathbf{k}) e^{i\mathbf{k}\cdot\mathbf{r}}, \tag{2.43}$$

where $\mathbf{k} = (k_x, k_y) = 2\pi(m, n)/L$ and the Fourier coefficients $\hat{u}_i(\mathbf{k})$ are given by

$$\hat{u}_i(\mathbf{k}) = \frac{1}{L^2} \int_{\mathcal{V}} d^2\mathbf{r}\ u_i(\mathbf{r}) e^{-i\mathbf{k}\cdot\mathbf{r}}. \tag{2.44}$$

By use of the Poisson equation Eq. (2.3), repeated use of integration by parts, and the identity $\frac{1}{L^2} \int_{\mathcal{V}} d^2\mathbf{r}\ e^{i(\mathbf{p}+\mathbf{q}-\mathbf{k})\cdot\mathbf{r}} = \delta_{\mathbf{k},\mathbf{p}+\mathbf{q}}$, where $\delta_{\mathbf{x},\mathbf{y}}$ is the Kronecker delta, the Navier-Stokes equations become

$$\left(\frac{\partial}{\partial t} + \nu k^2\right) \hat{u}_i(\mathbf{k}) = -ik_m \left(\delta_{i,j} - \frac{k_i k_j}{k^2}\right) \sum_{\mathbf{p}+\mathbf{q}=\mathbf{k}} \hat{u}_j(\mathbf{p}) \hat{u}_m(\mathbf{q}), \tag{2.45}$$

accompanied by the incompressibility condition

$$k_j \hat{u}_j(\mathbf{k}) = 0. \tag{2.46}$$

The terms on the right hand side of Eq. (2.45) correspond to the advection and pressure, respectively. In light of the incompressibility condition Eq. (2.46), the term in the parentheses on the right-hand side, $P_{ij}(k) = (\delta_{i,j} - k_i k_j / k^2)$, can be viewed as a *projector* onto the incompressible plane $k_j \hat{u}_j(\mathbf{k}) = 0$. The contribution from the pressure therefore removes the part of the inertial term that is parallel to $\mathbf{k}$, such that incompressibility is maintained.

2.7.1 The Effect of Viscosity

The Fourier-space representation provides insight into the roles of the various terms in the Navier-Stokes equations. Firstly notice that, for small Reynolds numbers (or during the late stages of turbulence decay) where pressure gradients and inertia are negligible in comparison with the viscosity term, Eq. (2.45) reduces to

$$\frac{\partial \hat{\mathbf{u}}(\mathbf{k})}{\partial t} = -\nu k^2 \hat{\mathbf{u}}(\mathbf{k}) \tag{2.47}$$

whose solutions are simply

$$\hat{\mathbf{u}}(\mathbf{k}, t) = \hat{\mathbf{u}}(\mathbf{k}, t_0) e^{-\nu k^2 (t - t_0)}. \tag{2.48}$$

The amplitudes of the Fourier coefficients decay independently, and viscosity is *most effective at small scales*, i.e., at large wavenumbers. Increasing the Reynolds number is therefore equivalent to increasing the range of wavenumbers over which the effects of viscosity are negligible. Note that this statement is true even in the presence of boundaries: near boundaries, viscous effects are always confined to a narrow *boundary layer*, whose thickness decreases as the Reynolds number increases. In this region, the velocity field rapidly changes from its background value to zero, in order to be consistent with the no-slip boundary condition. Under Fourier analysis, this rapid change in the velocity field is represented in the high wavenumber components.

2.7.2 The Effects of Pressure and Inertia

Meanwhile, inspecting the nonlinear effects of the inertia and pressure we are confronted with terms of considerable complexity; each Fourier mode is coupled to every other Fourier mode, in groups of three, known as *triads*, and in a way that depends on both the amplitudes and phases of each triad. The nonlinear terms thus provide a mechanism for the system to attempt to reach equilibrium. An excitation initially confined to one Fourier mode will be rapidly spread among the other modes in some complicated fashion when the effects of viscosity are negligible. Furthermore, notice that if we multiply both sides of Eq. (2.45) by $\hat{u}_i^*(\mathbf{k})$ to obtain the energy contained within each mode $\mathbf{k}$, the pressure term vanishes due to incompressibility. It follows from this observation that the role of inertia is to transfer energy between *different* wavenumbers for the *same* velocity component, whereas the pressure forces transfer energy within the *same* wavenumber among *different* velocity components. Unfortunately, met with terms of such complexity, often the best we can hope to achieve is to deduce general trends of the flow, based on physically plausible arguments. Batchelor [1] stresses that general transfer trends, valid under all conditions, cannot be expected, because the amplitudes and phases of the Fourier components can be constructed, at least initially, to give practically any desired spectral transport.

2.7.3 Spectral Transport

A fundamental consideration is the distribution and transport of conserved quantities (and in particular, the energy) in scale-space — as we have already noted, turbulent flows are very efficient at *mixing*. In the periodic box, the average kinetic energy (again, per unit mass ρL^2) is given by

$$E = 1/L^2 \int_{\mathcal{V}} d^2\mathbf{r}\ \tfrac{1}{2}\langle|\mathbf{u}(\mathbf{r})|^2\rangle = \tfrac{1}{2}\sum_{\mathbf{k}}\langle|\hat{\mathbf{u}}(\mathbf{k})|^2\rangle, \tag{2.49}$$

where $\langle\ \cdot\ \rangle$ denotes an ensemble average. Now define

$$U(\mathbf{k}) = \frac{\langle|\hat{\mathbf{u}}(\mathbf{k})|^2\rangle}{(\Delta k)^2} \tag{2.50}$$

where $\Delta k = 2\pi/L$ is the spacing between wavenumbers, such that the energy is expressed as the Riemann sum

$$E = \frac{1}{2}\sum_{\mathbf{k}} U(\mathbf{k})(\Delta k)^2 \tag{2.51}$$

and take the limit $L \to \infty$ to formally recover isotropy[7]

$$\lim_{L\to\infty}\frac{1}{2}\sum_{\mathbf{k}} U(\mathbf{k})(\Delta k)^2 = \frac{1}{2}\int d^2\mathbf{k}\, U(\mathbf{k}). \tag{2.52}$$

Then, assuming isotropy of averaged quantities ($U(\mathbf{k}) = U(k)$), we evaluate the angular part of the integral, which simply gives a factor of $2\pi k$, (or $4\pi k^2$ in three dimensions), yielding the *kinetic energy spectrum* $E(k)$

$$E(k) = \pi k U(k); \quad \int_0^\infty dk\ E(k) = E. \tag{2.53}$$

In addition to its obvious physical importance, when the turbulence is isotropic $E(k)$ contains all the information contained in the two-point velocity correlation tensor, since it is the Fourier transform of $R_{ii}(r)$ (see, e.g., Refs [1, 2] for detailed explanations). Furthermore, with the aid of the incompressibility condition, it is straightforward to show that the vorticity and velocity are related in k-space as

[7] Or, equivalently, we could confine our analysis to wavenumbers $k \gg \Delta k$.

$\langle|\boldsymbol{\omega}(\mathbf{k})|^2\rangle = k^2\langle|\mathbf{u}(\mathbf{k})|^2\rangle$, so that the *enstrophy spectrum* is given by

$$\Omega(k) = 2k^2E(k); \quad \Omega = \int_0^\infty dk\, \Omega(k). \tag{2.54}$$

To obtain the equation of motion for $E(k)$, we multiply Eq. (2.45) by $\hat{u}_i^*(\mathbf{k})$, take the ensemble average and add the complex conjugate to obtain

$$\begin{aligned}\left(\frac{\partial}{\partial t} + 2\nu k^2\right) U(k)(\Delta k)^2 \\ &= -ik_m\left(\delta_{ij} - \frac{k_ik_j}{k^2}\right)\sum_{\mathbf{p}+\mathbf{q}=\mathbf{k}}\langle\hat{u}_i^*(\mathbf{k})\hat{u}_j(\mathbf{p})\hat{u}_m(\mathbf{q})\rangle + \text{c.c} \\ &= 2\,\text{Im}\left\{k_m\delta_{ij}\sum_{\mathbf{p}+\mathbf{q}=\mathbf{k}}\langle\hat{u}_i^*(\mathbf{k})\hat{u}_j(\mathbf{p})\hat{u}_m(\mathbf{q})\rangle\right\}.\end{aligned} \tag{2.55}$$

We can write this more succinctly as the energy balance equation:

$$\boxed{\frac{\partial E(k)}{\partial t} = T(k) - 2\nu k^2E(k).} \tag{2.56}$$

The terms on the right correspond to transfer and dissipation, respectively, and the quantity $T(k)$ is called the *transfer function*. To gain any further insight, it is necessary to explicitly expose some symmetries that the transfer term possesses. A lengthy and somewhat tedious calculation yields $T(k)$ in the symmetric form

$$T(k) = \frac{1}{2}\int_0^\infty\int_0^\infty T(k\,|\,p,q)\,dp\,dq, \quad T(k\,|\,p,q) = T(k\,|\,q,p), \tag{2.57}$$

where the symmetric function $T(k\,|\,p,q)$ is a complicated function that depends only on the wavenumber magnitudes and the third-order product mean values[8]

$$T(k\,|\,p,q) = -\frac{4\pi k}{(\Delta k)^4}\,\text{Im}\left\{(k_m\delta_{ij} + k_j\delta_{im})\frac{\langle\hat{u}_i(\mathbf{k})\hat{u}_j(\mathbf{p})\hat{u}_m(\mathbf{q})\rangle}{|\sin\theta_{pq}|}\right\}\mathcal{D}(k,p,q). \tag{2.58}$$

Here

$$\mathcal{D}(k,p,q) = H(q+p-k) - H(q-p-k) - H(p-q-k), \tag{2.59}$$

is a construction of Heaviside functions $H(x)$, completely symmetric in k, p, and q, that encodes the integration domain of allowed wavenumbers, which can be rewritten

[8]The factor of $|\sin\theta_{pq}|$ can be expressed entirely in terms of the wavenumber magnitudes using the sine and cosine rules.

as

$$\mathbf{k} + \mathbf{p} + \mathbf{q} = \mathbf{0}. \tag{2.60}$$

The equation Eq. (2.58) itself is not of much particular interest. Rather, the explicit symmetry in the transfer function aids the identification of conservation laws. We have the *global* conservation laws

$$\int_0^\infty T(k)\, dk = 0; \qquad \int_0^\infty k^2 T(k)\, dk = 0; \tag{2.61}$$

which reflect the fact that the nonlinear interactions serve only to *redistribute* the energy and enstrophy across wavenumbers, without changing their total values. Notice that we could have also inferred these properties from Eqs. (2.35) and (2.36). Importantly, the second of these equations is *not* true for three-dimensional turbulence, because the vortex stretching term allows $T(k)$ to generate enstrophy. It follows from Eq. (2.61) that, in the absence of viscosity, Eq. (2.56) forms a continuity equation in k-space for the energy and enstrophy, where $T(k)$ is the divergence of the flux. We may thus define the energy flux

$$\Pi_\epsilon(k) = \int_k^\infty T(k')\, dk' = -\int_0^k T(k') dk' \tag{2.62}$$

and the enstrophy flux (only in 2D)

$$\Pi_\omega(k) = 2\int_k^\infty k'^2 T(k')\, dk' = -2\int_0^k k'^2 T(k')\, dk' \tag{2.63}$$

which give the transport of energy and enstrophy across k due to the conservative interactions. Furthermore, we also find the extremely important properties of *detailed* conservation

$$T(k\,|\,p,q) + T(p\,|\,q,k) + T(q\,|\,k,p) = 0 \tag{2.64}$$

$$k^2 T(k\,|\,p,q) + p^2 T(p\,|\,q,k) + q^2 T(q\,|\,k,p) = 0 \tag{2.65}$$

which can be verified using incompressibility, the laws of sines and cosines, and the identity $\mathbf{k} + \mathbf{p} + \mathbf{q} = \mathbf{0}$. Physically, $T(k\,|\,p,q)$ is the energy transfer rate into k from the pair (p,q); the detailed conservation laws simply tell us that the conserved quantities must be accounted for on each end of the transaction for every individual interacting wavenumber triad. Again, note that in three dimensions $T(k\,|\,p,q)$ only satisfies the detailed energy conservation property Eq. (2.64) and not the detailed

enstrophy conservation property Eq. (2.65).

2.8 Kolmogorov's K41 Phenomenology

It will be useful for a moment to discuss one of the most fundamental theories of 3D turbulence, to introduce some fundamental concepts, and in order to aid discussions of quantum turbulence in later sections. Understanding the general behaviour of 3D turbulence also helps understand why 2D turbulence is somewhat special.

Forcing from a boundary with some macroscopic scale L primarily excites wavenumbers $k \sim 1/L$. At higher wavenumbers, the energy spectrum is typically monotonically decreasing as $k \to \infty$, such that the macroscopic scales contain the vast majority of the energy. One can thus typically define some *integral scale* of the turbulence k_L, which is of order $1/L$, where the energy spectrum is a maximum (the average wavenumber, $k_L = [\int dk\ kE(k)]/E$ is another possible definition). Wavenumbers of order k_L define the *energy containing range* of the motion. Now, it has previously been mentioned that the energy dissipation rate is finite and constant at large Reynolds numbers in 3D flows. Clearly then, the interaction terms have a tendency to transport energy, on average, from $k \sim k_L$ to wavenumbers $k \gg k_L$ where viscosity can act efficiently.[9]

If the turbulence is sustained by a steady forcing mechanism, then naturally we might inquire about what kind of statistically steady distributions could arise from this transport process. However, even if the turbulence is freely decaying, we might be able to find some kind of steady distribution over some wavenumbers provided the decay is sufficiently slow compared to some characteristic evolution time for those wavenumbers. The empirical decay law, Eq. (2.39), rules out this possibility for the energy containing range of wavenumbers

$$\frac{E}{dE/dt} \sim \frac{U^2}{AU^3/L} \sim \frac{L}{U}, \tag{2.66}$$

since Eq. (2.66) shows that their decay is of the order of their own characteristic turnover time $\tau = L/U$. However, this does not rule out the smaller scales — the smaller scales might have a much shorter characteristic time, which is ultimately determined by precisely how the system decides to distribute the energy in k-space.

[9] This can also be shown by applying equilibrium statistical mechanics arguments to a finite set of the Fourier modes when $\nu = 0$, see, e.g., [101]. The 3D equilibrium is equipartition [$U(k) = \text{const.}$], giving $E(k) \sim k^2$.

The idea of a characteristic time is presently a very loose one, but it will be made more concrete shortly.

Based on the above idea, and some plausible assumptions, Kolmogorov proposed [102] that, at sufficiently large Reynolds numbers, the small scales of developed turbulence (forced or decaying) might have a universal structure. Firstly, although in reality energy transfer is permitted from any wavenumber to any other wavenumber, it seems likely that most of the transfer at a given wavenumber k is *local*, in the sense that it is dominated by wavenumbers p and q that are in the local neighbourhood of k. The physical intuition behind this argument is that the shear that acts to distort an eddy of scale $l \sim 1/k$ should come from other eddies of a similar scale. Eddies much larger will simply cause advection of this eddy, which, of course, does not contribute to energy transport. The influence of the much smaller eddies should be limited since they contain comparatively less energy, and their influence should cancel on average over the scale of the larger eddy. Then, provided that the Reynolds number is large enough such that the smallest excited scales are sufficiently far removed in wavenumber space, it may not matter precisely what the mechanical driving mechanism is doing (or was doing) to generate the turbulence at the large scales. The small scales could be statistically independent of this mechanism, since they are only fed energy indirectly, through a long chain of triadic interactions, through which the history of the flow could be "forgotten" during the haphazard motion. Then, in addition to the viscosity ν, it would seem that the only other available parameter to these scales is average energy dissipation rate (per unit mass) ϵ. However, by the universal decay law, ϵ is not determined by the small scales, but by the energy-containing eddies themselves. It is as if the small scales form a kind of self-adjusting (statistical) equilibrium, which merely adjusts to dissipate whatever the energy containing range delivers at a given instant. Furthermore, regardless of the state of the driving forces, the statistics of the small scales should be isotropic — as we have already seen in Sec 2.7.2, the pressure forces will strive to remove any directional preferences in the flow. Combining these considerations motivates a powerful assumption:

If the interactions between wavenumbers are predominantly local, then at large Reynolds numbers the small scales of the turbulence could be isotropic, statistically independent of the large scales, and in statistical equilibrium. Under such conditions, their properties will depend only on the viscosity ν, the energy dissipation rate ϵ, and the local wavenumber k.

If these are the only relevant parameters available, we may thus define the char-

acteristic wavenumber and velocity

$$k_d = \left(\frac{\epsilon}{\nu^3}\right)^{1/4}, \qquad v = (\nu\epsilon)^{1/4}, \tag{2.67}$$

and it follows that the kinetic energy spectrum would be of the form

$$E(k) = v^2 k_d^{-1} f(k/k_d) \tag{2.68}$$

where $f(x)$ is some dimensionless, presumably universal function. This range would be in a kind of equilibrium, with steady injection coming primarily from the low end, and viscous dissipation primarily from the high end. At a given instant, the spectrum must satisfy the energy decay law

$$\epsilon = 2\nu \int_0^\infty k^2 E(k) dk \tag{2.69}$$

which is consistent with Eq. (2.68), so long as $\int dx\ x^2 f(x) = \frac{1}{2}$. The condition for this equilibrium range to exist is that the Reynolds number must be large enough such that the integral scale of injection, $k_L \sim 1/L$, and the equilibrium range of dissipation are sufficiently separated

$$k_L \ll k_d, \tag{2.70}$$

such that the contributions to $\int dk\ E(k)$ (the total energy) and $\int dk\ k^2 E(k)$ (the energy loss) come from regions of wavenumber space that are approximately non-overlapping. Making use of the empirical decay law Eq. (2.39), an equivalent condition is

$$\frac{k_d}{k_L} \sim \left(\frac{UL}{\nu}\right)^{3/4} \gg 1, \tag{2.71}$$

i.e., $\mathrm{Re}^{3/4} \gg 1$. If the Reynolds number is even *larger*, such that we may identify a region

$$k_L \ll k \ll k_d \tag{2.72}$$

then viscosity must *also* be unimportant in this range. In this *inertial range*, the properties of the spectrum must be determined only by the local wavenumber k and the energy transfer rate. Because we have assumed that the energy transport is local, this must be a constant across k, and equal to the dissipation rate ϵ to be consistent with energy conservation. It immediately follows that the only dimensionally correct

combination that eliminates the viscosity is the famous Kolmogorov law

$$\boxed{E(k) = C\epsilon^{2/3}k^{-5/3}} \tag{2.73}$$

where C is the Kolmogorov constant, a dimensionless number of order unity. This notion of constant, lossless transport through an inertial range is known as a *turbulent cascade*, and this kind of cascade phenomenology is now a cornerstone of modern turbulence theory. The condition for the inertial range to exist is stricter than the equilibrium dissipation range. If

$$\mathrm{Re}^{3/8} \gg 1, \tag{2.74}$$

then wavenumbers of order $k_L\mathrm{Re}^{3/8} = (k_L k_d)^{1/2}$ can be considered to lie in the inertial range and by Eq. (2.70) wavenumbers $k_L\mathrm{Re}^{3/4}$ will lie in the dissipation range. Note that, via Eq. (2.73), k_d can be considered the scale at which the *local* Reynolds number becomes of order unity,

$$\frac{[E(k)k]^{1/2}}{\nu k} \sim 1. \tag{2.75}$$

As promised, we can also define a local characteristic turnover time

$$\tau(k) = [k^3E(k)]^{-1/2} \sim \epsilon^{-1/3}k^{-2/3} \tag{2.76}$$

which informs us that the cascade is an accelerated process. Eq. (2.76) is consistent with the statistical independence assumption; the much smaller characteristic time of the small scales should allow them sufficient time to "forget" their history from the energy containing range. It also means that the decay of the turbulence will occur over many turnover times for the small scales, thus supporting the equilibrium hypothesis. Finally, notice also that the condition Eq. (2.71) provides us with yet another interpretation of the Reynolds number: it measures the relevant number of degrees of freedom in a turbulent flow

$$N \sim \left(\frac{k_d}{k_L}\right)^3 \sim \mathrm{Re}^{9/4}. \tag{2.77}$$

Eqs. (2.71) and (2.76) encapsulate the ultimate difficulty in simulating large Reynolds number flows directly. The vast range of relevant length and time scales require

large spatial domains, and long integration times, but also high spatial and temporal resolution. Eq. (2.77) places a lower bound on the amount of computational memory required to store a fully-resolved simulation.

Much of the physical reasoning leading to the Kolmogorov law is not entirely correct [103, 104]. In fact, some argue that the whole cascade scenario should be considered as mostly pedagogical imagery [15]. Landau quickly showed the idea of universality was critically flawed [2, 105], and one also finds discrepancies between the theory and real turbulent flows when applying the Kolmogorov ideas to higher order statistics (this is related to *intermittency*, see Frisch [2] for a discussion). Nonetheless, the Kolmogorov law is remarkably well verified experimentally, and the Kolmogorov constant $C \approx 1.5$ is a nearly universal constant [106]. The Kolmogorov law is the starting point for most analysis of turbulent flows; armed with the Kolmogorov law for the inertial range, one can make predictions for the functional forms of, for example, the two-point covariance of temperature and pressure fluctuations [1, 2, 4]. The Kolmogorov law also immediately gave an explanation for the anomalous diffusion rate of particles in the atmosphere observed some years earlier by Richardson [107]. Furthermore, it opened the door to practical turbulence modelling — the idea not all scales of a turbulent flow must be remodelled for each new situation is central to, e.g., large eddy simulations (LES), in which the large scales are simulated but the small scales are modelled [4, 104]. Fig. 2.3 shows a particularly dramatic experimental verification of the Kolmogorov law, in measurements of a turbulent jet, spanning roughly two orders of magnitude in wavenumber.

2.9 The Cascade Phenomenology of 2D Turbulence

2.9.1 Fjörtoft's Argument

The appearance of the additional detailed conservation law for enstrophy in two dimensions dramatically changes the nature of spectral transport in comparison to three-dimensional turbulence. Although the actual situation is hopelessly complicated, a simple calculation from Fjörtoft [109][10] yields some considerable insight. Suppose for a moment that the Reynolds number is high enough that we may neglect viscosity, and the spectral equations are truncated to allow only three modes

[10]This presentation is actually a reformulation of Fjörtof's argument given by Lesieur [4]. Nazarenko [110] offers another nice reformulation, given in terms of "centroid" wavenumbers.

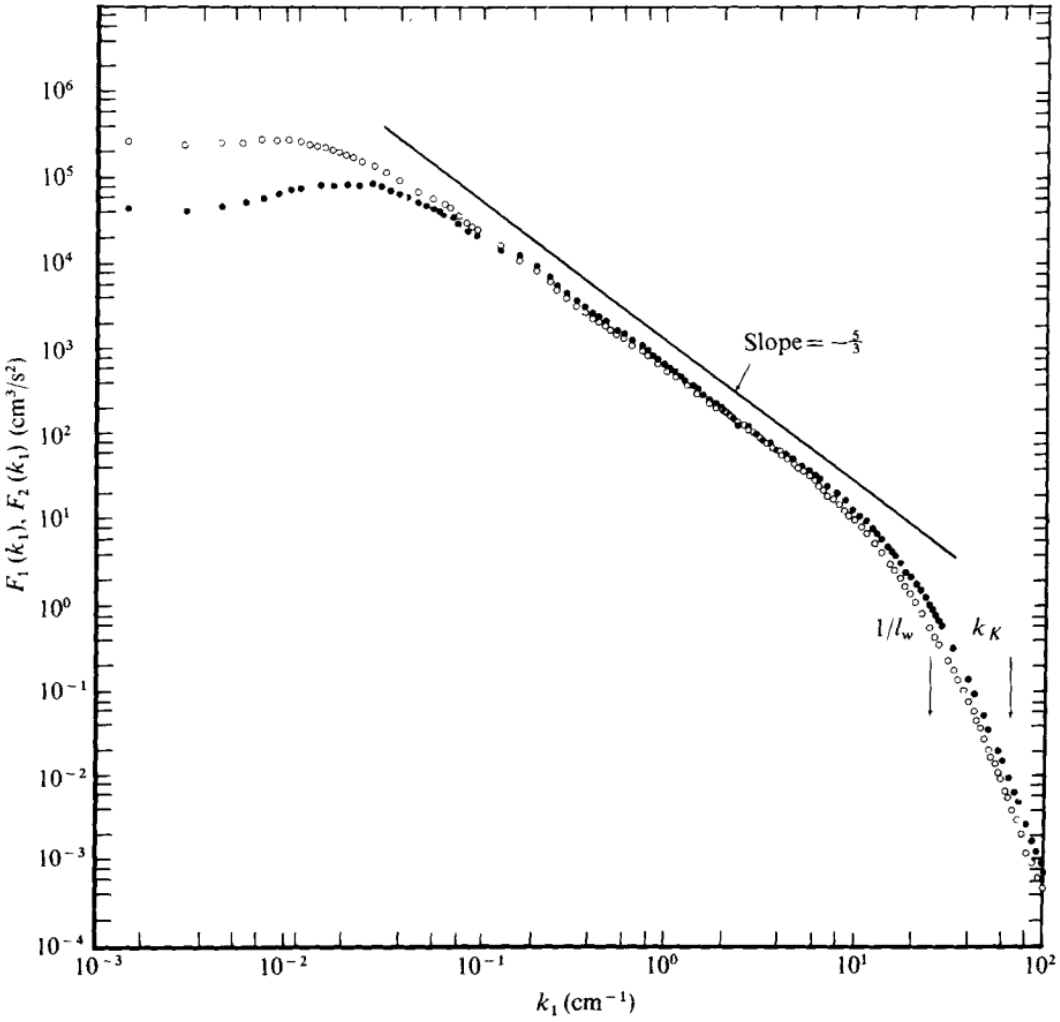

Figure 2.3: Figure reproduced from Champagne (1978), Ref. [108]. Kinetic energy spectra produced from an axis-symmetric turbulent jet. One can clearly see the three different qualitative regions: the energy containing range (low k), the Kolmogorov $k^{-5/3}$ inertial range (intermediate k), and the equilibrium/dissipation range (high k). The Reynolds number is $\mathrm{Re} = 3.7 \times 10^5$.

k **p**, and **q**, which satisfy the triad relation $\mathbf{p} + \mathbf{q} = \mathbf{k}$.[11] For simplicity we can suppose that $p = 2k$, and $q = 3k$. Then the change in the kinetic energy spectrum $\delta E_k = E(k, t_f) - E(k, t_i)$ must satisfy two constraints:

$$\delta E_k + \delta E_p + \delta E_q = 0 \tag{2.78}$$

$$k^2 \delta E_k + p^2 \delta E_p + q^2 \delta E_q = 0 \tag{2.79}$$

Now suppose that all the initial energy is contained in the intermediate wavenumber **p**. Some simple algebra yields

$$\delta E_k = -\frac{5}{8}\delta E_p \qquad \delta E_q = -\frac{3}{8}\delta E_p \tag{2.80}$$

$$k^2 \delta E_k = -\frac{5}{32}\, p^2 \delta E_p \qquad q^2 \delta E_q = -\frac{27}{32}\, p^2 \delta E_p. \tag{2.81}$$

Now, it seems likely that the system would strive to redistribute the excitation in some manner in order to attain equilibrium. From Eqs. (2.78) and (2.79) we find that when the excitation spreads out of the intermediate wavenumber ($\delta E_p < 0$) a transport of energy to $q > p$ requires a large amount of enstrophy to be carried with it. However, even *more* energy must be sent to $k < p$ (along with a small amount of enstrophy) to simultaneously satisfy both detailed conservation laws. In 3D the nonlinear interactions preferentially send energy to high wavenumbers — where most of the modes are — in an attempt to attain statistical equilibrium, and this can be achieved through a generation of enstrophy, because Eq. (2.79) doesn't need to be satisfied. It becomes clear that the Kolmogorov scenario described in the previous section simply *isn't* possible in two dimensions. Another short elementary proof of the inconsistency of the Kolmogorov scenario in two dimensions was given by Lee [111].

2.9.2 Batchelor's Enstrophy Cascade

It was quickly realized that two-dimensional turbulence must have a dramatically different behaviour to three-dimensional turbulence. However, by analogy to the Kolmogorov scenario for 3D turbulence, Batchelor [112] proposed an enstrophy cascade to high wavenumbers could occur, in the context of decaying 2D turbulence.

[11] Note that the detailed conservation laws for energy and enstrophy are preserved under such a truncation.

Recall from Sec. 2.6 that the enstrophy decay depends on vorticity gradients

$$\frac{1}{2}\frac{d\langle\omega^2\rangle}{dt} = \nu\langle\omega\nabla^2\omega\rangle = -\nu\langle|\nabla\omega|^2\rangle. \tag{2.82}$$

But analogous to the enstrophy in three dimensions, the evolution for vorticity gradients themselves involves a nonlinear term

$$\frac{1}{2}\frac{d}{dt}\langle|\nabla\omega|^2\rangle = -\left\langle\frac{\partial u_j}{\partial x_i}\frac{\partial\omega}{\partial x_i}\frac{\partial\omega}{\partial x_j}\right\rangle - \nu\left\langle\left(\frac{\partial^2\omega}{\partial x_i\partial x_j}\right)^2\right\rangle \tag{2.83}$$

which hints at the possibility of a dissipation anomaly for enstrophy. Physically, this would arise from the amplification of vorticity gradients by extension of isovorticity lines — because the vorticity of each fluid element is conserved, the stretching of a vorticity patch in one direction must be compensated by a thinning along the perpendicular. This filamentation process would increase the amount of enstrophy contained in the small scales, while amplifying the vorticity gradients in the process. Such filamentary structures appear during vortex merging events [see e.g., Fig. 2.4(b)], during which vortices form spiral-like arms. By analogy to three-dimensional turbulence, this suggests the enstrophy dissipation rate could be non-vanishing in the inviscid limit:

$$\lim_{\nu\to 0}\nu\langle(\partial\omega/\partial x_i)^2\rangle \to \chi \neq 0 \tag{2.84}$$

and hence that enstrophy would be cascaded to larger wavenumbers through this extension mechanism, until a wavenumber is reached such that dissipation could remove enstrophy from the system. Applying the Kolmogorov phenomenology of Sec. 2.8 gives the characteristic wavenumber and velocity

$$k_d = \left(\frac{\chi}{\nu^3}\right)^{1/6} \qquad\qquad v = (\nu^3\chi)^{1/6}, \tag{2.85}$$

and provided $k_L \ll k_d$ then the enstrophy spectrum in the equilibrium range would be of the form

$$\Omega(k) = v^2 k_d g(k/k_d). \tag{2.86}$$

Furthermore, if $k_L \ll k \ll k_d$, then in the inertial range the spectrum for the *enstrophy cascade* is

$$\Omega(k) = C'\chi^{2/3}k^{-1}, \tag{2.87}$$

or equivalently $E(k) = C'\chi^{2/3}k^{-3}$ for some constant C'. Note that the local Reynolds number argument $[E(k)k]^{1/2}/k\nu \sim 1$ once again recovers k_d. However, the spectrum

yields a logarithmic divergence of the enstrophy in the limit $\nu \to 0$

$$\Omega \propto \chi^{2/3} \ln(k_d/k_L). \tag{2.88}$$

Batchelor suggested that the resolution of this apparent paradox is either: a) if the source of enstrophy is very large, enstrophy will always eventually be removed at the (finite) dissipation wavenumber k_d, or b) if k_d is sufficiently large, the reservoir of enstrophy in the wavenumbers $k \sim L^{-1}$ would eventually become so depleted that the transfer rate χ would diminish to a value, consistent with the total enstrophy Eq. (2.88), such that Eq. (2.87) could be maintained. In other words, he hypothesised that the small scales will reorganise themselves to accomodate whatever the larger scales are delivering to them. Note however that we must therefore abandon the idea that χ remains finite as $\mathrm{Re} \to \infty$.[12]

We can nonetheless obtain Reynolds number estimates for the existence of the equilibrium and inertial ranges by using Eq. (2.87). If the inertial range is large, it follows from integrating the spectrum that the energy will be of the order $E \sim \chi^{2/3} k_L^{-2}$, and hence $U \sim \chi^{1/3} k_L^{-1}$. Since $k_L \sim L^{-1}$ it follows that the condition $k_L \ll k_d$ is equivalent to

$$\frac{k_d}{k_L} \sim \left(\frac{UL}{\nu}\right)^{1/2} \gg 1, \tag{2.89}$$

so we would expect the equilibrium range requires $\mathrm{Re}^{1/2} \gg 1$ and the inertial range requires $\mathrm{Re}^{1/4} \gg 1$. The number of relevant degrees of freedom is then

$$N \sim \left(\frac{k_d}{k_L}\right)^2 \sim \mathrm{Re}. \tag{2.90}$$

Comparing Eqs. (2.90) and (2.77), it follows that 2D flows are significantly less demanding to simulate computationally. Yet Eqs. (2.71) and (2.89) show there is a tradeoff — a larger Reynolds number is required to allow the inertial range to exist.

Meanwhile, by the detailed conservation laws, the energy must be drifting to the large scales through the merging of like-signed vortices or some similar process. In the energy-containing range, the only relevant parameters are the total energy E, which is presumably constant, and the time t. It follows that the characteristic wavenumber

[12] Bounds on the enstrophy dissipation rate at large Reynolds numbers have since been derived, and it has been shown that the dissipation rate does in fact vanish in the limit $\mathrm{Re} \to \infty$ for power-law scalings [113].

and velocity in this range are

$$k_L = (Et^2)^{-1/2} \qquad U = E^{1/2}, \tag{2.91}$$

such that the spectrum would be of the form

$$E(k) = U^2 k_L^{-1} h(k/k_L). \tag{2.92}$$

and the integral scale would grow linearly with time[13]: $L \sim k_L^{-1} \sim E^{1/2}t$. This growth of the integral scale would cause the enstrophy to decay as $\Omega = 2\int k^2 E(k)dk = 2At^{-2}$, where $A = \int x^2 h(x)dx$, and the decay rate would thus scale as $\chi = d\Omega/dt \sim At^{-3}$.

Batchelor's theory has since generated much debate. Firstly, notice that the form of Eq. (2.87) yields a local timescale that is the same for all scales in the cascade

$$\tau(k) \sim [k^3 E(k)]^{-1/2} \sim \chi^{-1/3} = \text{const.} \tag{2.93}$$

This is concerning, because it suggests that the small scales can be directly affected by the large scales; we are forced to question our original assumption of the small scales' ability to attain statistical independency by "forgetting" their history from the large scales. The idea that the decay process occurs over a timescale much longer than the characteristic timescale of the smaller scales now also rests on somewhat shaky foundations. The enstrophy cascade is, in effect, a (relatively) nonlocal process, in which most of the straining of the small scales comes directly from the large scales, and elongated triads rather than a series of local triads are the dominant transport mechanism [16, 114].

While early numerical investigations were found to be broadly consistent with Batchelor's hypothesis [115, 116], observations in later experiments and numerical simulations (at higher resolution) were not entirely consistent with Batchelor's theory, and the spectra observed were often much steeper. This discrepancy was eventually attributed to the formation of *coherent structures* — long-lived, strong regions of vorticity that spontaneously form during the decay process [see Fig 2.4]. These structures, which are stable and essentially laminar, are strongly sensitive to the initial conditions and can often disrupt the similarity state and the cascade process (see Refs [16, 117] and references therein for a detailed discussion). However a more

[13]The integral scale also grows in decaying 3D turbulence. However, the growth is instead because the small scales decay faster than the large ones, and the growth is therefore slower than in two dimensions [2].

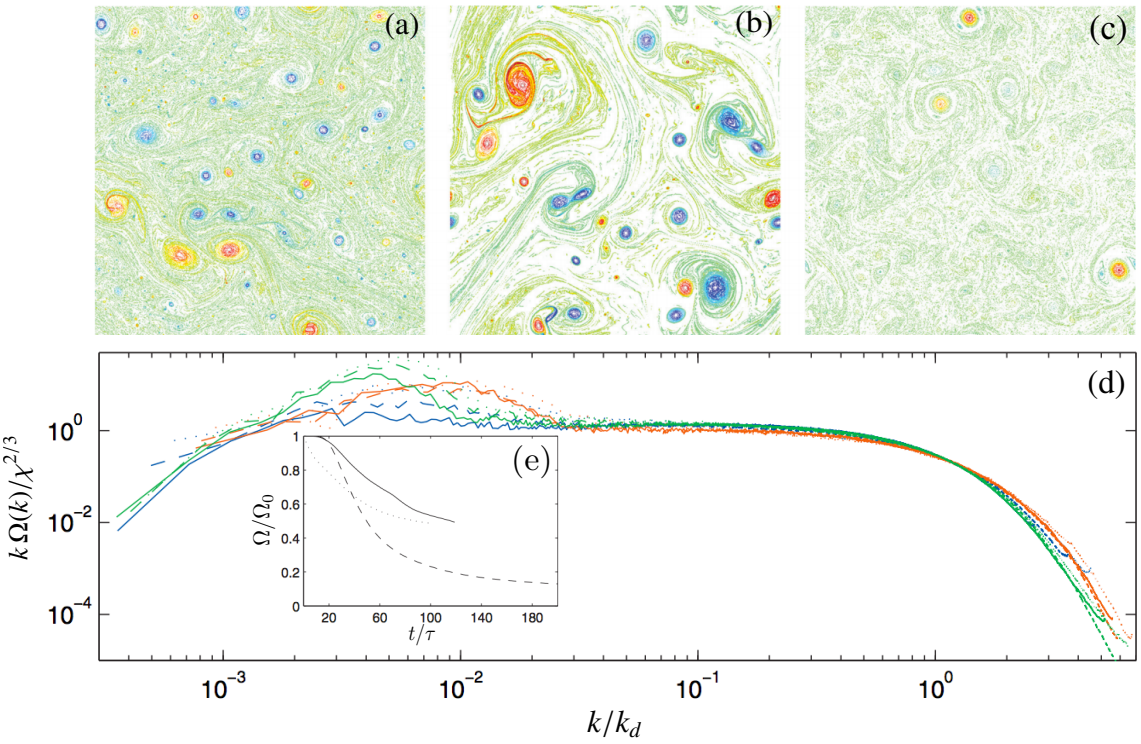

Figure 2.4: Images adapted from Lindborg and Vallgren (2010), Ref. [118]. Images in (a)-(c) show vorticity fields for different initial conditions in decaying 2D turbulence: (a) Random population of enstrophy within a wavenumber shell $k/\Delta k \in [12, 14]$; (b) a regular grid of 64 Gaussian vortices; (c) free decay after initial forcing at wavenumber $k/\Delta k = 30$. In (d), the "compensated" enstrophy spectra $k\Omega(k)/\chi^{2/3}$ are shown: (a) blue; (b) green; (c) red (linetypes show different times). The compensated spectra are seen to be flat over a broad region, indicating the region over which the spectrum conforms to Eq. (2.87), and allow an estimation of the constant C'. In (e), the decay of the normalised enstrophy is shown vs. the time in units of the initial turnover time $\tau = \Omega_0^{-1/2}$, and clearly exhibits non-universal behaviour.

recent numerical study at very large Reynolds numbers [118] found the scaling predicted by Batchelor's theory was robust [Fig. 2.4(d)], even despite the presence of coherent structures, whose size and strength were vastly different depending on the initial condition of the system [Fig. 2.4(a)-(c)]. Despite the apparent inconsistencies in the original assumptions, one can thus apply the theory and attain a value for Batchelor's constant $C' \approx 1.4$ [118], although it does vary more than the 3D Kolmogorov constant under different conditions. Although the k^{-1} scaling can be a robust feature, the Batchelor theory generally does not correctly predict the enstrophy dissipation rate, or the integral scale drift rate, which do not seem to exhibit any universal behaviour (see Fig 2.4(e)).

2.9.3 Kraichnan's Dual Cascade

In a remarkable paper, Kraichnan [119] proposed that 2D turbulence could support a dual cascade process. He envisioned a steady-state scenario in which an idealised external forcing mechanism $F(k) = \epsilon\delta(k-k_f)$ is added to Eq. (2.56), injecting energy at a steady rate ϵ and enstrophy at a steady rate $\eta = 2k_f^2\epsilon$. Kraichnan hypothesised an infinitely extending similarity state of the form

$$E(ak)/E(k) = a^{-n} \tag{2.94}$$

$$T(ak\,|\,ap, aq)/T(k\,|\,p, q) = a^{-(1+3n)/2}. \tag{2.95}$$

where the scaling of $T(k\,|\,p, q)$ is assumed to be the same as $[E(k)]^{3/2}k^{-1/2}$ from dimensional analysis. Through cunning use of the detailed conservation laws, and a series of transformations exploiting the symmetries of $T(k\,|\,p, q)$ to manipulate the flux integrals,[14] Kraichnan showed that two similarity states permitting constant fluxes could exist. A similarity state with $n = 3$ yields

$$\Pi_\epsilon(k) = 0; \qquad \Pi_\omega(k) = \eta, \tag{2.96}$$

which, of course, corresponds to the enstrophy cascade put forward independently by Batchelor. However, Kraichnan also found that the Kolmogorov similarity state with $n = 5/3$ yielded

$$\Pi_\epsilon(k) = \epsilon; \qquad \Pi_\omega(k) = 0. \tag{2.97}$$

Notice that the two similarity states are *mutually exclusive* — a constant flux of one quantity requires the other to vanish — and they could therefore exist simultaneously in different regions of wavenumber space. He thus hypothesised that the energy cascade *can* exist in two-dimensional turbulence, provided it is *downward* in wavenumber (i.e, provided $\Pi_\epsilon = -\epsilon$), in order to satisfy the detailed conservation laws. We may thus have simultaneously the spectrum for the *inverse energy cascade*

$$E(k) = C\epsilon^{2/3}k^{-5/3} \qquad k_L \ll k \ll k_f \tag{2.98}$$

[14] Ref. [120] and the appendix of Ref. [101] provide details regarding the flux calculations that are not so clearly explained in Kraichnan's original article, which is quite dense. Ref. [121]provides some helpful context.

and the *direct enstrophy cascade*[15]

$$E(k) = C'\eta^{2/3}k^{-3} \qquad k_f \ll k \ll k_d. \tag{2.100}$$

While the value of k_d is the same as in the Batchelor scenario, here energy conservation requires from Eq. (2.98) that the total energy grows as $E \sim \epsilon t \sim \epsilon^{2/3}k_L^{-2/3}$, and the integral scale of the turbulence thus grows faster than in the decaying scenario:

$$L \sim k_L^{-1} \sim (\epsilon t^3)^{1/2}. \tag{2.101}$$

Hence, unlike 3D turbulence, forced and decaying 2D turbulence are quite different. The inverse cascade only exists under forcing, and it is never stationary; it grows with time, requiring constant energy input, and the spectrum asymptotically approaches the $k^{-5/3}$ ever more closely over a broader range as time progresses (see Fig. 2.5).[16] Yet in any real physical system there is always a lowest attainable wavenumber. In a phenomenon analogous to Bose-Einstein condensation, two-dimensional turbulence thus exhibits *spectral condensation*. Here, through the inverse cascade, energy can pile up within the lowest available Fourier mode, causing the formation of large-scale vortices at the scale of the system size, creating a "giant dipole". While this spectral pile up can eventually become large enough to disrupt the cascade, it can also be kept in check by large scale frictional damping, which can originate from the three-dimensional system in which the two-dimensional system is embedded [20, 22, 125, 126]. Large scale drag has also been found to cause a steepening of the enstrophy cascade spectrum [123, 127].

Because of the large scale ranges required for the dual cascade, experiments and simulations are often optimised to study only one of the cascades [117, 128–130], for example by placing the forcing either near the largest scale and introducing large-scale

[15]Kraichnan later refined his theory, arguing that the kinetic energy spectrum would have to be compensated by a logarithmic term [122]

$$E(k) = C'\eta^{2/3}k^{-3}[\ln(k/k_f)]^{-1/3} \tag{2.99}$$

since otherwise the enstrophy flux diverges logarithmically. This expression further highlights the nonlocality of the cascade, because k_f is important regardless of the value of k. It appears even quite recent and extremely large simulations have not managed to definitively resolve this very slow logarithmic scaling — the k^{-3} law seems to be a robust feature [22, 123].

[16]This is the conventional view. However, a notable exception is a recent numerical study by Mininni and Pouquet [124]. They showed that decaying 2D turbulence could exhibit evidence of a $-5/3$ scaling under extensive ensemble and time averaging. However, the scaling is also temporally transient and over a somewhat limited scale range.

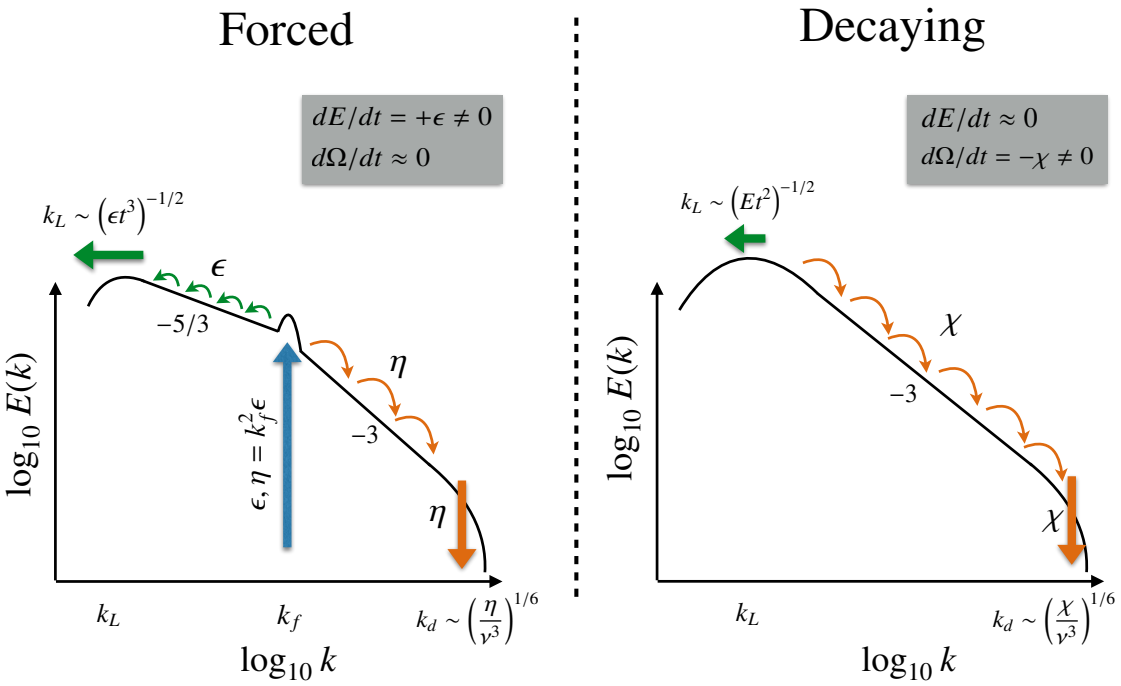

Figure 2.5: A schematic of spectral cascades in two-dimensional turbulence at high Reynolds number. Unlike three-dimensional turbulence, the cascade scenarios are quite different in the forced and decaying scenarios. The dual cascade only occurs when steady forcing is supplied (near some wavenumber k_f) to sustain the inverse energy cascade, with energy growing at the injection rate ϵ. The total enstrophy is approximately constant, being injected and dissipated at a steady rate $\eta = k_f^2 \epsilon$. In the decaying scenario, only the enstrophy cascade persists, and the integral wavenumber k_L decays at a slower rate. The total energy E is approximately conserved, and enstrophy decays at a rate χ.

dissipation [131], or forcing relatively near the dissipation wavenumber k_d [128, 132, 133]. Whereas Kraichnan envisaged the underlying processes to be vortex merger and the simultaneous filamentation of vorticity caused in the process [119], the inverse cascade appears to be a more subtle mechanism. It has been argued the underlying physical mechanism is instead same-sign vortex *aggregation* rather than actual *merger* into individual entities [16, 129], or by a similar but more local version of the thinning process responsible for the enstrophy cascade [134, 135]. Both cascades are known to be less local than the three-dimensional case [101], although the enstrophy cascade is the most nonlocal for the reasons already mentioned in Sec. 2.9.2. The Kraichnan-Batchelor constant in the forced scenario is again $C' \approx 1.4$ [114, 123, 130], whereas the Kraichnan-Kolmogorov constant is much larger, $C \approx 7$ [129]. The larger constant implies a much less efficient cascade (for a given $E(k)$ a large C implies a small ϵ, and vice versa). The enstrophy cascade is generally viewed to be slightly more robust in the forced case, because under certain conditions the continuous forcing provides a mechanism to disrupt the formation of coherent structures, thereby protecting the similarity state from their contamination [16, 114, 123, 130].

Although the cascades were individually verified somewhat earlier, it took 31 years for Kraichnan's prediction of the dual cascade to be verified experimentally. With the experimental developments of soap films and laser doppler velocimetry techniques, [23, 24] an experiment by Rutgers [25], using a vertically flowing soap film continuously forced by vertical combs, eventually provided evidence of the dual cascade scenario (see Fig 2.6).

2.10 Point Vortex Model

We end this chapter by introducing a model that will become highly relevant in those to come. Setting $\nu = 0$ in the Navier Stokes equations yields the *Euler equation*, which describes the motion of a perfect, inviscid incompressible fluid. In the vorticity formulation, it is

$$\frac{\partial \omega}{\partial t} + \mathbf{u} \cdot \nabla \omega = 0, \tag{2.102}$$

which mathematically expresses the fact that, in the absence of viscosity, vorticity is simply advected by the fluid (Sec 2.6). In many cases of interest the vorticity field may have a compact structure, and in such situations it is permissible to study

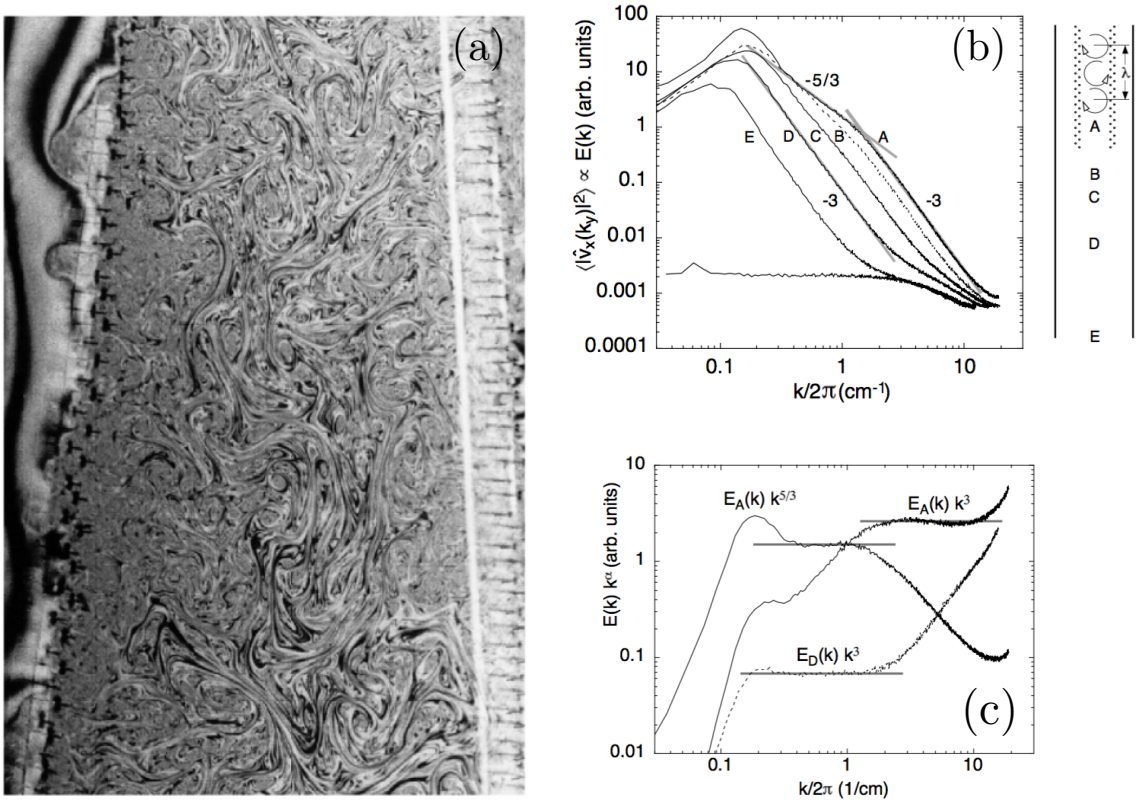

Figure 2.6: Images adapted from Rutgers (1998), Ref. [25]: (a) An image of the turbulent soap film, produced by interference of monochromatic light; (b) Measured kinetic energy spectra at various positions downstream. The case A, which is within the forced region, clearly exhibits a k^{-3} region, a $k^{-5/3}$ region, and a peak at low wavenumbers. The peak is located at a wavenumber corresponding to twice the width between the combs ($k = 2\pi/\lambda$), which sets an upper limit on the integral scale of the turbulence. Measurements at farther distances downstream (B-E) show a clear transition from the forced scenario to the decaying scenario, in which the $k^{-5/3}$ region is absent; (c) Compensated kinetic energy spectra for cases A and D, showing the quality and extent of the $k^{-5/3}$ and k^{-3} scaling regions.

solutions of the limiting form

$$\omega(\mathbf{x}) = \sum_i \Gamma_i \delta^{(2)}(\mathbf{x} - \mathbf{x}_i). \tag{2.103}$$

Analogous to the point masses of celestial mechanics, or the point charges of electromagnetism, these are called *point vortices*. Recall that any vector field can be expressed in terms of a Helmholtz decomposition as

$$\mathbf{u}(\mathbf{x}) = \mathbf{u}_p + \mathbf{u}_\omega = \nabla\theta + \nabla \times \boldsymbol{\psi}. \tag{2.104}$$

Here θ is called the velocity potential and $\boldsymbol{\psi}$ is the streamfunction. Like the vorticity, in two dimensions the streamfunction can be represented by a scalar function $\boldsymbol{\psi} = (0, 0, \psi(x, y))$. While the velocity potential contains the contribution due to irrotational flow, the streamfunction is related to the vorticity field via

$$\nabla^2\psi(\mathbf{x}) = -\omega(\mathbf{x}). \tag{2.105}$$

Since the stream function satisfies a Poisson equation with the vorticity as the source term, by the standard techniques one can write the solution in terms of the Green's function, satisfying

$$\nabla^2 G(\mathbf{x}, \mathbf{x}') = -\delta(\mathbf{x} - \mathbf{x}'), \tag{2.106}$$

as

$$\psi(\mathbf{x}) = \int G(\mathbf{x}, \mathbf{y})\omega(\mathbf{y})d^2\mathbf{y}. \tag{2.107}$$

In the unbounded 2D domain the solution is [136]

$$G(\mathbf{x}, \mathbf{x}') = -\frac{1}{2\pi} \ln \left| \frac{\mathbf{x} - \mathbf{x}'}{L} \right|, \tag{2.108}$$

where L is an arbitrary reference scale. It follows that

$$\psi(\mathbf{x}) = -\frac{1}{2\pi} \sum_i \Gamma_i \ln \left| \frac{\mathbf{x} - \mathbf{x}_i}{L} \right|, \tag{2.109}$$

producing the velocity field

$$\mathbf{u}(\mathbf{x}) = \sum_i \frac{\Gamma_i}{2\pi|\mathbf{x} - \mathbf{x}_i|} \hat{\boldsymbol{\phi}}_i. \tag{2.110}$$

where $\hat{\boldsymbol{\phi}}_i$ is the azimuthal unit vector around vortex i. This leads to an equation of motion for the vortex positions

$$\begin{pmatrix} \dot{x}_i \\ \dot{y}_i \end{pmatrix} = \frac{1}{2\pi} \sum_j{}' \frac{\Gamma_j}{r_{ij}^2} \begin{pmatrix} -y_{ij} \\ x_{ij} \end{pmatrix} \tag{2.111}$$

where $x_{ij} = x_i - x_j$ etc and the prime denotes the omission of the term $i = j$, such that each vortex is advected by every vortex in the fluid except itself. These point vortex equations have a long history in practical flow computation, particularly in situations where the vorticity field is compact [103, 136–138], because the problem is reduced to solving for the motion of only the vorticity containing regions, rather than the entire flow field. Point-vortex motion, modified to allow for vortex merging events, also happens to quite accurately describe the motion of the coherent structures that emerge in decaying two-dimensional turbulence [132, 139, 140].

However, these equations also form a very interesting dynamical system in their own right. Notice that the kinetic energy may be written in the form

$$H = \frac{1}{2} \int |\mathbf{u}(\mathbf{x})|^2 d^2\mathbf{x} = \frac{1}{2} \int |\nabla \psi(\mathbf{x})|^2 d^2\mathbf{x} = \frac{1}{2} \int \psi(\mathbf{x}) \omega(\mathbf{x}) d^2\mathbf{x} \tag{2.112}$$

from which we arrive at the Hamiltonian

$$H = -\frac{1}{2\pi} \sum_{i=1}^{N-1} \sum_{j=i+1}^{N} \Gamma_i \Gamma_j \ln \left| \frac{\mathbf{x}_i - \mathbf{x}_j}{L} \right|, \tag{2.113}$$

where the (infinite) constant self energy of the vortices has been subtracted. The equations of motion can thus be expressed in canonical form

$$\Gamma_i \frac{dx_i}{dt} = \frac{\partial H}{\partial y_i} \qquad\qquad \Gamma_i \frac{dy_i}{dt} = -\frac{\partial H}{\partial x_i}. \tag{2.114}$$

It is worth pausing here to remark on several rather unusual features of the point-vortex system. Firstly, notice that the Hamiltonian *looks* like it contains only an inter-particle interaction term, but in fact it is purely *kinetic*.[17] Second, notice that these "particles" are rather odd; they have no mass (and therefore no inertia), and are governed by a first order differential equation rather than Newton's second law. Thirdly, the interaction between particles has infinite range. In fact, the logarithmic interaction term in the Hamiltonian is identical to that for an interacting Coulomb

[17] Kraichnan rather aptly named it the "kinetic energy of interaction" [141, 142].

gas of point charges in two dimensions, and a two-dimensional plasma in the guiding-centre approximation [143]. Finally, possibly the most striking feature of this system is the nature of the canonical coordinates; the canonical coordinates and hence the phase space of the system are determined by the *physical* coordinates of the vortices. As we will soon see, this has a rather profound effect on the statistical mechanics of the system.

In addition to conserving the vortex number N, the translational and rotational invariance of H leads, by Noether's theorem, to the conservation of the following quantities

$$-\sum_{\alpha} \Gamma_\alpha x_\alpha = P_y \tag{2.115}$$

$$\sum_{\alpha} \Gamma_\alpha y_\alpha = P_x \tag{2.116}$$

$$-\sum_{\alpha} \Gamma_\alpha r_\alpha^2 = I \tag{2.117}$$

$$\sum_{\alpha,\beta} \Gamma_\alpha \Gamma_\beta r_{\alpha\beta}^2 = \ell. \tag{2.118}$$

where $r_{\alpha\beta}^2 = (x_\alpha - x_\beta)^2 + (y_\alpha - y_\beta)^2$. The first three correspond to linear and angular momentum, and the conservation of the last quantity is a consequence of the conservation of the first three. Naturally, due to the general structure of Hamilton's equations, H itself is also conserved since it does not explicitly depend on time:

$$\frac{dH}{dt} = \sum_{i=1}^{n} \left[\frac{\partial H}{\partial q_i} \dot{q}_i + \frac{\partial H}{\partial p_i} \dot{p}_i \right] + \frac{\partial H}{\partial t} = 0. \tag{2.119}$$

It follows from the above conservation properties that the separation d for two vortices is a constant of the motion. Two opposite vortices of equal strength (a vortex dipole) propagate in a straight line in a direction perpendicular to their separation vector, at a velocity $u_d = \Gamma/2\pi d$, while two vortices of the same sign orbit each other about their centre of mass at a fixed distance with angular velocity $\omega = \Gamma/\pi d^2$. The unbounded three-vortex system is unusual, since, by the standard analysis of Hamiltonian systems [136], it is a three-body problem which is integrable. It also holds a particular level of significance because it is the minimal system capable of generating *new* length scales, purely through its own internal motion — clearly there is some analogy with the wavenumber triads in the Navier-Stokes equations. It was solved by Novikov for three identical vortices [144], and generalised to arbitrary charges by Aref [145]. For four vortices or more, the system exhibits chaos [136].

2.10.1 Bounded Domains

The linear nature of the point-vortex problem makes it easily extendible to problems in bounded domains $\mathcal{D}$. Since there is no viscosity, instead of the no slip condition, continuity only requires that the normal component of the velocity field must vanish on the boundary

$$\mathbf{u} \cdot \hat{\mathbf{n}}\Big|_{\partial\mathcal{D}} = 0. \tag{2.120}$$

Since the stream function satisfies Laplace's equation $\nabla^2\psi = 0$ away from the vortex points, this permits use of the *method of images*, as is used in classical electromagnetism [146]. Provided one can find *any* solution that satisfies the boundary condition $\psi\Big|_{\partial\mathcal{D}} = \text{const.}$, Laplace's equation guarantees it is the *unique* solution. One can therefore find the stream function solution by introducing "imaginary" image charges outside the domain in order to enforce the boundary conditions. Note that introducing these images does not introduce additional degrees of freedom; their positions are always completely determined by the positions of the real vortices.

Circular Domain

One of the simplest bounded geometries is a circular domain of radius R (this system relevant to Chapter 4). Here the boundary conditions for a single vortex of strength Γ_i at $\mathbf{x}_i$ can be satisfied by placing an image vortex of strength $\bar{\Gamma}_i = -\Gamma_i$ at the position

$$\bar{\mathbf{x}}_i = \frac{R^2\mathbf{x}_i}{|\mathbf{x}_i|^2}. \tag{2.121}$$

Generalising to an arbitrary number of vortices this gives the Hamiltonian

$$H_\circ = -\frac{1}{2\pi}\sum_i\sum_{j>i}\Gamma_i\Gamma_j \ln\left|\frac{\mathbf{x}_i - \mathbf{x}_j}{R}\right| + \frac{1}{4\pi}\sum_i\sum_j\Gamma_i\bar{\Gamma}_j \ln\left|\frac{\mathbf{x}_i - \bar{\mathbf{x}}_j}{R}\right|, \tag{2.122}$$

and the equations of motion

$$\begin{pmatrix}\dot{x}_i\\ \dot{y}_i\end{pmatrix} = \frac{1}{2\pi}\sum_j{}' \frac{\Gamma_j}{r_{ij}^2}\begin{pmatrix}-y_{ij}\\ x_{ij}\end{pmatrix} + \frac{1}{2\pi}\sum_j^N \frac{\bar{\Gamma}_j}{\bar{r}_{ij}^2}\begin{pmatrix}-\bar{y}_{ij}\\ \bar{x}_{ij}\end{pmatrix} \tag{2.123}$$

where $\bar{x}_{ij} = x_i - \bar{x}_j$, etc., and $\bar{r}_{ij} = \bar{x}_{ij}^2 + \bar{y}_{ij}^2$.

Doubly Periodic Box

The doubly periodic domain, side length L containing a neutral distribution ($\sum_j \Gamma_j = 0$) of N point vortices, is of interest for making connections with homogeneous turbulence (Secs. 2.6 and 2.7), and is relevant in Chapters 4 and 6 of this work.[18] In this system one must evaluate the doubly infinite sum over all periodic image vortices (which here have the same sign as the real vortices) to determine the properties of the basic cell. Although no closed form can be obtained in terms of elementary functions, Weiss and McWilliams [148] have shown that one of the infinite sums can be done analytically, such that the Hamiltonian can be written as

$$H_{\square} = \sum_{i=1}^{N-1} \sum_{j=i+1}^{N} \Gamma_i \Gamma_j \; h\left(\frac{2\pi(\mathbf{r}_i - \mathbf{r}_j)}{L}\right), \tag{2.124}$$

where the vortex pair energy function is given by

$$h(x,y) = \sum_{m=-\infty}^{\infty} \ln\left[\frac{\cosh(x-2\pi m) - \cos(y)}{\cosh(2\pi m)}\right] - \frac{x^2}{2\pi} \tag{2.125}$$

giving the equations of motion[19]

$$\begin{pmatrix} \dot{x}_i \\ \dot{y}_i \end{pmatrix} = \frac{1}{2L} \sum_j{}' \; \Gamma_j \sum_{m=-\infty}^{\infty} \begin{pmatrix} \frac{-\sin(y'_{ij})}{\cosh(x'_{ij}-2\pi m)-\cos(y'_{ij})} \\ \frac{\sin(x'_{ij})}{\cosh(y'_{ij}-2\pi m)-\cos(x'_{ij})} \end{pmatrix} \tag{2.126}$$

where $(x'_{ij}, y'_{ij}) = 2\pi(x_{ij}, y_{ij})/L$, and the infinite sum over m is the sum over the remaining infinite strips in the unsummed (y-)direction. Due to the hyperbolic cosine in the denominators, the infinite sums are rapidly convergent and the replacement $\sum_{m=-\infty}^{\infty} \to \sum_{m=-5}^{5}$ is usually sufficient. Note that the asymmetry in $h(x,y)$ is only apparent, and is due to the arbitrary choice of which direction is summed over analytically; it can be shown that $h(x,y)$ is invariant under the exchange $x \rightleftharpoons y$, as is expected from the symmetry of the domain (Ref. [148] provides a clear derivation and explains this in detail). Campbell and O'Niel [147] provide an alternative expression for the Hamiltonian, which is equivalent to Eq. (2.124) apart from a constant shift.

[18] The more physical system of a (hard-walled) square region can also be understood in terms of a periodic system four times as large, constrained to have a four-fold rotational symmetry, see Ref. [147].

[19] If the prefactor of $1/2L$ seems odd, note that truncating the sum at $m = 0$ and expanding to second order in x'_{ij} and y'_{ij} recovers the equations for the unbounded domain (Eq. (2.111)).

2.10.2 Novikov's Point-Vortex Spectrum

The kinetic energy spectrum for a system of point vortices was first considered by Novikov [144]. Here it is more convenient to work with the vorticity field, and recall from the incompressibility condition that

$$E(\mathbf{k}) = \frac{1}{2}\langle|\mathbf{u}(\mathbf{k})|^2\rangle = \frac{1}{2}\frac{\langle|\omega(\mathbf{k})|^2\rangle}{k^2}. \tag{2.127}$$

For the point vortex system, we have

$$\hat{\omega}(\mathbf{k}) = (2\pi)^{-1}\int d^2\mathbf{x}\;\omega(\mathbf{x})e^{-i\mathbf{k}\cdot\mathbf{x}} = (2\pi)^{-1}\sum_\alpha \Gamma_\alpha e^{-i\mathbf{k}\cdot\mathbf{x}_\alpha} \tag{2.128}$$

which yields

$$\begin{aligned}|\hat{\omega}(\mathbf{k})|^2 &= (2\pi)^{-2}\left(\sum_\alpha \Gamma_\alpha e^{i\mathbf{k}\cdot\mathbf{x}_\alpha}\right)\left(\sum_\beta \Gamma_\beta e^{-i\mathbf{k}\cdot\mathbf{x}_\beta}\right)\\ &= (2\pi)^{-2}\left[\sum_\alpha \Gamma_\alpha^2 + 2\sum_{\alpha<\beta}\Gamma_\alpha\Gamma_\beta\cos(\mathbf{k}\cdot\mathbf{x}_{\alpha\beta})\right]\end{aligned} \tag{2.129}$$

where $\mathbf{x}_{\alpha\beta} \equiv \mathbf{x}_\alpha - \mathbf{x}_\beta$. Evaluating the angular integral, we obtain the kinetic energy spectrum:

$$E(k) = \frac{1}{4\pi k}\left[\sum_\alpha \Gamma_\alpha^2 + 2\sum_{\alpha<\beta}\Gamma_\alpha\Gamma_\beta J_0(kr_{\alpha\beta})\right] \tag{2.130}$$

where $r_{\alpha\beta}^2 = (x_\alpha - x_\beta)^2 + (y_\alpha - y_\beta)^2$. In the point-vortex model, the kinetic energy spectrum is thus determined by the interference of Bessel functions, whose oscillations depend on the distribution of the intervortex distances. The intervortex distances can therefore be considered the active scales of the motion. Aref [142] notes that the spectral formulation in the point vortex system is a bit of an "afterthought" in the sense that the only real reason to adopt a spectral formulation for the point-vortex system is to attempt to make connections with the continuum theory. Here the spectral formulation somewhat clouds interpretation, since the original simplicity of the model arises from being able to deal directly with the vortex positions. The parameter k only appears as an additional and somewhat redundant parameter, and we are ultimately stuck with an expression that explicitly contains the intervortex distances $r_{\alpha\beta}$. Possibly for this reason, in comparison with the other elements of the point-vortex model, the spectral formulation remains relatively unexplored [142, 149, 150].

2.10.3 Statistical Mechanics of the Point-Vortex System

Since two-dimensional, freely evolving flows at large Reynolds numbers are characterized by approximately constant energy, unlike three dimensional flows they invite a statistical mechanics treatment. Via the point vortex model, Onsager [151] offered a statistical mechanical explanation for the spontaneous formation of large scale structures. He realized that the unusual nature of the canonical coordinates results in a bounded phase space whenever the vortices are confined within a spatial boundary, and this bounded phase space has profound consequences on the statistical mechanics of the system. The volume of phase space occupied by states that have an energy below or equal to some value $\mathcal{E}$ may be written as

$$\Phi(\mathcal{E}) = \int d^2\mathbf{x}_1 \dots d^2\mathbf{x}_N \Theta(\mathcal{E} - H(\mathbf{x}_1, \dots \mathbf{x}_N)) \tag{2.131}$$

where we have used the Heaviside step function $\Theta(x)$ to pick out all values of H below or equal to $\mathcal{E}$. The function $\Phi(\mathcal{E})$ is everywhere positive and monotonically increasing, with lower and upper bounds $\Phi(-\infty) = 0$, and $\Phi(\infty) = A^N$ respectively, where A is the volume of the bounded domain and N is the number of vortices. This behaviour is in stark contrast with most systems, where Φ diverges as $\mathcal{E} \to \infty$. The number of states at some energy $\mathcal{E}$ is then given by

$$W(\mathcal{E}) = \Phi'(\mathcal{E}) = \int d^2\mathbf{x}_1 \dots d^2\mathbf{x}_N \delta(\mathcal{E} - H(\mathbf{x}_1, \dots, \mathbf{x}_N)) \tag{2.132}$$

and is everywhere positive. As a consequence of the finite phase-space volume, W must reach a maximum at some finite value, $\mathcal{E} = \mathcal{E}_m$, because it must tend to zero for $\mathcal{E} \to \pm\infty$, where $\Phi \to$ const. Recalling the familiar thermodynamic formulae for the entropy and temperature

$$S = k_B \ln W \qquad \frac{1}{T} = \left(\frac{\partial S}{\partial \mathcal{E}}\right)_{N,V} = \frac{1}{W}\left(\frac{\partial W}{\partial \mathcal{E}}\right)_{N,V} \tag{2.133}$$

it follows that T must be formally negative for $\mathcal{E} > \mathcal{E}_m$. With remarkable foresight, Onsager deduced that [151]:

> *"If $T < 0$, then vortices of the same sign will tend to cluster, — preferably the strongest ones —, so as to use up excess energy at the least possible cost in terms of degrees of freedom. It stands to reason that the large compound vortices formed in this manner will remain as the only conspicuous features of the motion; because the weaker vortices, free to roam practi-*

cally at random, will yield rather erratic and disorganised contributions to the flow."

It is worth reiterating that while the vortex clustering is associated a preferential transport of energy to large scales and formation of a spectral condensate, it is not necessarily associated with an inverse energy cascade. The statistical mechanics of the point vortex model only explains self-organisation, which occurs both in the forced and decaying scenarios. In the decaying scenario there is no inverse energy cascade, even though energy is still preferentially transported to large scales through vortex merger, eventually causing a macroscopic population of energy in the lowest k mode. The inverse energy cascade is a possible mechanism by which the system can try to *achieve* the spectrally condensed equilibrium, but it is a special state exhibiting scale invariance, constant flux, and approximately local spectral transport, and relies on continuous forcing.[20]

The statistical mechanics approach initiated by Onsager has contributed significantly to the understanding of the equilibrium end states of decaying 2D turbulent flows. In particular, considering neutral vortex configurations for vortices of equal magnitude, Joyce and Montgomery [152, 153] derived a nonlinear, mean-field "sinh-Poisson" equation for the streamfunction based on a maximum entropy principle. Remarkably, the Montgomery-Joyce approach was found to agree with the long time dynamics of Navier-Stokes simulations, even for only moderate Reynolds numbers of $\mathrm{Re} \sim 1000 - 10000$ [154]. The approach was generalized to arbitrary charges (relevant to the full Euler equation) by Miller [155] and Robert and Sommeria [156]. For a detailed discussion of the statistical mechanics approach we refer the reader to the review by Eyink and Sreenivasan [143], and references therein.

[20]Note that Kraichnan [119, 141] did however use the argument of negative temperatures to justify the flux direction for the inverse energy cascade. Instead of point vortices, he analysed the equilibrium states of the Euler equation in a truncated Fourier series. Whereas the point-vortex model exhibits negative temperatures for large values of E/N (the energy per vortex), he showed that the truncated Euler equilibria exhibit negative temperatures for large values of E/Ω. These equilibrium states exhibit a pile up of the energy at the low wavenumber cutoff, and a pileup of enstrophy at the high wavenumber cutoff.

Chapter 3

Quantum Fluids and Quantum Turbulence

This chapter introduces the relevant background on quantum fluids and quantum turbulence. The basic properties of the Gross-Pitaevskii equation and its hydrodynamic formulation, quantum vortices, and vortex dynamics are covered. While 2D quantum turbulence itself is a relatively new field, much of the relevant underlying physics of quantum vortices has been well studied, and some of the knowledge about 3D quantum turbulence in superfluid helium provides useful guidance. Towards the end of the chapter, the recent developments in the studies of wakes, cascades and negative temperature equilibrium states are reviewed, to provide motivational context for the original work presented in the subsequent chapters.

3.1 Gross-Pitaevskii Equation

Below certain critical temperatures, liquid helium and other substances comprised of particles obeying Bose statistics undergo *Bose-Einstein condensation*, in which a macroscopic population of particles condenses into the quantum mechanical ground state of the system. Provided the system is well below the critical temperature, and not too strongly interacting, one can model a dilute gas Bose condensate via the Gross-Pitaevskii equation (GPE) [40], which describes the evolution of the condensate order parameter or *condensate wavefunction* $\psi(\mathbf{x}, t)$

$$i\hbar\frac{\partial\psi(\mathbf{x},t)}{\partial t} = \left[-\frac{\hbar^2\nabla^2}{2m} + V(\mathbf{x},t) + g|\psi(\mathbf{x},t)|^2\right]\psi(\mathbf{x},t). \tag{3.1}$$

Here m is the atomic mass of a constituent particle, and $V(\mathbf{x}, t)$ embodies any external potentials. The nonlinear term arises from assuming two-body interactions mediated via a delta function pseudo-potential, where the interaction parameter

$$g = \frac{4\pi\hbar^2 a_s}{m} \tag{3.2}$$

characterises the strength of the two-body interactions in terms of the s-wave scattering length a_s. The energy of the collisions involved is assumed to be sufficiently low that only s-wave scattering processes occur within a partial waves expansion [157]. It is often convenient to introduce the GPE operator

$$\mathcal{L}[\psi] \equiv \left[-\frac{\hbar^2\nabla^2}{2m} + V(\mathbf{x}, t) + g|\psi(\mathbf{x}, t)|^2\right] \tag{3.3}$$

such that the GPE may be more succinctly written as

$$i\hbar\frac{\partial\psi}{\partial t} = \mathcal{L}\psi. \tag{3.4}$$

There are a number of ways to arrive at the GPE: it can be derived by factorising the full many-body wavefunction into a product of single-particle ground states [157], or, alternatively, it can be derived within the framework of second quantisation by replacing the quantum field operator with its expectation value in its Heisenberg equation of motion [158]. This amounts to assuming that the occupation of the system ground state is sufficiently large that quantum fluctuations can be neglected. Therefore, despite the explicit appearance of Planck's constant $\hbar$ in the Gross-Pitaevskii equation, it is in fact a (semi) *classical, mean-field* equation. It has precisely the same form as the nonlinear Schrodinger equation used to study other nonlinear wave phenomena, for example, ocean waves and optics in nonlinear materials, and the "rogue waves" that appear in these systems [14].

Dilute Atomic Bose-Einstein Condensates

The Gross-Pitaevskii equation is a zero temperature, classical field theory for a Bose-Einstein condensate, valid for low temperatures, weak interactions, and reasonably large condensate atom numbers [33]. As dilute atomic BECs satisfy precisely these assumptions, they are extremely well described by the GPE at sufficiently low temperatures and high condensate atom numbers, where condensate fractions of $\sim 99\%$ are typical [157]. While in atomic gases a_s can be either positive (repulsive) or negative

(attractive) depending on the atomic species, we will only focus on the case $a_s > 0$ throughout this thesis. It is difficult to overstate the success of this model in describing atomic condensates: it correctly captures many aspects of condensate dynamics, such as collective oscillations, vortex lattice formation, and soliton dynamics (see, e.g., Ref. [157]). While corrections are needed to incorporate the physics of higher temperatures, or quantum effects in smaller condensates, in this thesis we happen to be interested in physics where the conditions of low temperature and large atom numbers are required, such that the GPE should be a sufficiently accurate model.

Superfluid Helium

The Gross-Pitaevskii equation was in fact first derived as a model to better understand superfluid helium [159], and it is still used as a model of superfluid helium, particularly for physics involving vortex dynamics. However, since the GPE assumes only two-body interactions it is only a qualitatively accurate model of superfluid helium, which only has a condensate fraction of about 8%, even when the superfluid fraction is near unity [160]. This severe *quantum depletion* is due to the presence of strong interactions. Nonetheless it can be a very informative model for vortex dynamics and quantum turbulence in ^{4}He for temperatures $\lesssim$ 1K, below which the role of the normal fluid component becomes negligible at normal pressures [40, 161]. Here the main advantage of the Gross-Pitaevskii equation is that much of the essential physics is contained within it, including superfluidity, vortex nucleation, vortex reconnection and annihilation, and sound wave propagation. However, the Gross-Pitaevskii equation does not capture all the physics in superfluid helium; a well-known feature it fails to capture is the so-called "roton" minimum in the excitation spectrum [162]. Furthermore, being a cubic nonlinear equation, it can be quite demanding to simulate numerically for large systems. Turbulence in superfluid helium is therefore also typically studied by a number of other phenomenological models, such as vortex filament models [38], semi-classical, two-fluid models like the Hall-Vinen-Bekharivich-Khalatnikov (HVBK) equations [64] or modified Gross-Pitaevskii equations [66]. The Gross-Pitaevskii equation is also used as a phenomenological guide to investigate vortex dynamics in neutron stars, despite these systems being fermionic, relativistic, and strongly interacting [36, 37].

3.1.1 Integrals of Motion

The condensate wavefunction is normalised to the total number of atoms

$$\int d\mathbf{x}\, |\psi(\mathbf{x},t)|^2 = N, \tag{3.5}$$

and the total energy is given by

$$\mathcal{E} = \int d\mathbf{r} \left\{ \frac{\hbar^2}{2m} |\nabla\psi(\mathbf{x},t)|^2 + V(\mathbf{x},t)|\psi(\mathbf{x})|^2 + \frac{g}{2}|\psi(\mathbf{x},t)|^4 \right\}, \tag{3.6}$$

where the terms are the kinetic, potential, and interaction energies respectively. The particle number N is conserved by the dynamics, and $\mathcal{E}$ is conserved provided the external potential is time independent.

3.1.2 Time Independent GPE

Like the Schrodinger equation, the Gross-Pitaevskii equation allows stationary solutions of the form $\psi(\mathbf{r},t) = \psi(\mathbf{r})e^{-i\mu t/\hbar}$, yielding the time-independent equation

$$\left[-\frac{\hbar^2\nabla^2}{2m} + V(\mathbf{x}) + g|\psi(\mathbf{x})|^2 - \mu \right] \psi(\mathbf{x}) = 0 \tag{3.7}$$

where the energy eigenvalue now instead the μ is the *chemical potential*. In a uniform system with $V(\mathbf{x}) = 0$, the solution is $\psi = n_0^{1/2}$, where n_0 is the constant background atomic number density, and hence chemical potential has the value $\mu = n_0 g$. Since the time dependence of such nonlinear eigenstates is only a global phase, it is often useful to remove this trivial time dependence from the stationary solutions by working in a frame rotating with the chemical potential μ, redefining the time-dependent equation as

$$i\hbar\frac{\partial\psi(\mathbf{x},t)}{\partial t} = \left[-\frac{\hbar^2\nabla^2}{2m} + V(\mathbf{x},t) + g|\psi(\mathbf{x},t)|^2 - \mu \right] \psi(\mathbf{x},t). \tag{3.8}$$

3.1.3 Thomas Fermi Approximation

As a nonlinear partial differential equation, the GPE is not, in general, particularly analytically tractable. However, for condensates containing a large number of atoms, the interaction term can dominate over the kinetic energy term, and an approximate solution to the time independent equation can be obtained by dropping the kinetic

energy operator. This yields the solution

$$\psi(\mathbf{x}) = \sqrt{\frac{\mu - V(\mathbf{x})}{g}}, \quad V(\mathbf{x}) \leq \mu \tag{3.9}$$

and $\psi(\mathbf{x}) = 0$ otherwise. For the common case of a harmonically confined condensate with

$$V(\mathbf{x}) = \frac{1}{2} m\omega^2 r^2 \tag{3.10}$$

the density reaches zero at the *Thomas-Fermi radius*

$$R_{\mathrm{TF}} = \sqrt{\frac{2\mu}{m\omega^2}}, \tag{3.11}$$

but the definition naturally applies to any trapping potential. For the case of a repulsive Gaussian obstacle

$$V(\mathbf{x}) = V_0 \exp(-r^2/\sigma^2) \tag{3.12}$$

in an otherwise uniform density system, the *radius of depletion*

$$a = \sigma \left[\ln(V_0/\mu)\right]^{1/2}, \quad V_0 > \mu, \tag{3.13}$$

is a measure of the size of the density hole produced. We will find this parameter useful when studying the transition to quantum turbulence in Chapter 5.

3.1.4 Harmonic vs. Hard-Wall Trapping Potentials

Although the harmonic trap has been the workhorse potential for BECs since their first realisation [57, 58, 163], such confinement is highly undesirable for studying quantum turbulence [164]. The inhomogeneous density profile from such confinement is rather unique to BECs, and somewhat irrelevant for the practical situations of interest. Parabolic density profiles are not particularly relevant in, for example, superfluid helium or classical fluid turbulence. The harmonic density profile also introduces an additional degree of complexity to a problem that is in many respects already too difficult to solve: the turbulence in such an environment cannot be approximated as isotropic or even homogeneous, apart from within a very small region within the center of the system. Furthermore, some of the more interesting features of 2D quantum turbulence also happen to be completely destroyed by a harmonic confining potential

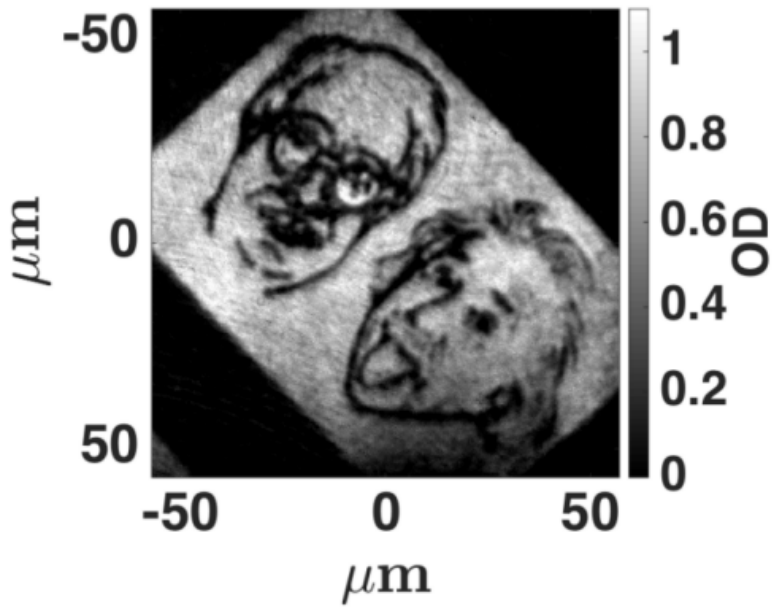

Figure 3.1: Image adapted from Gauthier *et al.* (2016), Ref. [71]. Artistic impressions of Bose and Einstein, within a nearly pure, and otherwise uniform Bose-Einstein condensate of $N = 5.2 \times 10^5$ ^{87}Rb atoms. Dark regions correspond to a low optical density, i.e., regions containing fewer atoms.

(see Sec. 3.9). Fortunately, hard-wall trapping potentials have been recently demonstrated experimentally [70]. Furthermore, techniques using time-averaged "painted potentials" [165], and digital micro-mirror devices [71], allow trapping potentials of virtually any desired geometry to be created in a 2D plane (see Fig. 3.1).

3.1.5 Quasi-2D Systems

If the condensate is strongly confined in the z-direction, a quasi two-dimensional system can be created. Consider for example the common case of harmonic confinement

$$V(\mathbf{x}) = \frac{1}{2}m(\omega_r^2 r^2 + \omega_z^2 z^2), \tag{3.14}$$

with $\hbar\omega_z \gg \hbar\omega_r$. Provided $\hbar\omega_z$ is much larger than any other characteristic energy in the problem, then in the z-direction, the system becomes "frozen" into the harmonic oscillator ground state $\phi(z)$, and one may thus write $\psi(\mathbf{x}) = \psi(x, y)\phi(z)$. The z-direction dependence can then be integrated out, yielding an effectively two-dimensional description. Integrating out the z-dependence is equivalent to making the replacements $g \to g/\sqrt{2\pi}l_z$ where $l_z = \sqrt{\hbar/m\omega_z}$ is the harmonic oscillator length

in the z direction, $\nabla^2 \to \partial_x^2 + \partial_y^2$ and $\mu \to \mu - \hbar\omega_z/2$. The work in this thesis is conducted exclusively within this quasi-2D framework. While assuming this kind of tight confinement is a useful theoretical simplification, note that it is not required to achieve effectively two-dimensional vortex dynamics. It is only required that the axial dimension is comparable to the characteristic size of a vortex $l_z \sim \xi$, such that excitations along the vortex lines (Kelvin waves), and vortex reconnections are suppressed [166] (see also Secs. 3.4.1 and 3.6.1). The case of strict two-dimensional confinement will result in a greater importance of phase fluctuations, which can destroy the phase coherence of the BEC [167].

3.2 Quantum Hydrodynamics

3.2.1 Hydrodynamic Formulation

By the standard polar representation of complex numbers, the wavefunction can be written as

$$\psi(\mathbf{x}, t) = \sqrt{n(\mathbf{x}, t)} e^{i\theta(\mathbf{x},t)}, \tag{3.15}$$

where $n(\mathbf{x}, t)$ and $\theta(\mathbf{x}, t)$ are real scalar fields, which physically correspond to the atomic number density and phase, respectively. In the context of Schrödinger-like equations, this transformation is often referred to as the Madelung transformation. Through this transformation, the Gross-Pitaevskii equation can be cast into hydrodynamical form. Firstly, by inspecting the probability current

$$\mathbf{j}(\mathbf{x}, \mathbf{t}) = \frac{i\hbar}{2m}(\psi\nabla\psi^* - \psi^*\nabla\psi) \tag{3.16}$$

we find from the Madelung transformation this can be written as $\mathbf{j} = n\mathbf{u}$, where

$$\mathbf{u}(\mathbf{x}, t) \equiv \frac{\hbar}{m}\nabla\theta(\mathbf{x}, t). \tag{3.17}$$

Clearly, the phase acts as a velocity potential, and it follows that the flow must have zero curl everywhere within the fluid interior. Inserting Eq. (3.15) into Eq. (3.8), gathering the imaginary terms yields the mass continuity equation

$$\frac{\partial n}{\partial t} + \nabla \cdot (n\mathbf{u}) = 0 \tag{3.18}$$

and the real part yields the quantum Euler equation

$$m\frac{\partial \mathbf{u}}{\partial t} = -\nabla\left(\delta\mu + \frac{1}{2}m\mathbf{u}^2\right), \tag{3.19}$$

which clearly resembles Newton's second law for a conservative system in which

$$\delta\mu = V_{\text{ext}} + gn - \frac{\hbar^2}{2m\sqrt{n}}\nabla^2\sqrt{n} - \mu \tag{3.20}$$

measures the change in the chemical potential relative to the groundstate value, behaving as an effective potential. The term involving the Laplacian is inherently quantum, and is called the *quantum pressure*. Introducing the mass density $\rho = mn$, we can expand the Euler equation to give a more familiar form [cf. Eq. (2.1)][1]

$$\rho\left(\frac{\partial u_i}{\partial t} + (u_j\partial_j)u_i\right) = -\partial_i p + \partial_j\Sigma_{ij} + f_i \tag{3.21}$$

where we have once again opted for index notation with the Einstein summation convention over repeated indices. Here

$$p = \frac{1}{2}\frac{g\rho^2}{m^2} \tag{3.22}$$

is a "classical" pressure,

$$f_i = -\frac{\rho}{m}\partial_i V \tag{3.23}$$

is an external forcing term, and

$$\Sigma_{ij} = \left(\frac{\hbar}{2m}\right)^2 \rho\,\partial_i\partial_j \ln\rho \tag{3.24}$$

is the *quantum stress* tensor. The Gross-Pitaevskii equation thus describes the evolution of a perfect (inviscid), compressible fluid [Eqs. (3.21) and (3.18)]. Notice that the diagonal elements of the quantum stress term (the quantum pressure) serve to prohibit rapid variations in the density. The off-diagonal elements of the quantum stress (*shear* stress) allow for the production of shear from density gradients. In contrast to a classical Euler fluid, the quantum stress therefore allows for the possibility of vortex formation and drag even though there is *no* viscosity [compare Eqs. (3.24) and (2.4)]. However, being proportional to $\nabla\ln\rho$, the quantum stresses only become

[1] Recall $\frac{1}{2}\nabla(\mathbf{u}\cdot\mathbf{u}) = \mathbf{u}\cdot\nabla\mathbf{u} + \mathbf{u}\times(\nabla\times\mathbf{u})$.

significant when both the density becomes comparatively small to the background value, and density gradients become quite rapid. Much like viscosity, the quantum stress is therefore most important near obstacles, boundaries, or density shocks. If it were not for the quantum stress, the BEC would be a simple *barotropic* fluid since the pressure would be only an algebraic function of the density: $p = p(\rho)$. However, for the full equation of state $p + p_Q \equiv \frac{1}{2}g(\rho/m)^2 - (\hbar/2m)^2\rho\left(\frac{\nabla^2}{2}\right)\ln\rho$, although the pressure is still uniquely related to the density, it is now related through a differential rather than algebraic equation [66, 168][2].

3.2.2 Healing Length

Consider a semi-infinite system confined by an impenetrable barrier for $x \leq 0$. By symmetry, the Gross-Pitaevskii equation is reduced to the one-dimensional problem

$$\left[-\frac{\hbar^2}{2m}\frac{d^2}{dx^2} + g|\psi(x)|^2 - \mu\right]\psi(x) = 0, \tag{3.25}$$

subject to the boundary conditions $\psi(0) = 0$ and $\psi \to \sqrt{n_0}$ as $x \to \infty$. A straightforward calculation yields the solution

$$\psi(x) = \sqrt{n_0}\tanh(x/\xi) \tag{3.26}$$

where

$$\xi = \frac{\hbar}{\sqrt{mn_0 g}} \tag{3.27}$$

is called the *healing length*. The healing length defines a fundamental length scale in this quantum fluid, and can be considered the "minimum" relevant length scale over which the condensate wavefunction may vary. It is equally valid to consider the healing length as being a characteristic length scale at which the kinetic energy term (quantum pressure) will reach a similar order of magnitude as the repulsive interactions:

$$\frac{\hbar^2}{2m\xi'^2} \sim n_0 g, \tag{3.28}$$

such that it becomes energetically unfavourable to lower the density by generating spatial variations of order ξ' or smaller, because the energy cost of creating such fluctuations outweighs that of a smoother profile with a larger interaction energy. It is common to define ξ' as the healing length in the literature, giving an extra factor

[2]Note that in d dimensions, the Laplacian in the p_Q term will be $\frac{\nabla^2}{d}$.

of $1/\sqrt{2}$, but we will use ξ, Eq. (3.27), throughout this thesis.

3.2.3 Speed of sound

Suppose we have a uniform system, which, at hydrostatic equilibrium has the solution $\psi = \sqrt{n_0}$. Now, suppose we disturb the equilibrium with a small, time-dependent velocity field $\delta\mathbf{u}(\mathbf{x}, t)$, which creates small density and pressure fluctuations so that $\rho = \rho_0 + \delta\rho$ and $p = p_0 + \delta p$ respectively. Expanding to first order in $\mathbf{u}$, $\delta\rho$, and δp, Eqs. (2.5) and (3.21) become

$$\frac{\partial \delta\rho}{\partial t} = -\rho_0 \nabla \cdot \delta\mathbf{u}, \qquad \frac{\partial \delta\mathbf{u}}{\partial t} = -\frac{1}{\rho_0}\nabla\delta p + \left(\frac{\hbar}{2m}\right)^2 \nabla(\nabla^2 \delta\rho). \tag{3.29}$$

Taking the time derivative of the first and making use of the second gives an equation for dispersive density waves

$$\frac{\partial^2 \delta\rho}{\partial t^2} = \left(\frac{\rho_0 g}{m^2}\right)\nabla^2\delta\rho - \left(\frac{\hbar}{2m}\right)^2 \nabla^4 \delta\rho \tag{3.30}$$

where Eq. (3.22) has eliminated the pressure in favour of the density. Assuming plane wave solutions of the form $\delta\rho = \varepsilon\cos(\mathbf{k}\cdot\mathbf{x} - \omega t)$, $\varepsilon \ll 1$ we obtain Bogoliubov's dispersion relation

$$\epsilon(\mathbf{k}) = \hbar\omega(\mathbf{k}) = \left[\frac{\hbar^2 k^2}{2m}\left(\frac{\hbar^2 k^2}{2m} + \frac{2\rho_0 g}{m}\right)\right]^{1/2}. \tag{3.31}$$

Clearly the dispersive effects only become noticeable for wavelengths $k \sim \xi^{-1}$. If $k\xi \ll 1$, we obtain an ordinary wave equation

$$\frac{\partial^2 \delta\rho}{\partial t^2} = c^2 \nabla^2 \delta\rho, \tag{3.32}$$

where

$$c = \sqrt{\frac{\rho_0 g}{m^2}} = \sqrt{\frac{n_0 g}{m}} = \sqrt{\frac{\mu}{m}} \tag{3.33}$$

is the speed of sound. Eq. (3.33) can be equivalently expressed as in terms of the thermodynamic relation $c^2 = (\partial p/\partial\rho)_S$, where, as usual, the subscript indicates that the derivative is taken at constant entropy S. In this limit it is therefore permissible

to define the *isentropic compressibility*

$$\beta_S = \frac{1}{\rho_0 c^2} = \frac{1}{g n_0^2} = \frac{g}{\mu^2}. \tag{3.34}$$

A straightforward calculation from the ideal gas law yields $\beta_s \sim 10^{-5}$ Pa^{-1} for air, whereas for water it is of order 10^{-9} Pa^{-1} (inverse of bulk modulus). In a typical BEC experiment using ^{87}Rb, where $m \sim 10^{-25}$ kg, $c \sim 10^{-3}$ ms^{-1}, and $n \sim 10^{20}$ m^{-3}, yields $\beta_S \sim 10^{11}$ Pa^{-1}. As we might expect from a dilute Bose gas, it is *very* compressible.

3.2.4 Superfluidity

Quantum fluids like He-II and atomic BECs exhibit superfluidity; below a certain *critical velocity*, the flow is perfectly frictionless, and an obstacle can move through the fluid unimpeded. This can be understood in terms of a simple argument given by Landau. Imagine an impurity of mass M (suppose it is a stirring cylinder) travels through the fluid with some initial velocity $\mathbf{u}_i$. If the impurity creates an excitation of the fluid of energy $\hbar\omega(\mathbf{k})$ and momentum $\hbar\mathbf{k}$, this leaves the impurity with a final velocity $\mathbf{u}_f$. The process must conserve energy

$$\frac{1}{2}Mu_i^2 = \frac{1}{2}Mu_f^2 + \hbar\omega \tag{3.35}$$

and momentum

$$M\mathbf{u}_i = M\mathbf{u}_f + \hbar\mathbf{k}. \tag{3.36}$$

Combining these equations and completing the square gives

$$\hbar\omega = \hbar\mathbf{k}\cdot\mathbf{u}_i - \frac{\hbar^2 k^2}{2M}, \tag{3.37}$$

and if M is very large or k is small, we may reasonably neglect the last term. Hence excitations cannot be created unless

$$u_i \geq \left|\frac{\mathbf{k}\cdot\mathbf{u}_i}{k}\right| \geq \frac{\omega(\mathbf{k})}{k}, \tag{3.38}$$

and we thus arrive at the *Landau criterion* for the critical velocity

$$u_c = \min\left(\frac{\omega(\mathbf{k})}{k}\right). \tag{3.39}$$

Recalling the dispersion relation from Sec. 3.2.3

$$\epsilon(\mathbf{k}) = \hbar\omega(\mathbf{k}) = \left[\frac{\hbar^2 k^2}{2m}\left(\frac{\hbar^2 k^2}{2m} + \frac{2\rho g}{m}\right)\right]^{1/2}$$

we find the minimum value occurs in the limit $k \to 0$, yielding $u_c = c$, or $\mathrm{Ma}_c = 1$. Hence, unless the velocity exceeds the speed of sound, a Bose condensate will exhibit superfluidity; no excitations of the fluid are permitted, and hence no reaction force can be exerted on the obstacle. Notice that the interactions of the Bose gas play a central role here — without the interatomic interactions, the spectrum would not be linear at low k, and thus the critical velocity would instead be $u_c = 0$.

3.2.5 Effectively Incompressible Flow

It is immediately evident from Eq. (3.18) that, unlike Eqs. (2.1) and (2.2), we are dealing with a compressible and not an incompressible fluid. In fact, we found in Sec. 3.2.3 that the dilute Bose gas has a compressibility that is orders of magnitude greater than air. However, all compressible fluids can achieve incompressible flow (that is $\nabla \cdot \mathbf{u} = 0$) to a very good approximation, provided certain conditions are satisfied.

Suppose a steady flow is produced by an obstacle, of characteristic dimension $D \gg \xi$, travelling through a large body of the fluid with a constant velocity u. With the exception of a thin region of width $\sim \xi$ in the immediate vicinity of the obstacle, the quantum stress may be neglected, and the hydrodynamic equations can be reduced to the form

$$\nabla \cdot (\rho\mathbf{u}) = 0, \qquad (\mathbf{u} \cdot \nabla)\mathbf{u} = -\frac{1}{\rho}\nabla p. \tag{3.40}$$

From the continuity equation we then obtain

$$\nabla \cdot \mathbf{u} = -\frac{1}{\rho}(\mathbf{u} \cdot \nabla)\rho, \tag{3.41}$$

and using Eq. (3.22), we may write $\nabla p = c^2 \nabla \rho$, where c is the speed of sound, giving

$$\nabla \cdot \mathbf{u} = -\frac{1}{\rho c^2}(\mathbf{u} \cdot \nabla)p = \frac{\mathbf{u} \cdot (\mathbf{u} \cdot \nabla)\mathbf{u}}{c^2} \tag{3.42}$$

Using the Schwarz inequality

$$\left|\sum_n A_n B_n\right|^2 \leq \left(\sum_n A_n^2\right)\left(\sum_m B_m^2\right), \tag{3.43}$$

we obtain

$$|\mathbf{u}\cdot(\mathbf{u}\cdot\nabla)\mathbf{u}|^2 \leq |\mathbf{u}|^2|\mathbf{u}\cdot\nabla\mathbf{u}|^2 \leq |\mathbf{u}|^2|\mathbf{u}|^2|\nabla\mathbf{u}|^2, \tag{3.44}$$

where $|\nabla\mathbf{u}| = \sqrt{\sum_i\sum_j(\partial_i u_j)^2}$ is the 2-norm of the velocity gradient tensor. We arrive at the condition

$$|\nabla\cdot\mathbf{u}| \leq \mathrm{Ma}^2|\nabla\mathbf{u}| \tag{3.45}$$

where

$$\boxed{\mathrm{Ma} = \frac{u}{c}} \tag{3.46}$$

is the *Mach number* [169]. By Eq. (3.45), it is conventional to define flows as incompressible when $\mathrm{Ma} \lesssim 0.3$, such that $\mathrm{Ma}^2 \sim \delta p/p \sim \delta\rho/\rho \lesssim 0.1$. If the flow speed u is everywhere much less than the speed of sound c, then the flow will be effectively incompressible. Although here the quantum pressure has been neglected, this classical estimate should nonetheless serve as a decent guide.

Importantly, however, this proof is only valid for steady flows. In unsteady flows an additional condition must be fulfilled, and an order of magnitude estimate can be obtained via dimensional analysis as follows [105]. Suppose the flow is characterised by a velocity scale U, length scale L and timescale τ, and that the terms $\partial\mathbf{u}/\partial t$ and $\nabla p/\rho$ are of comparable magnitude. Then $U/\tau \sim \delta p/\rho L$, or, equivalently, $\delta p \sim \rho LU/\tau$ and hence, via Eq. (3.22) $\delta\rho \sim \rho LU/\tau c^2$. We find then from the continuity equation that $\partial\rho/\partial t$ may be neglected when $\delta\rho/L \ll \rho U/L$, or equivalently

$$\tau \gg L/c. \tag{3.47}$$

The interpretation of Eq. (3.47) is that the time taken, L/c, by a sound signal to travel the distance L must be much smaller than the characteristic time τ of the flow over which "significant" changes take place. Effectively, the fluid must be able to transmit the information of a spatially localised disturbance instantaneously — which is precisely what we found for the incompressible Navier-Stokes equations Eq. (2.1). In the following sections, we will see how and when these conditions are satisfied in the presence of quantum vortices, and therefore in quantum turbulence.

3.3 Quantum vortices

Having learned that the GPE describes the evolution of a quantum fluid, we might naturally ask whether this fluid can support vortex solutions. This motivates us to look for cylindrically symmetric stationary solutions of the form

$$\psi(\mathbf{x},t) = n_0^{1/2}\chi_q(r/\xi)e^{iq\phi}. \tag{3.48}$$

We require q to be an integer quantum number, otherwise the wavefunction would not be a single-valued function, and hence not yield a unique probability amplitude. An immediate consequence is that the circulation is quantized:

$$\Gamma = \oint \mathbf{u}\cdot d\mathbf{l} = \frac{qh}{m}; \quad q\in\mathbb{Z}, \tag{3.49}$$

as was first appreciated in the context of superfluid helium by Onsager [151] and Feynman [170]. The quantum number q is often referred to as the *charge* of the vortex. Clearly, the velocity field of an isolated quantum vortex is precisely that produced by a point-vortex of integer circulation,

$$\mathbf{u}(r) = \left(\frac{\hbar}{m}\right)\frac{q}{r}\,\hat{\boldsymbol{\phi}} \tag{3.50}$$

where $\hat{\boldsymbol{\phi}}$ is the azimuthal unit vector. Naturally, the velocity field satisfies the incompressibility condition $\nabla\cdot\mathbf{u}=0$. The vorticity field is thus

$$\omega(\mathbf{x}) = \frac{qh}{m}\delta(\mathbf{x}). \tag{3.51}$$

Remarkably, vortices in a quasi two-dimensional condensate actually *are* point vortices, albeit a slightly modified manifestation. The difference, of course, is contained within the density envelope determined by χ_q.

3.3.1 The Structure of the Core

In terms of the scaled coordinate $\sigma = r/\xi$, exploiting the cylindrical symmetry we find that the vortex core function $\chi_q(\sigma)$ must satisfy

$$-\frac{1}{2}\left(\partial_\sigma^2 + \frac{\partial_\sigma}{\sigma} - \frac{q^2}{\sigma^2}\right)\chi_q + \chi_q^3 - \chi_q = 0 \tag{3.52}$$

along with the boundary conditions

$$\chi_q(0) = 0, \tag{3.53}$$

$$\chi_q \to 1 \text{ as } \sigma \to \infty, \tag{3.54}$$

such that the boundary condition at the origin regularises the infinite kinetic energy associated with the velocity field. Although this nonlinear boundary value problem must be solved numerically, the core function has the following useful asymptotic forms:[3]

$$\chi_q(\sigma) \sim J_q(\sqrt{2}\sigma) \propto \frac{1}{q!}\left(\frac{\sigma}{\sqrt{2}}\right)^q \qquad \sigma \ll q \tag{3.55}$$

$$\chi_q(\sigma) \sim 1 - \left(\frac{q}{2\sigma}\right)^2 \qquad \sigma \gg q \tag{3.56}$$

In practice, it turns out that only the singly-charged ($|q| = 1$) core solutions are stable [171, 172]. Vortices of higher charge disintegrate into an appropriate number of single-charge vortices (i.e. a number that conserves their total charge), apart from in certain cases where the confining potentials can be modified to stabilise them [172]. The singly-charged solutions on the other hand, are stable topological phase defects, and, since there is no viscosity, they cannot decay via viscous diffusion. The only relevant solutions for the study of quantum turbulence is thus the case $|q| = 1$. For an isolated, singly-charged vortex, the ansatz

$$\chi(\sigma) = \chi_1(\sigma) \approx \frac{\sigma}{\sqrt{\sigma^2 + \Lambda^{-2}}} \tag{3.57}$$

is a fairly decent approximation, and has the correct asymptotic behaviour [173]. The value

$$\Lambda = \left.\frac{d\chi}{d\sigma}\right|_{\sigma=0} = 0.82475449\ldots, \tag{3.58}$$

determined from the full numerical solution, ensures that the ansatz has the correct asymptotic behaviour. The first four solutions to Eq. (3.52), and a comparison of the $q = 1$ solution with its corresponding ansatz [Eq. (3.57)], are shown in Fig. 3.2

[3]For small σ where the wavefunction must go to zero, the nonlinear term may be neglected, reducing (3.52) to Bessel's equation. The solutions consistent with the boundary condition at the origin are the Bessel-J functions. For $\sigma \gg q$, the derivatives can be neglected.

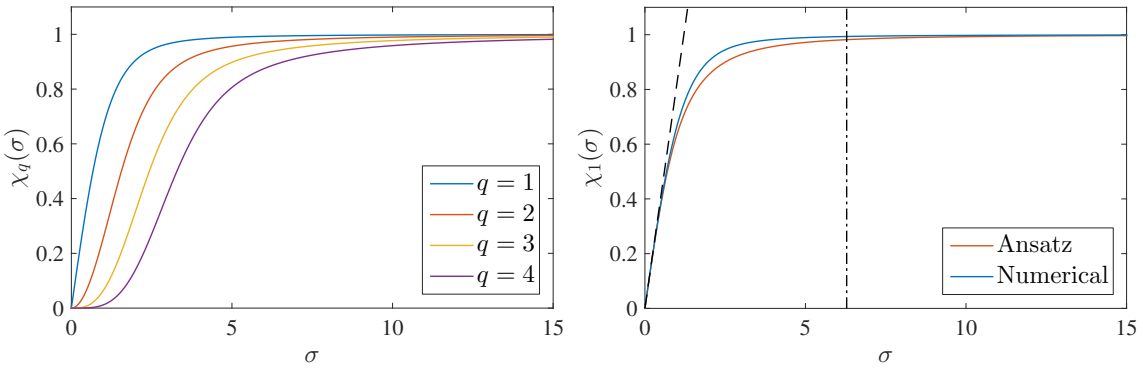

Figure 3.2: (Left) The first four solutions to the vortex core equation (3.52). (Right) The solution for $q = 1$ compared with the ansatz, Eq. (3.57). The inclined line has slope $\Lambda = 82475449\ldots$. The vertical line is at $\sigma = 2\pi$, which serves as a convenient reference point for distinguishing regimes of the core and the far-field. Solutions were obtained by using a pseudospectral method, using the rational Chebyshev $TL_n(r)$ basis for the semi-infinite interval, and a Newton-Raphson iteration scheme, see, e.g. Ref. [174].

3.4 Vortex Dynamics

3.4.1 Conservative Dynamics

Equation (3.50) strongly suggests that the vortex dynamics in a compressible Bose-Einstein condensate may be equivalent to the point-vortex model under certain conditions. Indeed, this can be shown in the limit of a *dilute vortex gas*, namely, in the limit where the intervortex distance $\ell \gg \xi$, such that vortex cores are well-separated and the motion of the vortices is adiabatic. We additionally require that the characteristic axial scale $l_z \lesssim \xi$, so that the vortices may be approximated as *rectilinear* (Sec. 3.1.5). As pointed out by both Pismen [175, 176], and Fetter [177], the recovery of conservative point-vortex dynamics is essentially a consequence of symmetry. The Gross-Pitaevskii equation is invariant under the Galilean transformation

$$\mathbf{x} \to \mathbf{x} - \mathbf{u}t, \qquad \nabla \to \nabla, \qquad \partial_t \to \partial_t - \mathbf{u}\cdot\nabla; \tag{3.59}$$

$$\psi \to \psi \exp[i(m\mathbf{u}\cdot\mathbf{x} - \tfrac{1}{2}mu^2 t)/\hbar]. \tag{3.60}$$

Since this transformation does not affect the modulus of the wavefunction, the stationary vortex solution thus remains symmetrical and stationary in the moving frame. Furthermore, the effect of Eqs. (3.59) and (3.60), aside from the unimportant global phase factor, is exactly the same as that produced by a uniform phase gradient

$\psi \to \psi e^{i\mathbf{k}\cdot\mathbf{x}}$. Hence, subject to such a phase gradient, a vortex is only rigidly translated at the local velocity $\mathbf{u} = (\hbar/m)\nabla\theta$. It follows that in a *slowly varying* phase field, which can be approximated as constant across the vortex core, a vortex will simply be advected by the local superfluid velocity. This is precisely the kind of phase field produced by well-separated quantum vortices.

Nonetheless, detailed proofs have been given by a number of authors [178–184]. The early proof by Fetter [177] is particularly nice, and for completeness we outline it here. The idea is simple; propose a suitable ansatz and show that it satisfies the Gross-Pitaevskii equation, namely, show that the left and right hand sides are equal. Introducing the convenient set of relative coordinates $\boldsymbol{\rho}_j = \mathbf{r} - \mathbf{r}_j$, with components (ρ_j, φ_j), we suppose that the wavefunction is well-approximated by an ansatz constructed from a product of individual vortex solutions

$$\psi(\mathbf{r}, t) = n_0^{1/2} \prod_j g_j(\mathbf{r}) \equiv n_0^{1/2} \left[\prod_j \chi_j(\rho/\xi)\right] \exp\left(\sum_j q_j \varphi_j(\mathbf{r})\right) \tag{3.61}$$

where we have introduced the shorthand notation $g_j(\mathbf{r}) \equiv g(\mathbf{r} - \mathbf{r}_j)$. Here $\chi_j(\rho/\xi) \equiv \chi(\rho_j/\xi)$ is the solution to Eq. (3.52) and $\varphi_j(\mathbf{r}) \equiv \text{atan}[(\mathbf{y} - \mathbf{y}_j)/(\mathbf{x} - \mathbf{x}_j)]$ is the polar angle about the jth vortex. The phase — which satisfies Laplace's equation $\nabla^2\theta = 0$ away from vortices and hence admits superposition — is exact, whereas the approximation of the density is valid provided $r_{ij} \gg \xi$, such that the vortex cores do not overlap appreciably [185]. Evaluating the time derivative of the ansatz gives[4]

$$\begin{aligned} i\hbar \frac{\partial \psi(\mathbf{r}, t)}{\partial t}\bigg|_{t=0} &= i\hbar n_0^{1/2} \left(\prod_j g_j\right) \sum_k \frac{\partial}{\partial t} \ln g(\mathbf{r} - \mathbf{r}_k - \mathbf{u}_k t) \\ &= -i\hbar n_0^{1/2} \left(\prod_j g_j\right) \sum_k \mathbf{u}_k \cdot \nabla \ln g_k. \end{aligned} \tag{3.62}$$

At an arbitrary vortex, which without loss of generality we can choose to be $k = 1$, this gives

$$-i\hbar n_0^{1/2} \left(\prod_j g_j\right) \mathbf{u}_1 \cdot \nabla \ln g_1. \tag{3.63}$$

Turning now to the right-hand side of Eq. (3.8), exploiting the property $(\mathcal{L} - \mu) g_k = 0$

[4] Note that $\partial_t \ln g(\mathbf{h}(t)) = \frac{\partial \ln g}{\partial g} \frac{\partial g}{\partial h_i} \frac{\partial h_i}{\partial t} = \frac{1}{g} \frac{\partial g}{\partial h_i}(-u_i) = -\frac{1}{g} \nabla g \cdot \mathbf{u}$, since $\frac{\partial h_i}{\partial x_j} = \delta_{ij} \implies \frac{\partial g}{\partial h_i} = \frac{\partial g}{\partial x_i}$.

allows one to write

$$(\mathcal{L}-\mu)\psi(\mathbf{r},t)|_{t=0} = n_0^{1/2}\left(\prod_j g_j\right)\left\{\mu\left[\sum_k(1-\chi_k)^2+\left(\prod_k\chi_k^2\right)-1\right]\right\} - \left(\frac{\hbar^2}{2m}\right)\sum_{k,l}{}'(\nabla\ln g_k\cdot\nabla\ln g_l) \tag{3.64}$$

where the prime denotes the omission of the term $k=l$. In the vicinity an arbitrary vortex (again e.g., $k=1$), the square bracket can be expanded as

$$\mu\left[\sum_k(1-\chi_k)^2+\left(\prod_k\chi_k^2\right)-1\right] \approx \begin{cases} \frac{1}{4}\frac{\hbar^2}{2m}\sum_{k,l}{}'\xi^2(\rho_k\rho_l)^{-2} & (\rho_1\gg\xi) \\ \frac{\hbar^2}{2m}\sum_k{}'(r_{1k})^{-2} & (\rho_1\ll\xi) \end{cases} \tag{3.65}$$

where as usual $r_{1k}=|\mathbf{r}_1-\mathbf{r}_k|$ and we have used the asymptotic core properties in Eqs. (3.55) and (3.56) and the binomial expansion. Similarly, the term involving the logarithms can be expanded as

$$\begin{aligned} &-\left(\frac{\hbar^2}{2m}\right)\sum_{k,l}{}'(\nabla\ln g_k\cdot\nabla\ln g_l) \\ &\approx -i\hbar\nabla\ln g_1\cdot\left\{\sum_{k\neq1}\frac{\hbar}{m}\nabla\theta_k|_{\mathbf{r}=\mathbf{r}_1}+\frac{\hbar}{m}\mathcal{O}(\xi^2/r_{1k}^3)\right\} \\ &+\frac{\hbar^2}{2m}\sum_{k\neq1}\sum_{l\neq1}\mathcal{O}(1/r_{1k}r_{1l}). \end{aligned} \tag{3.66}$$

So the leading order term is

$$-i\hbar\nabla\ln g_1\cdot\sum_{k\neq1}\frac{\hbar}{m}\nabla\theta_k|_{\mathbf{r}=\mathbf{r}_1}, \tag{3.67}$$

and hence, comparing with Eq. (3.63), to lowest order,

$$\boxed{\mathbf{u}_1=\frac{\hbar}{m}\sum_{k\neq1}\nabla\theta_k|_{\mathbf{r}=\mathbf{r}_1}.} \tag{3.68}$$

This reproduces the point-vortex equations [Eq. (2.111)], with leading corrections being $\mathcal{O}(\max|\mathbf{r}_{ij}|^{-2})$. Unfortunately this simple approach does not easily extend to three dimensions, or to dissipative systems, but these cases can be approached using a variational treatment [180, 181, 184] (see also Sec. 3.6.2). Turbulent flows in a

quasi-2D Bose-Einstein condensate are therefore a kind of *point-vortex turbulence*: spatiotemporally disordered flows containing many point-like vortices of unit charge.

3.4.2 Incompressibility for Quantum Vortex Flows

Knowing how the dynamics of a configuration of quantum vortices behaves, we can now address how the conditions for incompressibility discussed in Sec. 3.2.5 apply to quantum vortices. It is clear that we must consider the velocity of the vortices themselves, rather than the whole velocity field, since the latter diverges in the vortex core, yet it remains incompressible. If we suppose that the vortex configuration is characterised by some nearest-neighbour length ℓ, and the vortices are on average grouped into clusters of net charge q_c, then the characteristic velocity can be estimated as $u \sim q_c\hbar/m\ell \sim cq_c\ell/\xi$. The characteristic timescale is then $\tau \sim \ell/u \sim \ell^2/q_c c$. The condition Eq. (3.47), then becomes

$$\frac{\ell}{q_c\xi} \gg 1, \tag{3.69}$$

which is equivalent to

$$\boxed{\mathrm{Ma}_s = \frac{q_c\xi}{\ell} \ll 1.} \tag{3.70}$$

where Ma_s is the *superfluid* Mach number:[5] because of the very special relation between velocity and distance for quantum vortices, Eq. (3.70), Eq. (3.46) and Eq. (3.47) are equivalent for a quantum fluid. Note that the factor of q_c is important whenever vortices are grouped into like-signed clusters, since the velocity field of the cluster will behave as a vortex of charge q_c at large distances.

3.5 Kinetic Energy Spectra

Connection to classical turbulence theory is usually made through the hydrodynamical description. Once again making use of the Madelung transformation Eq. (3.15), the 2D Gross-Pitaevskii energy Eq. (3.6) can be decomposed as $\mathcal{E} = \mathcal{E}_H + \mathcal{E}_Q + \mathcal{E}_V + \mathcal{E}_I$,

[5] Pismen [175] defines this parameter without the factor of q_c.

where

$$\mathcal{E}_H = \frac{m}{2}\int d^2\mathbf{x}\; n(\mathbf{x},t)|\mathbf{u}(\mathbf{x},t)|^2, \tag{3.71}$$

$$\mathcal{E}_Q = \frac{\hbar^2}{2m}\int d^2\mathbf{x}\; |\nabla\sqrt{n(\mathbf{x},t)}|^2, \tag{3.72}$$

$$\mathcal{E}_V = \int d^2\mathbf{r}\; n(\mathbf{x},t)V(\mathbf{x},t), \tag{3.73}$$

$$\mathcal{E}_I = \frac{g_2}{2}\int d^2\mathbf{x}\; n(\mathbf{x},t)^2. \tag{3.74}$$

Respectively, these define the hydrodynamic kinetic energy, quantum pressure energy, potential energy, and interaction energy. The hydrodynamic and quantum pressure terms originate from the kinetic energy term, and $\mathcal{E}_K = \mathcal{E}_H + \mathcal{E}_Q$ is the total kinetic energy. The hydrodynamic term $\mathcal{E}_H$ is then typically further decomposed into incompressible and compressible parts via a Helmholtz decomposition, as was first introduced in Ref. [59]. Since the density of the quantum fluid is not constant, one defines a *density-weighted* velocity field

$$\mathbf{w} = \sqrt{\rho}\mathbf{u}, \tag{3.75}$$

such that the hydrodynamic kinetic energy can be written as $\mathcal{E}_H = \frac{1}{2}\int d^2\mathbf{x}\,|\mathbf{w}(\mathbf{x})|^2$. Then, writing $\mathbf{w} = \mathbf{w}^i + \mathbf{w}^c$, where

$$\nabla\cdot\mathbf{w}^i = 0, \qquad\qquad \nabla\times\mathbf{w}^c = 0, \tag{3.76}$$

one can evaluate the contributions due to the incompressible and compressible components as

$$\mathcal{E}^i = \frac{1}{2}\int d^2\mathbf{x}\,|\mathbf{w}^i(\mathbf{x})|^2 \qquad\qquad \mathcal{E}^c = \frac{1}{2}\int d^2\mathbf{x}\,|\mathbf{w}^c(\mathbf{x})|^2. \tag{3.77}$$

The fields $\mathbf{w}^i$ and $\mathbf{w}^c$ are easily calculated through the Fourier transform. In wavenumber space, the conditions become[6]

$$\mathbf{k}\cdot\hat{\mathbf{w}}^i = 0, \qquad\qquad \mathbf{k}\times\hat{\mathbf{w}}^c = \mathbf{0}, \tag{3.78}$$

[6]The singular point at $\mathbf{k} = \mathbf{0}$, which satisfies both conditions, should be neglected since it only corresponds to the mean flow.

and introducing the incompressible and compressible projection operators[7]

$$P_{ij}(k) = \left(\delta_{ij} - \frac{k_i k_j}{k^2}\right) \qquad Q_{ij}(k) = \frac{k_i k_j}{k^2} \tag{3.79}$$

the components of the incompressible and compressible density-weighted velocity fields are then given by

$$\hat{w}^i_\alpha(\mathbf{k}) = P_{\alpha\beta}\hat{w}_\beta(\mathbf{k}) \qquad \hat{w}^c_\alpha(\mathbf{k}) = Q_{\alpha\beta}\hat{w}_\beta(\mathbf{k}), \tag{3.80}$$

where as usual summation over the repeated indices is implied. The incompressible and compressible (total) kinetic energy spectra (c.f. Sec 2.7.3) are then defined in the usual way:

$$E^i(k) = \frac{1}{2}\int k d\theta_k |\hat{\mathbf{w}}^i(\mathbf{k})|^2 \qquad E^c(k) = \frac{1}{2}\int k d\theta_k |\hat{\mathbf{w}}^c(\mathbf{k})|^2. \tag{3.81}$$

Notice that the density-weighted velocity field for a single quantum vortex is purely incompressible:

$$\nabla \cdot \mathbf{w} = \rho_0^{1/2}[\chi(\nabla \cdot \mathbf{u}) + \nabla\chi \cdot \mathbf{u}] = 0. \tag{3.82}$$

The first term vanishes by Eq. (3.50) while the second vanishes because the density gradients and velocity field are always orthogonal. The incompressible part is thus associated with quantum vortices, whereas the compressible part is associated with acoustic excitations [173, 186]. In the low Mach number regime where the product state Eq. (3.61) is a reasonable approximation to the wavefunction, the kinetic energy is thus dominated by the incompressible component: $\mathcal{E}_H \approx \mathcal{E}^i$. As shown by Bradley and Anderson [173], under such conditions the basic properties of quantum vortices lead to a kinetic energy spectrum that is essentially a modified point-vortex spectrum. The kinetic energy spectrum for the product state of the form Eq. (3.61) can be written in the form

$$E^i(k) = \left(\frac{\rho_0\Gamma^2}{4\pi}\right)\frac{G_\Lambda(k\xi)}{k}\left[N + \sum_{\alpha,\beta}{}' q_\alpha q_\beta J_0(k r_{\alpha\beta})\right], \tag{3.83}$$

where the dimensionless function $G_\Lambda(k\xi)$ is an envelope function that incorporates the contribution of the vortex core function $\chi(r/\xi)$. The asymptotic scalings for

[7] Note these operators satisfy the usual properties of projection operators, namely completeness $P_{ij} + Q_{ij} = \delta_{ij}$, orthogonality $P_{ik}Q_{kj} = 0$ and idempotence $P_{ik}P_{kj} = P_{ij}$.

$\chi(r/\xi)$ yield the following asymptotic forms for $G_\Lambda(k\xi)$

$$G_\Lambda(k\xi) \simeq 1 \qquad k\xi \ll 1 \tag{3.84}$$

$$G_\Lambda(k\xi) \simeq \frac{\Lambda^2}{(k\xi)^2} \qquad k\xi \gg 1 \tag{3.85}$$

such that $G_\Lambda(k\xi)$ serves to regularise the ultraviolet divergence of the self energy in the point-vortex model, making the total energy a physically meaningful quantity. For wavenumbers satisfying $k\xi \ll 1$, there is essentially no deviation from the point-vortex model spectrum [Eq. (2.130)], because the density far from the vortex core is uniform (Fig. 3.2), and the velocity fields of quantum vortices and point vortices are identical [Eqs. (2.110) and (3.50)]. In the region $k\xi \sim 1$ (corresponding to $\sigma \sim 2\pi$ in Fig. 3.2) the spectrum transitions from the point vortex spectrum to the vortex core spectrum $E^i(k) \sim k^{-3}$ (see Fig. 3.3). The k^{-3} scaling is merely due to the shape of the vortex core, and this region of the spectrum thus only depends on the number of vortices rather than on any spectral transport processes.[8] It follows from Eq. (3.83) that the vortex energy can be written as

$$\mathcal{E}^i = -\left(\frac{\rho_0\Gamma^2}{4\pi}\right) {\sum_{\alpha\beta}}' q_\alpha q_\beta \ln\left|\frac{\mathbf{x}_\alpha - \mathbf{x}_\beta}{\xi}\right| + E_{\text{core}}. \tag{3.86}$$

The spectrum Eq. (3.83) has been found to give very good agreement with numerically calculated incompressible kinetic energy spectra, apart from in particularly violent, high Mach number situations where the sound field is significantly excited [93, 173, 187–189]. Previously, an unfortunate setback was that Eq. (3.83) was unable to be measured experimentally. Typical probing of atomic BECs is achieved via ballistic expansion and absorption imaging, which only provides density information, thus only providing information about the vortex locations. The study in Chapter 4, where an alternative route to attaining flow-field information is pursued, was partly motivated by this problem. However, at the time of writing, an experimental method for sign detection was demonstrated by Seo *et al.* [87], using Bragg spectroscopy. Another method has also been theoretically proposed using gyroscopic vortex precession [77], but it has not yet been implemented successfully. Nonetheless, the method we develop in Chapter 4 is not made redundant by these developments, as it happens to provide different flow-field information, and is readily accessible by the common

[8] Note however that the k^{-3} core scaling is a universal feature of any nonlinear Schrodinger-like equation, since it only depends on the linear Schrodinger behaviour near the vortex core.

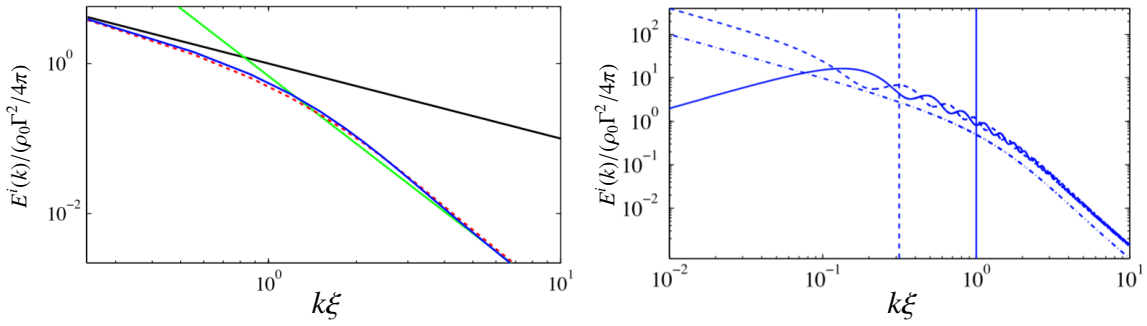

Figure 3.3: Images adapted from Bradley and Anderson (2012), Ref. [173]. [Left] Incompressible kinetic energy spectra for a single quantum vortex using the full numerical solution $G_\Lambda(k\xi)$ (solid, blue), or the core ansatz Eq. (3.57) (red,dashed). The k^{-1} and k^{-3} asymptotic spectra, obtained from the expressions Eq. (3.84) and Eq. (3.85), are shown by the black and green lines, respectively. [Right] Comparison of kinetic energy spectra for a single vortex (dash-dot line), a vortex dipole (solid line) and a same-sign vortex pair (dashed line), as obtained from Eq. (3.83). Here the vortex dipole and vortex pair have a spacing $d = 20\xi$, and the vertical dashed line shows the wavenumber $k_d \equiv 2\pi/d$. The core crossover scale $k\xi = 1$ is shown by the vertical solid line.

method of ballistic expansion.

3.6 Non-Conservative Processes

3.6.1 Vortex Sound Interactions

At sufficiently high Mach numbers, compressible effects lead to a rich variety of phenomena. For the incompressible subsystem of quantum vortices, these effects are thus nonconservative processes, corresponding to external forcing and dissipation.

Radiation and Absorption

Clusters of same-sign vortices, which chaotically orbit around each other and therefore are accelerating, radiate energy in the form of sound — there is obviously an analogy to point charges in electromagnetism. Similar to an electric dipole [146], a single pair of same-sign vortices is amenable to a detailed treatment, and it can be shown that the power radiated per unit length by a pair of straight-line vortices, separated by a distance $2a$, is $dE/dt = -J$, where [38, 175, 190]

$$J = \frac{\rho\Gamma^7}{(4\pi)^5 c^4 a^6} \tag{3.87}$$

which decays rapidly with the separation length. If the vortices are several healing lengths apart, their self (core) energy does not change, so up to a constant the energy of the pair is $E = -(\rho\Gamma^2/4\pi)\ln(2a/\xi)$, and hence the equation of motion for the separation distance a is

$$\frac{da}{dt} = \frac{\Gamma\xi^4}{a^5}, \tag{3.88}$$

from which it follows that the separation of the pair asymptotically grows as $a \sim t^{1/6}$. For arbitrary vortex configurations, the leading order term for the power radiated in the far field is proportional to the quadrupole moment of the configuration [175]. It follows that an isolated vortex dipole does not radiate,[9] and symmetric configurations, such as vortices placed evenly around a circle, will exhibit even weaker radiation, dominated by the octopole moment at leading order. Furthermore, in addition to radiation, vortices are able to *absorb* energy from the sound radiated by other vortices. Such an effect was systematically studied by Parker *et al.* [193]. They showed that separated vortices in a double-well potential could exchange energy with a high efficiency through sound wave interactions, in a mechanism they termed "coherent cross-talk".

Since in two dimensions the only radiation mechanism available is that embodied in Eq. (3.87), we would expect that the ability for vortices to radiatively dissipate energy will become considerably suppressed provided the characteristic inter-vortex spacing is on the order of several healing lengths. The same conclusion could be inferred from the findings of Lucas and Surówska [182], who investigated compressibility corrections to the point-vortex dynamics in a variational treatment of the 2D Gross-Pitaevskii equation, and found surprisingly weak corrections due to compressibility at leading order. This contrasts with the three-dimensional case, where helical excitations along the vortex lines (Kelvin waves), and vortex reconnections open more efficient channels for energy dissipation into the sound modes [38, 190]. Note that Kelvin waves can become heavily suppressed, even for rather modest condensate aspect ratios [166].

Dipole Annihilation

In an inviscid and incompressible or barotropic fluid described by the classical Euler equation, Kelvin's theorem states that the circulation around any closed contour following the flow is conserved. The appearance of the quantum stress in the quan-

[9] Alternatively, a vortex dipole does not accelerate, and hence is a stationary solution to the Gross-Pitaevskii equation in the moving frame [191, 192].

tum Euler equation allows this conservation to be broken when a vortex and an antivortex approach each other within a distance of order ξ. Under such conditions, vortex-antivortex pairs can unwind and annihilate, transforming into a solitary wave-like structure. These isolated sound pulse structures, extensively studied by Jones and Roberts [191, 192], and later by Berloff and Roberts [194] are often referred to as the Jones-Roberts soliton.[10] The vortex dipoles and the Jones-Roberts soliton form a continuous family of solutions to the Gross-Pitaevskii equation in a frame translating at constant velocity u. The low u solutions possess vorticity, corresponding to vortex dipoles whose separation distance $d \to \infty$ as $u \to 0$. At velocities above $u \approx 0.6081$ the solutions lose their vorticity, becoming the solitary wave structure, and the amplitude of the wave becomes vanishingly small as $u \to c$. Note that the annihilation process can also occur at a boundary, since this is equivalent to annihilation with an image vortex.

As pointed out by Jones and Roberts [192], this annihilation does not actually violate Kelvin's law. The annihilation is possible due to the density zero of the vortex core: consider what happens if we draw a closed contour C which threads between the vortices and then allow them to approach each other. Eventually, the vortex cores overlap, and the contour must then pass through a region containing no density. The contour — which is meant to be a material line — is no longer closed, because it now passes through a region containing "no material". Kelvin's theorem therefore ceases to be apply at the exact moment of annihilation. At the same time, one could draw another contour C' that encloses both vortices, in which case there is no problem in applying Kelvin's theorem because the circulation was always zero.

In the Navier Stokes equations the decay of circulation (vorticity) is due to the viscosity, and the circulation is conserved as $\nu \to 0$. In the Gross-Pitaevskii equation, the decay of circulation is provided by the sound field [196, 197] (with coupling provided by the quantum stress) and circulation is conserved in the limit $\xi \to 0$. Note that, in principle, the reverse process in which vortex dipoles spontaneously appear from the sound field is also possible, since the Gross-Pitaevskii equation possesses the time reversal symmetry $t \to -t$, $\psi \to \psi^*$. However, as one might expect from the irreversible process of turbulence, the present experimental and numerical data indicate that, apart from at very high Mach numbers, only the decay process is relevant [78, 84, 92, 189].

[10] Others have termed the structure a *vortexonium* [195].

Other Vortex-Sound Interactions

A plane acoustic wave, incident on a quantum vortex, will cause it to oscillate in a history-dependent manner; retardation effects due to finite compressibility mean the motion of the vortex will depend on where it *was*, in addition to where it *is*. Embedded in a plane wave, a vortex will feel both a *drag force* in the direction of the propagation wavevector, and a (charge-dependent) *lift* or *Magnus force* perpendicular to the oncoming wave. A differential equation for the a straight vortex filament in the limit of high frequency sound waves and low Mach numbers was derived by Lund [198]. A more detailed discussion of these effects can be found in Pismen [175], and references therein.

Wave Turbulence

Finally, it should also be mentioned that the sound degrees of freedom (the compressible subsystem) themselves form a nonlinear interacting system and can also become turbulent, exhibiting a form of turbulence known as weak-wave turbulence (WWT). When the wave degrees are forced and damped within different regions of scale-space, they too can support cascades (usually of the energy), just as in the hydrodynamic case. The theory of weak-wave turbulence is laid out in, e.g., the texts by Zakharov [199], or Nazarenko [14]. The theory is extremely general and is relevant to many systems, for example surface water waves, or waves in plasmas; it only discriminates between what kind of resonant n-wave interactions are permitted by the system (often a three-wave or four-wave interaction). Another rather nice element of the theory is that, due to the assumed weak nonlinearity, in contrast to hydrodynamic turbulence the "Kolmogorov-Zakharov" WWT cascade solutions can often be found as *exact* solutions. The Gross-Pitaevskii equation can exhibit both three-wave and four-wave regimes, depending whether or not there is a large condensate background present, and both scenarios have been studied by a number of authors, see for example the works by Proment, Nazarenko and Onorato [200–203].[11] Note also that a WWT cascade has been observed experimentally in a uniform 3D BEC very recently by Navon *et al.* [88]. Since the regimes of vortex and weak-wave turbulence seem to be able to exist simultaneously [187], it is quite possible that the random buffeting of a vortex due to the turbulent sound modes would lead to some

[11] Incidentally, the four-wave regime exhibits a dual cascade, of particles to low k and energy to high k [203]. It was by first studying this regime as a mechanism for condensate formation in a weakly interacting Bose gas that lead Kraichnan to propose the dual cascade of 2D turbulence, see Refs. [119, 204].

kind of Brownian or super-diffusive motion, that would depend on the spectrum of the sound modes. While some numerical evidence of such a scenario was observed in Gross-Pitaevskii simulations in Ref. [93], such a scenario is yet to be explored in detail. The theory of sound generated by turbulence ("vortex sound"), pioneered by Lighthill in the study of jet engines [205–207], might be of relevance here.

3.6.2 Thermal Dissipation

The Gross-Pitaevskii equation is a zero temperature theory, and therefore neglects the influence of any thermal, normal fluid fraction that will be present at finite temperatures. Whereas turbulence in superfluid helium at higher temperatures is usually studied phenomenologically via extensions of Landau's two-fluid model [208], a number of microscopically justified theories have been developed to investigate the dynamics of weakly-interacting Bose gases at finite temperatures. These include the so-called c-field methods like the stochastic projected Gross-Pitaevskii equation (SPGPE) [209–212], or the Zaremba-Nikuni-Griffin (ZNG) theory [208]. Such methods can be used to provide very detailed, realistic simulation of finite temperature experimental systems, each with their own benefits and disadvantages, and regimes of validity [208, 213]. A comparison and discussion of these methods can be found in Ref. [214].

However, at the present stage, fully implementing these methods for numerical simulation of quantum turbulence is computationally demanding, and one therefore typically resorts back to a (quasi) phenomenological approach. Thermal effects are usually included through the damped Gross-Pitaevskii equation

$$i\hbar\frac{\partial\psi}{\partial t} = (1 - i\gamma)(\mathcal{L} - \mu)\psi, \tag{3.89}$$

where $\mathcal{L}$ is the usual Gross-Pitaevskii operator: $\mathcal{L} = -\hbar^2\nabla^2/2m + V + g|\psi|^2$. Although phenomenological, this equation is not entirely ad hoc, since it is equivalent to the simple-growth SPGPE without the thermal noise term [209], and therefore still has a first-principles origin. The damping rate γ is associated with the coupling to an external thermal cloud of chemical potential μ, assumed to be stationary, and the role of the dissipation is to damp the system back to a state with the same value of μ. Realistic values for γ are typically of order 10^{-4} [78, 84, 173, 209]. The approximation of a stationary normal fluid component is reasonable particularly in an oblate geometry, since anisotropy helps lock the thermal component to the trap [79].

As such, the damped GPE has been found to give good qualitative [80] and even quantitative [78, 84] agreement with the experimental studies conducted thus far.

Obtaining an equation of motion for the vortex dynamics within Eq. (3.89) is not straightforward. This is mostly because the damped equation does not enjoy the same Galilean invariance as the Gross-Pitaevskii equation (obviously this stems from the stationary thermal cloud providing a preferred reference frame). Because of this lack of invariance, the vortex core is distorted when placed in a uniform phase gradient, giving rise to a nonlinear (logarithmic) correction [175].[12] Nonetheless, in the dilute vortex gas limit, where core effects are neglected, the dissipative contribution to the vortex motion can be derived, yielding the damped point-vortex equation [181, 184]

$$\mathbf{u}_i = \frac{\hbar}{m} \sum_{j \neq i} \left(\nabla \theta_j |_{\mathbf{r}=\mathbf{r}_i} - \gamma q_i \hat{\mathbf{z}} \times \nabla \theta |_{\mathbf{r}=\mathbf{r}_i} \right) . \tag{3.90}$$

The dissipative term pushes opposite-sign vortices together, and same-sign vortices apart, thus reducing the vortex-system energy. It has the form of the *Peach-Koehler force*, which arises in the dynamics of dislocation defects in crystals [215]. Similar terms are also present in the phenomenological vortex filament model often used to study superfluid helium, in which context they are termed *mutual friction* [190], since they arise from the interaction between the normal fluid and superfluid components. The dissipative term bears a closer resemblance to linear (Ekman) friction $-\alpha \mathbf{u}$ [127] than it does to viscosity, as in a discrete vortex method viscous diffusion is analogous to Brownian motion [103].

Despite the corrections due the vortex core distortion, and the abundance of complicated effects introduced by compressibility, there is nonetheless both numerical [93, 189], and experimental [79, 216] evidence that the dynamics of the vortex degrees of freedom in atomic BECs can be described, at least qualitatively, by a dissipative point-vortex model of the form in Eq. (3.90). In the presence of the Peach-Koeler force, opposite-sign point vortices can approach each other to zero distance within a finite time, and so vortex-antivortex annihilation must be put in "by hand" [93], when vortices approach each other within a distance of order ξ. As already mentioned, the empirical evidence collected thus far indicates that the overall contribution from the sound field is to introduce an additional source of effective dissipation for the incompressible subsystem. It therefore seems reasonable, at least at a phenomenological level, that the net effects of compressible losses could be modelled with Eq. (3.90)

[12] Note that the imaginary part of the time evolution is equivalent to the (real) Ginzburg-Landau equation [175].

through a modified value of γ that will depend on the Mach number; the value of γ can only be checked *a posteriori*. We will use this approach in our point-vortex simulations in Chapter 6.

3.7 Vortex Nucleation

3.7.1 Critical Velocity of a Cylinder

The Landau criterion (Sec. 3.2.4) can be applied to determine the critical velocity for vortex nucleation in the wake of a cylinder. A naive application of the Landau criterion gives the critical velocity $u_c = c$, which is much larger than what is typically observed. However, this is because the modifications of the flow field introduced by the cylinder have not been accounted for. But one can still understand the critical velocity in the spirit of the Landau argument provided one finds when the velocity field *locally* exceeds the speed of sound. One can begin by assuming incompressibility, constant density and a large impenetrable obstacle with $R \gg \xi$. Solving Laplace's equation for the velocity potential in the resulting potential flow problem [217], one finds that for an obstacle translating at velocity $\mathbf{U}$ the velocity field reaches a maximum at the edges of the disc with value $2|\mathbf{U}|$. This gives an upper bound of $u_c/c < 0.5$ [217–219]. The potential flow field yields zero drag, a manifestation of d'Alambert's paradox for perfect fluids [169]. Adding in compressible effects does not alter this description qualitatively — the flow is one of perfect compressibility, exhibiting zero drag [105, 218] — but rather the density depletion near the obstacle results in a locally lower speed of sound, and hence a lower critical velocity $u_c/c \approx 0.4$ [217, 218, 220].

In atomic BECs, the obstacle is typically provided by an optical potential created by blue-detuned laser light [85, 221] rather than a solid object. A more rigorous treatment, considering a penetrable cylinder with a large but finite background potential $V_0 \gg \mu$ and a radius $R \gg \xi$ can be shown to have a size-dependent critical velocity of [219]

$$u_c \simeq 7.61 \frac{\hbar}{mR} \tag{3.91}$$

which in practice is very accurate until $V_0 \lesssim 5\mu$. This happens to be similar in value to the critical velocity given by Feynman [170], based on the energy required

to nucleate a vortex dipole in a jet of superfluid helium flowing from an orifice:

$$u_c = \frac{\hbar}{mR} \ln\left(\frac{R}{\xi}\right). \tag{3.92}$$

However, in general the critical velocity will depend on the precise geometry of the obstacle [222]. Elliptical [89] or Gaussian [223] stirring obstacles, particularly with $V_0 \sim \mu$ [168] can be exploited to further lower the critical velocity.

The criterion for vortex nucleation quite obviously violates the assumptions for nearly incompressible flow in the vicinity of an obstacle. If the same critical Mach number were exceeded in a classical fluid, density shock waves would be formed [169]. But as noted by Frisch *et al.* [218], these shocks require viscous dissipation, and no such term is present in the Gross-Pitaevskii equation. The quantum fluid instead copes by forming localized "shocks", in the form of vortices, in order to produce shear that can match fluid domains with different velocities. So even though one has to violate the incompressibility condition by locally exceeding the speed of sound to form quantum vortices, provided the obstacle diameter D is larger than a few healing lengths, such that the critical velocity is sufficiently low, a regime can be achieved in which the resulting wake exhibits a low superfluid Mach number $\mathrm{Ma}_s \sim \xi/D \ll 1$, dominated by incompressible kinetic energy.

3.8 The 2D Quantum Cylinder Wake

Whereas early studies of the 2D cylinder wake system have considered basic properties such as vortex emission frequency and drag [168, 225], more recent studies have uncovered remarkable similarities between the wakes of bluff bodies in classical and quantum fluids. Sasaki *et al* [51] studied vortex shedding in the wake of an impenetrable ($V_0 \sim 100\mu$) Gaussian obstacle, over a range of speeds and sizes, and observed the emergence of the von Karman street [Fig. 3.4]. They found three qualitatively different regions of vortex shedding: an oblique dipole shedding regime in which vortex-antivortex pairs form a v-shaped wake somewhat reminiscent of a bow wave [Fig 3.4(a)]; a von-Karman regime, in which the vortex street is formed of corotating pairs of same-sign vortices [Fig 3.4(b), also cf. Fig. 2.1(c)]; and a turbulent regime of irregular shedding [Fig 3.4(c), cf. Fig. 2.1(d)]. However, in contrast to the classical behaviour, the von-Karman street was only observed over a narrow range of velocities and obstacle sizes. They also observed an oscillatory transverse force on the obstacle, even when the shedding became irregular. The oscillatory shedding

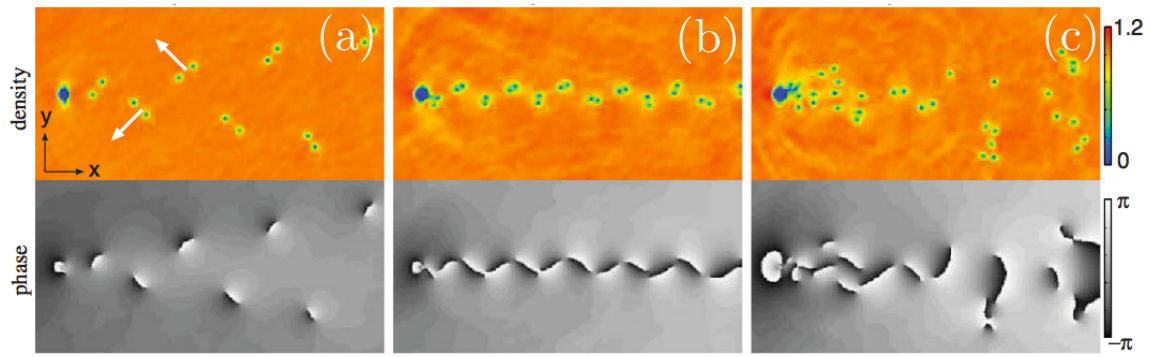

Figure 3.4: Image reproduced from Sasaki *et al.* (2010), Ref. [51]. Wakes produced by a, circular Gaussian obstacle at different velocities a two-dimensional Bose-Einstein condensate: (a) Oblique shedding of vortex dipoles, forming a v-shaped wake; (b) The von-Karman vortex street; (c) Irregular, turbulent shedding at higher velocity. In (b), the ratio of the streamwise and transverse distances between clusters was found to be in remarkably good agreement with the stable value 0.28, originally found by von-Karman using the point-vortex model for incompressible fluids [224]. Notice that the background density fluctuations are small, and a compression wave is only apparent at the front of the obstacle for the highest velocity.

hints at the existence of Strouhal oscillations (Sec. 2.3.1), but the simulation domain was not large enough to accurately resolve the shedding frequency. The first signatures of the street have recently been observed in an experiment by Kwon *et al.* [52]. Stagg *et al.* [89] studied the wakes of elliptical obstacles. They noted that when one traces out the trajectories of the early-time vortex dynamics, a flow pattern remarkably similar to the classical recirculation zone is observed [Fig. 3.5, cf. Fig. 2.1(a)]. These parallels, which suggest a deeper connection with hydrodynamic turbulence, and in particular the presence of a superfluid Reynolds number (see also Sec. 3.9.2), motivated the study of the cylinder wake presented in Chapter 5.

3.9 Cascades in Quantum Turbulence

3.9.1 The Direct Energy Cascade in 3DQT

Since the laminar behaviour of superfluid ^{4}He is so different to conventional fluids, it was initially very surprising how similar the properties of quantum turbulence can be to those of classical turbulence [64], and what was particularly surprising is that the Kolmogorov cascade phenomenology (Sec. 2.8) still seems to be valid. The direct cascade and the Kolmogorov law have been observed experimentally, in flows gener-

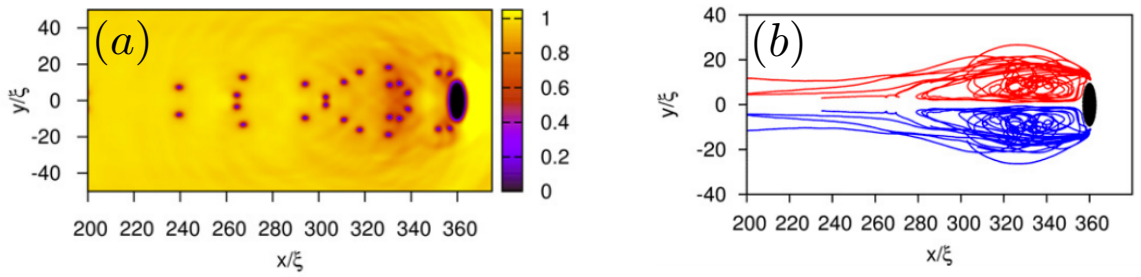

Figure 3.5: Images adapted from Stagg *et al.* (2014), Ref [89]. Wakes produced by an elliptical stirring obstacle in simulations of the 2D Gross-Pitaevskii equation: (a) Instantaneous density distribution of the early-time dynamics; (b) Map of the early-time trajectories traced out by individual vortices, revealing a recirculation zone remarkably similar to that shown in Fig. 2.1(b) for a classical fluid.

ated by, e.g., grids and bellows or propellors [44, 45, 47, 226], as well as in GPE [59, 60, 227], damped GPE [228], and vortex filament model [229, 230] simulations of decaying turbulence from various initial conditions. The Kolmogorov constant has been found to be the same above and below the lambda transition [44, 226], even at very low temperatures where the normal fluid component is negligible [40, 226]. Furthermore, the dissipation anomaly has been observed to persist in the form [cf. Sec. 2.6, Eqs. (2.35) and (2.39)]

$$\epsilon = \nu_{\text{eff}} \langle \omega^2 \rangle = \nu_{\text{eff}} \Gamma^2 \mathscr{L}^2, \tag{3.93}$$

where $\mathscr{L}$ is the vortex line length per unit volume, and ν_{eff} is an effective viscosity that is of the same order as helium's normal fluid viscosity ν regardless of the normal fluid concentration [46, 50, 76]. In the pure superfluid turbulence regime, it is now established that the compressible degrees of freedom provide a replacement for the viscosity as an energy sink for the incompressible energy [196, 197],[13] and it is now understood that the essential underlying mechanism is a bundling of many quantum vortices of the same circulation [40, 230]. This bundling allows them to collectively mimic a classical fluid at large scales; the bundle can lengthen and contract, thereby mimicking the vortex stretching mechanism (it is not possible for single vortices due to the quantisation condition), allowing them to undergo a Kolmogorov cascade in the usual sense [232]. The semiclassical cascade breaks down at scales on the order

[13]When normal and superfluid components are both present, the picture is more complicated. At large scales the superfluid and normal fluid are both turbulent, but become "locked" together through a mutual friction induced alignment, and effectively behave as one fluid. At small scales, dissipation can involve a combination of both normal viscosity and mutual friction [39, 46, 76, 231].

of the average intervortex distance. At these scales, it is argued that reconnections dissipate some energy, before a Kelvin-wave cascade takes over to transport the energy [233, 234] until it is radiated away as sound. In regimes where bundling does not occur, quantum turbulence exhibits quite different properties. A disorganised tangle of vortex filaments, without bundling, forms a kind of *ultraquantum* or *Vinen* turbulence, which does not exhibit the energy cascade, and exhibits slower decay properties [235, 236].

3.9.2 A Superfluid Reynolds Number

Since quantum turbulence can exhibit a Kolmogorov spectrum (Sec. 3.9.1), an immediate question that is raised is: what is the Reynolds number? There should be a large dimensionless parameter that assumes this role, and predicts, for example, the length of the inertial range [Sec. 2.8, Eq. (2.71)]. For turbulence in a pure superfluid, it is not immediately clear how one might define a Reynolds number since the viscosity is identically zero, such that naively one might expect it to be infinite or undefined [196, 227]. However, Onsager noted [237] that the only available parameter with the unit of viscosity is the unit of circulation $\Gamma = h/m$. He thus proposed the superfluid Reynolds number[14]

$$\mathrm{Re_s} = \frac{UL}{\Gamma}, \tag{3.94}$$

which essentially measures the characteristic flow parameters against those of a single vortex (note that $\Gamma = 2\pi c\xi$ in the Gross-Pitaevskii description). There is some evidence that Eq. (3.94) gives a good indication of the degree of turbulence in the fully developed regime $\mathrm{Re}_s \gg 1$ [45, 47, 59, 60, 220, 226, 233, 238–240]. Of particular note is a relatively recent study by Salort *et al.* [46]; by varying only the turbulent intensity (i.e., varying U) in HVBK simulations, they presented evidence that the inter-vortex spacing ℓ scales as $\mathrm{Re_s}^{-3/4}$, just like the viscous length scale (k_d^{-1}) in the classical Kolmogorov theory [see Eq. (2.71)]. Verification of this behaviour was also demonstrated in the recent experiment by Babuin *et al.* [76] over a wide range of superfluid fractions (0.9% to 97%). Unfortunately however, experiments have not yet managed to verify the scaling of the inertial range with $\mathrm{Re_s}$, as the smallest scales are below the currently available measurement resolution [45, 50, 76]. It also seems

[14] Although Re_s, unlike Re, is not rigorously derived from the governing equations, notice that the point vortex equations (or the vortex filament equations in 3D) and Onsager's superfluid Reynolds number do obey precisely the same scaling transformation as the Reynolds number and the Navier-Stokes equations, see Sec. 2.2.

$\mathrm{Re_s}$ has not yet been systematically tested near the transition to turbulence.

3.9.3 A Direct Energy Cascade in 2DQT?

The appearance of the Kolmogorov law in 3D quantum turbulence motivated the study of the classical 2D cascade phenomenology in 2D quantum turbulence. After a number of early works observed no convincing evidence for the inverse energy cascade [241–243] (Sec. 2.9.3), Numasato *et al.* [186] argued that compressibility and the mechanism of dipole recombination would instead lead to a direct cascade of energy to small scales through a $k^{-5/3}$ spectrum, as in three dimensions (Sec. 2.8). Studying GPE dynamics starting from a random phase initial condition, they observed the nucleation and subsequent decay of many vortex dipoles. Although the enstrophy of quantum vortices, being proportional to a squared delta function, is formally undefined, they noted that the total enstrophy is nonetheless proportional to the number of vortices: $\Omega = \Gamma^2 N\delta(\mathbf{0})$. Thus attributing to the vortex number N the role of enstrophy, they argued that the lack of enstrophy conservation caused by dipole annihilation prevents the possibility of the enstrophy cascade. They argued that this invalidates Kraichnan's arguments, ruling out the inverse energy cascade, since it could not be accompanied by a k^{-3} spectrum.

An early counter argument [173, 187], was that this dipole annihilation mechanism would be inhibited by a distribution that contained initial clustering of same-sign vortices; the clustering would self-consistently separate opposite-sign vortices spatially, restoring enstrophy conservation, and thereby preventing this "direct cascade" mechanism. Unfortunately, this debate has now caused some confusion in the literature over the role of enstrophy conservation, in particular the misconception that enstrophy needs to be conserved to achieve energy transport to large scales (see e.g. [78, 83, 195, 244–246]). It is therefore worth taking a moment to explain a few important points. First and foremost, enstrophy does *not* have to be conserved for energy to be transported to large scales: the 2D Navier-Stokes equations do not conserve enstrophy either [see Eq. (2.36) and Sec. 2.9.2]. Under free evolution, at large Reynolds numbers the *energy* is approximately conserved, but the enstrophy decays monotonically (see, e.g., Fig. 2.4(e), or Ref. [247]). It is only important that the inviscid transfer processes in $T(k)$ (i.e., the incompressible Euler equations) conserve the enstrophy [Eqs. (2.61) and (2.65)]. Most importantly, they must not allow the enstrophy to *grow*, because this is the process that permits energy to travel to small scales via vortex stretching (Sec. 2.9.1). Furthermore, the inverse energy cascade does

not *require* the enstrophy cascade to be simultaneously present; it only requires the transfer properties encoded within the detailed conservation laws. As already noted in Sec. 2.9.3, studies are often optimised to only study the inverse energy cascade by forcing near the dissipation wavenumber. This leaves "no room" in scale space for the enstrophy cascade to develop, even though the underlying transfer mechanisms are still occurring.

The direct cascade scenario of Numasato *et al.* seems to be at odds with a number of basic principles. Firstly, since it has already been established that the conservative contribution to quantum vortex dynamics is point-vortex motion, it is difficult then to see how introducing the non-conservative processes via sound coupling could change this in any fundamental way; dipoles approaching each other in this manner is not consistent with point-vortex dynamics unless radiation or thermal dissipation is included. In the GPE, as $\mathrm{Ma_s} \sim \xi/\ell \to 0$ annihilation becomes negligible and enstrophy conservation is restored in 2D, just as for the classical Euler limit $\nu \to 0$.[15] In 3D this is not so, because the vortex lines can lengthen.[16] In 2D, without the possibility for bundles to lengthen, the only way to amplify enstrophy would be to nucleate dipoles from the sound field — but this is forcing, not an energy-conserving transfer process of the incompressible subsystem. If, as in the scenario of Numasato *et al.*, the sound coupling is strong, one could also argue that hydrodynamic cascade arguments for the incompressible energy become largely irrelevant, because there is unlikely to be a region of scale space over which conservative transport processes alone are dominant. Indeed, the $k^{-5/3}$ scaling observed is both temporally transient and of limited scale range, and the flux that is evaluated is an approximation. Finally, note that the dipole annihilation mechanism described is in no way inconsistent with the role of viscosity in the Navier-Stokes picture: since only closely paired vortex-antivortex pairs can annihilate, this process removes two vortices while only removing a comparatively small fraction of the energy (see Sec. 2.6 and also Sec. 3.10). In fact, Ref. [147], a (classical) point-vortex study, uses precisely this mechanism to model viscosity! While it is true that Kraichnan's arguments are irrelevant for the scenario of Numasato *et al.*, it is not due to a lack of enstrophy conservation. Rather, in their situation, (a) the turbulence is not subject to steady forcing, and (b) the Mach number is high and the sound coupling is strong, such that the incompressible subsystem most likely experiences a large effective viscosity. In this sense it is analogous to

[15] A distinction of course is that quantum vortices do not move when $\xi/\ell \to 0$.

[16] Growth of the vortex line length in 3D and vortex number conservation in 2D is clearly demonstrated in the Gross-Pitaevskii simulations of Ref. [60], see their Figs. 17 and 9 respectively.

a low Reynolds number flow, where dissipation rather than inertia is the dominant mechanism.

In Ref. [248] a direct cascade was also inferred from this dipole recombination process. Here the decay of a lattice of multiply charged vortices was investigated, in holographic duality simulations within the AdS-CFT framework. The same-sign clusters nucleated from the multi-quantum vortex decay were observed to rapidly form dipoles and annihilate. In Ref. [93], which studied the same scenario within the damped GPE and damped point-vortex models, it was shown that the apparent Kolmogorov scaling attributed to a cascade in Ref. [248] vanished when the core-envelope function $G_\Lambda(k\xi)$ was removed (Sec 3.5, and Fig 3.3), suggesting the apparent scaling was instead merely due to the core crossover region. Although there is no direct mapping between the holographic model and the Gross-Pitaevskii theory, the vortices do still exhibit the same near-field and far field properties in both models [Eqs. (3.53) and (3.54)]. It was noted in Ref. [93] that the dynamics in [248] look remarkably similar to Gross-Pitaevksii simulations with very large damping $\gamma \sim \mathcal{O}(10^{-1})$, and it was suggested that the system instead underwent a "dissipative collapse" rather than a cascade.

3.9.4 The Inverse Energy Cascade in 2DQT?

Contrary to the direct cascade argument, the experiment of Neely *et al.* [80], observed small but long-lived clusters of same sign vortices in a toroidal BEC, and the numerical modelling of the experiment revealed a Kolmogorov spectrum at the end of the forcing cycle. This prompted a number of studies to revisit the inverse energy cascade directly within the Gross-Pitaevskii model. In Ref. [187], the damped GPE was used to investigate turbulence in a harmonically confined BEC, stirred by a repulsive Gaussian potential. While fairly convincing evidence of wave turbulence was found, the findings were inconclusive regarding hydrodynamic cascades. In particular, it was found that the system exhibited a spectral scaling close to the $k^{-5/3}$ law over some range, even when the vortex shedding dynamics was highly regular. It was noted that system did not contain a great number of vortices, and the scale range was severely limited by the system size. White *et al* [249, 250] and Skaugen and Angheluta [246] conducted similar studies within the GPE, obtaining similar results. Kobyakov *et al.* [244] observed the $k^{-5/3}$ scaling in turbulence generated in binary condensates via the Rayliegh-Taylor instability. However, since the turbulence was decaying, the observation goes against the current understanding of the theory and

is therefore not readily explained in terms of the inverse energy cascade.

It became apparent that clear cascade realisations would not be possible in any currently available experimental systems, since the system scale L, the intervortex distance ℓ and the healing length ξ typically only satisfy the relation $L > \ell \gtrsim \xi$, whereas the hydrodynamic regime, which superfluid helium satisfies, requires $L \gg \ell \gg \xi$. Hence Ref [188] simulated two-dimensional quantum turbulence in a large, uniform system continuously forced by a stirring grid, within the damped GPE framework. Some signatures consistent with an inverse energy cascade were observed, including a quasi-steady accumulation of incompressible kinetic energy in the lowest modes of the system, and a spectrum in reasonable agreement with the $k^{-5/3}$ law. However, one could offer a number of possible criticisms. The range of the observed power law behaviour was still rather narrow (nearly 1 decade). Additionally, unfortunately a relatively high value of dissipation ($\gamma \sim 10^{-2}$) was needed to consistently inject vortices without too much compressible energy; for the chosen system parameters, turbulent shedding from the small-scale forcing could only be achieved at a relatively high Mach number ($u/c \sim 0.8$), and the dissipation was needed in to suppress the resulting sound waves. Values for the Kraichnan constant and the integral scale growth rate were not obtained.

3.9.5 Can Hydrodynamic Cascades Really Occur in 2DQT?

Due to the lack of a truly definitive demonstration, there is no consensus on the inverse energy cascade in two dimensional quantum turbulence. Meanwhile, the enstrophy cascade has yet to be explored at all, and as such the relevance of the entire 2D cascade phenomenology is presently uncertain. The only hint that the cascades might occur is that the energy cascade does occur in 3D, but this is a fairly strong indication that classical signatures should emerge. In light of this result, the question is probably not *if*, but rather *when?*: How many vortices are needed before the laws of turbulence reveal themselves, and how large do the systems need to be?

It is already clear that realising the cascades may be challenging in the presently available experimental systems. However, in some sense this does not matter. Regardless of whether or not the cascades can be realistically achieved experimentally, their theoretical investigation is useful and necessary at a fundamental level. They provide a means to test our general ideas about how turbulent flows in quantum fluids behave, and could provide some further insight into the universality of the ideas behind cascade phenomenology. As already mentioned, the appearance of the Kol-

mogorov law in superfluid helium was not initially expected. A clear demonstration of either of the 2D cascades under the right conditions would make matters considerably clearer, and would provide a guide for what kind of conditions would be required in reality. It would also provide information about how to quantify turbulence in a 2D quantum fluid — since fundamental measures like the Reynolds number are currently absent in the 2DQT literature, a validation of Eq. (3.94) as a suitable parameter, through the inertial range length, or any other benchmark for comparison, would be immensely beneficial.

The studies summarized in this section highlight issues with both the scale limitations of the systems considered, and the danger of inferring cascade mechanisms from the kinetic energy spectrum alone, without flux measurements or similar corroborating evidence. Clearly this is particularly problematic with quantum vortices, since the spectrum has a permanent k^{-1} background (and a k^{-3} crossover) that, accompanied by broad Bessel function oscillations, can very easily lead to a spurious $k^{-5/3}$ scaling. In fact, in Ref. [251] it was demonstrated that a $k^{-5/3}$ scaling seems to appear, over nearly a decade of wavenumbers and for a substantial timeframe, for only two vortices in a harmonic trap (in three dimensions). It is somewhat difficult to believe that a system of two vortices has much to do with the transport processes of fully-developed turbulence. Such results suggest that it would be beneficial to investigate a very large, idealised system and work back towards a more realistic scenario. This is the focus of Chapter 6 where we first study the enstrophy cascade for very large vortex numbers, and then systematically decrease to more realistic values.

3.10 Spectral Condensate Formation in 2DQT

Since negative temperature states are a somewhat rare phenomenon, there has been some considerable interest in testing whether the negative temperature, spectrally condensed equilibrium states (Sec. 2.10.3) can be realized with quantum vortices.[17] Initially, this idea was met with some skepticism, since the negative temperature state might be too unstable, imparting too much of its energy to the sound field. As a proof of principle, Billam *et al.* [92] demonstrated that spectral condensation could occur within Gross-Pitaevskii dynamics with periodic boundary conditions. In a moderately large system ($500\xi \times 500\xi$) containing ~ 300 vortices they showed that a high energy, low entropy, non-equilibrium distribution could evolve towards the equi-

[17] Spectral condensation has been called "Onsager-Kraichnan condensation", and "Onsager vortex formation" in the quantum fluids literature. They are all the same thing.

librium spectral condensate — despite compressibility, the weak radiative coupling in 2D (Sec. 3.6.1) allowed the incompressible subsystem to retain most of its energy. Simula *et al.* [189] showed that the spectral condensate could form by a completely different mechanism, in a more experimentally realistic system. Simulating the full 3D Gross-Pitaevskii evolution of random vortex configurations within a quasi-2D bucket trap, they showed that the vortices could *spontaneously* condense from a low energy state via vortex losses. Since the only way vortices may be removed from the system is via dipole annihilation, or leaving at the boundary (annihilation with their image), these processes can only remove the low energy vortices from the system. Although under annihilation the total vortex energy decreases, the energy *per vortex* is substantially increased with each event. The gradual energy increase from this annihilation causes same-sign vortices to slowly cluster, eventually shutting off the loss mechanism altogether [see Fig. 3.6]. By analogy to evaporative cooling mechanism used to achieve Bose condensation, they termed this mechanism *evaporative heating*. The evaporative heating mechanism was studied further by Grozek *et al.* [195]. They emphasised that the evaporative heating mechanism does not depend on the initial conditions of the system: with enough vortices, the system could in principle evaporatively heat even from deep within the low energy, positive temperature regime. They also showed, importantly, that the spectral condensation phenomenon could not occur in a harmonic confining potential. Spectral condensation was also recently investigated by Salman and Maestrini [252], in a box potential. They found that the condensed states formed in the Gross-Pitaevskii equation were in reasonable agreement with the solutions predicted by the Montgomery-Joyce equation. Yu *et al.* [94], building on the work of Smith and O'Niel [253, 254], obtained mean-field results for the condensate formation for a neutral point vortex system in the disc. Casting the problem in the language of phase transitions, they obtained the critical temperature and scaling results for the growth of the global dipole moment (the order parameter), finding good agreement with Monte-Carlo simulations. Many other details of the condensation mechanism were elucidated from the solution obtained for the mean-field vorticity distribution. In Chapter 4, we explore the detection of spectral condensate formation via an experimentally accessible measure.

3.11 Natural Units

In computational physics it is always a good idea to express equations in dimensionless form, such that the important numerical quantities are of order unity. Doing so is

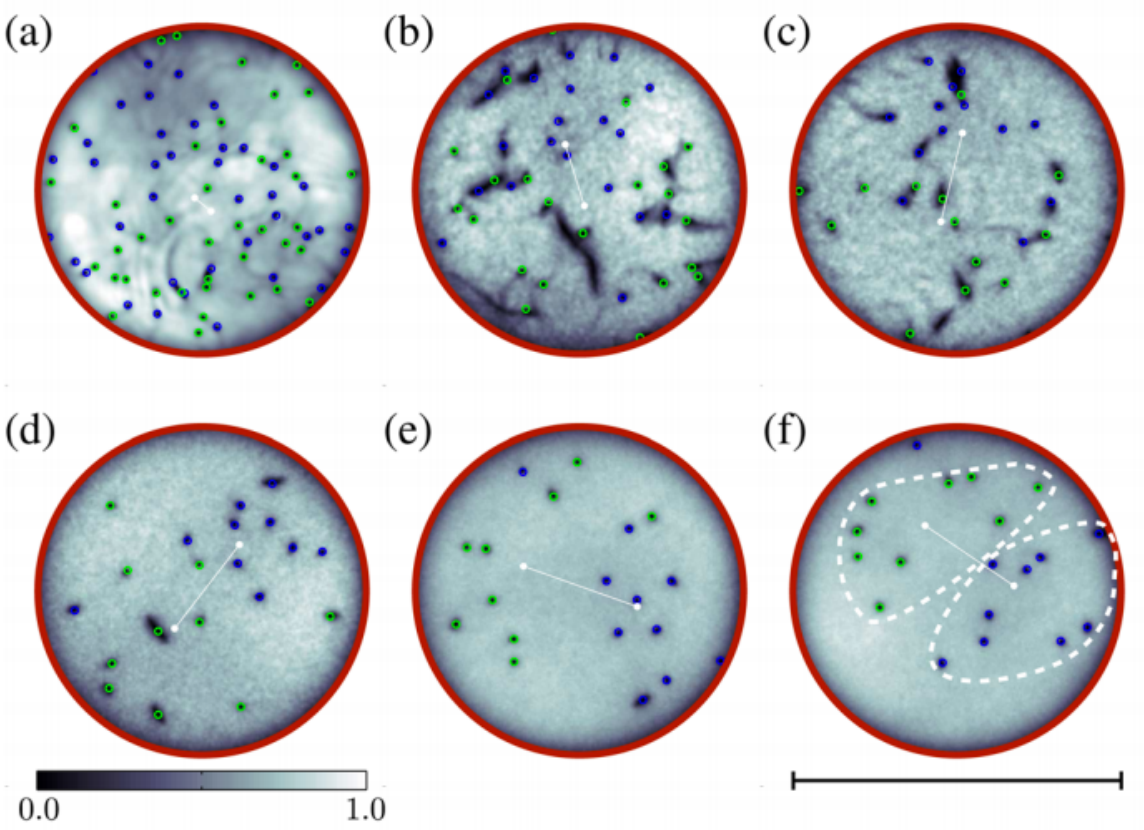

Figure 3.6: Image reproduced from Simula *et al.* (2014), Ref [189]. Column integrated density images showing spectral condensate formation within the Gross-Pitaevskii model. From an initially random configuration of vortices, vortex annihilation events cause an *evaporative heating* of the vortex distribution, driving it towards the negative temperature equilibrium state. The final state clearly exhibits macroscopic flow structures, formed from clusters of same-sign vortices.

beneficial, because it both aids interpretation by providing natural reference scales, and also improves numerical accuracy. The healing length ξ, and the speed of sound c, together with the natural timescale $\tau = \xi/c = \hbar/\mu$ and the chemical potential $\mu = ng = mc^2$ define convenient reference scales for length, speed, time and energy in an atomic BEC. These units are especially useful in quantum turbulence, since they are directly related to quantum vortices and have a clear meaning. In particular, the velocity field at a distance ξ from a vortex is precisely the (background) speed of sound c:

$$c = \frac{\hbar}{m\xi}. \tag{3.95}$$

In natural units, $c = \xi = \mu = 1$, and $\Gamma = 2\pi$. Denoting dimensionless variables with tildes, in these units, we make the replacements

$$\nabla \to \frac{1}{\xi}\tilde{\nabla} \qquad \frac{\partial}{\partial t} \to \left(\frac{c}{\xi}\right)\frac{\partial}{\partial \tilde{t}} \qquad \psi \to \tilde{\psi}/\xi \qquad V \to \mu\tilde{V}, \tag{3.96}$$

such that the quasi-2D Gross-Pitaevskii equation (Sec 3.1.5) takes the dimensionless form

$$i\frac{\partial\psi(\mathbf{x})}{\partial t} = \left[-\frac{\nabla^2}{2} + V(\mathbf{x},t) + C_{nl}|\psi(\mathbf{x})|^2 - 1\right]\psi(\mathbf{x}), \tag{3.97}$$

where $C_{nl} = \sqrt{8\pi}a_s/l_z$, and the tildes have been dropped for notational convenience. However, we also have the freedom of redefining the wavefunction normalization via $\psi \to \sqrt{C_{nl}}\psi$, such that the GPE takes the form

$$i\frac{\partial\psi(\mathbf{x})}{\partial t} = \left[-\frac{\nabla^2}{2} + V(\mathbf{x},t) + |\psi(\mathbf{x})|^2 - 1\right]\psi(\mathbf{x}), \tag{3.98}$$

Note that in this form the total effective strength of the nonlinearity (gN) is now implicitly contained within the system size L. Natural units will be used in all numerical work in this thesis.

Chapter 4

Signatures of Coherent Vortex Structures in a 2D Quantum Fluid

In this chapter we study coherent vortex structure formation via an experimentally accessible measure. We introduce the so-called quantum kinetic energy spectrum, and demonstrate how it is related to the velocity probability distribution of the quantum fluid. We then analytically show how coherent vortices give rise to a k^3 law in this energy spectrum. Then, we test our analytical predictions against numerically generated vortex distributions, and, furthermore, demonstrate that the k^3 law spontaneously emerges in Gross-Pitaevskii dynamics of a trapped system.

4.1 Introduction

The emergence of coherent rotating structures from disordered flows is a central feature of 2D classical turbulence [16, 22, 255]. In two-dimensional quantum turbulence (2DQT) [80, 83, 173, 186, 187, 243, 245], the analogous phenomenon involves large-scale clustering of quantum vortices of the same sign of circulation; such clustering can occur in negative temperature equilibrium states [92, 143, 151], and as a result of a turbulent inverse-energy cascade induced by small-scale forcing [188]. The characterisation of such clustered vortex states, which tend to be highly disordered arrangements of same-sign vortices, poses a theoretical challenge of recent interest [187, 249]. In many respects, these states strongly contrast with a rotating superfluid in its ground state, which will form a regular Abrikosov lattice comprised of co-rotating vortices, exhibiting a sixfold rotational symmetry, and obeying Feynman's rule of constant areal vortex density [170, 256]. Although the velocity field of the superfluid

is formally curl-free, the velocity field of a large lattice approaches that of rigid-body rotation under appropriate coarse-graining over many vortex cores [257], as required by Bohr's correspondence principle. Furthermore, the self-similar expansion of the atomic density of a 3D turbulent cloud [54] can be modelled by introducing a rotational velocity field [258], suggesting that the development of a *rotational* velocity field in an *irrotational* superfluid may be a fundamental property of quantum turbulence. In the context of the negative temperature states arising as the end states of decaying 2DQT [92], these considerations motivate the question: *what kind of rotational velocity field emerges in the interior of a large, coherent vortex cluster?*

In this work we address the problem of characterising emergent coherent vortex structures in a 2D Bose-Einstein condensate (BEC), a compressible superfluid, with an emphasis on experimentally accessible measures. While measurements of vortex locations and circulations has been recently demonstrated [87], allowing inference of the *classical* (point-vortex-like) energy spectrum [59, 173] (Sec. 3.5), it is also desirable to consider measures that may be more readily accessible by current standard measurement techniques [80, 83]. Here, we consider information contained in the quantum kinetic energy spectrum of the quantum fluid; provided interactions can be suppressed using, for example, an appropriate Feshbach resonance, this information may be readily available in experiments via ballistic expansion [259]. We develop a link between the quantum kinetic energy spectrum over wavenumber k and the superfluid velocity probability distribution, and show analytically that a spectrum $E(k) \propto k^3$ in the infrared arises from the coherent quantum vortex structures emerging in negative-temperature vortex configurations. We show analytically that such a spectrum can correspond to rigid-body rotation, extending to a scale determined by the size of the coherent vortex structures, and, additionally, can arise due to quadrupole velocity fields resulting from the interaction between the coherent structures and the superfluid boundary.

We numerically sample vortex configurations over a range of energies, exploring a number of measures with which to characterise the vortex distributions. We verify the emergence of a k^3 spectrum and demonstrate that the coherent structures produce a well-defined peak in the quantum kinetic energy spectrum. This peak can be quantitatively understood by considering the largest vortex structures. We further find that the largest structures exhibit a constant areal vortex density, and conclude that the clustered states that emerge in negative-temperature configurations obey Feynman's rule while being spatially disordered. We consider the outlook for observing quasi-classical coherent vortex structures in atomic BEC experiments. Dynamical

simulations of a trapped BEC (within the damped Gross-Pitaevskii description) show that, for well-chosen non-equilibrium vortex configurations that may be accessible via laser-stirring protocols [82], the resulting vortex dynamics can form long-lived, high-energy coherent vortex structures despite some loss of energy to sound.

Our main result is that quasi-classical coherent structures exhibiting rigid-body rotation can emerge in negative-temperature vortex states, establishing a new link between classical and quantum turbulence that may be explored experimentally.

This chapter is structured as follows. So that this chapter may be read in a self-contained manner, in Sec. 4.2 we briefly recapitulate some relevant background from Chapter 3, and discuss some aspects of the classical spectral decomposition frequently used in the literature. In Sec. 4.3 we develop a decomposition of the quantum kinetic energy spectrum of the quantum fluid, and show its connection to the velocity probability distribution for a compressible superfluid in the hydrodynamic regime. In Sec. 4.4 we present our numerical methods for sampling and analysing clustered states, and analyse kinetic energy spectra of vortex distributions over a range of energies for vortex configurations in a doubly-periodic box. In Sec. 4.5 we analytically and numerically investigate the emergence of quasi-classical flows for negative-temperature states. In Sec. 4.6 we show that high-energy coherent vortex structures, and the associated spectral signatures, can emerge dynamically in a trapped BEC, and compare the properties of the dynamically-generated structures to the properties predicted by microcanonical sampling. Sec. 4.7 presents concluding remarks.

4.2 System

Here we briefly outline our system and restate some basic properties previously discussed in Chapter 3. We consider a BEC that is tightly confined in the z-direction. The Gross-Pitaevskii equation describing this homogeneous 2D Bose gas is written in terms of an effective 2D interaction parameter g_2:

$$i\hbar\frac{\partial\psi(\mathbf{r},t)}{\partial t} = \left(-\frac{\hbar^2\nabla_\perp^2}{2m} + g_2|\psi(\mathbf{r},t)|^2\right)\psi(\mathbf{r},t), \tag{4.1}$$

where $g_2 = g/l$, l is the characteristic thickness of the 3D system [186], and $g = 4\pi\hbar^2 a_s/m$ for s-wave scattering length a_s and atomic mass m. For example, in a system with harmonic trapping in the z-direction characterized by trapping frequency ω_z, the length scale is $l = \sqrt{2\pi}l_z$ where $l_z = \sqrt{\hbar/m\omega_z}$ is the z-axis harmonic oscillator

length, and the confinement is assumed sufficient to put the wavefunction into the z-direction single-particle harmonic oscillator ground state (Sec. 3.1.5). Note, however, that such tight confinement in one direction is not necessarily required for effectively two-dimensional vortex dynamics [80, 166].

4.2.1 Properties of a 2D Quantum Vortex

For solutions with chemical potential μ containing a single vortex at the origin (with circulation necessarily normal to the plane of the 2D quantum fluid) we can write [257]

$$\psi_1(\mathbf{r},t) = \sqrt{n_0}e^{-i\mu t/\hbar}\chi(r/\xi)\, e^{\pm i\theta} \tag{4.2}$$

where $\xi = \hbar/mc$ is the healing length for speed of sound $c = \sqrt{\mu/m}$, and $n_0 = \mu/g_2$ is the 2D particle density for $r \gg \xi$ and is taken to be a constant. The vortex radial amplitude function $\chi(\sigma)$, where $\sigma = r/\xi$ is a scaled radial coordinate, is a solution of

$$\left(-\sigma^{-1}\partial_\sigma\,\sigma\partial_\sigma + \sigma^{-2}\right)\chi = 2(\chi - \chi^3). \tag{4.3}$$

The boundary conditions are $\chi(0) = 0$, and the derivative $\chi' \equiv d\chi/d\sigma$ evaluated at $\sigma = 0$ must be chosen such that it is consistent with $\chi(\infty) = 1$ and $\chi'(\infty) = 0$. The value

$$\Lambda \equiv \chi'(0) = \lim_{r\to 0}\frac{\xi}{\sqrt{n_0}}\left|\frac{d\psi_1}{dr}\right| \tag{4.4}$$

is a universal feature of the vortex core, and numerically is found to be $\Lambda = 82475449\ldots$ (see Sec 3.3). The quantum vortex state (4.2) has the velocity field of a point-vortex

$$\mathbf{v}(\mathbf{r}) = \frac{\hbar}{mr}(\mp\sin\theta, \pm\cos\theta) = (v_x, v_y), \tag{4.5}$$

which has vorticity, $\omega(\mathbf{r}) = \partial_x v_y - \partial_y v_x$, given by

$$\omega(\mathbf{r}) = \pm\frac{h}{m}\delta(\mathbf{r}), \tag{4.6}$$

where $\delta(\mathbf{r})$ is the Dirac δ-function.

4.2.2 Hydrodynamic decomposition

The 2D Gross-Pitaevskii energy in the homogeneous system is given by

$$\mathcal{E} = \int d^2\mathbf{r} \left\{ \frac{\hbar^2}{2m} |\nabla\psi(\mathbf{r},t)|^2 + \frac{g_2}{2}|\psi(\mathbf{r},t)|^4 \right\}. \tag{4.7}$$

Using the Madelung representation $\psi(\mathbf{r},t) = \sqrt{n(\mathbf{r},t)}e^{i\theta(\mathbf{r},t)}$ which gives the superfluid velocity as $\mathbf{v}(\mathbf{r},t) = \hbar\nabla\theta(\mathbf{r},t)/m$, the energy can be decomposed as $\mathcal{E} = \mathcal{E}_H + \mathcal{E}_Q + \mathcal{E}_I$, where

$$\mathcal{E}_H = \frac{m}{2}\int d^2\mathbf{r}\; n(\mathbf{r},t)|\mathbf{v}(\mathbf{r},t)|^2, \tag{4.8}$$

$$\mathcal{E}_Q = \frac{\hbar^2}{2m}\int d^2\mathbf{r}\; |\nabla\sqrt{n(\mathbf{r},t)}|^2, \tag{4.9}$$

$$\mathcal{E}_I = \frac{g_2}{2}\int d^2\mathbf{r}\; n(\mathbf{r},t)^2. \tag{4.10}$$

Respectively, these define the hydrodynamic kinetic energy, quantum pressure energy, and interaction energy. The hydrodynamic and quantum pressure terms originate from the kinetic energy term, and $\mathcal{E}_K = \mathcal{E}_H + \mathcal{E}_Q$ is the total kinetic energy.

4.2.3 Classical Kinetic Energy Spectrum

It is worthwhile to briefly discuss some additional aspects of the spectral decomposition introduced in Sec. 3.5. We call this the *classical* kinetic energy spectrum, as in a classical fluid it is exactly the kinetic energy power spectrum. This spectrum is obtained by applying the general correspondence between a two-point correlation function and its associated power spectrum to the velocity field (Secs. 2.7.3 and 3.5). However, as we will show in Sec. 4.3, in a quantum fluid the existence of a quantum phase $\theta(\mathbf{r})$ breaks this correspondence. While in a quantum fluid this classical spectrum is no longer the only way to construct a kinetic energy spectrum, it provides a useful link to classical turbulence theory, allowing the identification of, for example, the Kolmogorov $k^{-5/3}$ law associated with an inertial range (Sec. 2.8).

As we will only focus on particular instants in time, we now drop the explicit time dependence from our notation. By Parseval's theorem, (4.8) may be equivalently written in wavenumber (k)-space as

$$\mathcal{E}_H = \frac{m}{2}\int d^2\mathbf{k}\; |\tilde{\mathbf{u}}(\mathbf{k})|^2, \tag{4.11}$$

where

$$\tilde{\mathbf{u}}(\mathbf{k}) = \mathcal{F}[\mathbf{u}(\mathbf{r})] \equiv \frac{1}{2\pi}\int d^2\mathbf{r}\; e^{-i\mathbf{k}\cdot\mathbf{r}}\mathbf{u}(\mathbf{r}), \tag{4.12}$$

and $\mathbf{u}(\mathbf{r}) = \sqrt{n(\mathbf{r})}\mathbf{v}(\mathbf{r})$ is the density-weighted velocity field. The one-dimensional *spectral density* in k-space is given in polar coordinates by integrating over the azimuthal angle to give

$$\epsilon_H(k) = \frac{mk}{2}\int_0^{2\pi} d\theta_k\; |\tilde{\mathbf{u}}(\mathbf{k})|^2 \tag{4.13}$$

$$= \frac{mk}{2}\int_0^{2\pi} d\theta_k\; \left|\frac{1}{2\pi}\int d^2\mathbf{r}\; e^{-i\mathbf{k}\cdot\mathbf{r}}\mathbf{u}(\mathbf{r})\right|^2 \tag{4.14}$$

which, when integrated over all k, gives the total hydrodynamic kinetic energy $\mathcal{E}_H = \int_0^\infty dk\; \epsilon_H(k)$. Similarly, for the quantum pressure we have

$$\epsilon_Q(k) \equiv \frac{\hbar^2}{2m}k\int_0^{2\pi} d\theta_k \left|\frac{1}{2\pi}\int d^2\mathbf{r}\; e^{-i\mathbf{k}\cdot\mathbf{r}}\nabla\sqrt{n(\mathbf{r})}\right|^2, \tag{4.15}$$

and the total kinetic energy is given by $\mathcal{E}_K = \mathcal{E}_H + \mathcal{E}_Q = \int dk\; [\epsilon_H(k) + \epsilon_Q(k)]$.

As detailed in Sec 3.5, the hydrodynamic spectrum $\epsilon_H(k)$ can be further decomposed into incompressible and compressible parts via a Helmholtz decomposition, writing $\mathbf{u} = \mathbf{u}^i + \mathbf{u}^c$, where $\nabla\cdot\mathbf{u}^i = 0$ and $\nabla\times\mathbf{u}^c = 0$. The incompressible part is associated with quantum vortices, whereas the compressible part is associated with acoustic excitations [173, 186]. Although we do not make direct use of this decomposition here, we are generally interested in the incompressible limit, where $\mathbf{u} \approx \mathbf{u}^i$. As a single vortex is purely incompressible [Eq. (3.82)], the incompressible limit corresponds to a fluid for which the background density is smoothly varying, and the quantum vortices are sufficiently well-separated that their cores do not overlap [see Eq. (3.61)].

It has become standard in the literature to interpret the incompressible and compressible parts of $\epsilon_H(k)$ as kinetic energy densities in k-space [186, 188, 228], as is the case for classical fluids, and thus these kinetic energy densities are generally referred to as "incompressible" and "compressible" kinetic energy spectra. However, this approach does not provide a kinetic energy spectrum that can be directly connected to the momentum distribution of a quantum fluid.

4.3 Kinetic Energy Spectrum and Velocity Probability Distribution

In this section we pursue an alternative route to decomposing the kinetic energy of the quantum fluid, and develop a link between the true quantum kinetic energy spectrum and the velocity probability distribution.

4.3.1 Quantum Kinetic Energy Spectrum

The kinetic energy of the quantum fluid is given by

$$\mathcal{E}_K = \frac{\hbar^2}{2m} \int d^2\mathbf{r} \, |\nabla\psi(\mathbf{r})|^2. \tag{4.16}$$

This may be equivalently written in momentum space as

$$\mathcal{E}_K = \frac{\hbar^2}{2m} \int d^2\mathbf{k} \, |\mathbf{k}\phi(\mathbf{k})|^2, \tag{4.17}$$

where

$$\phi(\mathbf{k}) = \frac{1}{2\pi} \int d^2\mathbf{r} \, e^{-i\mathbf{k}\cdot\mathbf{r}} \psi(\mathbf{r}). \tag{4.18}$$

Writing $\mathbf{k} = k(\cos\theta_k, \sin\theta_k)$, and performing the angular integration, we obtain the *quantum* kinetic energy spectrum

$$E(k) = \frac{\hbar^2 k^3}{2m} \int_0^{2\pi} d\theta_k \, |\phi(\mathbf{k})|^2, \tag{4.19}$$

and the total kinetic energy via $\mathcal{E}_K = \int_0^\infty dk \; E(k)$.

We now provide a decomposition of the quantum kinetic energy spectrum that allows the identification of hydrodynamic and quantum pressure components, and their relationship to the momentum distribution. Returning to Eq. (4.17), the integrand can be decomposed using (4.18) and the Madelung transformation, Eq. (3.15).

We thus write the total kinetic energy as

$$\mathcal{E}_K = \int_0^\infty dk \; E(k) \tag{4.20}$$

$$= \int_0^\infty dk \; \left[E_H(k) + E_Q(k) + E_{QH}(k)\right], \tag{4.21}$$

where

$$E_H(k) = \frac{mk}{2}\int_0^{2\pi} d\theta_k \left|\frac{1}{2\pi}\int d^2\mathbf{r}\; e^{-i\mathbf{k}\cdot\mathbf{r}+i\theta(\mathbf{r})}\mathbf{u}(\mathbf{r})\right|^2, \tag{4.22}$$

$$E_Q(k) = \frac{\hbar^2 k}{2m}\int_0^{2\pi} d\theta_k \left|\frac{1}{2\pi}\int d^2\mathbf{r}\; e^{-i\mathbf{k}\cdot\mathbf{r}+i\theta(\mathbf{r})}\nabla\sqrt{n(\mathbf{r})}\right|^2, \tag{4.23}$$

$$E_{QH}(k) = \frac{\hbar k}{2}\int_0^{2\pi} d\theta_k \Phi(\mathbf{k}), \tag{4.24}$$

and

$$\Phi(\mathbf{k}) = \frac{-i}{(2\pi)^2}\int d^2\mathbf{r} e^{-i\mathbf{k}\cdot\mathbf{r}+i\theta(\mathbf{r})}\nabla\sqrt{n(\mathbf{r})}\cdot\int d^2\mathbf{r}' e^{i\mathbf{k}\cdot\mathbf{r}'-i\theta(\mathbf{r}')}\mathbf{u}(\mathbf{r}') + \text{c.c.}, \tag{4.25}$$

with c.c. denoting the complex conjugate. Equations (4.22), (4.23), and (4.24) give the kinetic energy spectra for the hydrodynamic, quantum pressure, and quantum-hydrodynamic components respectively.

The decomposition derived above provides spectral energy densities that are locally additive in k-space: $E_H(k) + E_Q(k) + E_{QH}(k) = E(k)$. In contrast, although *integrating* the classical spectra yields $\mathcal{E}_H + \mathcal{E}_Q = \mathcal{E}_K$, the classical spectra are not locally additive in k-space: $\epsilon_H(k) + \epsilon_Q(k) \neq E(k)$. The hydrodynamic and quantum pressure terms here differ to those of the classical spectral decomposition by the formal replacement $\mathbf{u}(\mathbf{r}) \to e^{i\theta(\mathbf{r})}\mathbf{u}(\mathbf{r})$ from (4.14) to (4.22) and $\nabla\sqrt{n(\mathbf{r})} \to e^{i\theta(\mathbf{r})}\nabla\sqrt{n(\mathbf{r})}$ from (4.15) to (4.23). Notice also that there is no term corresponding to the quantum-hydrodynamic term (4.24) in the classical kinetic energy decomposition. Furthermore, as

$$\mathcal{E}_K = \mathcal{E}_H + \mathcal{E}_Q = \int_0^\infty dk\; [\epsilon_H(k) + \epsilon_Q(k)] \tag{4.26}$$

$$= \int_0^\infty dk\; [E_H(k) + E_Q(k) + E_{QH}(k)], \tag{4.27}$$

we may conclude that

$$\int_0^\infty dk\; E_{QH}(k) = 0, \tag{4.28}$$

illustrating that the quantum-hydrodynamic term is only an "interference" term: it does not contribute to the total energy, and only redistributes the energy in k-space. An important property of the quantum kinetic energy spectrum [Eq. (4.19)] is its potential experimental accessibility: The momentum distribution of a non-interacting condensate, $|\phi(\mathbf{k})|^2$, can be obtained through ballistic (time-of-flight) expansion [33, 259]. Thus, after suppressing interatomic interactions via an appropriate Feshbach

resonance, one can obtain $E(k)$ to high accuracy.

The spectral decomposition we have introduced here thus highlights an important distinction between classical and quantum fluids. In a quantum fluid Eq. (4.22) could be considered the "true" hydrodynamic kinetic energy spectrum, whereas Eq. (4.13) is the power spectrum of the velocity autocorrelation function (Secs. 3.5 and 2.7.3). In a classical fluid there is no quantum phase, and hence there is no distinction between these two measures. We remark that the quantum spectra may resemble the classical spectra in regimes where the phase $\theta(\mathbf{r})$ is approximately constant over large regions of the system, for example in the vortex-dipole gas regime (see also Sec. 4.4).

4.3.2 Velocity Probability Distribution

The probability, $P(v)$, that an atom has velocity $v = |\mathbf{v}|$ is

$$P(v) = \frac{1}{N_{\rm tot}} \int d^2\mathbf{r}\; \delta(v - |\mathbf{v}(\mathbf{r})|)|\psi(\mathbf{r})|^2, \tag{4.29}$$

for $N_{\rm tot} = \int d^2\mathbf{r}\; |\psi(\mathbf{r})|^2$ atoms, where the normalization is $\int_0^\infty dv\; P(v) = 1$. Note that binning the velocity neglects the density weighting, and so in the context of 2DQT is equivalent to the above for a homogenous superfluid with coreless vortices [260, 261]. The physical distinction is important in regions where the atomic density is rapidly varying, such as near a quantum vortex core.

Let us briefly consider the velocity probability distribution of a single vortex in a homogeneous, compressible superfluid. We start by calculating $P(v)$ for atoms in a superfluid vortex, given by (4.2), in an otherwise homogeneous 2D system. Using (4.2), (4.5), and (4.29), and exploiting cylindrical symmetry, yields

$$P(v) = \frac{2\pi n_0 \xi^2}{c N_{\rm tot}} \left(\frac{c}{v}\right)^3 \left|\chi\left(\frac{c}{v}\right)\right|^2 H(v - v_R), \tag{4.30}$$

where we have introduced the system size R, and the Heaviside function H restricts the range of velocities to $v \geq v_R \equiv c\xi/R = \hbar/mR$, avoiding infrared divergence. Two regimes can be identified within (4.30), namely a *point-vortex regime* for $v_R \leq v \ll c$ (where $r \gg \xi$)

$$P(v)\Big|_{v\ll c} \simeq \frac{\xi^2}{R^2}\frac{2}{c}\left(\frac{c}{v}\right)^3, \tag{4.31}$$

and a *vortex core regime* for $v \gg c$ ($r \ll \xi$)

$$P(v)\Big|_{v\gg c} \simeq \frac{\xi^2}{R^2}\frac{2\Lambda^2}{c}\left(\frac{c}{v}\right)^5. \tag{4.32}$$

Notice the parameter Λ [Eq. (4.4)] appears in the vortex core regime, whereas this is absent in (4.31). The v^{-5} power law seen here stems from the structure of a vortex core in an atomic Bose-gas superfluid. In a macroscopically occupied BEC with small healing length, the vortex core region only corresponds to a tiny fraction of the atoms. However, it might be possible to observe the v^{-5} power law when the system contains many vortices and few particles, namely, in the vortex-liquid phase [256].

The v^{-3} power-law tail of Eq. (4.31) is a universal result for quantum vortices [34], and has been identified in the 2D and 3D GPE [260], the point-vortex model in 2D [262, 263], and in superfluid helium [261, 264], which is well-described by a vortex-filament model at larger scales. Previous works [260, 261] have emphasised the v^{-3} law as a feature distinguishing quantum turbulence from classical turbulence. However, as the v^{-3} power law is a single vortex effect, note that it will always be present in, but is not indicative of, turbulent vortex dynamics. For scales smaller than the minimum inter-vortex distance but appreciably larger than the healing length, the single-vortex velocity field can be expected to dominate the distribution. However, effects due to cooperative behaviour of many quantum vortices are central to quantum turbulence [92, 173], and may lead to different behaviour for scales greater than the minimum inter-vortex distance [264, 265].

4.3.3 Quantum Kinetic Energy Spectrum in the Hydrodynamic Regime

We now evaluate the definition of the spectrum (4.22) within a hydrodynamic approximation that neglects high-order density and phase gradients. This approximation gives a rigorous link between the velocity probability distribution and the quantum kinetic energy spectrum, applicable for a system of quantum vortices in a smoothly varying background density, while neglecting the density variations occurring within distance ξ of a vortex core.

We confine our attention to the hydrodynamic kinetic energy spectrum $E_H(k)$.

Performing the integral over θ_k, the spectrum (4.22) becomes

$$\begin{aligned} E_H(k) &= \frac{mk}{2}\frac{1}{2\pi}\int d^2\mathbf{r}\int d^2\mathbf{r}' e^{i[\theta(\mathbf{r})-\theta(\mathbf{r}')]} \\ &\quad \times\sqrt{n(\mathbf{r})n(\mathbf{r}')}\mathbf{v}(\mathbf{r})\cdot\mathbf{v}(\mathbf{r}')J_0(k|\mathbf{r}-\mathbf{r}'|). \end{aligned} \tag{4.33}$$

Transforming to coordinates $\mathbf{x} = (\mathbf{r}+\mathbf{r}')/2$, and $\mathbf{y} = \mathbf{r}-\mathbf{r}'$, Taylor expanding in powers of $\mathbf{y}$ gives

$$\theta(\mathbf{x}+\mathbf{y}/2) - \theta(\mathbf{x}-\mathbf{y}/2) \approx \mathbf{y}\cdot\nabla\theta(\mathbf{x}) = \frac{m}{\hbar}\mathbf{y}\cdot\mathbf{v}(\mathbf{x}), \tag{4.34}$$

$$\sqrt{n(\mathbf{x}+\mathbf{y}/2)}\sqrt{n(\mathbf{x}-\mathbf{y}/2)} \approx n(\mathbf{x}) - \frac{1}{4}\left(\mathbf{y}\cdot\nabla\sqrt{n(\mathbf{x})}\right)^2, \tag{4.35}$$

$$\mathbf{v}(\mathbf{x}+\mathbf{y}/2)\cdot\mathbf{v}(\mathbf{x}-\mathbf{y}/2) \approx |\mathbf{v}(\mathbf{x})|^2 - \frac{1}{4}\left|(\mathbf{y}\cdot\nabla)\mathbf{v}(\mathbf{x})\right|^2, \tag{4.36}$$

yielding the expression

$$\begin{aligned} E_H(k) &\approx \frac{mk}{2}\frac{1}{2\pi}\int d^2\mathbf{x}\int d^2\mathbf{y}\; e^{im\mathbf{v}(\mathbf{x})\cdot\mathbf{y}/\hbar}J_0(ky) \\ &\quad \times\Bigg[n(\mathbf{x})|\mathbf{v}(\mathbf{x})|^2 \qquad (4.37) \\ &\quad -\frac{n(\mathbf{x})}{4}\left|(\mathbf{y}\cdot\nabla)\mathbf{v}(\mathbf{x})\right|^2 - \frac{|\mathbf{v}(\mathbf{x})|^2}{4}\left(\mathbf{y}\cdot\nabla\sqrt{n(\mathbf{x})}\right)^2 \qquad (4.38) \\ &\quad +\frac{1}{16}\left(\mathbf{y}\cdot\nabla\sqrt{n(\mathbf{x})}\right)^2\left|(\mathbf{y}\cdot\nabla)\mathbf{v}(\mathbf{x})\right|^2\Bigg]. \qquad (4.39) \end{aligned}$$

This may be written as $E_H(k) \approx E_H^{(0)}(k) + E_H^{(2)}(k) + E_H^{(4)}(k)$, where the superscripts denote the orders of ∇ involved in each term. We now take a hydrodynamic approach and treat the lowest order term, validating the results against a full numerical treatment. Considering the lowest order term, Eq. (4.37), and performing the angular integral in $\mathbf{y}$ gives

$$\begin{aligned} E_H^{(0)}(k) &= \frac{mk}{2}\frac{1}{2\pi}\int d^2\mathbf{x}\; n(\mathbf{x})|\mathbf{v}(\mathbf{x})|^2 \\ &\quad \times\int_0^\infty ydy\; J_0\left(\frac{ym|\mathbf{v}(\mathbf{x})|}{\hbar}\right)J_0(ky). \end{aligned} \tag{4.40}$$

This can be evaluated using the Bessel closure relation $\int_0^\infty xdx\; J_\alpha(ux)J_\alpha(vx) = \delta(u-$

$v)/u$, to give the useful result

$$E_H^{(0)}(k) = \frac{m}{2}\int d^2\mathbf{r}\; n(\mathbf{r})|\mathbf{v}(\mathbf{r})|^2\delta\left(k - \frac{m|\mathbf{v}(\mathbf{r})|}{\hbar}\right). \tag{4.41}$$

At this level of approximation, the kinetic energy is a simple local transform of the hydrodynamic kinetic energy.

Given the above, let us note that integrating over k gives

$$\int_0^\infty dk\; E_H^{(0)}(k) = \frac{m}{2}\int d^2\mathbf{r}\; n(\mathbf{r})|\mathbf{v}(\mathbf{r})|^2 \equiv \mathcal{E}_H, \tag{4.42}$$

such that our approximations have not affected the total energy. Furthermore, using (4.29) with (4.41), we have

$$E_H^{(0)}(k) = N_{\rm tot}\frac{\hbar}{2}\left(\frac{\hbar k}{m}\right)^2 P\left(\frac{\hbar k}{m}\right), \tag{4.43}$$

where the total hydrodynamic kinetic energy is given by

$$\int_0^\infty E_H^{(0)}(k)dk = N_{\rm tot}\int_0^\infty dv\; P(v)\frac{mv^2}{2}. \tag{4.44}$$

The expression (4.43) is our main analytical result, providing a rigorous link between the velocity distribution and the kinetic energy spectrum in the hydrodynamic regime. A superfluid state comprised of quantized vortices in a homogeneous background will be very well described by this expression for the kinetic energy in the regime $k \ll \xi^{-1}$, provided $\mathcal{E}_H$ is the dominant energy contribution, and the system does not contain a significant amount of acoustic energy.

Eq. (4.43) further emphasises the difference between the classical and quantum kinetic energy spectra in a quantum fluid. The classical spectrum, Eq. (4.13), contains information about the *spatial structure* of velocity correlations, and is thus the quantity that will for example exhibit the Kolmogorov scaling [188, 228, 266], and a pileup at low k in the presence of spectral condensation (Secs. 2.9.3 and 3.10). In contrast, whilst the quantum kinetic energy spectrum, Eq. (4.22), draws information from the velocity *probability distribution* [as shown in Eq. (4.43)], it has no obvious classical counterpart.

4.3.4 Spectral Signatures of Coherent Structure Formation

For systems containing many vortices and little compressible energy, the quantum kinetic energy spectrum should be well described by the hydrodynamic approximation Eq. (4.43). We now consider the spectral features that may be observed for systems containing coherent vortex structures.

A fundamental property of superfluidity is the constraint that the vorticity $\omega(\mathbf{r}) = 0$ except at vortex cores where it is singular. However, as is well known from the study of Abrikosov vortex lattices, the coarse-grained velocity field *can* acquire a rotational component as the system approaches a classical state [257], consistent with Bohr's correspondence principle. Denoting the classical velocity field by $\mathbf{v}_c(\mathbf{r})$, the rotational part can be described by the ansatz

$$\mathbf{v}_c(\mathbf{r}) \;=\; \mathbf{\Omega}_c \times \mathbf{r}, \tag{4.45}$$

for some $\mathbf{\Omega}_c = \Omega_c \hat{\mathbf{z}}$. Ignoring the vortex core structure, the probability distribution for a cluster of radius R_c exhibiting rigid-body rotation is found from (4.29) as

$$\begin{aligned} P(v) &= \frac{n_0}{N_{\rm tot}} \int d^2\mathbf{r}\; \delta(v - \Omega_c r) = \frac{2\pi n_0}{\Omega_c N_{\rm tot}} \int_0^{R_c} r dr\; \delta(r - v/\Omega_c) \\ &= \frac{2\pi n_0}{\Omega_c^2 N_{\rm tot}} v\; H(\Omega_c R_c - v), \end{aligned} \tag{4.46}$$

where the Heaviside function limits this behaviour to the cluster interior. This distribution, with (4.43), gives the power-law form $E_H^{(0)}(k) \sim k^3$ for $k \leq k_c$, where

$$k_c = m\Omega_c R_c/\hbar, \tag{4.47}$$

giving a relation between the cluster size, classical vorticity field, and the k^3 scale range in the spectrum. Note that the k^3 form is quite distinct from the infrared result for a single vortex, for which (4.31) and (4.43) immediately yield $E_H^{(0)}(k) \propto k^{-1}$.

For any finite system with a sufficiently high level of clustering, there will be significant modifications to the velocity field due to the interactions between the coherent structures and the boundary (or, equivalently, the image vortices that ensure the flow obeys the boundary conditions). For vortex distributions containing both positive and negative vortices, highly energetic, maximum-entropy configurations take the form of a macroscopic dipole [92, 143]. The interaction between the clusters that form this dipole with their image vortices will induce a quadrupole mode in the phase,

which will generate a stagnation point in the velocity field. The phase in the vicinity of a stagnation point may be modelled as $\theta(\mathbf{r}) = \alpha xy$, where α is a constant with dimensions of inverse area [267] (see Sec. 4.4 for examples of this phase structure). The velocity field is thus given by

$$\mathbf{v}_s = \frac{\hbar\alpha}{m}(y, x), \tag{4.48}$$

and from Eq. (4.29), one finds

$$P(v) = \frac{2\pi n_0 m^2}{\hbar^2|\alpha|^2 N_{\rm tot}} v \; H\left(R_s - \frac{mv}{\hbar|\alpha|}\right) \tag{4.49}$$

with the Heaviside function again limiting the behaviour to some region $r < R_s$. Here $P(v)$ again yields the spectrum $E_H^{(0)}(k) \sim k^3$. Eqs. (4.46) and (4.49) suggest that a significant region of the quantum kinetic energy spectrum may exhibit a k^3 power law if coherent vortex structures are present in the system. We also note from Eq. (4.19) that a k^3 spectrum corresponds to a constant momentum distribution. We explore the quantum kinetic energy spectrum further in the following section, where we examine vortex distributions via numerical sampling.

4.4 Numerical Sampling and Spectral Analysis of Coherent Vortex Structures

In order to characterize the emergence of coherent vortex structures, we consider the end-states of freely decaying (i.e., unforced) 2DQT. Such states can be sampled using microcanonical methods [92] and, in the case of appropriate experimental small-scale forcing [188], are expected to form via the subsequent freely-evolving vortex dynamics after switching off the forcing mechanism.

4.4.1 Microcanonical Sampling

We consider neutral (zero net circulation) vortex configurations within a doubly-periodic box. We consider configurations of varying point-vortex energy per vortex, which correspond to varying degrees of clustering, and directly correspond to Gross-Pitaevskii energies in the incompressible regime [92]. Following Refs. [92, 148] the energy per vortex for a neutral configuration of N point-vortices with charges $\{\kappa_j\} = \pm 1$ (circulations $h\kappa_j/m$), located at positions $\{\mathbf{r}_j\}$ within a square box of side length

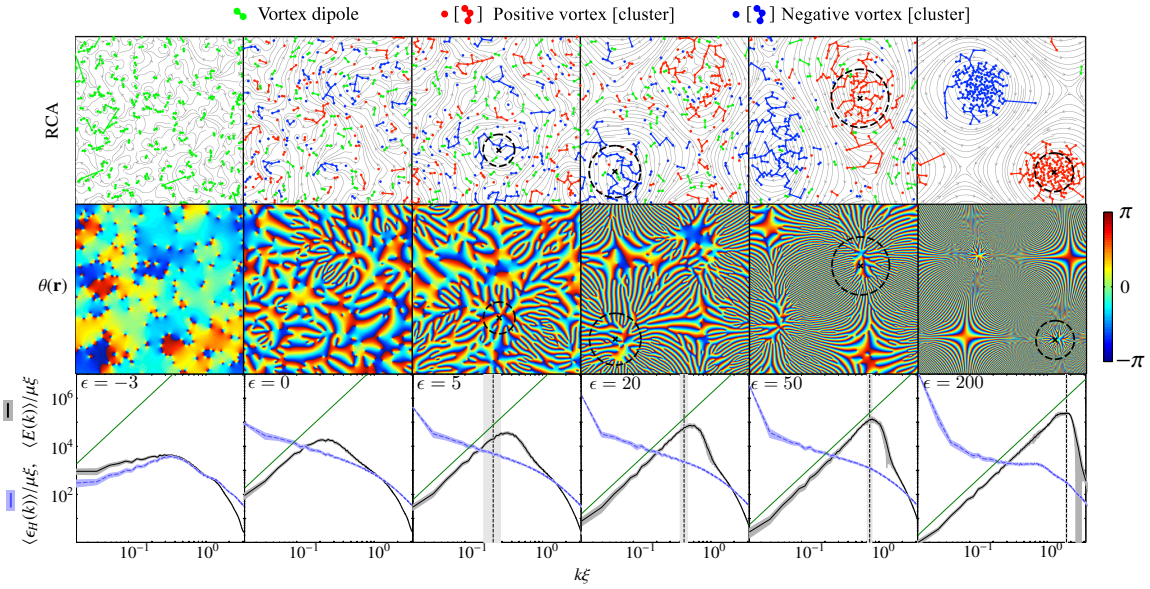

Figure 4.1: (Top row) Vortex distributions for a range of point-vortex energies. The distribution has been decomposed into clusters, dipoles and free vortices using the RCA [188] (see text). For $\epsilon \geq 5$, $\mathbf{R}$ and $|\mathbf{r} - \mathbf{R}| = R_c$ are shown by crosses and dashed lines respectively. Vortices in clusters are connected by solid lines showing the minimal spanning tree of the cluster, determined by Kruskal's algorithm. In each panel the field of view is $L \times L$, where $L = 512\xi$. (Middle row) Phase profiles $\theta(\mathbf{r})$ for the corresponding vortex distributions. (Bottom row) Log-log graphs of the quantum kinetic energy spectrum $\langle E(k)\rangle$ [ensemble average of Eq. (4.19)], and the classical hydrodynamic spectrum $\langle \epsilon_H(k)\rangle$ [ensemble average of Eq. (4.13)] for a range of point-vortex energies, averaged over 40 random walk trajectories at each energy. Shaded regions show ± 1 standard deviations. Lines proportional to k^3 (green) are shown for comparison. For $\epsilon \geq 5$ the vertical dashed line and shaded regions show k_c^{RCA}, and ± 1 standard deviation respectively (see text).

L is given in terms of the vortex-pair energy [148]

$$h(\mathbf{r}) = \sum_{m=-\infty}^{\infty} \ln\left[\frac{\cosh(x - 2\pi m) - \cos(y)}{\cosh(2\pi m)}\right] - \frac{x^2}{2\pi} \tag{4.50}$$

as

$$\epsilon(\{\mathbf{r}_j\}, \{\kappa_j\}) = \epsilon_0 + \frac{1}{N}\sum_{p=1}^{N-1}\sum_{q=p+1}^{N} \kappa_p \kappa_q \, h\left(\frac{2\pi(\mathbf{r}_p - \mathbf{r}_q)}{L}\right), \tag{4.51}$$

where the point-vortex energy is in units of $\rho_0\Gamma^2/4\pi$, for background density $\rho_0 = mn_0$ and circulation Γ, and $\epsilon_0 = -0.1170...$ is a constant that shifts the energy axis such that $\epsilon = 0$ corresponds to an uncorrelated vortex distribution (see Sec 2.10.1).[1]

[1]This shifting of the energy axis is in fact equivalent to using the alternative expression for the point-vortex energy derived in [147], although we use Eq. (4.51) for our computations as it is more

As detailed in Sec. 2.10.3, the canonical momenta of the point-vortex system are the vortex coordinates (up to circulation prefactors) and, as a result, if the spatial domain is bounded so is the volume of accessible phase space [151]. Consequently, in this system at $\epsilon = \epsilon_{\rm max} \approx -0.255$ [92, 147] the structure function $W(\epsilon)$ (i.e. the number of available states at a given energy) reaches a maximum and is monotonically decreasing thereafter as $\epsilon \to \infty$. Hence for $\epsilon > \epsilon_{\rm max}$, the temperature $T = W(\partial W/\partial\epsilon)^{-1}$ is formally negative. These negative temperature states are associated with a tendency for like-sign vortices to aggregate, and the emergence of macroscopic vortex clusters in maximal entropy (equilibrium) configurations [143]. Averaging over the microcanonical ensemble at a given energy (provided N is sufficiently large, to ensure ergodicity) characterises the end states of decaying 2DQT at that energy.

In a quantum fluid, the validity of this point vortex description is dependent on the system size (relative to the healing length), the point-vortex energy, and the vortex density of the system. In particular, increasing the energy or vortex density, or decreasing the system size, eventually leads to strong coupling between vortex and sound degrees of freedom. Note, however, that making the incompressible velocity everywhere small compared to the sound speed c greatly reduces the strength of this coupling: a regime where the point vortex description is valid can always be reached by increasing the system size (or alternatively reducing the vortex number, although this approach will cause larger statistical fluctuations and eventually violate the ergodicity assumption). As detailed in Sec. 3.4.2, we would expect the point vortex description to be valid when the superfluid Mach number $\mathrm{Ma_s} \sim q_c\xi/\ell \ll 1$, where ℓ is the average intervortex distance and q_c is the average cluster charge. Previous work has confirmed that the statistical approach correctly describes the end states of decaying turbulence in the damped GPE for energies up to $\epsilon = 6$ [92] (in a box of length 512ξ for 384 vortices). In this work we provide further confirmation of the approach for even higher energies in trapped systems (see Sec. 4.6).

We investigate the equilibrium states over a range of point-vortex energies via a random-walk procedure. We start with an uncorrelated distribution of $N = 386$ vortices in a box of length $L = 512\xi$. For an uncorrelated distribution the nearest-neighbour correlation functions $c_B = \sum_{p=1}^{N}\sum_{q=1}^{B}\kappa_p\kappa_p^{(q)}/BN$ (where $\kappa_p^{(q)}$ is the qth nearest neighbour to vortex p) are equal to zero [92, 188, 249]. The vortices undergo a random walk towards a state with a desired point-vortex energy ϵ, specified within a tolerance of $\Delta\epsilon = \pm 0.01$. A minimum inter-vortex separation of $2\pi\xi$ is enforced to ensure the vortex cores are non-overlapping [173], such that higher order density

convenient to work with numerically.

gradients may be neglected, consistent with the analysis of Sec. 4.3.3. This effective hard vortex core can also be viewed physically as an approximation to the energy barrier associated with the formation of multiply-quantized vortices in Gross–Pitaevskii theory [257].

Once a configuration with the desired energy is obtained, we find the corresponding Gross-Pitaevskii wavefunction using the constructive approach developed in Ref. [92]. In brief, the modulus of the wavefunction $\sqrt{n(\mathbf{r})}$ is constructed as the product of the individual vortex core wavefunctions [the numerical solution to Eq. (4.3)] and the phase $\theta(\mathbf{r})$ is constructed from the sum of the phases due to individual vortex dipoles [see also Eq. (3.61)]. We work in units of the healing length ξ and the chemical potential μ. The wavefunctions are constructed on a standard pseudospectral Fourier tensor grid of resolution $M = 2048^2$, i.e., 2048 grid points in the x and y directions. We sample within the range of point-vortex energies $\epsilon = [-3, 200]$, sampling over 40 random walk trajectories at each value of ϵ.

4.4.2 Recursive Clustering Algorithm

To analyse the vortex distributions, we make use of the recursive clustering algorithm (RCA) first presented in [188]. The algorithm yields detailed spatial information about a neutral vortex configuration by decomposing it into clusters, dipoles and free vortices. The algorithm consists of two rules:

(i) *Mutual* nearest-neighbours of the opposite sign constitute a dipole. Since isolated dipoles have a relatively weak far-field velocity due to screening effects ($1/r^3$ vs. the $1/r$ field of a lone vortex), they are removed from subsequent consideration by the algorithm.

(ii) Same-sign vortices which are nearer to each other than either is to a vortex of the opposite sign are allocated to the same cluster.

Rule (i) is applied first, recursively, until no more vortices can be added to dipoles. Rule (ii) is then applied to the remaining vortices, until no more can be added to clusters. Vortices that cannot be allocated to either a dipole or a cluster are considered to be "free". Clusters are initially grown from "seeds" which consist of a pair of same-sign vortices that are mutual nearest neighbours and are therefore guaranteed to be part of the same cluster. The search radius for cluster candidates is limited

by the nearest oppositely signed vortex. The domain periodicity is accounted for by determining the shortest minimal spanning tree of the cluster over all possible wrappings, by implementing Kruskal's algorithm [268] with sparse matrix routines. The spanning tree allows for a correct determination of spatially dependent cluster properties such as the centre of mass, and also provides a convenient means for cluster visualisation (see e.g. Fig 4.1).

This simple algorithm provides a unique decomposition of the vortex distribution, and seems to faithfully capture the qualitative features of the flow relatively well: vortices attributed to dipoles tend to traverse the system in straight-line trajectories, whereas clustered vortices orbit about their cluster centre (see, e.g., Ref. [92]). The RCA has been shown to extract useful flow-field information such as a "spectral condensate fraction" analogous to a BEC fraction [269], and has also been used to study free vortices as (quasi) passive tracers [246].

From the decomposition of the vortex distribution, we may acquire characteristic information about each cluster. In particular, the physical location of the cluster is estimated by the center of mass

$$\mathbf{R} = \frac{1}{N_c} \sum_{j \in C} \mathbf{r}_j \tag{4.52}$$

where C denotes the set of all vortices that belong to a particular cluster, and $N_c \equiv |\kappa_c|$ denotes the number of vortices in the cluster. Additionally, the spatial extent of a cluster can be estimated by the cluster radius, which we define as the mean distance from the center of mass

$$R_c = \frac{1}{N_c} \sum_{j \in C} |\mathbf{r}_j - \mathbf{R}|. \tag{4.53}$$

Although the cluster algorithm yields values for $\mathbf{R}$ and R_c for every cluster in a given distribution, throughout this section we are primarily concerned with the *largest* clusters in the system. Hereafter we will use the above notation to refer to the position and radius of the largest cluster only.

We show the resulting decomposition of the vortex distribution for a range of point-vortex energies in the top row of Fig. 4.1. Qualitatively, the algorithm captures the well-known physics of the point-vortex model: at negative point-vortex energy, the distribution takes the form of a dipole gas, with many or all vortices being bound in vortex-antivortex pairs. As the point-vortex energy is increased, clusters of same-sign vortices emerge, accumulating more vortices with increasing energy. With further increase of the point-vortex energy, clusters continue to accumulate vortices, but also

contract spatially, storing more energy internally rather than accumulating more vortices from the remaining vortex field (as the latter would lower the entropy). At sufficiently high energy ($\epsilon \sim 200$) the phenomenon of supercondensation occurs [255], and the distribution collapses into two macroscopic clusters, each of charge $N/2$. While such a state is unlikely to be achievable in atomic BEC, the supercondensed state nonetheless demonstrates the limiting physics at very high energy.

4.4.3 Spectral Analysis

In the bottom row of Fig. 4.1 we show the (ensemble-averaged) quantum kinetic energy spectrum $\langle E(k) \rangle$ [Eq. (4.21)] over a range of point-vortex energies. It is evident that, for positive energies, the spectrum acquires a k^3 scaling in the infrared. The scaling begins at low k and progresses towards larger wavenumbers as the point-vortex energy of the system is increased. The behavior of the spectrum is in stark contrast with the classical spectrum [Eq. (4.13)], for which the emergence of large-scale structure is signified by a spectral "pile-up" at length scales of order the system size, as is shown in Fig. 4.1. Notice however that the two spectra are very similar in the low energy vortex-dipole regime. Even for the relatively modest point-vortex energy $\epsilon = 5$ the spectrum exhibits nearly a decade of k^3 scaling in this system. For sufficiently high energy ($\epsilon \approx 100$) the range of the k^3 scaling extends past the point $k = \xi^{-1}$. In *dynamical* simulations, it is unlikely that the k^3 scaling would extend this far, as effects due to compressibility are non-negligible at velocities comparable to c (see Sec. 4.6). At high energy, the regions of slowly-varying phase that contribute to the infrared spectrum are clearly seen at the stagnation points and in the interior regions of the largest clusters. In the supercondensed state, the stagnation point phase structure $\theta(\mathbf{r}) = \alpha xy$ becomes particularly evident.

The location of the peak in the kinetic energy spectrum, which we label k_c, gives an indication of the k^3 scale-range observed in the negative-temperature regime. In light of Eq. (4.43), in the hydrodynamic approximation where $v = \hbar k/m$, this wavenumber indicates a most probable or "characteristic" velocity. This characteristic velocity is associated with the coherent structures; as the energy is increased and large structures emerge, we observe that phase fluctuations of a characteristic wavelength develop around these structures, and throughout the system [Fig. 4.1]. The characteristic wavelength of the fluctuations shortens as ϵ increases. These observations are consistent with Onsager's prediction – that the velocity field of a negative-temperature equilibrium state will be dominated by the coherent motion of the macroscopic vortex

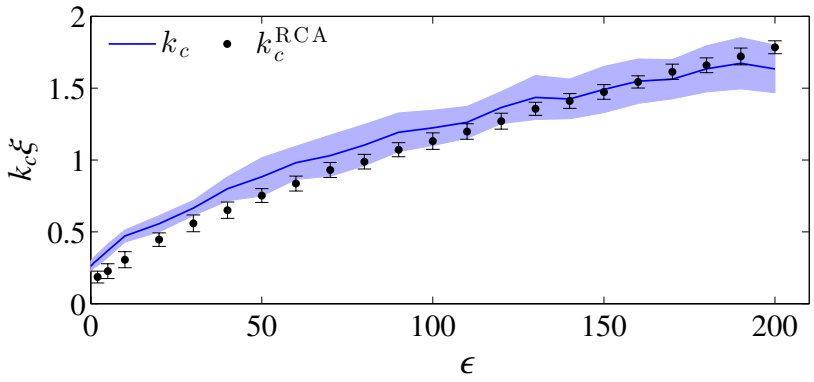

Figure 4.2: Wavenumber corresponding to the peak of the spectrum k_c, as a function of the point-vortex energy per vortex ϵ. The shaded region and errorbars show $\pm$ 1 standard deviations.

clusters, since the motion of the remaining vortices is essentially random [143].

We find that the characteristic velocity can be estimated from the RCA by considering only the largest cluster (in terms of charge) in a given configuration. The wavelength of the phase variations at a distance r from a large cluster will be $\lambda = 2\pi r/\kappa_{\mathrm{net}}$, where κ_{net} denotes the net charge within the region enclosed by a circle of radius r. The corresponding wavenumber is thus $k = \kappa_{\mathrm{net}}/r$. To calculate a value for k_c from the RCA data, which we denote k_c^{RCA}, we take the largest cluster and calculate the net charge enclosed within the cluster's radius R_c. We only consider energies at which we may unambiguously define the largest cluster ($\epsilon \geq 5$);[2] for these values, k_c^{RCA} is shown in Fig. 4.1 (bottom row), where it clearly provides a good indication of the location of the spectral peak. Conversely, the location of the peak provides a good estimator of the scale of the largest cluster in the system. We also compare k_c as calculated directly from the kinetic energy spectrum to k_c^{RCA} in Fig. 4.2. In general there is very good agreement in the data, even though the RCA does not account for cluster anisotropy [e.g. see Fig. 4.1, $\epsilon = 50$]. Agreement is poorest at lower energies ($\epsilon \lesssim 10$), when the largest clusters are not significantly larger than those in the background vortex distribution. However, as the energy is increased, agreement improves as the largest clusters begin to dominate the velocity field.

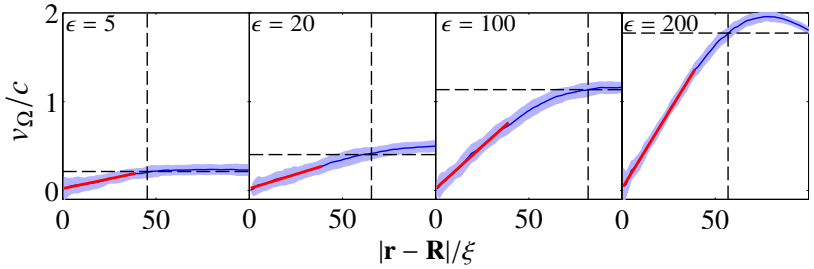

Figure 4.3: Azimuthal velocity field v_Ω of the largest cluster, as a function of distance from the cluster center $|\mathbf{r}-\mathbf{R}|$, for a range of point-vortex energies ϵ. Shaded regions show ± 1 standard deviations. Solid (red) lines show a linear fit to the averaged velocity field within the region $0 \leq |\mathbf{r}-\mathbf{R}| \leq 40\xi$. The slope yields a value for $\Omega_c^{\rm fit}$ (see text and Fig.4.4). Horizontal and vertical dashed lines show the values $v_c^{\rm RCA}/c \equiv k_c^{\rm RCA}\xi$ (see Fig. 4.2) and $\langle R_c \rangle$ respectively.

4.5 Emergence of Rigid-Body Rotation

4.5.1 Azimuthal Velocity Field

According to the analysis in Sec. 4.3.4, the presence of a k^3 spectrum suggests that the azimuthal velocity field in the vicinity of a large cluster may mimic that of a rigid body, that is $v_\theta(\mathbf{r}') = \Omega_c|\mathbf{r}'|$, where $|\mathbf{r}'| = |\mathbf{r}-\mathbf{R}|$ is the distance from the cluster center. However, we have shown that the k^3 spectrum may also be due to the stagnation points of the velocity field. Due to the non-local nature of the Fourier transform, it is difficult to disentangle the spectral contributions from rigid-body rotation and the stagnation points. This motivates us to analyse the clusters directly, to determine the extent to which they exhibit rigid-body characteristics.

Again considering energies $\epsilon \geq 5$, we calculate the angular velocity field relative to the cluster center, averaging over the azimuthal direction and the ensemble:

$$v_\Omega(r') = \left\langle \frac{1}{2\pi}\int_0^{2\pi} d\theta' \; |v_\theta(\mathbf{r}')| \right\rangle . \tag{4.54}$$

The resulting velocity field for a range of point-vortex energies is shown in Fig. 4.3. The averaged velocity field is approximately linear over the cluster interior, although fluctuations are larger at lower energy. The linear behaviour is typically maintained up to scales comparable to the average cluster radius $\langle R_c \rangle$. At $\langle R_c \rangle$ the velocity is well approximated by the characteristic velocity $v_c^{\rm RCA} \equiv \hbar k_c^{\rm RCA}/m$. We find v_Ω to

[2]We analyse energies for which there is a unique $N_c = \max(\{N_{c,i}\})$ for at least 90% of the random walk trajectories. In the few cases where multiple clusters satisfy $N_c = \max(\{N_{c,i}\})$, one of these clusters is selected at random.

be linear for at least $r' \lesssim 40\xi$ for $\epsilon \geq 5$, and that the slope of v_Ω steepens with increasing ϵ. Note that although the RCA sometimes overestimates the region of linear behaviour, the velocity is always well described by v_c^{RCA} at $\langle R_c \rangle$. Additionally, notice $v_\Omega(0) \approx 0$, suggesting that the RCA accurately determines the location of the cluster center.

4.5.2 Measures of Classical Vorticity

To further characterise the rigid-body flow field, we may determine the rigid-body rotation frequency Ω_c, thus also determining the characteristic turnover time $T = 2\pi/\Omega_c$ for the largest cluster. We describe four measures:

Ω_c^{fit}: A value may be obtained from the slope of a linear fit to v_Ω. We fit over the region $0 \leq r' \leq 40\xi$, where linearity holds for all ϵ, as shown by the lines of best fit in Fig. 4.3. We show Ω_c^{fit} as a function of ϵ in Fig. 4.4(a). There is a clear linear trend in the data, which are well described by the relation $\Omega_c^{\mathrm{fit}} = (1.5\epsilon + 36) \times 10^{-4}$. We use Ω_c^{fit} as a base measure, which we compare against other measures.

Ω_c^{Feyn}: The positive-temperature ground state for a system rotating at frequency Ω_c is an ordered vortex lattice that has a constant vortex density given by Feynman's rule, $n_v = m\Omega_c/\pi\hbar$ [170]. In order to maintain rigid-body rotation, the negative-temperature clustered states considered in this work must still exhibit a constant area per vortex on average, even though they do not maintain crystalline order. Applying Feynman's argument, we expect a rotation frequency

$$\Omega_c^{\mathrm{Feyn}} = \frac{\pi\hbar\langle n_v \rangle}{m}, \tag{4.55}$$

where $\langle n_v \rangle$ denotes the average vortex density of the largest cluster in each sample, averaged over the ensemble. Considering the cumulative distribution $N_v(r)$, which counts the number of vortices with $|\mathbf{r}_i - \mathbf{R}| \leq r$, we find the distribution is well described by $N_v(r) = \pi n_v r^2$ (as required for constant n_v) over the region where v_Ω is linear. We verify that this is not an artifact of the vortex-separation minimum by reducing the separation cutoff used in our microcanonical sampling from $2\pi\xi$ to ξ, finding nearly identical results. Fitting over the same region $0 \leq r' \leq 40\xi$ yields values for Ω_c^{Feyn} which are in excellent agreement with Ω_c^{fit}, as shown in Fig. 4.4(b). We emphasise that Ω_c^{fit} is obtained from the velocity field, while Ω_c^{Feyn} is determined by the vortex distribution.

Ω_c^{RCA}: A value for Ω_c may also be calculated from the RCA data. Since the rigid-

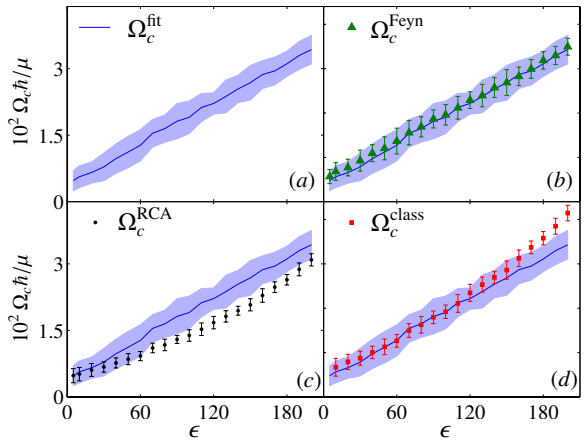

Figure 4.4: Measures of the rigid-body rotation frequency Ω_c. The shaded regions ($\Omega_c^{\rm fit}$) and error bars (other measures) indicate ± 1 standard deviations. In (b)-(d) $\Omega_c^{\rm fit}$ is shown for comparison.

body velocity field persists up to the characteristic wavenumber $k_c = m\Omega_c R_c/\hbar$, and k_c is well described by $k_c^{\rm RCA} = \kappa_{\rm net}/R_c$, clearly we may consider

$$\Omega_c^{\rm RCA} \equiv \left\langle \frac{\hbar\kappa_{\rm net}}{mR_c^2} \right\rangle = \frac{1}{2}\left\langle \frac{1}{\pi R_c^2}\int_{\mathcal{R}} d^2\mathbf{r}\;\omega(\mathbf{r}) \right\rangle, \tag{4.56}$$

where $\mathcal{R}$ is the region enclosed by a circle of radius R_c centered on $\mathbf{R}$. This is equivalent to averaging the vorticity distribution over the region of the cluster. The values $\Omega_c^{\rm RCA}$ are shown in Fig. 4.4(c). There is reasonable quantitative agreement between the data obtained directly from the wavefunction ($\Omega_c^{\rm fit}$) and that extracted from the RCA. It is clear that there is some discrepancy in qualitative trend however, and agreement between the two quantities is poorest for $\epsilon \sim 120$. This "sag" at intermediate energies is due to a decline in vortex density in the outer region of the cluster, which causes $N_v(r)$ to deviate from the expected quadratic behaviour, and consequently v_Ω to deviate from rigid-body behaviour (Fig. 4.3, $\epsilon = 100$). For perfect rigid body rotation extending out to R_c, one would expect $\Omega_c^{\rm fit}$ and $\Omega_c^{\rm RCA}$ to yield exactly the same values. Thus $\Omega_c^{\rm RCA}$ indicates the extent to which the velocity field deviates from perfect rigid-body rotation over the scale of the cluster as defined by the RCA value R_c.

$\Omega_c^{\rm class}$: The presence of a rigid-body velocity field requires that, under an appropriate *coarse graining* procedure (see also, e.g., [230, 270]), the formally singular vorticity field becomes constant over the central region of the cluster, i.e., $\omega(\mathbf{r}) = h/m\sum_i \delta(\mathbf{r}-\mathbf{r}_i) \to \omega_c(\mathbf{r}) \simeq 2\Omega_c$ for $|\mathbf{r}-\mathbf{R}| \lesssim R_c$. Defining an average over

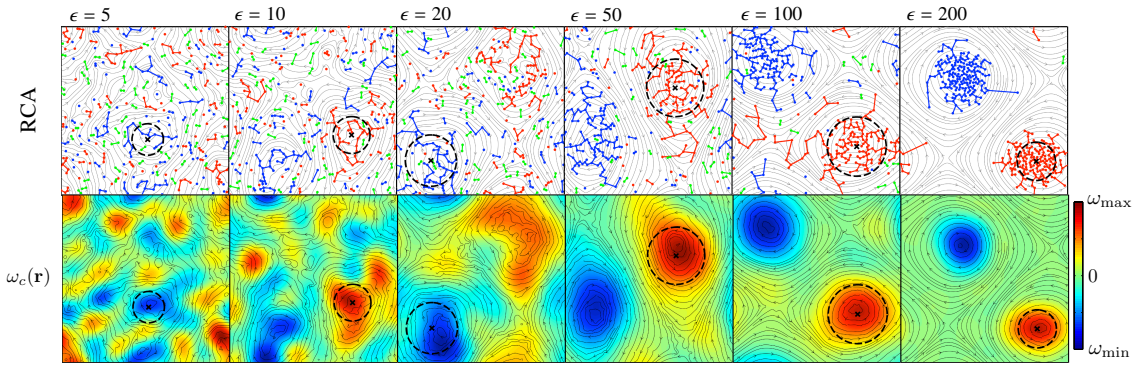

Figure 4.5: The emergence of classical flows: Exemplar RCA vortex distributions and coarse grained vorticity fields $\omega_c(\mathbf{r})$ [the latter obtained by including only spatial modes $k \leq k_{\rm cut} = 2\pi/(2R_c)$] for a range of ϵ. Streamlines show the velocity field $\mathbf{v}(\mathbf{r}) = \hbar\nabla\theta(\mathbf{r})/m$. Crosses show the center-of-mass position of the largest cluster in each sample, $\mathbf{R}$, as determine by the RCA. The RCA radius R_c is shown by the dashed line.

many quantum vortices, we consider the coarse-grained *classical* vorticity field

$$\omega_c(\mathbf{r}) \equiv \frac{1}{2\pi}\int_{\mathcal{K}} d^2\mathbf{k}\, \tilde{\omega}(\mathbf{k}) e^{i\mathbf{k}\cdot\mathbf{r}} \tag{4.57}$$

where $\tilde{\omega}(\mathbf{k}) = \mathcal{F}[\omega(\mathbf{r})]$ and $\mathcal{K}$ is the k-space domain satisfying $|\mathbf{k}| < k_{\rm cut} = 2\pi/\ell_{\rm cut}$ for a chosen cutoff length-scale $\ell_{\rm cut} \gg \xi$. Coarse graining over the spatial extent of the largest vortex cluster ($\ell_{\rm cut} = 2R_c$) yields a value consistent with the other measures if we consider $\omega_c(\mathbf{r})$ at the cluster center:

$$\Omega_c^{\rm class} = \left\langle \frac{1}{2}\omega_c(\mathbf{R}) \right\rangle . \tag{4.58}$$

Values for $\Omega_c^{\rm class}$ are shown in Fig. 4.4(d). We find excellent agreement between $\Omega_c^{\rm class}$ and $\Omega_c^{\rm fit}$ until $\epsilon \sim 150$, at which point $\Omega_c^{\rm class}$ deviates to higher values. This discrepancy is due to taking the value locally at $\mathbf{R}$, where the vorticity can be slightly more concentrated, particularly for large clusters, whereas $\Omega_c^{\rm fit}$ incorporates information away from the cluster center. $\Omega_c^{\rm class}$ indicates that, apart from at very high energy, the clusters do not deviate significantly from rigid-body motion in their interior.

Coarse graining over $\ell_{\rm cut} = 2\bar{d}$ for mean nearest-neighbour distance $\bar{d}$ (typically $\bar{d} \simeq R_c/3$) yields similar values for $\Omega_c^{\rm class}$, but with larger fluctuations. For this value of $\ell_{\rm cut}$ we also verify that $\omega_c(\mathbf{r}') \approx$ const. for $|\mathbf{r}'| \lesssim R_c$. Averaging over the azimuthal direction and ensemble to obtain $\omega_c(r')$, we find $\langle\omega_c(40\xi)\rangle \gtrsim 0.9\langle\omega_c(0)\rangle$

at all energies, consistent with the linear v_Ω and quadratic N_v observed up to this scale. At the cluster radius, $\langle\omega_c(R_c)\rangle/\langle\omega_c(0)\rangle \sim 0.6 - 0.8$ for low ($\epsilon \lesssim 50$), and high ($\epsilon \gtrsim 150$) energies respectively, and $\langle\omega_c(R_c)\rangle/\langle\omega_c(0)\rangle \sim 0.5$ for intermediate energies. This is consistent with the deviation from rigid-body behaviour at larger scales as seen in Fig. 4.3, and as indicated by the qualitative trend of $\Omega_c^{\rm RCA}$.

The emergence of a classical flow field from the quantum vortex distribution is qualitatively captured in Fig. 4.5, where we present particular examples of the vortex distribution (as decomposed by the RCA) and the classical vorticity field $\omega_c(\mathbf{r})$ (for $\ell_{\rm cut} = 2R_c$), generated at various ϵ. As large clusters emerge, they generate macroscopic regions of approximately uniform vorticity, capturing the qualitative features of the emergent quasi-classical velocity field, as shown by the velocity streamlines.

It is interesting to compare the rigid-body rotation property observed here to the rotational properties of coherent structures in classical fluids. The states we have considered here are the freely-decayed states of a turbulent superfluid. Decaying turbulence described by the inviscid Euler equations has been shown to approach the statistical equilibrium predicted by the mean-field Montgomery-Joyce (sinh-Poisson) equation [153, 271]. With quantum vortices we would expect to recover this regime in the limit $N \to \infty$. Indeed, the rigid-body rotation observed here in quantum vortex clusters for large N is qualitatively consistent with the form of the doubly-periodic vortex dipole solution of the Montgomery-Joyce equation [272].

4.6 Dynamical Emergence in a Trapped System

Finally, we demonstrate that coherent structures and the associated k^3 power law can emerge dynamically in a trapped system, and compare the dynamical results against sampling. The model we use to describe the dynamics of a 2D Bose gas is the damped Gross-Pitaevskii equation (dGPE):

$$i\hbar\frac{\partial\psi(\mathbf{r},t)}{\partial t} = (1 - i\gamma)(\mathcal{L} - \mu)\psi(\mathbf{r},t), \tag{4.59}$$

where

$$\mathcal{L} = \left(-\frac{\hbar^2\nabla_\perp^2}{2m} + V_{\rm ext}(\mathbf{r}) + g_2|\psi(\mathbf{r},t)|^2\right), \tag{4.60}$$

for an external confining potential $V_{\rm ext}(\mathbf{r})$. The damping parameter γ describes the finite-temperature effects due to collisions between the condensate and a stationary thermal reservoir with chemical potential μ. Within the framework of c-field theory,

the dGPE can be obtained from the stochastic projected Gross-Pitaevskii equation for a large BEC in the low-temperature regime, for which the thermal noise is negligible [209]. The dGPE has been used extensively in quantum turbulence studies [80, 82, 187, 228, 243], and has been demonstrated to give qualitative agreement with experiment even for relatively high temperatures [82]. We set $\gamma = 10^{-5}$, an experimentally realistic value under the conditions for which the dGPE theory is valid [173]. For such a value of γ, the modifications to the vortex dynamics [184] are essentially negligible over the integration time we consider. The primary effect of the damping is thus to suppress compressible excitations at very high k, which are numerically demanding to resolve, yet have little physical effect on the vortex dynamics in the regime of interest here.

We simulate a 2D BEC confined within a circular well or "bucket" potential of radius R, i.e.,

$$V_{\rm ext}(\mathbf{r}) = V_0\{1 + \tanh[(r - R)/a]\}, \tag{4.61}$$

and set $V_0/\mu = 10$, $R/\xi = 200$, and $a/\xi = 3$, such that $V_{\rm ext}$ approximates a hard-wall potential. We remark that Bose condensation in a quasi-uniform cylinder has been recently demonstrated experimentally [70].

In this system, the energy of an N-vortex configuration may be characterized by the energy per vortex for point-vortices (in units of $\rho_0\Gamma^2/4\pi$) within a circular domain D of radius R (see Sec. 2.10.1):

$$\begin{aligned}\epsilon_\circ(\{\mathbf{r}_j\},\{\kappa_j\}) = \tilde{\epsilon} &- \frac{1}{N}\sum_{p=1}^{N}\sum_{q\neq p}^{N}\kappa_p\kappa_q \ln\left|\frac{\mathbf{r}_p - \mathbf{r}_q}{\xi}\right| \\ &- \frac{1}{N}\sum_{p=1}^{N}\sum_{q=1}^{N}\kappa_p\bar{\kappa}_q \ln\left|\frac{\mathbf{r}_p - \bar{\mathbf{r}}_q}{\xi}\right|,\end{aligned} \tag{4.62}$$

where $\bar{\mathbf{r}}_j = R^2\mathbf{r}_j/|\mathbf{r}_j|^2$ is the location of an image vortex with charge $\bar{\kappa}_j = -\kappa_j$ and $\tilde{\epsilon} \approx -4.158$ shifts the axis such that $\epsilon_\circ = 0$ corresponds to an uncorrelated distribution, as does ϵ_0 in Eq. (4.51). The images ensure that the velocity field satisfies the boundary condition $\mathbf{v}\cdot\hat{\mathbf{n}}\,|_{\partial D} = 0$, i.e., that the flow perpendicular to the boundary ∂D is zero everywhere on ∂D.

We set the vortex number to $N = 112$. Whilst fewer vortices will inevitably lead to larger statistical fluctuations, a lower vortex density is beneficial here as it reduces the radiative loss of vortex energy into the sound field. Reducing the vortex density ensures that the incompressible velocity field is everywhere small compared to the speed of sound c, and also lowers the chance of vortex core overlap, thus ensuring

that the vortices remain sufficiently well separated such that their Gross–Pitaevskii dynamics are well-approximated by a point-vortex description (see Secs 3.4.1 and Sec. 3.4.2).

The initial condition, $\psi_\circ(\mathbf{r}, 0)$, is generated via a similar method to that outlined in Sec. 4.4:

$$\psi_\circ(\mathbf{r}) = \psi_{\rm TF}(\mathbf{r}) e^{i\theta_\circ(\mathbf{r})} \prod_{j=1}^{N} \chi(|\mathbf{r} - \mathbf{r}_j|/\xi). \tag{4.63}$$

Here the Thomas-Fermi wavefunction $\psi_{\rm TF}(\mathbf{r}) = \sqrt{(\mu - V_{\rm ext}(\mathbf{r}))/g_2}$ for $V_{\rm ext}(\mathbf{r}) \leq \mu$ and 0 otherwise, $\chi(r)$ is the radial core profile of an individual quantum vortex [the numerical solution to Eq. (4.3)], and

$$\theta_\circ(\mathbf{r}) = \sum_{j=1}^{N} \kappa_j \theta_j(\mathbf{r}) + \bar{\kappa}_j \theta_j(\bar{\mathbf{r}}), \tag{4.64}$$

where $\theta_j(\mathbf{r})$ is the phase due to an individual positive vortex at $\mathbf{r}_j$. We prepare a high-energy [$\epsilon_\circ(t_i) = 10.1$], non-equilibrium initial vortex configuration, as shown in Fig 4.6. The wavefunction is constructed on a spatial domain of length $L = 512\xi$, and is discretised on a uniform grid of $M = 1024^2$ points. We numerically integrate the dGPE pseudo-spectrally, using an adaptive 4th-5th order Runge-Kutta method [273, 274], and a relative error tolerance of $\tau = 10^{-5}$. We have confirmed that all statistical measures of the vortex dynamics remain the same for $L = 700$, $M = 2048$, $\tau = 10^{-6}$.

The initial configuration is highly unstable, and the horizontal lines of like-charge clusters undergo a *roll-up*, due to the Kelvin-Helmholtz instability. The initial kinetic energy spectrum, shown in Fig. 4.6, does not follow the k^3 power law, but does exhibit a well-defined peak. The peak is due to the initial clustering in the configuration, which produces phase fluctuations of a characteristic wavelength $\lambda \sim 10\xi - 20\xi$. Full relaxation to equilibrium is slow, requiring an integration time of order $10^4\hbar/\mu$. However, clear signs of a k^3 power law emerge after $t \sim 3000\hbar/\mu$, as, at this stage of the evolution, large, quasi-equilibrium clusters have already formed. This is consistent with the observations in Ref. [92], where it is shown that the macroscopic clusters begin to form well before the equilibration time. After $t_f = 11300\hbar/\mu$ of evolution, the system has clearly reached the equilibrium state containing coherent vortex structures, as shown in Fig 4.6. Although during the evolution some of the vortex energy is lost to sound, most of the vortex energy is retained [$\epsilon_\circ(t_f) \sim 7.8$], and thus the configuration is still well within the negative temperature regime. It may be

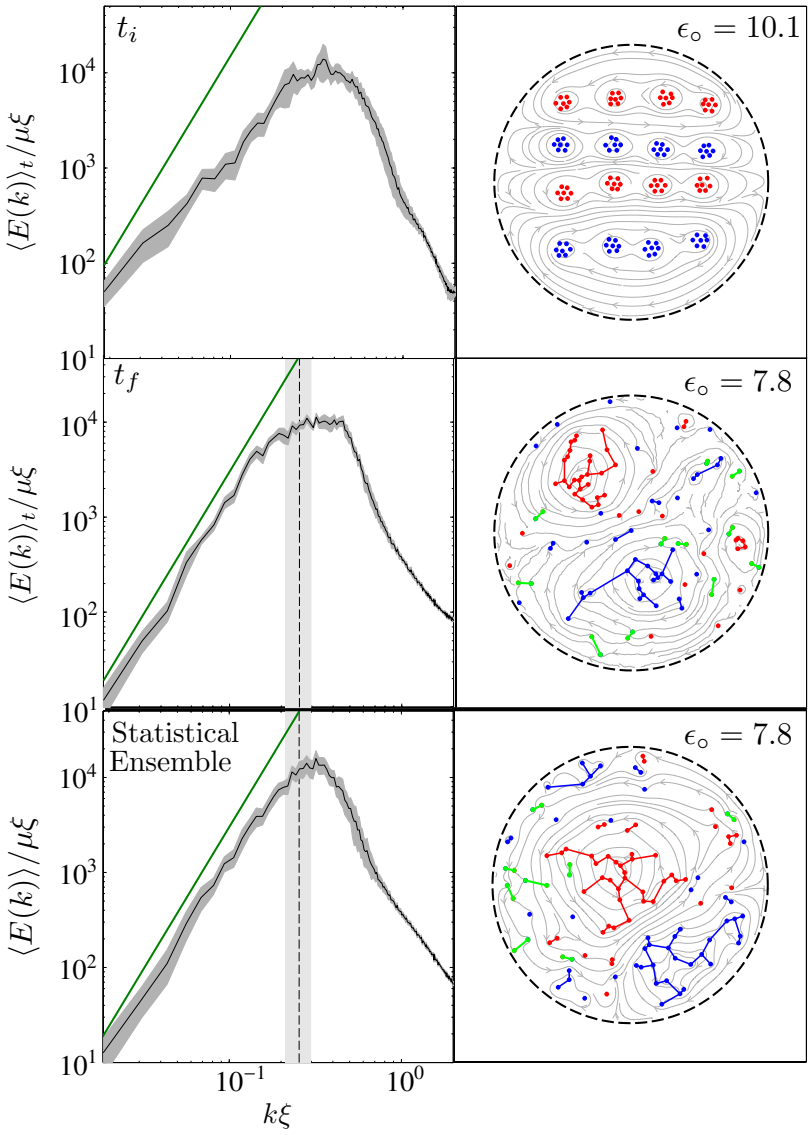

Figure 4.6: Time-averaged quantum kinetic energy spectra (left) and vortex distributions (right) for the dynamical system at $t_i = 0\hbar/\mu$ (top row) and $t_f = 11300\hbar/\mu$ (middle row). The spectra for the dynamical system are averaged from t to $t{+}500\hbar/\mu$. The spectrum and distribution at t_f can be compared against those of the statistical ensemble (40 samples) at the same point-vortex energy (bottom row). On the spectrum plots, lines proportional to k^3 are shown for comparison, shaded regions show ± 1 standard deviation, the vertical dashed line shows k_c as calculated from the ensemble using Eq. 4.47, with the shaded vertical band showing ± 1 standard deviation. Symbols for the vortex distribution plots are as denoted in Fig.4.1

that radiative energy loss of the vortex distribution as a whole is partially inhibited by vortex "cross-talk", a mechanism via which vortices of the same sign can efficiently impart energy to each other through radiation and absorption of sound [193].

We emphasise that the final energy per vortex $\epsilon_\circ = 7.8$ is substantial, being analogous to a point-vortex energy in the periodic system considered in Sec. 4.4 of $\epsilon \gg 7.8$. Indeed, using the supercondensation energy ($\epsilon_\circ \approx 70$) as a reference, one can consider the final point-vortex energy in the simulation, $\epsilon_\circ(t_f) = 7.8$, to be roughly equivalent (interpreted as a fraction of the supercondensation energy) to $\epsilon \approx 22$ in the doubly-periodic system considered in Sec. 4.4 (where supercondensation occurs at $\epsilon \approx 200$). A more quantitative estimate of equivalence can be obtained using the nearest neighbour clustering measure c_1 (as defined in Sec. 4.4.1); we find the equilibrium values to be approximately the same ($c_1 = 0.35$) for $\epsilon_\circ = 7.8$ and $\epsilon \approx 25$, supporting the above analysis. The quantum kinetic energy spectrum and vortex distribution at t_f can be compared against the same quantities obtained from a statistical ensemble, as shown in Fig. 4.6. The spectra are qualitatively very similar, and nearly identical in the k^3 region. The RCA value for k_c still gives a reasonable indication of the range of k^3 behaviour and the location of the spectral peak. The vortex distribution as determined by the RCA is also very similar [see Fig. 4.6].

We propose that the most direct way initial conditions similar to those shown in Fig. 4.6 could be created is by carefully-controlled laser stirring and manipulation protocols: The field of two-dimensional quantum turbulence has seen several numerical studies of the injection of clustered vortices via optical stirring potentials in recent years [83, 89, 187, 249, 250], and injection of small vortex clusters has indeed already been demonstrated experimentally [82]. While neutral systems having similar spatial extent (relative to the healing length) and containing as many vortices as we have considered here may be challenging to achieve, they are nonetheless within the scope of current experimental technology.

4.7 Conclusion

In this work we have shown that the coherent vortex structures that emerge in decaying 2DQT can exhibit quasi-classical rigid-body rotation, obeying the Feynman rule of constant areal vortex density while remaining spatially disordered. By developing a rigorous link between the velocity probability distribution and the quantum kinetic energy spectrum we have shown that these coherent structures are associated with a k^3 power-law in the infrared region of the spectrum. The power-law region

terminates at a peak located near the inverse spatial scale of the largest cluster. The k^3 spectrum and associated peak provide signatures of coherent structure formation that may be measured independently of the vortex configuration data, and should be accessible in atomic BEC experiments. Furthermore, our analysis illuminates the important distinction between the quantum kinetic energy spectrum and the power spectrum of the velocity autocorrelation function in a quantum fluid, namely, the classical hydrodynamic kinetic energy spectrum.

By identifying a clear spectral signature that is accessible via ballistic expansion imaging, this work provides an additional measurement tool for experimental observations of negative-temperature coherent vortex structures in two-dimensional atomic Bose-Einstein condensates. Experimental confirmation of the Feynman rule at negative temperature may provide further indication of the appearance of rigid-body rotation and the universality of rotational velocity fields in quantum turbulence.

Chapter 5

Identifying a Superfluid Reynolds Number via Dynamical Similarity

In this chapter, we study the transition to turbulence, in the wake of a cylinder in a 2D quantum fluid, as a means to test Onsager's superfluid Reynolds number across the transition. We develop a new numerical method to gain access to the steady-state properties of the wake, allowing a detailed investigation of Strouhal oscillations to be conducted. Dynamical similarity is found to be recovered in the Strouhal-Reynolds number relation when the superfluid Reynolds number is modified to account for the critical velocity for vortex nucleation. For obstacles larger than a few healing lengths, the transition from laminar flow to turbulent vortex shedding is found to occur at the same value of this modified Reynolds number, regardless of obstacle size.

5.1 Motivation

Turbulence in classical fluid flows emerges from the competition between viscous and inertial forces. For a flow with characteristic length scale L, velocity u, and kinematic viscosity ν, the dimensionless Reynolds number $\mathrm{Re} = uL/\nu$ characterises the onset and degree of turbulent motion (Sec. 2.2). An analogous quantity can be defined for a finite-temperature superfluid through an effective quantum viscosity that arises due to interactions with the normal fluid component [173]. However, a naive evaluation of the Reynolds number for an ideal, zero-temperature superfluid is thwarted by the absence of kinematic viscosity, suggesting that the classical Reynolds number of a pure superfluid is formally undefined [51, 89, 196]. Nonetheless, for sufficiently rapid flows, perfect inviscid flow breaks down and an effective viscosity

emerges dynamically via the nucleation of quantized vortices [218]. As discussed in Sec. 3.9.2, Onsager [237], noted that the quantum of circulation of a superfluid vortex, given by the ratio of Planck's constant to the atomic mass, h/m, has the same dimension as ν, and provides the only dimensionally consistent quantity that can be made from the available parameters in the problem. This suggests making the replacement $\nu \to h/m$, giving a superfluid Reynolds number $\mathrm{Re_s} \sim uL/(h/m)$ [238–240]. This approach is supported by evidence that this quantity accounts for the degree of superfluid turbulence when $\mathrm{Re_s} \gg 1$ [45–47, 59, 60, 76, 220, 226, 233, 238–240], but has yet to be tested by a detailed study of the transition to turbulence.

The wake of a cylinder embedded in a uniform flow is a paradigmatic example of the transition to turbulence [275], and has been partially explored in the context of quantum turbulence in atomic Bose-Einstein condensates (BECs) [51, 89, 168, 218, 225], see Sec. 3.8. The classical fluid wakes (Sec. 2.3) exhibit *dynamical similarity:* for cylinder diameter D, and free-stream velocity u, their physical characteristics are parametrised entirely by $\mathrm{Re} = uD/\nu$, such that any combination of u, D, and ν that yields the same Reynolds number will produce a wake that is identical after appropriate rescaling. Above a critical Reynolds number, vortices of alternating circulation shed from the obstacle with characteristic frequency f, and, because of dynamical similarity, the associated dimensionless Strouhal number $\mathrm{St} \equiv fD/u$ is a universal function of the Reynolds number (Sec. 2.3.1). In the context of a zero-temperature superfluid, the Strouhal number is a measurable quantity that can be used to *define* the superfluid Reynolds number as a dimensionless combination of flow parameters that reveals dynamical similarity.

In this chapter we numerically study the Strouhal–Reynolds relation across the transition to turbulence in quantum cylinder wakes of the two-dimensional Gross-Pitaevskii equation. We develop a numerical approach to gain access to quasi-steady-state properties of the wake for a wide range of system parameters, and to accurately determine the Strouhal number St. We find that plotting St against a superfluid Reynolds number defined as

$$\boxed{\mathrm{Re_s} \equiv \frac{(u - u_c)D}{\kappa},} \tag{5.1}$$

where u_c is the superfluid critical velocity and $\kappa \equiv \hbar/m$,[1] reveals dynamical similarity in the quantum cylinder wake: for obstacles larger than a few healing lengths the

[1]Here choosing κ rather than h/m results in a transition to turbulence near $\mathrm{Re}_s \sim 1$.

wakes exhibit a universal St–$\mathrm{Re_s}$ relation similar to the classical form. Furthermore, for these obstacles $\mathrm{Re_s}$ characterises the transition to quantum turbulence, with irregularities spontaneously developing in the wake when $\mathrm{Re_s} \approx 0.7$, irrespective of cylinder size.

5.2 System

We consider a Gaussian stirring potential moving at a steady velocity $\mathbf{u}$ through a superfluid that is otherwise uniform in the xy-plane and subject to tight harmonic confinement in the z-direction. In the obstacle reference frame with coordinate $\mathbf{r} = \mathbf{r}_L + \mathbf{u}t$, the time evolution of the lab-frame wavefunction $\psi(\mathbf{r}, t) = \psi_L(\mathbf{r}_L, t)$ is governed by the Gross-Pitaevskii equation (GPE);

$$i\hbar \frac{\partial \psi(\mathbf{r}, t)}{\partial t} = (\mathcal{L} - \mathbf{u} \cdot \mathbf{p} - \mu)\psi(\mathbf{r}, t), \tag{5.2}$$

where μ is the chemical potential, $\mathbf{p} = -i\hbar\nabla$, and

$$\mathcal{L}\psi(\mathbf{r}, t) \equiv \left[-\frac{\hbar^2 \nabla^2}{2m} + V_s(\mathbf{r}) + g_2 |\psi(\mathbf{r}, t)|^2 \right] \psi(\mathbf{r}, t). \tag{5.3}$$

Here, $g_2 = \sqrt{8\pi}\hbar^2 a_s / m l_z$, where m is the atomic mass, a_s is the s-wave scattering length, and $l_z = \sqrt{\hbar / m\omega_z}$ is the harmonic oscillator length in the z-direction. The trapping in the z-direction is assumed strong enough to suppress excitations along this direction (Sec. 3.1.5).[2] The stirring potential is of the form

$$V_s(\mathbf{r}) = V_0 \exp\{-[(x - x_0)^2 - y^2]/\sigma^2\}, \tag{5.4}$$

giving an effective cylinder width

$$D = 2a = 2\sigma[\ln(V_0/\mu)]^{1/2}, \tag{5.5}$$

defined by the zero-density region in the Thomas-Fermi approximation. The parameter a is a reasonable measure of the cylinder radius provided V_0 and σ are appreciably larger than μ and ξ respectively, so that the tunnelling depth of the wavefunction is small relative to the obstacle size, and vortices therefore enter the bulk of the super-

[2] Note that particularly strong confinement is not necessary to obtain effectively two-dimensional vortex dynamics [166].

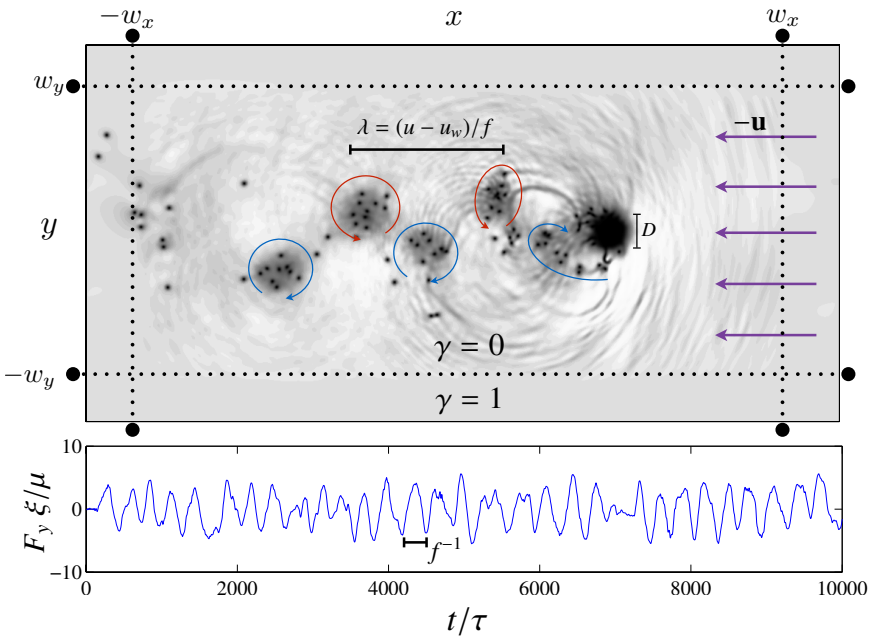

Figure 5.1: (Top) A quantum cylinder wake in the quasi-steady state. Same-sign vortices aggregate into clusters to form a semi-classical vortex street. Vortices within the fringe region $|x| > w_x$ are unwound in pairs by imprinting opposite-signed vortices on top of them, thus recycling the flow to the uniformly translating state as indicated at the right of the domain. (Bottom) Time series data of the transverse force on the obstacle. The force exhibits a well-defined frequency, which determines the Strouhal number for the flow.

fluid at approximately $y = \pm a$. For all obstacles we consider, we find that vortices unpin from the obstacle at $y \approx \pm a$, indicating that D gives a good indication of the effective cylinder width (see Fig. 5.1).

In contrast to previous studies [51, 89] employing strong potentials ($V_0 \sim 100\mu$) to approximate a hard-walled obstacle, we use *soft-walled* obstacles (with $V_0 = e\mu$, such that $D = 2\sigma$): these obstacles exhibit a well-defined vanishing-density region, but have a much lower critical velocity than hard-wall obstacles (see Sec. 3.7.1, and Refs. [223, 225]). A low critical velocity makes the transition to turbulence — which must occur between the critical velocity and the supersonic regime — more gradual, aiding our numerical characterisation. Lower velocities will minimise the importance of sound waves (Sec. 3.2.5), making it easier to compare results with classical hydrodynamic turbulence (Sec. 2.1).

5.3 A Fringe Method for Superfluids

To facilitate our study of quasi-steady-state quantum cylinder wakes we develop a numerical method to maintain approximately steady inflow-outflow boundary conditions in the presence of quantum vortices. This method enables us to evolve cylinder wakes for extremely long times in a smaller spatial domain, making our numerical experiment computationally feasible. In essence, we extend the *sponge* or *fringe method* [138, 276–278], which implements steady inflow/outflow boundary conditions by "recycling" flow in a periodic domain, to deal with quantum vortices. The essential idea of the fringe method is to divide the spatial region of the numerical simulation into a "computational domain" of interest and a "fringe domain". Inside the fringe domain, the solution is usually damped to an exactly known solution to the equation of motion. Inside the fringe domain, we use a damped GPE [209, 279] to rapidly drive the wavefunction to the lab-frame ground state with chemical potential μ; a uniform state, free from excitations and moving at velocity $-\mathbf{u}$ relative to the obstacle, is thus produced at the outer boundary of the fringe regions. The modified equation of motion becomes

$$i\hbar\frac{\partial\psi(\mathbf{r},t)}{\partial t} = (\mathcal{L} - \mathbf{u}\cdot\mathbf{p} - \mu)\psi(\mathbf{r},t) - i\gamma(\mathbf{r})(\mathcal{L}_f - \mu)\psi(\mathbf{r},t), \tag{5.6}$$

where the free GPE evolution operator $\mathcal{L}_f \equiv \mathcal{L} - V_s(\mathbf{r})$. At the computational/fringe boundary $(x,y) = (\pm w_x, \pm w_y)$, γ must be chosen to ramp smoothly from zero to a large value to prevent reflections, with hyperbolic tangent functions a common choice [276]. We set $\gamma(\mathbf{r}) = \max[\gamma(x), \gamma(y)]$, where

$$\gamma(x) = \frac{\gamma_0}{2}\left\{2 + \tanh\left[\frac{x - w_x}{d}\right] - \tanh\left[\frac{x + w_x}{d}\right]\right\} \tag{5.7}$$

and similarly for $\gamma(y)$.

Quantum vortices, as topological excitations, decay only at the fluid boundary or by annihilation with opposite-sign vortices (Sec 3.6.1). While damping drives opposite-signed vortices together at a rate proportional to γ [184], relying on this mechanism to avoid vortices being "recycled" around the simulation domain requires a prohibitively large fringe domain when the wake exhibits clustering of like-sign vortices, a key feature of the transition to turbulence. Instead, we *unwind* vortex-antivortex pairs within the fringe domain by phase imprinting an antivortex-vortex pair on top them, using the expression for the phase of a vortex dipole in a periodic domain derived in Ref. [92]. For a vortex dipole, with positive/negative vortices

positioned at $(x_k^{\pm}, y_k^{\pm})$ in a periodic box of length 2π, the phase is given by

$$\theta_k(x,y) = \sum_{n=-\infty}^{\infty} \Bigg\{ \mathrm{atan}\left[\tanh\left(\frac{Y_k^- + 2\pi n}{2}\right)\tan\left(\frac{X_k^- - \pi}{2}\right)\right] - \mathrm{atan}\left[\tanh\left(\frac{Y_k^+ + 2\pi n}{2}\right)\tan\left(\frac{X_k^+ - \pi}{2}\right)\right] + \pi\left[H(X_k^+) - H(X_k^-)\right]\Bigg\} - \frac{x_k^+ - x_k^-}{2\pi} y. \quad (5.8)$$

where $X_k^+ = x - x_k^+$ etc are the relative coordinates and $H(x)$ is the Heaviside step function. For arbitrary box lengths one makes the replacement $x_k^+ \to 2\pi x_k^+/L$ etc. In practice, this sum is rapidly convergent, and making the replacement $\sum_{n=-\infty}^{\infty} \to \sum_{n=-5}^{5}$ is sufficient. When vortices of only one sign exist within the fringe region, the same method is used to "reset" vortices back near the start of the fringe ($x = -w_x$) to prevent them being recycled. The high damping in the fringe domain rapidly absorbs the energy added by imprinting and annihilation events.

5.4 Numerical Implementation

Working in units of the healing length $\xi = \hbar/\sqrt{m\mu}$, the speed of sound $c = \sqrt{\mu/m}$ and time unit $\tau = \hbar/\mu$, we discretise a spatial domain of $L_x = 512\xi$ by $L_y = 256\xi$ on a Fourier collocation grid of $M_x = 1024$ by $M_y = 512$ points. The obstacle is positioned at $x_0 = 100\xi$, and the fringe domain parameters are $w_x = 220\xi$, $w_y = 100\xi$, $d = 7\xi$ and $\gamma_0 = 1$.[3] The magnitude (and frequency) of the streamwise (transverse) force on the obstacle was verified to be independent of the choice of resolution, spatial domain size, details of the fringe domain, and obstacle location. It was also verified that the simulations replicated the properties of vortex street for the parameters given in Ref. [51], to ensure that the fringe region was not affecting the results. We integrate Eq. (5.6) using standard Fourier pseudospectral methods for spatial derivatives, and the time stepping scheme is a fourth-fifth order adaptive Runge-Kutta algorithm (Cash-Karp variety). A small amount of initial noise is added to break the symmetry. We integrate Eq. (5.6) for sufficient time to accurately resolve the cluster shedding frequency f (see Fig. 5.1, bottom panel). Analysing obstacles in

[3] A slightly larger domain than quoted was required for the largest obstacle $D/\xi = 24$. For this obstacle, we verified that rescaling $\{L_x, L_y, w_x, w_y, x_0\} \to \alpha\{L_x, L_y, w_x, w_y, x_0\}$ (while also scaling M_x, M_y to maintain the same spatial resolution) yielded very similar Strouhal numbers (to within error bars) for $\alpha \approx 1.2$ and $\alpha = 2$.

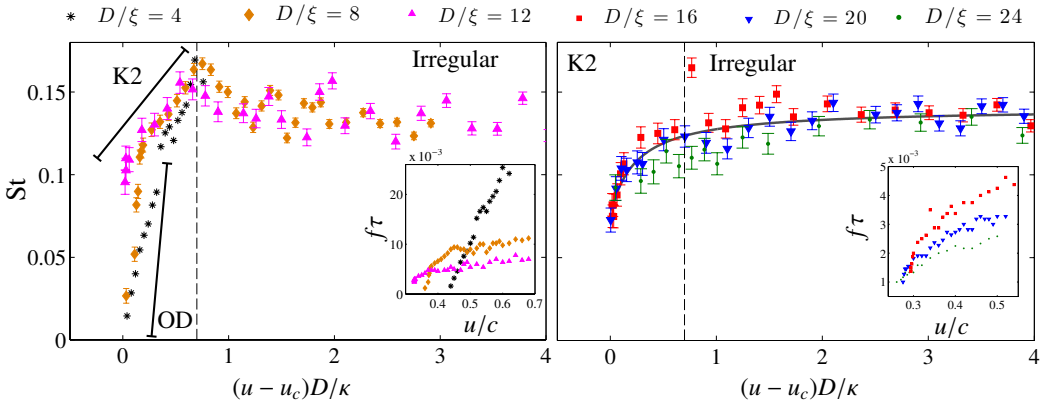

Figure 5.2: Strouhal number plotted as a function of the superfluid Reynolds number for obstacles of different diameters D. The dashed lines indicate the transition between regular and irregular wakes (see text). Solid lines in the left panel indicate regions of oblique dipole (OD) and charge-2 von Kármán (K2) shedding. The solid grey line shows the best-fit curve $\mathrm{St} = 0.1402[1 - 0.1126/(\mathrm{Re_s} + 0.2456)]$. Error bars give an indication of the uncertainty in St due to the Fourier-space resolution $\Delta f = 1/T$. Insets show the original shedding frequency data as a function of velocity. The data for $D/\xi = 4$ is truncated as the shedding frequency becomes poorly defined at higher velocities for this particular obstacle.

the range $4 \leq D/\xi \leq 24$ requires integration times $5000 \leq T/\tau \leq 12000$, representing a significant computational challenge. The tolerance for acceptance for the adaptive scheme is set to ensure that the fourth and fifth order solutions to the wavefunction agree to within $\mathrm{tol} = 10^{-6}$ at each grid point. The vortex-deleting algorithm for the fringe region is evaluated every 5τ, which was found to be sufficiently rapid to prevent all vortices from escaping the fringe region for all parameters considered. To optimise the algorithm, vortices in the fringe are prioritised by how "urgently" they need to be deleted: vortices closest to the exit of the fringe region $x = w_x$ are highest priority, and vortices closest to the entrance $x = -w_x$ are lowest priority. A typical result from the numerical setup is shown in Fig. 5.1.

5.5 Strouhal Number

To determine the Strouhal number $\mathrm{St} = fD/u$ we calculate the transverse force on the obstacle from the Ehrenfest relation, $F_y = \int d^2\mathbf{r}\ \psi^*(\partial_y V_s)\psi$, with f being defined by the dominant mode in the frequency power spectrum of F_y. Our main results are shown in Fig. 5.2, where the Strouhal number St is plotted against the superfluid Reynolds number $\mathrm{Re_s} = (u - u_c)D/\kappa$ for a range of obstacle diameters

D [insets show shedding frequency f against velocity u].[4] The obstacles are broadly classified as quantum ($\sigma \leq 12\xi$, left) or semi-classical ($\sigma > 12\xi$, right). For quantum obstacles the vortex core size influences the shedding dynamics, and the St-$\mathrm{Re_s}$ curve exhibits three distinct regimes (see also Fig. 3.4): At low $\mathrm{Re_s}$, vortex dipoles are released obliquely from the obstacle (OD regime), and St rises sharply with $\mathrm{Re_s}$. As $\mathrm{Re_s}$ is increased, the gradient of the St-$\mathrm{Re_s}$ curve drops sharply when a charge-2 von Kármán vortex street [51] appears (K2 regime). The Strouhal number peaks at $\mathrm{Re_s} \sim 0.7, \mathrm{St} \approx 0.16$, and beyond this point the shedding becomes irregular, and the Strouhal number gradually decreases towards $\mathrm{St} \approx 0.14$. The St-$\mathrm{Re_s}$ data conform to a single curve rather well when compared against the f vs. u data shown in the inset, apart from variation in the OD regime at low $\mathrm{Re_s}$. This can be attributed to the influence of vortex core structure on shedding, which is most pronounced for $D/\xi = 4$. At $D/\xi = 12$ the curve becomes very steep, and dipole shedding seems to disappear.

For semi-classical obstacles (right panel of Fig. 5.2), the St-$\mathrm{Re_s}$ curve is qualitatively different. Obstacles with $D/\xi \geq 12$ appear to lack a stable OD regime,[5] and the most steeply-rising region of the St-Re curve corresponds to the K2 regime. The peak seen in the St-$\mathrm{Re_s}$ curve for quantum obstacles is generally absent (with a remnant for $D/\xi = 16$), and the St-$\mathrm{Re_s}$ data conform to a universal curve extremely well for $\mathrm{Re_s} \lesssim 0.5$ and $\mathrm{Re_s} \gtrsim 2$, and to a lesser extent around $\mathrm{Re_s} = 1$. This discrepancy may be an effect of using a soft-walled obstacle, for which varying σ for fixed V_0 leads to a slight change in the density profile near the obstacle. Remarkably, the St-$\mathrm{Re_s}$ curve for the semiclassical obstacles is well-fitted by the formula $\mathrm{St} = \mathrm{St}_\infty[1-\alpha/(\mathrm{Re_s}+\beta)]$,[6] which is similar to the classical form $\mathrm{St} = \mathrm{St}_\infty(1 - A/\mathrm{Re})$, see Sec. 2.3.1.

5.6 Transition to Turbulence

To test whether $\mathrm{Re_s}$ provides an accurate indicator of the transition to quantum turbulence, in Fig. 5.3 we show the vortex-cluster charge probability distribution, $\mathcal{P}(\kappa_c, \mathrm{Re_s})$. This indicates the probability of any vortex belonging to a cluster of

[4] Movies showing condensate density and vortex-cluster dynamics for representative sets of parameters can be found in the Supplemental Material of Ref. [91].

[5] For $D/\xi = 16$, even resolving the critical velocity to within $\Delta u/c = 2 \times 10^{-4}$ does not reveal a clear OD regime.

[6] The need for the shift β in the fit shown in Fig. 5.2 is a consequence of the fact that the vortex street in a classical fluid does not appear until $\mathrm{Re} \gtrsim 40$, whereas for our semiclassical obstacles it emerges immediately above u_c (i.e., for $\mathrm{Re_s} > 0$).

charge κ_c, as determined by the recursive cluster algorithm outlined in Sec. 4.4.2. The transition to turbulence manifests as an abrupt spreading in $\mathcal{P}$ at $\mathrm{Re_s} \approx 0.7$. The distribution $\mathcal{P}$ is similar for all obstacles except the smallest ($D/\xi = 4$) where high $\mathrm{Re_s}$ vortex turbulence is suppressed by compressible effects due to the transsonic velocities involved. Notice that the distribution is close to independent of obstacle size for larger obstacles ($D \geq 12\xi$). We find that the K2 regime persists for a significant range of $\mathrm{Re_s}$ even for large D, in contrast to Ref. [51]. We suggest the vanishing of the K2 regime at large D seen in Ref. [51] may be due to the higher critical velocity of the hard-walled obstacle. We find no regular charge-κ_c von Kármán regimes (Kκ_c regimes) other than K2. The lack of a K1 regime, the focus of von Kármán's original analysis of vortex streets [280], suggests that the additional degree of freedom provided by the internal length scale of the charge-2 cluster is what enables stable vortex shedding in the K2 regime. The lack of Kκ_c regimes for $\kappa_c > 2$ appears to be due to instabilities; although regimes do exist where $\mathcal{P}$ is strongly peaked around $|\kappa_c| > 2$, such regimes do not appear to be stable.

5.7 Discussion

The superfluid Reynolds number $\mathrm{Re_s}$ introduced in Eq. (5.1) serves as a good control parameter for the transition to turbulence, which occurs at $\mathrm{Re_s} \approx 0.7$ for all obstacle sizes investigated except $D/\xi = 4$. Note however that dynamical similarity is not expected for $D \to \xi$. Here, due to the small scales and transonic velocities, the healing length and Mach number become important parameters. The definition of $\mathrm{Re_s}$ in terms of $u - u_c$ is intuitively appealing: the subtraction of u_c becomes unimportant in the classical limit (where u_c vanishes) and when $\mathrm{Re_s} \gg 1$, consistent with previous observations (Sec. 3.9.2). Furthermore, notice from Eq. (3.91) for the critical velocity of sufficiently large, hard-walled obstacles, it does not matter whether one uses a critical velocity $\mathrm{Re_s} = (u - u_c)D/\kappa$ or a critical diameter $\mathrm{Re_s} = u(D - D_c)/\kappa$; the definitions are equivalent and the correction merely corresponds to an appropriate shift of the origin by a dimensionless constant, which depends on the particular geometry of the problem. Subtracting u_c is consistent with previous arguments that corrections to the Reynolds number formula are necessary for quantum obstacles [233], and reflects the fact that in a pure superfluid an effective viscosity due to quantum vortices is only activated through vortex nucleation — it does not make much sense to talk about the vortex circulation κ unless vortices are present in the system. Note that $\mathrm{Re_s}$ is distinct from the quantum Reynolds number defined in Ref. [173]; the latter stems

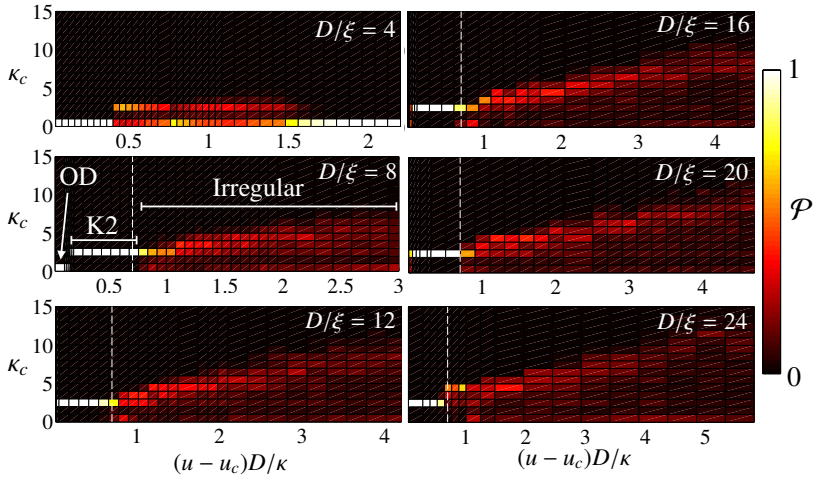

Figure 5.3: Cluster charge probability distribution $\mathcal{P}(\kappa_c, \mathrm{Re_s})$, which shows the probability that a vortex belongs to a cluster of charge magnitude κ_c. Note that $\kappa_c = 0$ corresponds to a dipole and $\kappa_c = 1$ corresponds to a free vortex. The vertical dashed line shows the value $\mathrm{Re_s} = 0.7$ at which the probability distribution suddenly spreads, indicating that the wake has developed irregularities. The three different shedding regimes observed are labelled for the case $D/\xi = 8$.

from interactions between superfluid and thermal fractions at finite-temperature.

Although $\mathrm{Re_s}$ takes on small values here compared to the Reynolds number of classical cylinder wakes, we note the close correspondence between the St-$\mathrm{Re_s}$ curve obtained here and the classical St-Re curve. Typically the St-Re curve (for any obstacle shape) rises steeply when the shedding is regular, and reaches a plateau as the shedding becomes irregular (compare Figs. 2.2 and 5.2). This correspondence suggests that $\mathrm{Re}_s \sim 0.7$ may be roughly equivalent to $\mathrm{Re} \sim 200$ for the cylinder. The fact that the St-$\mathrm{Re_s}$ curves approach a universal form for different obstacle sizes suggests that the shedding is insensitive to considerable changes in Mach number, which occur between different obstacle widths at fixed $\mathrm{Re_s}$. Although this behaviour is somewhat surprising, it is consistent with a previous study, where it was noted that the drag force is dominated by vortex shedding even into the transonic regime [168]. The discrepancy between the asymptotic values of St found here and in the classical case appears to be mainly due to the use of soft-walled obstacles: we have confirmed that simulations with $V_0/\mu = 10\exp(1)$ and $D/\xi = 20$ produce an St-$\mathrm{Re_s}$ curve qualitatively similar to Fig. 5.2, but with higher asymptote $\mathrm{St}_\infty \approx 0.16$. For the hard-wall obstacle[7] of Ref. [51] we find $\mathrm{St} \approx 0.18$ for the narrow window of velocities that give a vortex street. This asymptote is in reasonable agreement with classical

[7] $V_0/\mu = 100$, $u/c = 0.51659$, $\sigma/\xi = 1.5811$ ($D/\xi = 6.7861$)

observations where $\mathrm{St}_\infty \approx 0.2$ [281, 282]. The lower Strouhal number of the soft-walled obstacle suggests that it is "bluffer" than the hard-walled one, in the sense that it has a larger drag coefficient, and produces a wider wake for a given obstacle dimension D [282].

The K2 regime should be accessible to current BEC experiments [51], since the wake is stable and easily identified. Although accessing the high $\mathrm{Re_s}$ regime with fine resolution may be experimentally challenging, the low $\mathrm{Re_s}$ turbulent regime, particularly near the transition, should be accessible in current BEC experiments. In this regime the Strouhal number should be measurable, since the induced wake velocity $u_w \to 0$ [99] and thus the average streamwise cluster spacing $\lambda = (u - u_w)/f \to u/f$ determines $\mathrm{St} = D/\lambda$.

5.8 Conclusion

In conclusion, we have developed a vortex-unwinding fringe method to study quasi-steady-state quantum cylinder wakes, revealing a superfluid Reynolds number $\mathrm{Re_s}$ that controls the transition to turbulence in the wake of an obstacle in a planar quantum fluid. The expression for $\mathrm{Re_s}$ resembles the classical form, modified to account for the critical velocity at which effective superfluid viscosity emerges. As the critical velocity encodes details of geometry and the microscopic nature of the superfluid, the general form of $\mathrm{Re_s}$ suggests that it may apply to a broad range of systems, much like the classical Reynolds number. We thus conjecture that $\mathrm{Re_s}$ may provide a useful starting point for characterising turbulence in a broader class of superfluids that involve physics beyond GPE theory, such as liquid helium [283], polariton condensates [284], or BEC-BCS superfluidity in Fermi gases [285]. The fringe method we have developed here should prove useful for future numerical studies of bluff-body wakes in quantum fluids, especially if the method can be extended to three-dimensional flow problems.

Shortly after publication of this work [91], some evidence that Re_s may serve as a useful parameter in superfluid helium experiments was presented by Schoepe [286, 287]. Schoepe has shown that Re_s reveals dynamical similarity in the lifetime τ^* of transient turbulence, generated by oscillating wires, in superfluid helium at milliKelvin temperatures. The lifetime was found to obey a relation of the form $\tau^* \sim [\exp(c\mathrm{Re}_s)]^2$, with $c = 1.22$. Note also that Kwon *et al.* have recently observed the first signatures of the von Karman street in a quasi-2D BEC [223]. While a direct comparison between our results and their results is limited due to the harmonic pro-

file of the experimental setup, they found the transition between the K2 and irregular regimes occurred in their system at $\mathrm{Re}_s \approx 1.2$.

Chapter 6

The Direct Enstrophy Cascade in Decaying 2D Quantum Turbulence

In this chapter we study the direct enstrophy cascade in decaying 2D quantum turbulence, for very large vortex numbers, in order to elucidate the nature of spectral transport and the emergence of cascade solutions in 2D quantum turbulence. We show that the 2D quantum fluid can indeed exhibit the universal scaling properties associated with the direct enstrophy cascade, provided a few hundred vortices are present with suitable initial conditions. The decaying system is found to be well-characterised by Onsager's superfluid Reynolds number, Re_s, equivalent to our newly proposed Reynolds number from Chapter 5 in the limit $\mathrm{Re}_s \gg 1$. The quantum fluid is found to manifest key features of the classical cascade, including Batchelor's -3 law of the inertial range, scaling of the inertial range against the superfluid Reynolds number, and a value for the Kraichnan-Batchelor constant close to the accepted value.

6.1 Motivation

The Kolmogorov phenomenology of three-dimensional (3D), classical turbulence at large Reynolds numbers (Sec. 2.8) has been shown to also apply to 3D quantum turbulence in regimes where a bundling of same-sign quantum vortices occurs (Sec. 3.9.1). The bundling leads to an emergent Kolmogorov direct energy cascade [40, 230, 288], which conservatively transports energy through an inertial scale range, and down to the scale of the average inter-vortex distance. In contrast, the question of whether the cascade phenomenology of classical 2D turbulence (Secs. 2.9.2 and 2.9.3) can emerge in 2D quantum turbulence remains unclear [93, 164, 186, 188, 189, 243, 248, 266, 289]

(see Sec. 3.9 for a detailed discussion), despite the fact that quantized vortices in 2D, when well-separated compared to the healing length, realise a simple point-vortex model (Secs. 2.10 and 3.4.1).

As discussed in Sec. 2.9.1, the phenomenology of classical 2D turbulence hinges on the observation that, in contrast to the 3D case, the nonlinear advection must simultaneously conserve both energy and enstrophy (mean square vorticity). In the canonical scenario of fully developed 2D turbulence formulated by Kraichnan, Leith and Batchelor (KLB) [112, 119, 290], narrowband forcing at scales much smaller than the system size leads to a dual cascade (Sec. 2.9.3). For both quantities to be simultaneously conserved, the energy cascade must reverse; same-sign vortices aggregate, transporting energy to low wavenumbers k, at a steady rate ϵ through a kinetic energy spectrum $E(k) = C\epsilon^{2/3}k^{-5/3}$, where C is the Kraichnan-Kolmogorov constant. Over a separate inertial range of wavenumbers, enstrophy cascades to high k through the filamentation of vortex patches, creating steady spectrum $E(k) = C'\eta^{2/3}k^{-3}$, where η is the constant enstrophy flux, and C' is the Kraichnan–Batchelor constant. For freely decaying turbulence (Sec. 2.9.2), the enstrophy cascade persists [112, 123], but the steady inverse cascade is replaced by generic, non-universal energy transport through vortex merging events. While this still results in growth of the integral scale of the turbulence, the $k^{-5/3}$ spectrum is generally not observed [124].

Due to the similarities between 3D classical and quantum turbulence, one might reasonably expect the KLB phenomenology to apply to 2D quantum turbulence. Other close correspondences, for example the fact that the point-vortex model provides a (finite-time) convergent numerical approximation to the Euler equation [291, 292], are also suggestive. Indeed, a number of studies have attempted to verify whether the KLB phenomenology can emerge in quantum turbulence or point vortex turbulence by studying the inverse energy cascade within the Gross-Pitaevskii equation [80, 92, 186, 188, 189, 243, 244, 248], or the point-vortex model [293, 294]. Yet conflicting results have emerged from these studies, and a definitive demonstration has not been achieved. As discussed in Sec. 3.9.4, the systems studied within the Gross-Pitaevskii framework have departed from the idealised KLB scenario in a number of ways, having either: relatively few degrees of freedom [$\lesssim$100 vortices]; no direct evidence of flux; short power-law ranges; strong dissipation; or strong coupling to sound. A number of inconsistencies also appear in the point vortex studies conducted. Sedov [293] investigated the cascades in the point-vortex model, and claimed to observe simultaneous k^{-3} and $k^{-5/3}$ scalings. However, as noted by Aref [149], because the system contained only 100 vortices of the same sign the scalings are

questionable, since homogeneous, isotropic turbulence requires a neutral vortex configuration. Siggia and Aref [294] obtained a convincing $k^{-5/3}$ scaling accompanied by steady energy growth in a forced point vortex model. However, they obtained a Kraichnan-Kolmogorov constant that was double the accepted value. This result seems at odds with the studies of three dimensional turbulence, where the Kolmogorov constant is the same in the classical and quantum cases. Additionally, a recent study of point vortex flows on the sphere [289] found no evidence of cascades at all, only a rapid relaxation to equilibrium.

The departures listed make it difficult to distinguish an inverse energy cascade from more generic non-equilibrium energy transport. Furthermore, it appears that no studies have yet investigated the enstrophy cascade, which is equally fundamental to the theory. Consequently, the question of whether the KLB phenomenology can truly apply to 2D quantum turbulence remains an open problem. Many fundamental questions remain: How many vortices are needed to achieve fully-developed 2D quantum turbulence? Do the cascades occur, and at realistically attainable vortex numbers? If so, are the cascade constants the same as the classical values? And how do the extents of the inertial ranges scale with the (superfluid) Reynolds number? Some of these questions might be more readily answered by putting aside the inverse energy cascade and studying whether the enstrophy cascade can emerge for decaying turbulence, at larger vortex numbers, and in a situation that more closely approximates the idealised KLB scenario.

In this chapter we study a damped N-point-vortex model of decaying 2D quantum turbulence at large N via direct simulation. First we discuss some general properties of spectral transport within the model, and discuss under what conditions the cascades might be expected. Then, by constructing appropriate initial conditions, we create a direct superfluid analog of a scenario where, for a classical 2D fluid described by the Navier-Stokes equations, the existence of an enstrophy cascade is well established (see Fig. 6.1). We show that under dynamical evolution the characteristic k^{-3} spectrum of the cascade emerges over nearly a decade of wavenumbers for $N \sim 500$. The associated enstrophy and energy fluxes are found to agree with KLB theory. By simulating up to very large N (up to $32,768$), clear features of the KLB theory can be verified. The Kraichnan–Batchelor constant for 2D quantum turbulence is found to be $C' \approx 1.6$, close to the classical value. We find that the system is well-characterised by Onsager's superfluid Reynolds number Re_s; here Re_s is found to be proportional to the number of vortices N, and the inertial range is found to scale as $\sqrt{\mathrm{Re}_s}$, as in the classical scenario. These results definitively demonstrate that the phenomenology

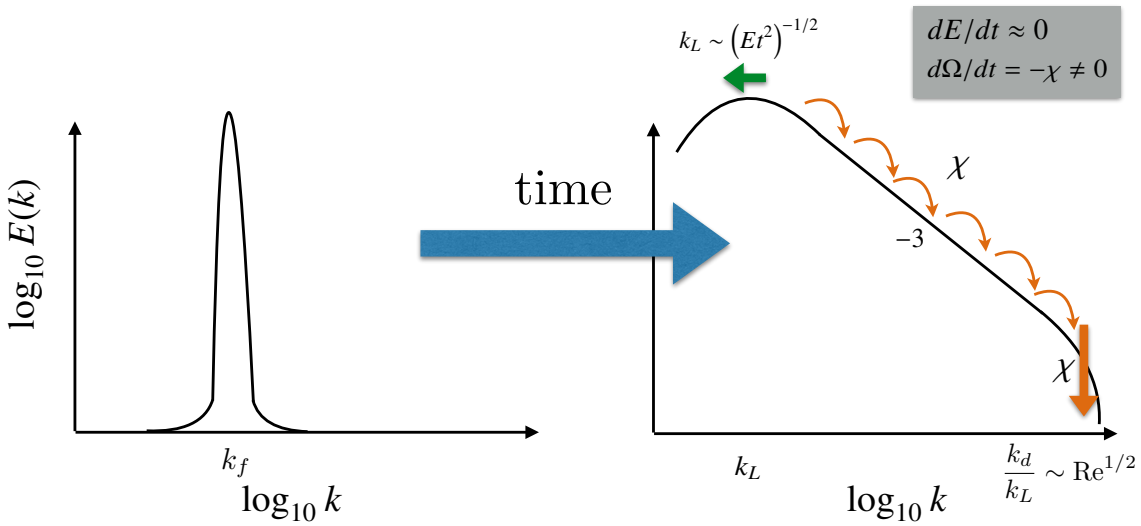

Figure 6.1: A schematic of the direct enstrophy cascade in decaying two-dimensional classical turbulence at large Reynolds numbers Re. A generic initial state, with kinetic energy spectrally localised near some wavenumber k_f, spontaneously self-organises under free evolution into a k^{-3} similarity state, in which enstrophy is cascaded to high wavenumbers at a rate χ until it reaches wavenumbers $k_d \sim k_L \mathrm{Re}^{1/2}$ where it is dissipated by viscosity. The total energy E is approximately conserved, and drifts towards low wavenumbers, causing a decay of the integral growth scale k_L (see Sec 2.9.2 for more details).

of classical 2D fluid turbulence *can* apply to 2D quantum turbulence under the right conditions, even for fairly modest vortex numbers.

6.2 Model

We consider a quantum fluid characterized by healing length ξ and speed of sound c, carrying quantized vortices of charge $q_i = \pm 1$ and circulation $\Gamma_i = q_i \Gamma$.[1] For a quasi-2D system (Sec. 3.1.5), vortex bending is suppressed and the dynamics become effectively two-dimensional [166]. In the low Mach number limit, where the vortices are separated by scales appreciably larger than the healing length (Sec. 3.4.2), the motion of the ith quantum vortex, located at $\mathbf{r}_i$, can be described by a dissipative point-vortex model (Sec. 3.6.2)

[1] In the case of a superfluid described by a (damped) Gross-Pitaevskii equation, such as an atomic BEC, one has $\xi = \hbar/\sqrt{\mu m}$, $c = \sqrt{\mu/m}$, and $\Gamma = h/m$, where μ is the chemical potential and m is the mass of a constituent particle.

$$\frac{d\mathbf{r}_i}{dt} = \mathbf{v}_i + \mathbf{w}_i; \quad \mathbf{v}_i = \sum_{j=1, j\neq i}^{N} \mathbf{v}_i^{(j)}; \quad \mathbf{w}_i = -\gamma q_i \hat{\mathbf{e}}_3 \times \mathbf{v}_i, \tag{6.1}$$

where γ is the dissipation rate, $\hat{\mathbf{e}}_3$ is a unit vector perpendicular to the fluid plane, and $\mathbf{v}_i$ and $\mathbf{w}_i$ are the conservative and dissipative parts of the velocity respectively. Physically, the dissipation rate γ arises from thermal friction due to the normal fluid component, here assumed to be stationary. The velocity of the ith vortex due to the jth, $\mathbf{v}_i^{(j)}$, is obtained from a Hamiltonian point-vortex model subject to appropriate boundary conditions. As often considered classically [115, 116, 118], we will consider a doubly-periodic square box, of size $L \times L$, with $L \gg \xi$ for which (Sec. 2.10.1)

$$\mathbf{v}_i^{(j)} = \frac{\pi c q_j}{(L/\xi)} \sum_{m=-\infty}^{\infty} \begin{pmatrix} \frac{-\sin(y'_{ij})}{\cosh(x'_{ij}-2\pi m)-\cos(y'_{ij})} \\ \frac{\sin(x'_{ij})}{\cosh(y'_{ij}-2\pi m)-\cos(x'_{ij})} \end{pmatrix}, \tag{6.2}$$

where $(x_{ij}, y_{ij}) \equiv \mathbf{r}_{ij} \equiv \mathbf{r}_i - \mathbf{r}_j$, and $(x'_{ij}, y'_{ij}) = 2\pi(x_{ij}, y_{ij})/L$. The absence of a physical boundary offers the usual advantage: vortices cannot reach their own images, enforcing conservation of net vorticity (here equal to zero). This helps achieve statistical homogeneity and isotropy, as required for comparisons with KLB theory.

Vortices in a compressible superfluid also interact with density fluctuations. While such interactions can be modelled in detail using, for example, a Gross-Pitaevskii description [209], modelling the full compressible dynamics complicates the calculation of fluxes [93], and, in the large systems considered here, would be prohibitively expensive computationally. However, as described in Ref. [93], Eq. (6.1) can be extended to account for these effects phenomenologically. The physics not captured by Eq. (6.1) alone primarily influence the dynamics when vortices approach each other at healing-length scales. These close approaches can be accounted for by: 1) removing opposite-sign vortex pairs separated by less than ξ, and 2) by smoothly increasing the dissipation γ for same-sign vortex pairs with

$$\gamma_i = \max\left(\exp\left[\ln(\gamma)\frac{r_{is} - r_1}{r_2 - r_1}\right],\ \gamma\right), \tag{6.3}$$

where r_{is} is the distance to the nearest same-sign neighbour of vortex i, $r_2 = \xi$, and $r_1 = 0.1\xi$. These effects model, respectively, dipole annihilation events and sound radiation emitted by rapidly accelerating vortices.

Although the dissipation introduced in Eq. (6.1) and its modification in Eq. (6.3) are only approximate, it should be stressed that for determining the existence of

a turbulent cascade it should not matter exactly what the form of the dissipation is. A turbulent cascade, by definition, occurs over a region of scale-space where dissipation is not important. In classical turbulence studies of the enstrophy cascade it is common to replace the viscous term ∇^2 in the Navier-Stokes equations with the "hyperviscosity" ∇^8, [16] which allows for a larger inertial range to be established with the use of fewer grid points. In fact, although modifying γ as in Eq. (6.3) is physically motivated by sound radiation for rapidly accelerating vortices, it could also be viewed as a superfluid analog of hyperviscosity, since it alleviates the problem of close approaches.

6.2.1 Spectral Formulation

The (average) kinetic energy spectrum, per unit mass, in the periodic box is given by [92]

$$E(\mathbf{k}) \;=\; E_{\rm self}(\mathbf{k}) + E_{\rm int}(\mathbf{k}) \;=\; \frac{\Gamma^2}{8(\pi k L)^2}\left[N + 2\left\langle \sum_{i=1}^{N}\sum_{j=i+1}^{N} q_i q_j \cos(\mathbf{k}\cdot\mathbf{r}_{ij})\right\rangle\right], \quad (6.4)$$

where $\mathbf{k} = (n_x\Delta k, n_y\Delta k)$ for $n_x, n_y \in \mathbb{Z}$, $\Delta k = 2\pi/L$, and $\langle\cdot\rangle$ denotes ensemble averaging. The total kinetic energy per unit mass is $\sum_{\mathbf{k}} E(\mathbf{k})(\Delta k)^2 = E_{\rm self} + E_{\rm int}$. At fixed N, the self-energy term is a cutoff-dependent constant, set by ξ and L. The time evolution of $E(\mathbf{k})$ governs the spectral transport of kinetic energy:

$$\frac{dE(\mathbf{k})}{dt} = T(\mathbf{k}) + D(\mathbf{k}), \quad (6.5)$$

where $T(\mathbf{k})$ is the transfer function, given by

$$T(\mathbf{k}) = -\frac{\Gamma^2}{4(\pi k L)^2}\left\langle \sum_{i=1}^{N}\sum_{j=i+1}^{N} q_i q_j \sin(\mathbf{k}\cdot\mathbf{r}_{ij})\mathbf{k}\cdot(\mathbf{v}_i - \mathbf{v}_j)\right\rangle, \quad (6.6)$$

and $D(\mathbf{k})$ is the dissipation spectrum, obtained from Eq. (6.6) by setting $\mathbf{v} \to \mathbf{w}$. As usual, the enstrophy and energy spectra are related via $\Omega(\mathbf{k}) = k^2 E(\mathbf{k})$. While $\Omega(\mathbf{k})$ is well-defined, the total enstrophy is divergent, but nonetheless proportional to the number of vortices: $\Omega = \Gamma^2 N\delta(\mathbf{0})$. Like its classical counterpart, the superfluid transfer function $T(\mathbf{k})$ conservatively redistributes energy, with $\sum_{\mathbf{k}} T(\mathbf{k})(\Delta k^2) = 0$. The dissipation spectrum $D(\mathbf{k})$ assumes a role normally played by the enstrophy spectrum in a viscous classical fluid, governing the rate of energy loss: $\sum_{\mathbf{k}} D(\mathbf{k})(\Delta k)^2 =$

$dE/dt < 0$. Turbulent cascades can be expected to develop when $\gamma \ll 1$ and $T(\mathbf{k})$ is large, such that it dominates $D(\mathbf{k})$, allowing a lossless inertial range to be established over some range of k.

To ensure an accurate representation of the one-dimensional spectral measures $E(k) = \int d\phi_k k E(\mathbf{k})$ etc., we avoid approximating angular integrals analytically. Instead, for $n = 1, 2, \ldots$, we define the discrete angular integral of a function $f(\mathbf{k})$ as $\tilde{f}(n\Delta k) = \sum_{k\in\mathcal{D}_n} f(\mathbf{k})\,\Delta k$, where $\mathcal{D}_n = \{\mathbf{k} \,|\, (n-1/2)\Delta k \leq |\mathbf{k}| \leq (n+1/2)\Delta k\}$. This defines the discrete energy and enstrophy fluxes for $n = 1, 2, \ldots,$

$$\tilde{\Pi}_\epsilon\,(n\Delta k) \equiv -\sum_{m=1}^{n} \tilde{T}(m\Delta k)\,\Delta k, \tag{6.7}$$

$$\tilde{\Pi}_\omega\,(n\Delta k) \equiv -2\sum_{m=1}^{n} (m\Delta k)^2 \tilde{T}(m\Delta k)\,\Delta k, \tag{6.8}$$

which represent the instantaneous energy and enstrophy flux through the k-space bin $|\mathbf{k}| = n\Delta k$ due to the conservative interactions.[2]

6.3 Transfer Properties for Isotropic Turbulence

Before proceeding to directly investigate the enstrophy cascade, it is natural to ask under what conditions cascades can exist in quantum turbulence, and some insight into the fundamental nature of the transfer processes of 2D quantum turbulence can be gained by considering the equations for the unbounded domain (Sec. 2.10.2). These equations should be a good indication of the dynamics for the motion on scales where modes are dense and the statistics are isotropic, i.e., $L^{-1} \ll k \ll \xi^{-1}$. Taking the limit of continuous k, and performing an angular integral gives (ignoring ensemble averaging for the moment)

$$E(k) = \frac{\Gamma^2}{4\pi k L^2}\left[N + \sum_{\alpha,\beta}{}' q_\alpha q_\beta J_0(k r_{\alpha\beta})\right] \tag{6.9}$$

$$T(k) = -\frac{\Gamma^2}{4\pi L^2}\sum_{\alpha,\beta}{}' q_\alpha q_\beta J_1(k r_{\alpha\beta}) \frac{dr_{\alpha\beta}^{(u)}}{dt} \tag{6.10}$$

$$D(k) = -\frac{\Gamma^2}{4\pi L^2}\sum_{\alpha,\beta}{}' q_\alpha q_\beta J_1(k r_{\alpha\beta}) \frac{dr_{\alpha\beta}^{(w)}}{dt} \tag{6.11}$$

[2]This becomes equal to the conventional continuum flux $\Pi(k) = -\int_0^k T(k')dk'$ in the high-k limit, by setting $k = n\Delta k$ (see Sec. 2.7.3).

where the superscripts (u) and (w) denote the contribution from the conservative and dissipative velocity fields, respectively. Notice that the integrals for the fluxes can be evaluated analytically:

$$\Pi_\epsilon(k) = \frac{\Gamma^2}{4\pi L^2} \sum_{\alpha,\beta}{}' q_\alpha q_\beta \frac{J_0(kr_{\alpha\beta})}{r_{\alpha\beta}} \frac{dr_{\alpha\beta}^{(u)}}{dt}, \tag{6.12}$$

$$\Pi_\omega(k) = \frac{\Gamma^2 k^2}{2\pi L^2} \sum_{\alpha,\beta}{}' q_\alpha q_\beta \frac{J_2(kr_{\alpha\beta})}{r_{\alpha\beta}} \frac{dr_{\alpha\beta}^{(u)}}{dt}. \tag{6.13}$$

The expression for $\Pi_\omega(k)$ does not converge as $k \to \infty$ (it oscillates indefinitely). However, wavenumbers $k \gg \ell^{-1}$ for an average inter-vortex distance ℓ do not have a clear meaning unless close approaches play a significant role in the vortex distribution. This point was previously stressed by Kraichnan [141], who qualitatively argued that under such conditions the spectral formulation could be truncated, thereby effectively creating a system of rigid discs of uniform vorticity rather than point-like vortices.

Since $dr_{\alpha\beta}^{(u)}/dt$ comes from the conservative part of the dynamics, it follows that this change can only come from vortices other than α and β. Naturally it follows that $T(k) = 0$ everywhere for a system of two vortices because their separation is a constant of the motion in the absence of dissipation. At the fundamental level, energy transport is therefore a three vortex process. For three vortices, projecting the velocity field from vortex γ along $\mathbf{r}_{\alpha\beta}$ gives:

$$\frac{dr_{\alpha\beta}}{dt} = \frac{\Gamma q_\gamma}{2\pi} \left(\frac{\sin\varphi_\beta}{r_{\beta\gamma}} - \frac{\sin\varphi_\alpha}{r_{\gamma\alpha}} \right) \varepsilon_{\alpha\beta\gamma}, \tag{6.14}$$

where $\varepsilon_{\alpha\beta\gamma}$ is the alternating pseudo-tensor (positive when $\{\alpha, \beta, \gamma\}$ appear in counter-clockwise order) and φ_α is the internal angle of the triangle formed by the vortex triple at vortex α. For isotropic turbulence it is desirable to eliminate the angles. We can express the transfer function entirely in terms of the lengths of the triple, and using $A_{\alpha\beta\gamma} = r_{\alpha\beta} r_{\beta\gamma} \sin\varphi_\beta$ etc. where $A_{\alpha\beta\gamma}$ is the area of the triangle

$$\frac{dr_{\alpha\beta}}{dt} = \frac{\Gamma q_\gamma}{2\pi} \frac{A_{\alpha\beta\gamma}}{r_{\alpha\beta}} \left(\frac{1}{r_{\beta\gamma}^2} - \frac{1}{r_{\gamma\alpha}^2} \right) \varepsilon_{\alpha\beta\gamma}, \tag{6.15}$$

and therefore

$$T(k) = \sum_{\Delta} T_{\alpha\beta\gamma}(k), \tag{6.16}$$

where

$$T_{\alpha\beta\gamma}(k) = \left(\frac{\Gamma^3}{8\pi^2 L^2}\right) q_\alpha q_\beta q_\gamma A_{\alpha\beta\gamma}\varepsilon_{\alpha\beta\gamma}\frac{J_1(kr_{\alpha\beta})}{r_{\alpha\beta}}\left(\frac{1}{r_{\beta\gamma}^2}-\frac{1}{r_{\gamma\alpha}^2}\right), \tag{6.17}$$

and $\sum_\Delta \equiv \sum_\alpha \sum'_\beta \sum''_\gamma$ is the sum over all vortex triples. The transfer function is expectedly complicated, and, much like in the classical case, we do not expect to be able to make definitive statements regarding transfer that will be valid under all conditions. Similar to the Navier-Stokes transfer function in Sec. 2.7.3, the transfer ultimately depends on the nature of the triple vortex charge product $q_\alpha q_\beta q_\gamma$, which here plays the role of the triple vorticity correlation, and is unknown in general (the probability distributions in turbulence are not shape-preserving [1]). Nonetheless, some important qualitative features of the transfer function can be identified from Eq. (6.17)

- *Locality* — Although ultimately determined by the distribution of $q_\alpha q_\beta q_\gamma$, it seems likely that spectrally local transfer could arise from Eq. (6.17). Firstly, we expect the majority of transfer at a given mode k to come from scales $r_{\alpha\beta} \sim k^{-1}$, since the Bessel function is largest in the local neighbourhood $kr_{\alpha\beta} \sim 1$, and obviously $r_{\alpha\beta}$ must change continuously. For small arguments, $J_1(kr_{\alpha\beta})$ vanishes, and for large arguments $J_1(kr_{\alpha\beta})$ is highly oscillatory and it therefore could plausibly average to zero. Locality could be further ensured by the term in parentheses: whenever one leg of the triple is significantly shorter than the other two, strong cancellations will occur in the sum for that triple: $T_{\alpha\beta\gamma}(k) + T_{\beta\gamma\alpha}(k) + T_{\gamma\alpha\beta}(k) \approx 0$. Recall however from Sec. 2.9.2 that local transfer, while dominant in the inverse energy cascade, is not necessarily dominant for the enstrophy cascade.

- *Screening* – For two reasons, transfer will be suppressed when the distribution exhibits negative interaction energy ($E_{\text{int}} < 0$). Firstly, although the contribution from any one triple $\{+,-,-\}$ may be non-negligible, because at negative energies the vortices are on average grouped into vortex-antivortex pairs, a significant proportion of this transfer will be cancelled by screening from the triple formed with the adjacent vortex $\{+,-,+\}$, which will form a triple of similar lengths. At distances larger than the average dipole distance, the configurations will be close to uncorrelated ($q_\alpha q_\beta q_\gamma$ will average to zero at these scales), yielding vanishing transport. Secondly, related to the point noted above, as the energy becomes increasingly negative, the vortex-anti vortex pairs in the distribution become ever more isolated, and hence all triples formed will have

one leg significantly shorter than the other two. These arguments are consistent with the findings of Ref. [93] where vortex dipole states were found to exhibit very little energy transport.

6.3.1 Detailed Conservation Laws

The special nature of spectral transport in two-dimensional classical fluids ultimately stems from the detailed conservation laws. However, for point vortices, if the transfer function does satisfy detailed conservation properties in wavenumber space, it is not immediately evident from Eq. (6.17). Curiously, however, notice that integrating over k the transfer function becomes

$$T_{\alpha\beta\gamma} = -\left(\frac{\Gamma^3}{8\pi^2 L^2}\right) q_\alpha q_\beta q_\gamma A_{\alpha\beta\gamma}\epsilon_{\alpha\beta\gamma}\frac{1}{r_{\alpha\beta}^2}\left(\frac{1}{r_{\beta\gamma}^2}-\frac{1}{r_{\gamma\alpha}^2}\right), \tag{6.18}$$

$$T_{\alpha\beta\gamma} = T_{\beta\alpha\gamma}. \tag{6.19}$$

It is then straightforward to verify that

$$T_{\alpha\beta\gamma} + T_{\beta\gamma\alpha} + T_{\gamma\alpha\beta} = 0, \tag{6.20}$$

$$r_{\alpha\beta}^2 T_{\alpha\beta\gamma} + r_{\beta\gamma}^2 T_{\beta\gamma\alpha} + r_{\gamma\alpha}^2 T_{\gamma\alpha\beta} = 0, \tag{6.21}$$

and

$$\sum_{\Delta} T_{\alpha\beta\gamma} = 0, \qquad \sum_{\Delta} r_{\alpha\beta} T_{\alpha\beta\gamma} = 0, \tag{6.22}$$

which shows that both the energy and the quantity $l = \sum_{\alpha,\beta} q_\alpha q_\beta r_{\alpha\beta}^2$ are conserved both globally, and in detail, by every individual triple. Note however that conservation of l only strictly applies in the unbounded domain. If the sums are expressed in terms of the lengths of each triple rather than the vortices, these conservation laws have the exact same mathematical form as the detailed conservation laws of the Navier-Stokes equations [Eqs. (2.64) and (2.65)]. This suggests that Kraichnan's analysis [119] might be applicable to the point vortex system in "separation space". However, since in this study we are primarily interested in the wavenumber-space formulation and the enstrophy cascade, this possibility will not be pursued further here.

6.3.2 When Could Cascades Exist?

The analysis of the previous sections provides some insight into when the cascades could exist in two-dimensional quantum turbulence. The analysis of the transfer function suggests that the interaction energy must be positive in order to obtain a large transfer in wavenumber space, because screening will suppress transfer at negative energies (the vorticity correlations need to be long ranged). This is consistent with the knowledge of 3D quantum turbulence, where a "bundling" of same-sign vortices is needed to observe the direct energy cascade [40]. Further supporting evidence for this statement can be obtained from inspection of Eq. (6.9). If we propose an ansatz with nontrivial power-law scaling of the form

$$E(k) = \begin{cases} Bk^{-\mu}, & k_L \leq k \leq k_\ell \\ 0 & \text{otherwise} \end{cases} \qquad \mu \neq 1,\ B > 0; \tag{6.23}$$

first notice that this scaling can only ever come from $E_{\text{int}}(k)$, because at any given instant of time the *full* spectrum could only ever be of the form

$$E(k) = E_{\text{self}}(k) + E_{\text{int}}(k) = \frac{\Gamma^2}{4\pi L^2}\left[\frac{N}{k} + Bk^{-\mu}\right]. \tag{6.24}$$

This result seems to have gone unnoticed in the literature.[3] The condition $B > 0$ does not completely rule out the possibility of such a scaling existing when $E_{\text{int}} < 0$, since one could imagine a scenario where $E_{\text{int}}(k)$ is positive over some region and negative over another (larger) region. However, it seems unlikely that such a state would arise spontaneously through the dynamics, since the transfer function (at least classically) tends to fill the "emptiest" regions of wavenumber space [1]. It thus seems likely that the negative energy region would be preferentially filled, thereby depleting the source of energy required to establish the power-law scaling over an inertial range. We are therefore lead to suggest that $B > 0$ implies $E_{\text{int}} > 0$ also, and the range of any power law scaling will ultimately be limited by the amount of energy available to fill the area under the curve. Importantly however, note that we expect that the condition $E_{\text{int}} > 0$ is necessary but not sufficient for the development of a cascade. Two dimensional turbulence is special; unlike in three dimensions, a large Reynolds number does not guarantee that a flow will become turbulent [16, 117]. For example, a state such as the spectral condensate, i.e. a solution to the Montgomery-Joyce

[3] All of the previously noted studies of 2D quantum turbulence [80, 92, 186, 188, 189, 243, 244, 248] inspected the full spectrum, suggesting that some results may need to be revisited.

equation, will not exhibit strong spectral transfer (it is an equilibrium distribution), despite having a large positive interaction energy (and therefore a large characteristic velocity), a large integral scale, and hence a large Reynolds number.

6.4 Initial Condition

Previous studies of decaying superfluid turbulence have considered initial conditions including regular lattices [93], and configurations generated from the snake instability of solitons [150]. However, spectral transport in such systems can be difficult to interpret due to the broadband initial spectrum, and choosing a simple initial condition is desirable for making comparisons with the KLB scenario. This is especially true if, as in the case of the N-body problem here, very large Reynolds numbers might be difficult to attain. Consequently, to investigate the enstrophy cascade we would like to consider the ideal, spectrally localised, and highly non-equilibrium initial states that are often considered classically in, e.g., [116, 118]. The difficulty in creating such states in a quantum fluid is that quantum vortices have a broadband spectrum — it is not immediately clear from Eq. (6.9) what kind of vortex distribution would create such an initial state.

Suppose the turbulence is generated by some initial rapid forcing localised near a forcing wavenumber k_f. The forcing is then switched off so that the turbulence freely decays under its own evolution. A simple method was devised to create a superfluid analogue of such initial states as follows: we define a set of wavenumbers $\mathcal{D}_f$ that form a shell of width w localised around k_f: $\mathcal{D}_f = \{\mathbf{k} \,|\, k_f - w/2 \leq |\mathbf{k}| \leq k_f + w/2\}$. Each mode in $\mathcal{D}_f$ is occupied with a random complex phase $\theta(\mathbf{k})$, uniformly sampled on $[0, 2\pi]$ to define a (Hermitian) vorticity field: $\hat{\omega}(\mathbf{k}) = e^{i\theta(\mathbf{k})}$ if $\mathbf{k} \in D_f$ and $\hat{\omega}(\mathbf{k}) = 0$ otherwise. The real-space vorticity field, $\omega(\mathbf{r}) = \int d^2\mathbf{k}\ e^{i\mathbf{k}\cdot\mathbf{r}}\hat{\omega}(\mathbf{k})$, is then separated into positive and negative regions $\omega_\pm(\mathbf{r})$ such that $\omega_-(\mathbf{r}) = |\omega(\mathbf{r})|$ if $\omega(\mathbf{r}) < 0$ and $\omega_-(\mathbf{r}) = 0$ otherwise, and similarly for $\omega_+(\mathbf{r})$. The components are then normalised to unity [$\int d^2\mathbf{r}\omega_\pm(\mathbf{r}) = 1$]. The fields $\omega_\pm(\mathbf{r})$ are then used as probability distributions to create an N-point-vortex initial condition via rejection sampling. This procedure creates an initial condition with the vast majority of the interaction energy contained within one k-mode, even for quite small vortex numbers $N \sim \mathcal{O}(10^2)$.

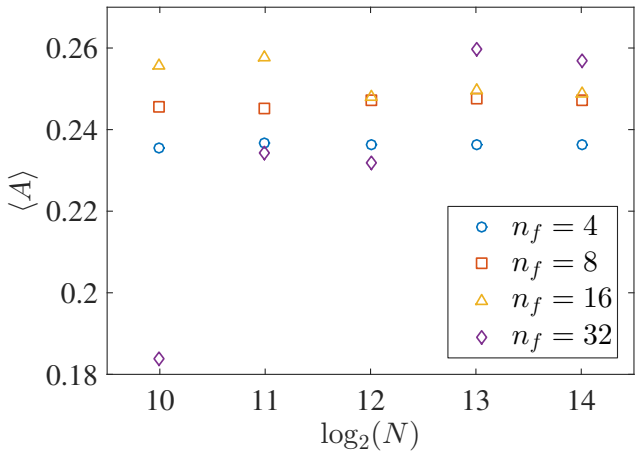

Figure 6.2: Average values for the parameter $\langle A \rangle$ as defined in Eq. (6.27), for different values of the vortex number N and the (dimensionless) forcing wavenumber $n_f = k_f/\Delta k$. Averages were calculated from 100 initial condition samples.

6.5 System Parameters

The system parameters chosen were a fixed box length $L/\xi = 10^4$, fixed dissipation $\gamma = 10^{-4}$ [78, 84, 173], and increasing vortex numbers $N = 2^n, n = \{9, 10, \ldots, 15\}$.[4] We characterise the system by the superfluid Reynolds number Re_s (Sec. 3.9.2) and the characteristic eddy turnover time τ

$$\mathrm{Re}_s = \frac{u_{\mathrm{rms}} L_f}{\Gamma}, \qquad \tau = \frac{L_f}{u_{\mathrm{rms}}}, \tag{6.25}$$

where $L_f = 2\pi/k_f$ and u_{rms} is the root-mean-square vortex velocity. To obtain clear scaling laws over a wide range of wavenumbers, it is desirable to maximise the Reynolds number. Instead of u_{rms} it would be equally valid to use $E_{\mathrm{int}}^{1/2}$ (which has the same dimensions), and a useful formula for the Reynolds number can thus be obtained from Eq. (6.4). For the positive energy states relevant here, the $N^2 - N \approx N^2$ terms in the double sum of Eq. (6.4) also yield $E_{\mathrm{int}} \propto N^2$ [94, 153] (at negative energies $E_{\mathrm{int}} \sim N$). Furthermore, since the sum has been explicitly constructed to form a delta function shell of the radial wavevector, we are motivated to propose the (continuum)

[4] The point-vortex approximation requires that $u_{\mathrm{rms}} \lesssim 0.3c$, so, for the given parameters, the largest N simulations (ignoring that N is also unrealistically large) are not physically reasonable. However, provided $L \gg \xi$ the choice of L is somewhat arbitrary, since rescaling $\{\mathbf{x}, L\} \to \alpha\{\mathbf{x}, L\}$ (for fixed ξ) yields $u_{\mathrm{rms}} \to u_{\mathrm{rms}}/\alpha$, and $\tau \to \alpha^2\tau$. For the smaller values of N, the box length L can be reduced by roughly an order of magnitude without invalidating the point-vortex approximation, in order to make the parameters more realistic.

ansatz

$$\lim_{\Delta k\to 0} E_{\rm int}(\mathbf{k}) = \frac{\Gamma^2}{8(\pi n \Delta k L)^2}\left[N^2 \frac{\delta(n-n_f)}{n}\langle A(N,n_f)\rangle\right] \tag{6.26}$$

where $n = k/\Delta k$ and $n_f = k_f/\Delta k \equiv L/L_f$, and $A(N, n_f)$ is a random function that allows for additional, "anomalous" dependence on N and n_f. For the continuum, we make the replacement $\sum_{\mathbf{k}}(\Delta k)^2 \to \iint n\, dn\, d\theta_n\, (\Delta k)^2$, yielding

$$E_{\rm int} = \left(\frac{\Gamma^2}{4\pi L^2}\right)\left(\frac{N^2}{n_f^2}\right)\langle A(N,n_f)\rangle. \tag{6.27}$$

The average values $\langle A\rangle$ for a range of N and n_f, as calculated from the numerical initial conditions, are presented in Fig. 6.2. Remarkably, $\langle A\rangle$ is virtually constant, and of order unity. The surprising result that $\langle A\rangle$ is close to constant leads to a remarkably simple formula for the Reynolds number as the ratio of two dimensionless quantities

$$\boxed{{\rm Re_s}' = \frac{N}{n_f^2}} \tag{6.28}$$

where we have neglected the unimportant factor of $\sqrt{\langle A\rangle/4\pi}$. According to Eq. (6.28), in 2DQT there are only two ways to increase the Reynolds number: either increase the vortex number N, or decrease n_f to increase the degree of same-sign vortex clustering. Uncorrelated vortex distributions with $E_{\rm int} \sim 0$, (i.e. the "ultraquantum" regime) correspond to $n_f \gtrsim L/\ell$ (giving ${\rm Re_s}' \sim 1$), where ℓ is the average intervortex distance, since the discrete vorticity field will not be able to (on average) resolve higher spatial frequencies than ℓ^{-1}. However, we expect the ansatz may break down when $E_{\rm int} \lesssim 0$, since the energy will no longer scale as N^2. Indeed, in Fig. 6.2, the case $N = 1024$, $n_f = 32$ (for which ${\rm Re_s}' = 1$) deviates from the general trend. For states that are not spectrally localised, the constancy of $\langle A\rangle$ suggests n_f can simply be replaced with the average wavenumber

$$\langle n_f\rangle = \frac{1}{\Delta k E_{\rm int}}\int_0^\infty dk\, k E_{\rm int}(k). \tag{6.29}$$

or, equivalently, the average cluster size. Based on the above analysis, to maximise the Reynolds number while still maintaining approximate isotropy, we choose $L_f = L/4$. The energy was found to be rather insensitive to the value of w, and we thus choose the narrowest window, $w = \Delta k$. Note that such behaviour is consistent with Eqs. (6.27) and (6.29): for example, an equal superposition of the values $n_f = \{3, 4, 5\}$ gives

N	$\langle u_{\rm rms}\rangle/c$	$\tau c/\xi$ (approx.)	$\mathrm{Re_s}$	$\mathrm{Re_s}'$	# runs
512	$(2.5 \pm 0.7) \times 10^{-2}$	9.9×10^4	10	32	40
1024	$(4.3 \pm 0.9) \times 10^{-2}$	5.8×10^4	17	64	20
2048	$(7.4 \pm 0.7) \times 10^{-2}$	3.4×10^4	30	128	16
4096	$(14 \pm 0.7) \times 10^{-2}$	1.8×10^4	54	256	12
8192	$(26 \pm 0.7) \times 10^{-2}$	9.7×10^3	102	512	8
16384	0.51 ± 0.01	4.9×10^3	202	1024	4
32768	~ 0.97	2.5×10^3	385	2048	1

Table 6.1: Parameters for the $L = 10^4\xi$ periodic box.

$(1/3^2 + 1/4^2 + 1/5^2)/3 = 0.0712 \approx 1/4^2 = 0.0625$. Values of Re_s, Re_s' and τ for the chosen values of L_f and w, for different values of N, are presented in Table 6.1.

6.6 Numerical Implementation

Starting from the initial conditions described above, we directly simulate the point vortex model [Eqs. (6.1) and (6.2)] and calculate ensemble-averaged spectra and fluxes [Eqs. (6.4) – (6.8)], using GPU codes programmed in Nvidia CUDA-C++ [295]. Utilising this hardware allowed the dynamics of very large N to be simulated within a reasonable computational timeframe, without the need for any approximation methods. The CUDA kernel that evaluated the vortex velocities was based on the CUDA N-body gravity problem example [295], (using shared memory), but modified to cope with positive and negative charges, and a variable body number N to allow for annihilation events. The time stepping scheme was an adaptive 4th-5th order Runge-Kutta scheme (Cash-Karp variety). The tolerance of the adaptive scheme was set to ensure that the absolute difference between the 4th and 5th order solutions agreed to within $\mathrm{tol} = 10^{-5}$ for all vortices. For this tolerance, the infinite sum in Eq. (6.2) was truncated at $m = \pm 3$, at which point it converges to within 10^{-11}. Testing the case $N = 16,384$ against a simulation using $m = \pm 5$, and $\mathrm{tol} = 10^{-8}$ did not alter the results presented. For the same value of N, increasing γ, r_1 and r_2 each by an order of magnitude, to increase the importance of damping, also did not alter the results at a qualitative level, in the sense that a k^{-3} spectrum was still observed for a significant number of turnover times. Simulations were run for $t = 10\tau$ in each case, with outputs generated every $\delta t \approx \tau/20$. The number of trajectories varied with N depending on what was required to obtain smooth spectral flux data (see Ta-

ble 6.1), subject to the constraint of practical computation time. Two Nvidia Tesla K40 cards (Kepler architecture, 12GB RAM), and three GTX Titan Black cards (Kepler Architecture, 6GB RAM) with compute capability 3.5 were used to perform the calculations in double precision. The required computing time varied greatly with N: the entire 40-run ensemble for $N = 512$ took $1 - 2$ days, including the spectral calculations for every output; each run for $N = 16,384$ took on the order of 1 week of calculation time, and a similar amount of time to calculate the spectra at every output per run; the $N = 32,768$ run took about 3 weeks, and another 3 weeks to calculate the spectral measures.

6.7 Spectral Dynamics

6.7.1 Vorticity, Spectra and Flux

Fig. 6.3 shows the dynamics of the vorticity field, kinetic energy spectra, and fluxes for $N = 16,384$ ($\mathrm{Re}_s \sim 200$). The qualitative behaviour is similar for all N considered, but naturally large N yields clearer power-laws. Very early times [Fig. 6.3(a)] show the flux rapidly grows from zero, causing the spectrum to rapidly spread from the initial state well-localised at $k_f = 4(\Delta k)$ [Fig. 6.3(a), inset]. Times $t \approx 2\tau$ mark the onset of power-law scaling. At the onset, the spectrum agrees quite well with the Saffman scaling k^{-4} [224], consistent with the formation of sharp, isolated vorticity-gradient filaments [Fig. 6.3, (b)]. These filaments are repeatedly stretched and packed, and the spectral slope gradually transitions, settling to the k^{-3} scaling at $t \sim 4\tau$ [Fig. 6.3, (c)]. A transition from k^{-4} to k^{-3} scaling was also reported in pseudospectral Navier-Stokes simulations of decaying 2D turbulence [296]. Note that in Fig. 6.3 only the interaction term $E_{\mathrm{int}}(k)$ is shown, as the self-energy term can only ever contribute a trivial N/k scaling. Removal of the self term is necessary to observe the very steep k^{-3} law, which otherwise quickly becomes dominated by the N/k scaling unless the energy is extremely large. Without the subtraction of the self term, the spectrum was found to exhibit transient agreement with k^{-3} over a shorter range of the spectrum at $t \approx 2\tau$, when the interaction spectrum scales as k^{-4}.

Inspection of the energy and enstrophy fluxes confirms the directions of spectral transport. During the early developing stages before the peak is depleted [Fig. 6.3(b)] the fluxes are quite similar to the scenario of forced turbulence envisaged by Kraichnan: the flux ranges of energy and enstrophy are mutually exclusive and quasi-constant, with negative energy flux indicating flow to low k and positive enstrophy

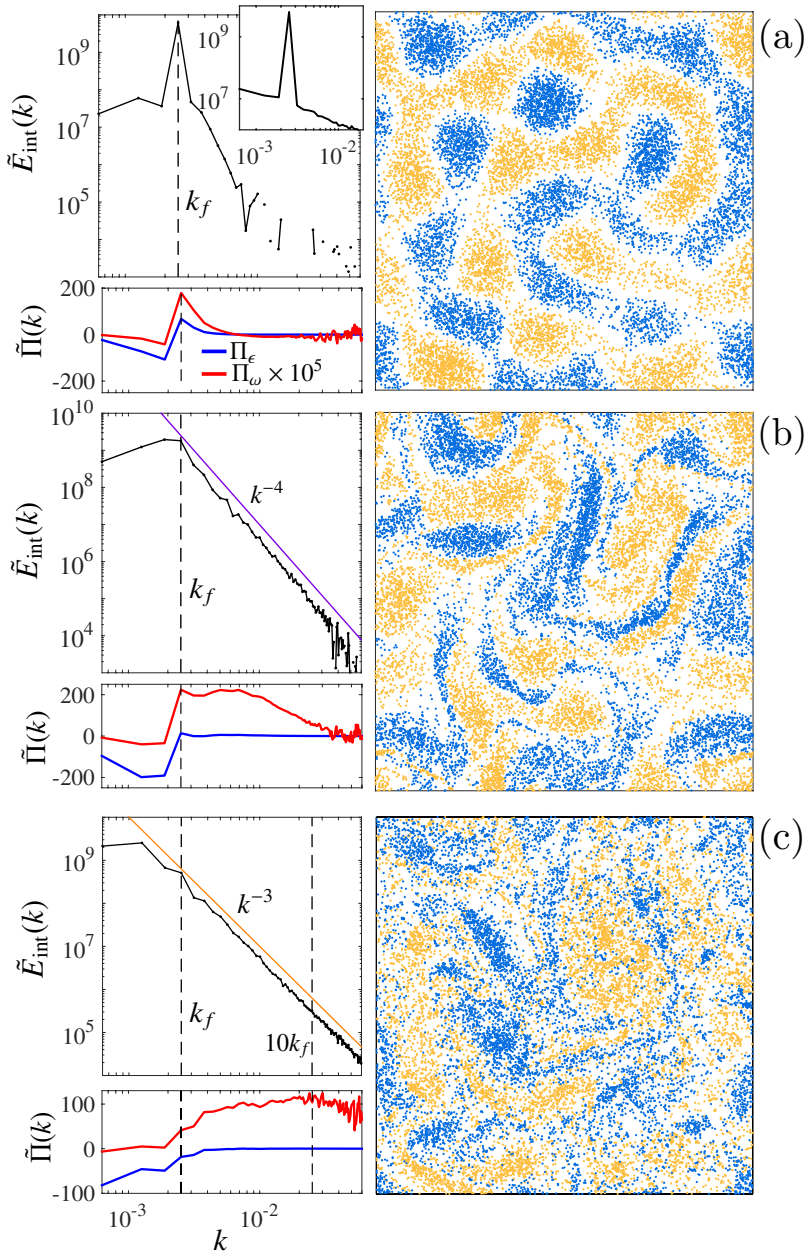

Figure 6.3: Vorticity distributions, kinetic energy spectra, and fluxes for $N = 16,384$ at (a) $t \approx 0.25\tau$, (b) $t \approx 1.85\tau$, and (c) $t \approx 4\tau$. Inset in (a) shows the full spectrum, $E_{\rm self}(k) + E_{\rm int}(k)$, at $t = 0$. Spectra and flux (shown in units of $\Gamma^2/4\pi L^2$) are averaged over 4 runs. A narrow window of time averaging is also used to obtain better statistical data, by averaging over a window of $\sim 0.5\tau$, using 9 time samples with time-spacing $\delta t \approx \tau/20$. In the top panel, at high k, $E_{\rm int}(k)$ is comparatively small and oscillates about zero. The negative values cannot be shown on the log scale, causing the broken data line. In (c), over the decade of wavenumbers indicated, linear fit to the logarithmic data yields a slope of -3.12, with an R-squared goodness of fit value $R^2 = 0.997$.

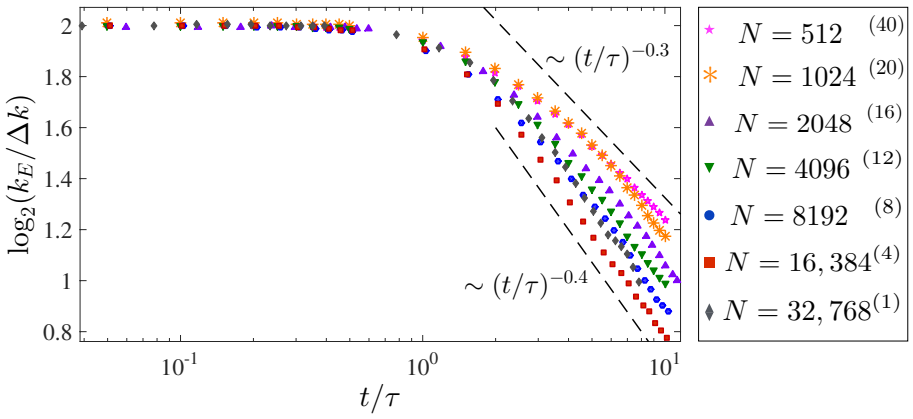

Figure 6.4: Time evolution of the energy centroid wavenumber k_E, Eq. (6.30)

flux indicating flow to high k.

6.7.2 Integral Scale Growth

The flux of energy towards low k causes a growth of the integral scale, or, equivalently, decay of the integral wavenumber. To quantify the integral scale growth with time, we measure the energy centroid wavenumber

$$k_E = \frac{\int k E_{\text{int}}(k) dk}{\int E_{\text{int}}(k) dk}. \tag{6.30}$$

Due to the steep nature of the spectrum, k_E has a very similar value to k_L (which we define as the wavenumber where $E_{\text{int}}(k)$ is largest), but exhibits smoother evolution with time. The evolution of k_E is shown in Fig. 6.4. At low N, k_E decays approximately as $\sim (t/\tau)^{-0.3}$, but as N increases the decay appears to converge to a power law $\sim (t/\tau)^{-0.4}$. While the decay is considerably slower than Batchelor's prediction $k_E \sim (t/\tau)^{-1}$, such behaviour is typical and expected [16, 117]. A systematic study across different values of k_f would be needed to determine if the scaling is universal. However, since this is not the case classically (Sec. 2.9.2), a universal scaling seems unlikely.

6.7.3 Kraichnan-Batchelor Constant

The k^{-3} spectrum [Fig. 6.3(c)] is corroborated by a nearly constant enstrophy flux over approximately one decade of wavenumbers, allowing for a determination of the Kraichnan-Batchelor constant via the so-called compensated kinetic energy spectrum:

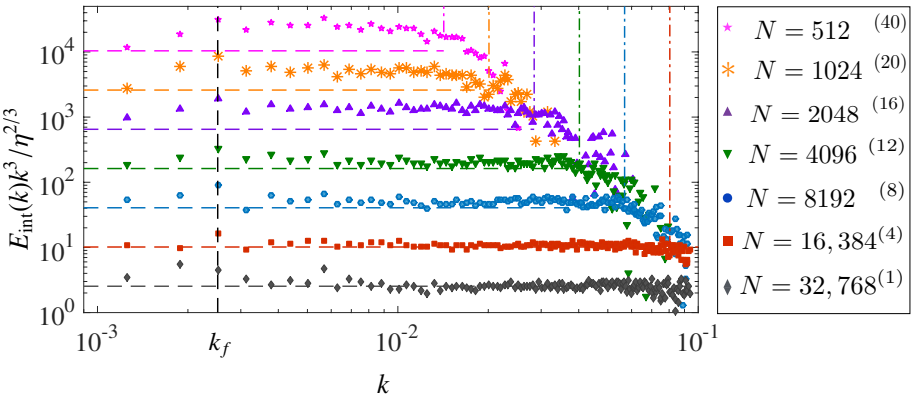

Figure 6.5: Compensated kinetic energy spectra for a range of N, averaged over ensemble and a time window $\sim 0.5\tau$. For clarity the spectra are vertically shifted by increasing powers of 4. The horizontal dashed lines shows the value $C' = 1.6$ (also vertically shifted for comparison at different N). Dash-dot lines indicate the inter-vortex spacing wavenumber k_ℓ at different N (see text). In the legend the bracketed superscripts indicate the number of independent realisations used in the ensemble average.

$C' = E(k)k^3/\eta^{2/3}$, where $\eta = \Pi_\omega$ averaged over k, time window, and ensemble. Fig. 6.5 shows the compensated spectrum for different N at $t \sim 4\tau$. The k^{-3} scaling is observed to some degree for all N considered, albeit over less than a decade for small N (~ 0.7 decades for $N = 512$). However the quality and range of the scaling increases dramatically as N is increased. For smaller N, C' is quite large ($C' \approx 3.8$),[5] but as N increases C' decreases and tends towards a constant value $C' \approx 1.6$. A simulation with $N = 16,384$ and $k_f = 8(\Delta k)$ ($\mathrm{Re}_s \sim 50$) yielded $C' \approx 2.0$, in good agreement with $N = 4096$, $k_f = 4(\Delta k)$ (which has roughly the same Re_s) and yielded $C' \approx 1.9$. Very flat behaviour over the entire compensated spectrum (as is evident in Fig. 6.5) is rather short-lived, existing for around 1 turnover time. This is somewhat expected: in decaying 2D turbulence, the formation of coherent structures [16] or low Reynolds number effects [118] can cause significant deviations from the k^{-3} scaling. The k^{-3} range is found to persist up to $k_\ell = 2\pi/\ell$, the wavenumber associated with the average intervortex distance $\ell = L/\sqrt{N}$. Notice that for $N \geq 16,384$ this means the compensated spectrum is constant over a significant range, roughly 1.5 decades above the original forcing scale, and two decades above the integral scale $k_L = 2\Delta k$ (where $E_{\rm int}(k)$ is largest) at $t = 4\tau$, see Fig. 6.3(c). Above k_ℓ, the interaction spectrum quickly decreases, indicating a transition from many-vortex to single-vortex physics.

[5] Slight variation of C' with the forcing scale or Reynolds number is not unusual [118, 119, 123]

6.8 Analysis of Spectral Exponents

We now investigate the quality of the power-law behaviour and degree to which the spectrum conforms to the k^{-3} scaling via best-fit analysis. For this analysis, the mean of $E_{\rm int}(k)$ was taken at each value of k by averaging over ensemble and a narrow time window containing 9 time samples of spacing $\delta t \approx \tau/20$ at a given time step. Uncertainty in $E_{\rm int}(k)$ was calculated from the standard deviation of the sample. Inspecting the distribution of $E_{\rm int}(k)$ at each value of k gave no indication of outliers (the distributions appeared to be normal or at worst quasi-normal), so standard least-squares fitting with weights was used. Uncertainties in the logarithmic data were then calculated using standard error propagation methods [297]. Quality of the linear fit was measured using the R^2 value. Defining $z = \log_{10}(k)$ and $\mathcal{E}(z) = \log_{10}[E_{\rm int}(z)]$, we consider two functional forms:

$$\mathcal{E}(z,t) = -n(t)z + a(t) \tag{6.31}$$

and

$$\mathcal{E}(z,t) = -nz + a(t), \qquad n = \ldots, 2.9, 3.0, 3.1, \ldots \tag{6.32}$$

Figs. 6.6 (a) and (b) show the exponent n and goodness of fit measure R^2 as functions of time as obtained from fitting Eq. (6.31). The data confirm the qualitative remarks in Sec. 6.7: Early times exhibit a rapid decrease in n and a rapid increase in R^2 as the spectrum enters the scaling regime. The onset of power-law behaviour is seen in the flattening of R^2 at $t \approx 1.6\tau$, at which time the exponent is $n \approx 4$. Between $t \approx 1.6\tau$ and $t \approx 4\tau$, there is then a more gradual transition from $n = 4$ to $n = 3$. Interestingly, the transition from $n = 4$ to $n = 3$ was found to be well described as exponential decay: $n(t) = 3 + e^{-\beta t/\tau}$, with $\beta \approx 2$. During this time window, the fit quality is quite high with $R^2 > 0.995$. At $t \approx 4\tau$ the exponent is very close to 3, and the goodness of fit is exceptionally high: $R^2 = 0.998$. During subsequent evolution the spectral exponent is close to $n = 3$, and although the quality of the fit gradually decreases, it is always > 0.988. An example of the spectrum and best-fit line when the exponent is close to 3 is shown in Fig. 6.6 (c). Fig. 6.6 (d) shows the time-averaged goodness of fit $\langle R^2 \rangle_t$ for different n, as obtained using Eq. (6.32). The time average is computed over all values $t \geq 2\tau$, i.e., over the entire time range over which the spectrum appears to exhibit power law scaling. Clearly, $n = 3$ yields the highest average goodness of fit. Figure 6.7, shows the same as Fig. 6.6, but for the case $N = 512$. The qualitative behaviour is essentially identical to that in Fig. 6.6,

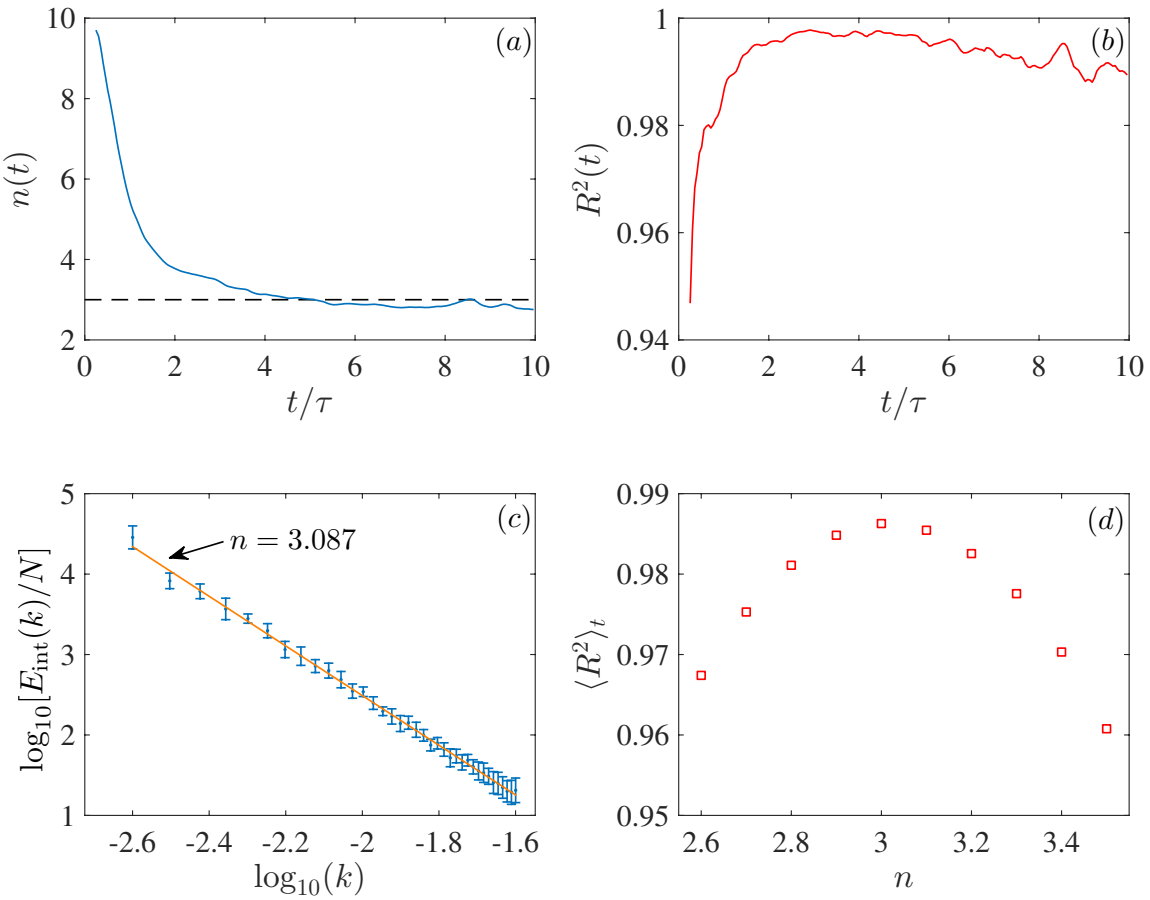

Figure 6.6: Best-fit analysis for the $N = 16,384$ simulations: (a) exponent n and (b) goodness of fit R^2 (b) obtained from a weighted linear least-squares fit to the spectrum for values $k \in [k_f, 10k_f]$ as functions of time (in units of eddy turnover time τ). Values are averaged over 4 runs and 9 time samples of spacing $\delta t \approx \tau/20$ centered around t. (c) An example fit when the spectrum is close to k^{-3}. (d) Time-averaged goodness of fit $\langle R^2\rangle_t$, for lines with different fixed slopes n, averaged over all times $t \geq 2\tau$.

except the range of scaling is smaller, the fluctuations are larger, and the quality of fit is somewhat poorer.

6.9 Two-Point Vorticity Correlations

While the data already presented provide considerable evidence of an enstrophy cascade, it is nonetheless desirable to verify that some other measure behaves in a way that is consistent with the process, especially since the slope of the spectrum fluctuates, and the fitting analysis of the previous section shows that the spectrum is never

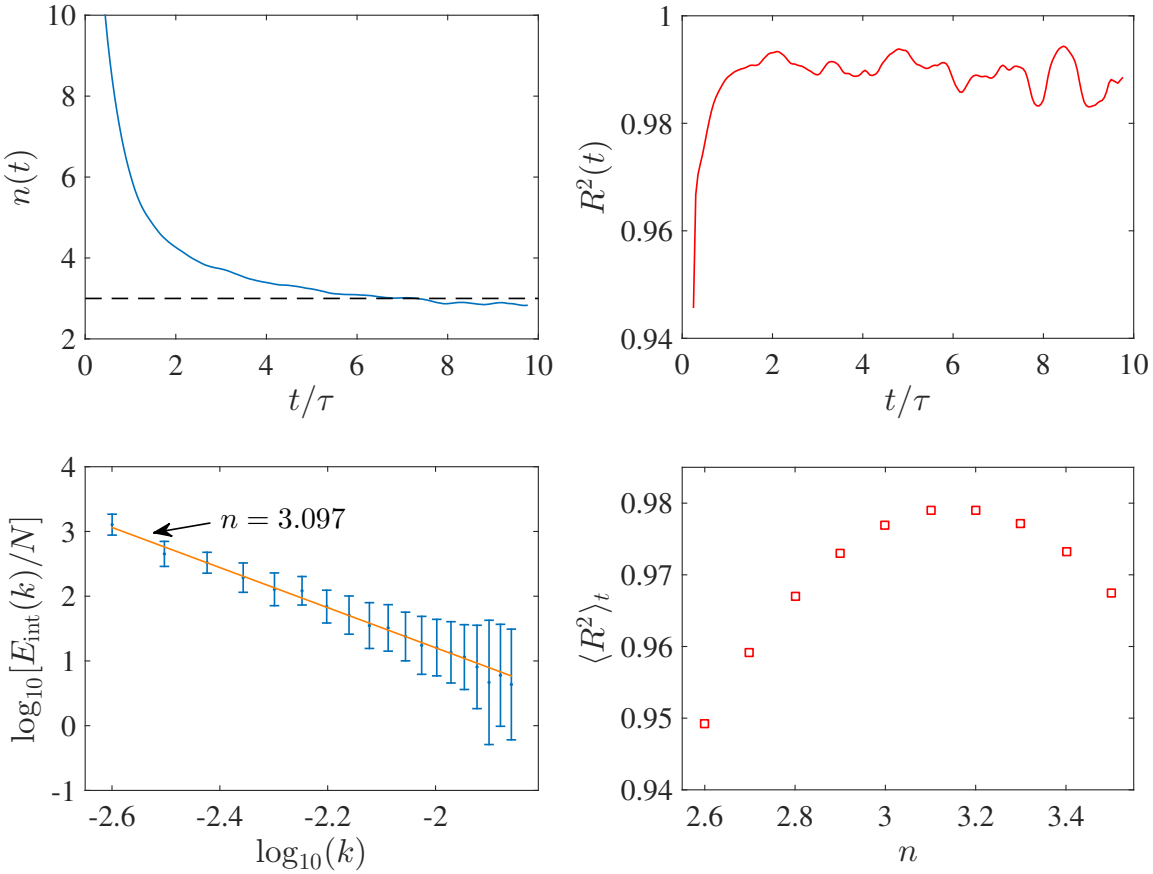

Figure 6.7: Same as Fig. 6.6, but for $N = 512$. Here fits were only over the range $k \in [k_f, k_\ell]$, where $k_\ell = 2\pi/\sqrt{N}/L \approx 5.65k_f$ (about 0.75 decades), since the interaction spectrum $E_{\rm int}(k)$ virtually vanishes beyond k_ℓ (see Fig.6.5). Values are averaged over 40 runs and 9 time samples of spacing $\delta t \approx \tau/20$, centered around t.

perfectly k^{-3}. Here we consider the two-point vorticity correlation function, which is related to the kinetic energy spectrum. In the limit $L \to \infty$, strict isotropy can be recovered, and we may write

$$R_\omega(\mathbf{r}) = \langle \omega(\mathbf{x})\omega(\mathbf{x}+\mathbf{r})\rangle = \int d^2\mathbf{k}\, \langle |\omega(\mathbf{k})|^2\rangle e^{i\mathbf{k}\cdot\mathbf{r}} \tag{6.33}$$

Using the definition of the vorticity field $\omega(\mathbf{x}) = \Gamma \sum_\alpha q_\alpha \delta(\mathbf{x} - \mathbf{r}_\alpha)$, and performing an angular average yields

$$R_\omega(r) = \frac{\Gamma^2}{2\pi r}\left[N\delta(r) + \left\langle \sum_{\alpha,\,\beta}{}' q_\alpha q_\beta \delta(r - r_{\alpha\beta})\right\rangle\right]. \tag{6.34}$$

In a similar manner, the angular dependence of Eq. (6.4) can be integrated out yielding

$$kE(k) = \frac{\Gamma^2}{4\pi L^2}\left[N + \left\langle \sum_{\alpha,\,\beta} q_\alpha q_\beta J_0(kr_{\alpha\beta})\right\rangle\right] = \frac{1}{2L^2}\int dr\, r\, R_\omega(r) J_0(kr). \tag{6.35}$$

Eq. (6.34) hence defines $R_\omega(r)$ such that $kE(k)$ and $R_\omega(r)$ are related in the usual way, via the Hankel transform [Eq. (6.35)]. Here it becomes evident that neglecting the N/k self spectrum is equivalent to explicitly ignoring the self correlation at $r = 0$. The normalised vorticity correlation function can then be expressed in terms of the kinetic energy spectrum in the usual way [298]

$$R_\omega(r) = \frac{\int_0^\infty dk\; k^2 E_{\text{int}}(k) J_0(kr)}{\int_0^\infty dk\; k^2 E_{\text{int}}(k)}; \quad r \neq 0, \tag{6.36}$$

and, for the interaction spectrum, we may use the ansatz

$$E_{\text{int}}(k) = \begin{cases} Bk^{-3} & 2\pi/l < k < 2\pi/a \\ 0 & \text{otherwise.} \end{cases} \tag{6.37}$$

By inserting Eq. (6.37) into Eq. (6.36), we may derive an expression for the two-point vorticity correlations, provided the inertial range is well developed, i.e., $l \gg r \gg a$. Adding and subtracting $1/k$, we may write

$$\int_{2\pi/l}^{2\pi/a} dk \frac{J_0(kr)}{k} = \ln(l/a) - \int_{2\pi/l}^{2\pi/a} dk\; \frac{1 - J_0(kr)}{k}. \tag{6.38}$$

A change of variables to $q = ka$ yields for the remaining integral

$$\int_{2\pi a/l}^{2\pi} dq \frac{1 - J_0(qr/a)}{q} \simeq \int_0^{2\pi} dq \, \frac{1 - J_0(qr/a)}{q} - \mathcal{O}\left(\frac{r}{l}\right)^2, \tag{6.39}$$

where we have exploited the property $l \gg r \gg a$ for a well-developed inertial range. Finally, the remaining integral can be split into two parts: $\int_0^{2\pi} dq = \int_0^1 dq + \int_1^{2\pi} dq$, yielding

$$\int_0^1 dq \, \frac{1 - J_0(qr/a)}{q} + \ln 2\pi - \int_1^{2\pi} dq \, \frac{J_0(qr/a)}{q}. \tag{6.40}$$

For the well-developed inertial range, the Bessel function is highly oscillatory in the term on the right, where $q \geq 1$. Extending the integration region to infinity will therefore not significantly alter the integral, yielding

$$\int_1^\infty dq \, \frac{J_0(qr/a)}{q} = -\gamma + \ln 2 - \ln(r/a) + \int_0^1 dq \, \frac{1 - J_0(qr/a)}{q}, \tag{6.41}$$

where γ is the Euler-Mascheroni constant. The remaining integrals cancel, and hence

$$\boxed{R_\omega(r) \simeq \frac{\ln(l/r) - \gamma - \ln \pi}{\ln(l/a)}; \quad l \gg r \gg a.} \tag{6.42}$$

This expression provides a robust test for the k^{-3} scaling, because exponents larger or smaller than -3 yield power-law rather than logarithmic scaling of the correlation function [298]. The expression will also contrast strongly with early times, where we may use the ansatz

$$E_{\rm int}(k) = E_{\rm int}\delta(k - k_f) \Longleftrightarrow R_\omega(r) = J_0(k_f r). \tag{6.43}$$

In Fig. 6.8 we show $R_\omega(r/\xi)$ for the $N = 16,384$ vortex system (as is shown in Fig. 6.3), for $t = 0$ and $t \approx 5\tau$ and $t \approx 10\tau$. The correlation function was calculated from a single run and time frame. At early times, the correlation function is very similar to the predicted Bessel function behaviour, especially considering it contains no fitted parameters. At $t = 5\tau$, when the k^{-3} spectrum has developed, the correlation function agrees remarkably well with Eq. (6.42). Fitting within the range $r/\xi \in [10, 1000]$ yields $a \approx 25$ and $l \approx 9775$. These values are in quite good agreement with the predictions based on the kinetic energy spectrum: the integral scale l can be estimated from the wavenumber where $E_{\rm int}(k)$ is the largest, which by $t = 6\tau$, is at $k = \Delta k$, giving $l \approx 10^4$. Since the spectrum drops rapidly beyond k_ℓ, the wavenum-

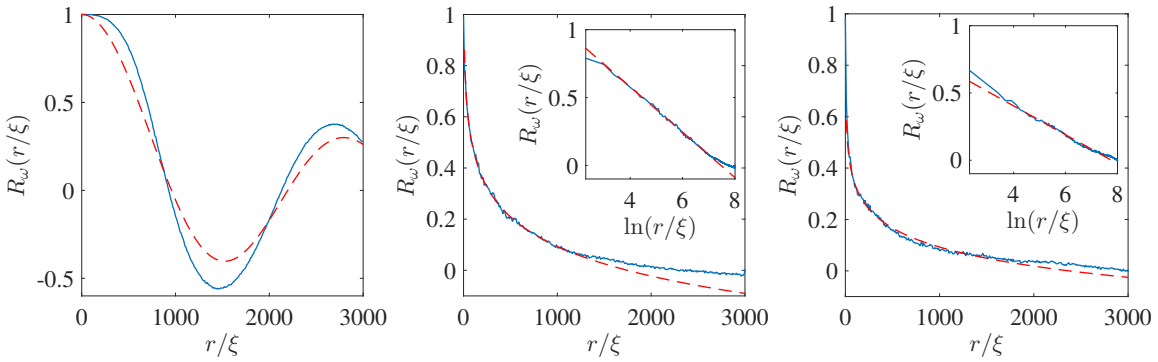

Figure 6.8: Two-point vorticity correlation function $R_\omega(r/\xi)$ for the $N = 16384$ vortex configuration in Fig. 6.3, shown at $t = 0$ (left), $t \approx 5\tau$ (middle) and $t \approx 10\tau$ (right). Dashed lines show analytical predictions $J_0(k_f r)$, [no fitted parameters, (left)] and a line of best fit using Eq. (6.42) [(middle, right), see text]. Insets show the same data against $\ln(r/\xi)$ for comparison.

ber associated with the intervortex distance, the microscale can be estimated from the intervortex distance, $a = L/\sqrt{N} \approx 78$. By $t \approx 10\tau$, the range of logarithmic behaviour has extended, and fitting over $r \in [10, 2000]$ yields $l \approx 1.327 \times 10^4$, and $a \approx 1.17$. The simultaneous increase of l and decrease of a leads to a shallower slope of the correlation function.

6.10 Discussion

It appears that, under the appropriate conditions, the basic KLB phenomenology of classical 2D turbulence applies to superfluids as well. As in 3D, the bundling of same-sign vortices is the crucial element responsible for mimicking classical behaviour [40, 230, 288]. Here the "bundled" states that exhibit strong spectral transport have positive interaction energies and negative-temperature equilibria [92, 141, 151]. In contrast, the analysis of Sec. 6.3 suggests that the states with positive temperature equilibria (negative energies) exhibit essentially no spectral transport in comparison. This is consistent with the findings of Ref. [93], where only clustered states were found to exhibit significant energy transport.[6]

Our results suggest Re_s' as defined in Eq. (6.28) is a good measure for quantifying the degree of turbulence, and can be used to estimate the range of the enstrophy cascade. Specifically, figure 6.5 shows that the k^{-3} scaling extends from wavenumbers of

[6] A number of simulations of states with negative energies also showed virtually no spectral transport compared to the clustered states, despite the fact that our value of γ is much smaller than that in Ref. [93].

order $k_f = 2\pi n_f/L$ up to the wavenumber associated with the mean intervortex distance, $k_\ell = 2\pi/\ell = 2\pi\sqrt{N}/L$. Hence the range of wavenumbers is $k_\ell/k_f = \sqrt{N}/n_f$. Since in Eq. (6.28) gives $\mathrm{Re}_s' = N/n_f^2$, it follows that $k_\ell/k_f = \sqrt{\mathrm{Re}_s'}$, which is exactly the same as in Batchelor's classical theory (see Fig. 6.1 and Sec. 2.9.2). Note, however, that here the high wavenumber cutoff is set by the discrete nature of the vorticity field rather than viscous dissipation. Nonetheless it appears that the full KLB phenomenology can be carried over to the quantum fluid. The sudden drop in $E_{\mathrm{int}}(k)$ at k_ℓ suggests that the point-vortex system can be truncated at wavenumbers $k \sim k_\ell$. This is consistent with the arguments put forward by Kraichnan [141]; he argued that the point-vortex and truncated Euler equations should be similar when close approaches are not significant. It would be interesting to analyse the drop-off region further, to determine if it shares any similarities with the dissipation range.

It is somewhat surprising that the k^{-3} scaling can be seen even for $N = 512$ ($\mathrm{Re}_s \sim 10$), since the same number of degrees of freedom would be achieved by a mere 20×20 Fourier modes contributing to the inertial range in a Navier-Stokes description. On the other hand, in contrast to a classical fluid, the dissipation rate γ is independent from the Reynolds number [238, 239], and lossless transport can be sustained through all the accessible Fourier modes if $\gamma \ll 1$. Although for small N the uncertainty in C' is larger due to larger fluctuations in η, a larger value of C' for smaller N is perhaps intuitively sensible; it suggests that fewer available degrees of freedom results in less efficient spectral transport (given $E(k)$, larger C' indicates smaller η).

For large Re_s, the Kraichnan-Batchelor constant $C' \approx 1.6$ was found to be close to the accepted value for a classical fluid, $C' = 1.4$ [118, 130]. Similarly, the Kolmogorov constant in 3D has been found to be the same above and below the λ-transition in superfluid He^4 [40]. In constrast, a study of the inverse energy cascade using a forced point-vortex model [294], found the associated Kraichnan-Kolmogorov constant to be double the accepted value, seemingly at odds with the results from 3DQT as well as those obtained here. Further study is certainly warranted. In Ref. [294], a forcing term was introduced by essentially reversing the sign of γ. A more physical scenario would be to introduce vorticity instead, possibly via the rejection sampling method described earlier, which could be considered as a more realistic minimal model of a stirring grid in a 2D superfluid [25, 128, 299]. The forced case would reveal whether both cascades can exist simultaneously in the point-vortex system, and would allow a more accurate estimate of the cascade constants if stationarity could be obtained. Intermittency effects, if present [130], could also be explored.

Full Gross-Pitaevskii simulations for the smaller values of N considered here are well within computational reach, and would be highly informative regarding the effective viscosity arising from the coupling to compressible modes. Furthermore, the physical mechanism of enstrophy loss could be elucidated in this more realistic model, since in principle there are two possible mechanisms. The first is a physical loss of vortices through dipole annihilation events, which, similar to viscous effects in the Navier-Stokes equations, remove enstrophy while removing comparably little energy [189].[7] The second would be enstrophy loss as a coarse-grained effect; as the vortex distribution reorders towards the "final dipole", a greater fraction of the distribution becomes uncorrelated (Sec. 2.10.3), and would be lost under a coarse-graining operation. This would be similar to the behaviour of the (conservative) Fourier-truncated Euler equation, in which thermalized high-k modes can form a fictitious "dissipative micro-world", for the non-equilibrium lower k modes [121, 300, 301]. In our system the second mechanism appears to be more significant, since the ratio ℓ/ξ is large, and consequently physical vortex losses are relatively small, $\lesssim 1\%$.

Finally, regarding the prospect of observing the cascade in atomic condensates, the difficulty would ultimately be achieving a system large enough relative to the healing length ξ. From Table 6.1, for our smallest vortex number $N = 512$, the system size could be reduced to $L \sim 850\xi$ without invalidating the incompressibility assumption $u_{\rm rms} \lesssim 0.3c$ [see Sec. 3.2.5 and recall $\mathbf{x} \to \lambda\mathbf{x}$ yields $\mathbf{u} \to \lambda^{-1}\mathbf{u}$ and $t \to \lambda^2 t$ in Eq. (6.2)]. For comparison, current experimental setups have achieved $L \sim 200\xi$ in 2D uniform systems [71], and for similar parameters such a large system would require $N_a \sim 10^7 - 10^8$ atoms, which is the upper limit of what has been achieved in harmonically confined systems [302]. Some further additional freedom is possible by tuning $\xi \propto a_s^{-1/2}$ through a Feshbach resonance [67, 68], or through tuning the effective 2D interaction parameter $g_{2D} = g/\sqrt{2\pi}l_z$ (Sec 3.1.5), although this would eventually enhance three-body losses [303]. Condensate lifetimes, on the other hand, appear to be less of an issue. Lifetimes on the order of $T = 60$s are not uncommon [78], and, with a natural timescale of e.g. $\xi/c \approx 0.13$ ms [78], this gives $T \approx 4.6 \times 10^5$ ξ/c. For the rescaled $N = 512$ system this corresponds to $T/\tau \approx 460$ turnover times, easily long enough to investigate the cascade (see Table 6.1). Furthermore, simple stirring protocols (such as in Chapter 5) also show promise for efficient injection of large vortex clusters. We therefore argue that, although undoubtedly challenging, the required experimental conditions do not seem out of reach.

[7] Similarly, in 3D quantum turbulence at very low temperatures, the effective "viscous" loss is measured through the decay of the vortex line length [47, 76, 196, 197].

6.11 Conclusion

We have demonstrated that, under the appropriate conditions, 2D quantum turbulence can support an enstrophy cascade as predicted by classical KLB theory, thus broadening the universality of the KLB scenario. Providing firm evidence that this fundamental process occurs in the ideal limit is a step towards understanding 2D quantum turbulence in real systems, and strongly implies that the inverse energy cascade can indeed occur in 2D quantum turbulence. The simplicity of the 2D point vortex system allowed the determination of a simple formula for the Reynolds number in decaying 2DQT. The formula was verified as a useful measure by demonstrating that it predicts the length of the inertial range. The scaling of the inertial range also demonstrates that the ideas of fully-developed turbulence become a meaningful description for quantum fluids once the vortex number reaches the order of several hundred, possibly less than one might expect. Validating that Re_s faithfully measures the degree of turbulence ensures that it can be used in future work to allow for a more quantitative comparison between different studies.

Chapter 7

Conclusions

In this thesis we have numerically and theoretically studied analogues of 2D classical turbulence in quantum fluids. Here we briefly summarize the studies and results that have been presented in Chapters 4, 5, and 6, before discussing some practical and theoretical implications of the results. We conclude by offering an outlook and suggestions for future work.

7.1 Summary

The studies presented in Chapters 4, 5, and 6 have broadly focussed on coherent vortex formation, the transition to turbulence in bluff-body wakes, and the cascade phenomena of fully-developed turbulence, respectively.

In Chapter 4, we presented a new hydrodynamic decomposition of the kinetic energy spectrum for a quantum fluid. Interestingly, it was found that this decomposition provided completely different flow-field information to the "classical" kinetic energy spectrum usually considered in the literature. Whereas the classical spectrum contains information regarding velocity correlations, the quantum kinetic energy spectrum contains information of the velocity probability distribution. We then used this new decomposition to analyse negative temperature equilibrium distributions of 2D quantum turbulence, a subject of current interest. We showed that the quantum spectrum would exhibit a k^3 power law in the presence of large, coherent vortices that emerge in negative temperature equilibria. The k^3 law was demonstrated to emerge in damped Gross-Pitaevskii dynamics in a trapped system, and the coherent vortex clusters were found to obey the Feynman rule of constant areal density, exhibiting rigid body rotation. The infrared k^3 law and the generalized Feynman rule

provide new accessible measures for characterizing negative temperature states in 2D quantum turbulence.

In Chapter 5 we studied the transition to turbulence in the wake of a cylindrical object in a 2D quantum fluid. To study this system, we developed a new numerical fringe method to cope with quantum vortices, allowing for steady-state wake properties to be investigated. The Strouhal-Reynolds number relation, which exhibits universal behaviour in the classical analogue, was then investigated as a means to test Onsager's superfluid Reynolds number across the transition to quantum turbulence. It was found that a seemingly universal Strouhal-Reynolds relation, similar to the classical form, emerged for large cylinders when Onsager's superfluid Reynolds number was modified to account for the critical velocity for vortex shedding: for cylinder width D, velocity u, and critical velocity u_c, and quantum of circulation $\kappa = \hbar/m$, the parameter

$$\mathrm{Re}_s = \frac{(u - u_c)D}{\kappa}$$

was found to recover dynamical similarity in the wake. For this modified Reynolds number, the transition to turbulence was observed to occur at $\mathrm{Re}_s \approx 0.7$ regardless of obstacle size, providing further evidence for dynamical similarity.

In Chapter 6 we studied the direct enstrophy cascade in decaying 2D quantum turbulence, for very large vortex numbers, in order to elucidate the nature of spectral transport and the emergence of cascade solutions in 2D quantum turbulence. We showed that quantum fluids can indeed exhibit the universal scaling properties associated with the direct enstrophy cascade, provided a few hundred vortices are present with suitable initial conditions. The decaying system was found to be well-characterised by Onsager's superfluid Reynolds number, equivalent to our newly proposed Reynolds number in the limit $\mathrm{Re}_s \gg 1$. The scaling of the inertial range versus the superfluid Reynolds number was found to be the same as in the classical scenario. This work shows that classical cascade phenomena can emerge quite readily in both 3D and 2D quantum turbulence under the right conditions. This could be considered as a rather remarkable and highly nontrivial demonstration of Bohr's correspondence principle.

7.2 Theoretical and Practical Implications

Regarding the results of Chapter 4: while the velocity probability distribution information contained within the quantum kinetic energy spectrum is useful, it does

not inform us of the spatial structure of turbulence, which is contained within the joint probability distributions for two or more points. Whereas the one-point velocity statistics in turbulence are usually of the pure-chance type (i.e., Gaussian), the statistics of the two-points and higher measures, being related through the equations of motion, exhibit highly nontrivial behaviour. Nonetheless, access to the probability distribution through expansion imaging offers an experimentally accessible method for detecting negative temperature equilibrium states, a subject where some considerable interest currently lies. As the signatures of negative temperature states emerge at low k in the quantum spectrum, this may make it less susceptible to high frequency spatial noise from the sound field or other noise sources, and it therefore may serve as a complementary approach to the recently demonstrated method for vortex sign detection [87]. The k^3 law is in principle universal, and should appear under the right conditions regardless of the confining geometry of the system.

Recent experimental results suggest that the superfluid Reynolds number proposed in Chapter 5 may have some real predictive power beyond 2D quantum turbulence. In particular, Shoepe has shown experimentally that the superfluid Reynolds number revealed dynamical similarity in the lifetime of transient turbulence in 3D superfluid helium at milliKelvin temperatures [286, 287]. If the superfluid Reynolds number stands up to further investigation across a diverse range of systems, it would provide a very useful quantitative measure of quantum turbulence. A universal quantitative measure of quantum turbulence near the transition might even provide information about how to control it. However, it is also worth bearing in mind that all practical applications of superfluid helium are significantly more complex, involving two-fluid behaviour. Nonetheless, given the much lower superfluid Mach numbers attainable in superfluid helium, we might expect the superfluid Reynolds number to be more useful there than in BECs, where the Mach number is more often sufficiently large that it cannot be neglected.

From Chapter 6 we have learned the somewhat unfortunate reality that probing the classical limit of fully-developed turbulence in BECs is likely to be quite demanding. The systems are required to have many vortices (at least several hundred degrees of freedom), yet, simultaneously, the vortices must also be well-separated, such that inertial effects can become dominant over radiation and forcing effects from the sound coupling. Although numerically these large systems, while computationally demanding, are straightforward to achieve, creating such large systems in reality is likely to be a considerable experimental challenge. The situation does however appear much more promising for 2D systems, where experiments are already making condensates

spanning several hundred healing lengths [71, 78], and the conditions required do not appear to be completely out of reach. From a theoretical perspective, the cascade studies summarized in Chapter 3, combined with the results of Chapter 6, demonstrate that the spectral formulation quite easily leads to spurious scaling "laws" for the kinetic energy spectrum of quantum vortices, and, furthermore, clear spectral laws are difficult to achieve unless quite a large number of vortices are present. For quantum fluids, the spectral formulation isn't all that helpful; Fourier transforming everything and looking at the same information in wavenumber space is mostly detrimental, removing the nice feature that 2D quantum vortices are localized objects in position space. The spectral formulation needs to be used with caution, scrutinized using compensated spectra, and corroborated by either flux calculations or real-space vorticity correlations whenever possible.

7.3 Future Work and Outlook

The present research has explored parallels between classical and quantum 2D turbulence, and investigated whether some of the fundamental principles of classical turbulence can be used to understand similar quantum fluid phenomena. The findings from this work have provided some new insight into the applicability of universal concepts such as the Reynolds number and turbulent cascades in quantum fluids.

As was originally believed for 2D turbulence, it may turn out that much of 2D quantum turbulence will be limited to the realm of numerical simulation. This of course does not mean that its study cannot contribute to the understanding of real systems. The fact that the superfluid Reynolds number proposed in Chapter 5 has already been shown to be useful in superfluid helium is a perfect example of how the simplicities of two dimensions can be exploited to conduct more detailed studies than would otherwise be possible in order to learn something new. The systematic study of the enstrophy cascade up to very large vortex numbers (Chapter 6), which clearly demonstrated the validity of Onsager's superfluid Reynolds number and the Kraichnan-Batchelor theory, is another such example.

Since our proposed superfluid Reynolds number appears to be an idea of some merit, it would be worthwhile to test its validity in a variety of scenarios. If the superfluid Reynolds number truly recovers dynamical similarity, it should recover universal relations for *all* dimensionless parameters of interest. Testing drag coefficients and Strouhal numbers for a variety of obstacle shapes, and in other scenarios like grid turbulence or pipe flow, would be a good place to start. If steady-state problems

can be extended to three dimensions through the fringe method we have developed (or any other method), this would also be worthwhile. Recent experimental developments [52, 71], suggest the transition to turbulence could be explored experimentally within the near future.

While larger Reynolds numbers are always desirable to push turbulence ever closer to its "purest" form, it seems likely that experimental studies of quantum turbulence in BECs will be limited to relatively small superfluid Reynolds numbers. Nonetheless, the crossover from quantum to classical physics is usually an interesting topic, and this region of parameter space should be within experimental reach. It has been recently suggested that Fermi gases, with a much smaller coherence length, could be a viable alternative for experimental endeavours [32]. Numerical studies on the other hand may be able to achieve quite large Reynolds numbers in 2D quantum turbulence by exploiting time-saving schemes such as tree algorithms, and this could yield some interesting results in quantum turbulence that remain to be discovered.

Bibliography

[1] G. K. Batchelor, *The theory of homogeneous turbulence* (Cambridge University Press, Cambridge, United Kingdom, 1953).

[2] U. Frisch, *Turbulence: the legacy of A. N. Kolmogorov* (Cambridge University Press, Cambridge, United Kingdom, 1995).

[3] S. B. Pope, *Turbulent flows* (Cambridge University Press, Cambridge, United Kingdom, 2001).

[4] M. Lesieur, *Turbulence in fluids*, 4th (Kluwer Academic Publishers, Netherlands, 1990).

[5] P. D. Williams and M. M. Joshi, "Intensification of winter transatlantic aviation turbulence in response to climate change", Nature Climate Change **3**, 644–648 (2013).

[6] F. De Lillo, M. Cencini, W. M. Durham, M. Barry, R. Stocker, E. Climent, and G. Boffetta, "Turbulent fluid acceleration generates clusters of gyrotactic microorganisms", Phys. Rev. Lett. **112**, 044502 (2014).

[7] W. M. Durham, E. Climent, M. Barry, F. De Lillo, G. Boffetta, M. Cencini, and R. Stocker, "Turbulence drives microscale patches of motile phytoplankton", Nature communications **4** (2013).

[8] B. Hof, A. de Lozar, M. Avila, X. Tu, and T. M. Schneider, "Eliminating turbulence in spatially intermittent flows", Science **327**, 1491–1494 (2010).

[9] I. Glassman, R. A. Yetter, and N. G. Glumac, *Combustion*, Fourth Edition (Academic press, Burlington, Massachusetts, 2014).

[10] R. Grappin, U. Frisch, J. Léorat, and A. Pouquet, "Alfvenic fluctuations as asymptotic states of mhd turbulence", Astron. Astrophys **105**, 6–14 (1982).

[11] R. Monchaux, M. Berhanu, M. Bourgoin, M. Moulin, P. Odier, J.-F. Pinton, R. Volk, S. Fauve, N. Mordant, F. Pétrélis, A. Chiffaudel, F. Daviaud, B. Dubrulle, C. Gasquet, L. Marié, and F. Ravelet, "Generation of a magnetic field by dynamo action in a turbulent flow of liquid sodium", Phys. Rev. Lett. **98**, 044502 (2007).

[12] X. Garbet, "Turbulence in fusion plasmas: key issues and impact on transport modelling", Plasma Physics and Controlled Fusion **43**, A251 (2001).

[13] G. D. Conway, "Turbulence measurements in fusion plasmas", Plasma Physics and Controlled Fusion **50**, 124026 (2008).

[14] S. Nazarenko, *Wave turbulence*, 1st ed., Lecture Notes in Physics 825 (Springer-Verlag, Berlin Heidelberg, 2011).

[15] G. Falkovich and K. R. Sreenivasan, "Lessons from hydrodynamic turbulence", Physics Today **59**, 43 (2006).

[16] P. Tabeling, "Two-dimensional turbulence: a physicist approach", Physics Reports **362**, 1 (2002).

[17] A. Tsinober, *An informal introduction to turbulence* (Kluwer Academic Publishers, Dordrecht, Netherlands, 2001).

[18] W. Frost, *Handbook of turbulence: volume 1 fundamentals and applications* (Plenum Press, New York, 1977).

[19] H. Tennekes and J. L. Lumley, *A first course in turbulence* (MIT press, Cambridge, Massachusetts, 1972).

[20] M. Shats, H. Xia, and H. Punzmann, "Spectral condensation of turbulence in plasmas and fluids and its role in low-to-high phase transitions in toroidal plasma", Phys. Rev. E **71**, 046409 (2005).

[21] E. Lindborg, "Can the atmospheric kinetic energy spectrum be explained by two-dimensional turbulence?", Journal of Fluid Mechanics **388**, 259–288 (1999).

[22] G. Boffetta and R. E. Ecke, "Two-dimensional turbulence", Annual Review of Fluid Mechanics **44**, 427–451 (2012).

[23] M. Gharib and P. Derango, "A liquid film (soap film) tunnel to study two-dimensional laminar and turbulent shear flows", Physica D: Nonlinear Phenomena **37**, 406–416 (1989).

[24] B. K. Martin, X. L. Wu, W. I. Goldburg, and M. A. Rutgers, "Spectra of decaying turbulence in a soap film", Phys. Rev. Lett. **80**, 3964–3967 (1998).

[25] M. Rutgers, "Forced 2D turbulence: experimental evidence of simultaneous inverse energy and forward enstrophy cascades", Phys. Rev. Lett. **81**, 2244–2247 (1998).

[26] P. Vorobieff and R. E. Ecke, "Cylinder wakes in flowing soap films", Phys. Rev. E **60**, 2953–2956 (1999).

[27] C.-Y. Wen and C.-Y. Lin, "Two-dimensional vortex shedding of a circular cylinder", Phys. Fluids **13**, 557–560 (2001).

[28] F. Bouchet and J. Sommeria, "Emergence of intense jets and Jupiter's Great Red Spot as maximum-entropy structures", J. Fluid Mech. **464**, 165–207 (2002).

[29] P. S. Marcus, "Numerical simulation of Jupiter's Great Red Spot", Nature **331**, 693–696 (1988).

[30] J. Sommeria, S. D. Meyers, and H. L. Swinney, "Laboratory simulation of Jupiter's Great Red Spot", Nature **331**, 689–693 (1988).

[31] R. J. Donnelly, "Quantized vortices and turbulence in helium II", Annual review of fluid mechanics **25**, 325–371 (1993).

[32] A. Bulgac, M. M. Forbes, and G. Wlazłowski, "Towards quantum turbulence in cold atomic fermionic superfluids", arXiv preprint arXiv:1609.00363 (2016).

[33] F. Dalfovo, S. Giorgini, L. P. Pitaevskii, and S. Stringari, "Theory of Bose-Einstein condensation in trapped gases", Rev. Mod. Phys. **71**, 463 (1999).

[34] M. S. Paoletti and D. P. Lathrop, "Quantum turbulence", Annual Review of Condensed Matter Physics **2**, 213 (2011).

[35] S. W. Van Sciver, "Applications of superfluid helium in large-scale superconducting systems", in *Quantized vortex dynamics and superfluid turbulence* (Springer Verlag, Berlin Heidelberg, 2001), pp. 51–65.

[36] L. Warszawski and A. Melatos, "Gross-Pitaevskii model of pulsar glitches", Monthly Notices of the Royal Astronomical Society **415**, 1611–1630 (2011).

[37] A. Melatos and B. Link, "Pulsar timing noise from superfluid turbulence", Monthly Notices of the Royal Astronomical Society **437**, 21–31 (2014).

[38] W. F. Vinen and J. J. Niemela, "Quantum turbulence", Journal of Low Temperature Physics **128**, 167–231 (2002).

[39] W. Vinen, "An introduction to quantum turbulence", Journal of Low Temperature Physics **145**, 7–24 (2006).

[40] C. F. Barenghi, V. S. L'vov, and P.-E. Roche, "Experimental, numerical, and analytical velocity spectra in turbulent quantum fluid", Proceedings of the National Academy of Sciences **111**, 4683–4690 (2014).

[41] C. F. Barenghi, R. J. Donnelly, and W. F. Vinen, *Quantized Vortex Dynamics and Superfluid Turbulence* (Springer-Verlag, Berlin, 2001).

[42] W. F. Vinen and R. J. Donnelly, "Quantum turbulence", Physics Today **60**, 43–48 (2007).

[43] W. Vinen, "An introduction to the theory of superfluid turbulence", in *Quantized vortex dynamics and superfluid turbulence* (Springer, 2001), pp. 149–161.

[44] J. Maurer and P. Tabeling, "Local investigation of superfluid turbulence", Europhys. Lett. **43**, 29–34 (1998).

[45] J. Salort, C. Baudet, B. Castaing, B. Chabaud, F. Daviaud, T. Didelot, P. Diribarne, B. Dubrulle, Y. Gagne, F. Gauthier, et al., "Turbulent velocity spectra in superfluid flows", Physics of Fluids (1994-present) **22**, 125102 (2010).

[46] J. Salort, P.-E. Roche, and E. Leveque, "Mesoscale equipartition of kinetic energy in quantum turbulence", Europhysics Letters **94**, 24001 (2011).

[47] Salort, J., Chabaud, B., Lavaque, E., and Roche, P.-E., "Energy cascade and the four-fifths law in superfluid turbulence", Europhysics Letters **97**, 34006 (2012).

[48] S. R. Stalp, L. Skrbek, and R. J. Donnelly, "Decay of grid turbulence in a finite channel", Phys. Rev. Lett. **82**, 4831–4834 (1999).

[49] W. F. Vinen, "Classical character of turbulence in a quantum liquid", Phys. Rev. B **61**, 1410–1420 (2000).

[50] B. Saint-Michel, E. Herbert, J. Salort, C. Baudet, M. B. Mardion, P. Bonnay, M. Bourgoin, B. Castaing, L. Chevillard, F. Daviaud, et al., "Probing quantum and classical turbulence analogy in von Kármán liquid helium, nitrogen, and water experiments", Physics of Fluids (1994-present) **26**, 125109 (2014).

[51] K. Sasaki, N. Suzuki, and H. Saito, "Benard-von Karman vortex street in a Bose-Einstein condensate", Phys. Rev. Lett. **104**, 150404 (2010).

[52] W. J. Kwon, J. H. Kim, S. W. Seo, and Y. Shin, "Observation of a von Kármán vortex street in a Bose-Einstein condensate", ArXiv e-prints (2016).

[53] G. Stagg, N. Parker, and C. Barenghi, "A superfluid boundary layer", arXiv preprint arXiv:1603.01165 (2016).

[54] E. A. L. Henn, J. A. Seman, G. Roati, K. M. F. Magalhaes, and V. S. Bagnato, "Emergence of turbulence in an oscillating Bose-Einstein condensate", Phys. Rev. Lett. **103**, 045301 (2009).

[55] E. A. L. Henn, J. A. Seman, G. Roati, K. M. F. Magalhães, and V. S. Bagnato, "Generation of vortices and observation of quantum turbulence in an oscillating Bose-Einstein condensate", J. Low Temp. Phys. **158**, 435 (2011).

[56] J. A. Seman, E. A. L. Henn, R. F. Shiozaki, G. Roati, F. J. Poveda-Cuevas, K. M. F. Magalhães, V. I. Yukalov, M. Tsubota, M. Kobayashi, K. Kasamatsu, and V. S. Bagnato, "Generation of turbulence in a trapped Bose-Einstein condensate", Laser Phys. Lett. **8**, 691 (2011).

[57] K. B. Davis, M. O. Mewes, M. R. Andrews, N. J. van Druten, D. S. Durfee, D. M. Kurn, and W. Ketterle, "Bose-Einstein condensation in a gas of sodium atoms", Phys. Rev. Lett. **75**, 3969–3973 (1995).

[58] M. H. Anderson, J. R. Ensher, M. R. Matthews, C. E. Wieman, and E. A. Cornell, "Observation of Bose-Einstein condensation in a dilute atomic vapor", Science, 198.

[59] C. Nore, M. Abid, and M. E. Brachet, "Kolmogorov turbulence in low-temperature superflows", Phys. Rev. Lett. **78**, 3896 (1997).

[60] C. Nore, M. Abid, and M. E. Brachet, "Decaying Kolmogorov turbulence in a model of superflow", Physics of Fluids **9**, 2644–2669 (1997).

[61] M. Tsubota, "Quantum turbulence: from superfluid helium to atomic Bose-Einstein condensates", Contemporary Physics **50**, 463–475 (2009).

[62] C. F. Barenghi, "Classical aspects of quantum turbulence", Journal of Physics: Condensed Matter **11**, 7751 (1999).

[63] J. Niemela, K. Sreenivasan, and R. Donnelly, "Grid generated turbulence in helium II", Journal of Low Temperature Physics **138**, 537–542 (2005).

[64] C. F. Barenghi, "Vortex lines and vortex tangles in superfluid helium", in *Turbulence structure and vortex dynamics* (Cambridge University Press, Cambridge, United Kingdom, 2000), p. 104.

[65] P. H. Roberts and N. G. Berloff, "The nonlinear Schrödinger equation as a model of superfluidity", in *Quantized vortex dynamics and superfluid turbulence* (Springer-Verlag, Berlin Heidelberg, 2001), pp. 235–257.

[66] N. G. Berloff and P. H. Roberts, "Vortices in nonlocal condensate models of superfluid helium", in *Quantized vortex dynamics and superfluid turbulence* (Springer-Verlag, Berlin Heidelberg, 2001), pp. 268–275.

[67] S. Inouye, M. R. Andrews, J. Stenger, H.-J. Miesner, D. M. Stamper-Kurn, and W. Ketterle, "Observation of Feshbach resonances in a Bose-Einstein condensate", Nature **392**, 151–154 (1998).

[68] C. Chin, R. Grimm, P. Julienne, and E. Tiesinga, "Feshbach resonances in ultracold gases", Rev. Mod. Phys. **82**, 1225–1286 (2010).

[69] I. Bloch, J. Dalibard, and W. Zwerger, "Many-body physics with ultracold gases", Rev. Mod. Phys. **80**, 885–964 (2008).

[70] A. L. Gaunt, T. F. Schmidutz, I. Gotlibovych, R. P. Smith, and Z. Hadzibabic, "Bose-Einstein condensation of atoms in a uniform potential", Phys. Rev. Lett. **110**, 200406 (2013).

[71] G. Gauthier, I. Lenton, N. McKay Parry, M. Baker, M. J. Davis, H. Rubinsztein-Dunlop, and T. W. Neely, "Configurable microscopic optical potentials for Bose-Einstein condensates using a digital-micromirror device", ArXiv e-prints (2016).

[72] L. Fallani, C. Fort, and M. Inguscio, "Bose-Einstein condensates in disordered potentials", Advances In Atomic, Molecular, and Optical Physics **56**, 119–160 (2008).

[73] M. Lu, N. Q. Burdick, S. H. Youn, and B. L. Lev, "Strongly dipolar Bose-Einstein condensate of dysprosium", Phys. Rev. Lett. **107**, 190401 (2011).

[74] G. P. Bewley, D. P. Lathrop, and K. R. Sreenivasan, "Superfluid helium: visualization of quantized vortices", Nature **441**, 588–588 (2006).

[75] R. J. Donnelly, "An introduction to experiments on superfluid turbulence", in *Quantized vortex dynamics and superfluid turbulence*, edited by C. F. Barenghi, R. J. Donnelly, and W. F. Vinen (Springer Verlag, Berlin, Heidelberg, 2001), pp. 17–35.

[76] S. Babuin, E. Varga, L. Skrbek, E. Leveque, and P.-E. Roche, "Effective viscosity in quantum turbulence: a steady-state approach", Europhysics Letters **106**, 24006 (2014).

[77] A. Powis, S. Sammut, and T. Simula, "Vortex gyroscope imaging of planar superfluids", Phys. Rev. Lett. **113**, 165303 (2014).

[78] W. J. Kwon, G. Moon, J.-y. Choi, S. W. Seo, and Y.-i. Shin, "Relaxation of superfluid turbulence in highly oblate Bose-Einstein condensates", Phys. Rev. A **90**, 063627 (2014).

[79] G. Moon, W. J. Kwon, H. Lee, and Y.-i. Shin, "Thermal friction on quantum vortices in a Bose-Einstein condensate", Phys. Rev. A **92**, 051601 (2015).

[80] T. W. Neely, A. S. Bradley, E. C. Samson, S. J. Rooney, E. M. Wright, K. J. H. Law, R. Carretero-González, P. G. Kevrekidis, M. J. Davis, and B. P. Anderson, "Characteristics of two-dimensional quantum turbulence in a compressible superfluid", Phys. Rev. Lett. **111**, 235301 (2013).

[81] T. W. Neely, "Formation, dynamics, and decay of quantized vortices in Bose-Einstein condensates: elements of quantum turbulence", PhD thesis (University of Arizona, Tucson Arizona, USA, 2010).

[82] T. W. Neely, E. C. Samson, A. S. Bradley, M. J. Davis, and B. P. Anderson, "Observation of vortex dipoles in an oblate Bose-Einstein condensate", Phys. Rev. Lett. **104**, 160401 (2010).

[83] K. E. Wilson, E. C. Samson, Z. L. Newman, T. W. Neely, and B. P. Anderson, "Experimental methods for generating two-dimensional quantum turbulence in Bose-Einstein condensates", Annual Review of Cold Atoms and Molecules **1**, 261 (2013).

[84] G. W. Stagg, A. J. Allen, N. G. Parker, and C. F. Barenghi, "Generation and decay of two-dimensional quantum turbulence in a trapped Bose-Einstein condensate", Phys. Rev. A **91**, 013612 (2015).

[85] E. C. Samson, K. E. Wilson, Z. L. Newman, and B. P. Anderson, "Deterministic creation, pinning, and manipulation of quantized vortices in a Bose-Einstein condensate", Phys. Rev. A **93**, 023603 (2016).

[86] K. Henderson, C. Ryu, C. MacCormick, and M. G. Boshier, "Experimental demonstration of painting arbitrary and dynamic potentials for Bose-Einstein condensates", New J. Phys. **11**, 043030 (2009).

[87] S. W. Seo, B. Ko, J. H. Kim, and Y.-i. Shin, "Probing 2D quantum turbulence in atomic superfluid gas using Bragg scattering", arXiv preprint arXiv:1610.06635 (2016).

[88] N. Navon, A. Gaunt, R. Smith, and Z. Hadzibabic, "Emergence of a turbulent cascade in a quantum gas", ArXiv e-prints (2016).

[89] G. W. Stagg, N. G. Parker, and C. F. Barenghi, "Quantum analogues of classical wakes in Bose-Einstein condensates", J. Phys. B **47**, 095304 (2014).

[90] M. T. Reeves, T. P. Billam, B. P. Anderson, and A. S. Bradley, "Signatures of coherent vortex structures in a disordered two-dimensional quantum fluid", Phys. Rev. A **89**, 053631 (2014).

[91] M. T. Reeves, T. P. Billam, B. P. Anderson, and A. S. Bradley, "Identifying a superfluid Reynolds number via dynamical similarity", Phys. Rev. Lett. **114**, 155302 (2015).

[92] T. P. Billam, M. T. Reeves, B. P. Anderson, and A. S. Bradley, "Onsager-Kraichnan condensation in decaying two-dimensional quantum turbulence", Phys. Rev. Lett. **112**, 145301 (2014).

[93] T. P. Billam, M. T. Reeves, and A. S. Bradley, "Spectral energy transport in two-dimensional quantum vortex dynamics", Phys. Rev. A **91**, 023615 (2015).

[94] X. Yu, T. P. Billam, J. Nian, M. T. Reeves, and A. S. Bradley, "Theory of the vortex-clustering transition in a confined two-dimensional quantum fluid", Phys. Rev. A **94**, 023602 (2016).

[95] A. S. Monin and R. V. Ozmidov, *Turbulence in the ocean*, Vol. 3 (Kluwer Academic Publishers, Dordrecht, Netherlands, 1985).

[96] K. Avila, D. Moxey, A. de Lozar, M. Avila, D. Barkley, and B. Hof, "The onset of turbulence in pipe flow", Science **333**, 192–196 (2011).

[97] M. Van Dyke and M. Van Dyke, *An album of fluid motion*, Vol. 176 (Parabolic Press, Stanford, 1982).

[98] V. Strouhal, "Über eine besondere art der tonerregung", Annalen der Physik **241**, 216–251 (1878).

[99] A. Roshko, *On the development of turbulent wakes from vortex streets*, tech. rep. 1191 (National Advisory Committee on Aeronautics (NACA), 1954).

[100] G. K. Batchelor, *An introduction to fluid dynamics* (Cambridge University Press, Cambridge, United Kingdom, 1967).

[101] Rose, H.A. and Sulem, P.L., "Fully developed turbulence and statistical mechanics", J. Phys. France **39**, 441–484 (1978).

[102] A. N. Kolmogorov, "The Local Structure of Turbulence in Incompressible Viscous Fluid for Very Large Reynolds Numbers.", Dokl. Akad. Nauk. SSSR **30**, 301 (1941).

[103] A. J. Chorin, *Vorticity and turbulence*, Vol. 103 (Springer-Verlag, New York, 1994).

[104] A. Chorin, "Book review: Kolmogorov spectra of turbulence I: Wave turbulence, by V. E. Zakharov, V. S. L'vov, and G. Falkovich", Bulletin of the American Mathematical Society **29**, 304–306.

[105] L. D. Landau and E. M. Lifshitz, *Fluid mechanics, second edition: Volume 6 (course of theoretical physics)* (Pergamon Press, Oxford, 1987).

[106] K. R. Sreenivasan, "On the universality of the Kolmogorov constant", Physics of Fluids (1994-present) **7**, 2778–2784 (1995).

[107] L. F. Richardson, "Atmospheric diffusion shown on a distance-neighbour graph", Proceedings of the Royal Society of London, Series A **110**, 709–737 (1926).

[108] F. H. Champagne, "The fine-scale structure of the turbulent velocity field", Journal of Fluid Mechanics **86**, 67–108 (1978).

[109] R. Fjørtoft, "On the changes in the spectral distribution of kinetic energy for two-dimensional, non-divergent flow", Tellus A **5** (1953).

[110] S. Nazarenko, *Fluid dynamics via examples and solutions* (CRC Press, Boca Raton, 2014).

[111] T. D. Lee, "Difference between turbulence in a two-dimensional fluid and in a three-dimensional fluid", Journal of Applied Physics **22**, 524 (1951).

[112] G. K. Batchelor, "Computation of the energy spectrum in homogeneous two-dimensional turbulence", Phys. Fluids Suppl. II **12**, 233 (1969).

[113] C. V. Tran and D. G. Dritschel, "Vanishing enstrophy dissipation in two-dimensional Navier–Stokes turbulence in the inviscid limit", Journal of Fluid Mechanics **559**, 107–116 (2006).

[114] V. Borue, "Spectral exponents of enstrophy cascade in stationary two-dimensional homogeneous turbulence", Phys. Rev. Lett. **71**, 3967–3970 (1993).

[115] D. K. Lilly, "Numerical simulation of two-dimensional turbulence", Physics of Fluids **12**, 240–249 (1969).

[116] D. K. Lilly, "Numerical simulation of developing and decaying two-dimensional turbulence", Journal of Fluid Mechanics **45**, 395–415 (1971).

[117] J. Sommeria, "Two-dimensional turbulence", in *New trends in turbulence*, edited by M. Lesieur, A. Yaglom, and F. David, Les Houches - Ecole d'Ete de Physique Theorique (EDP Sciences-Springer, Berlin, 2001), p. 385.

[118] E. Lindborg and A. Vallgren, "Testing Batchelor's similarity hypotheses for decaying two-dimensional turbulence", Physics of Fluids (1994-present) **22**, 091704 (2010).

[119] R. H. Kraichnan, "Inertial ranges in two-dimensional turbulence", Physics of Fluids **10**, 1417–1423 (1967).

[120] R. H. Kraichnan, "The structure of isotropic turbulence at very high Reynolds numbers", Journal of Fluid Mechanics **5**, 497–543 (1959).

[121] G. Eyink and U. Frisch, "Robert H. Kraichnan", ArXiv e-prints (2010).

[122] R. H. Kraichnan, "Inertial-range transfer in two-and three-dimensional turbulence", Journal of Fluid Mechanics **47**, 525–535 (1971).

[123] A. Vallgren and E. Lindborg, "The enstrophy cascade in forced two-dimensional turbulence", Journal of Fluid Mechanics **671**, 168–183 (2011).

[124] P. D. Mininni and A. Pouquet, "Inverse cascade behavior in freely decaying two-dimensional fluid turbulence", Phys. Rev. E **87**, 033002 (2013).

[125] H. Xia, H. Punzmann, G. Falkovich, and M. G. Shats, "Turbulence-condensate interaction in two dimensions", Phys. Rev. Lett. **101**, 194504 (2008).

[126] C.-k. Chan, D. Mitra, and A. Brandenburg, "Dynamics of saturated energy condensation in two-dimensional turbulence", Phys. Rev. E **85**, 036315 (2012).

[127] G. Boffetta, A. Celani, S. Musacchio, and M. Vergassola, "Intermittency in two-dimensional Ekman-Navier-Stokes turbulence", Phys. Rev. E **66**, 026304 (2002).

[128] J. Sommeria, "Experimental study of the two-dimensional inverse energy cascade in a square box", Journal of fluid mechanics **170**, 139–168 (1986).

[129] J. Paret and P. Tabeling, "Intermittency in the two-dimensional inverse cascade of energy: Experimental observations", Physics of Fluids (1994-present) **10**, 3126–3136 (1998).

[130] J. Paret, M.-C. Jullien, and P. Tabeling, "Vorticity statistics in the two-dimensional enstrophy cascade", Phys. Rev. Lett. **83**, 3418 (1999).

[131] E. Lindborg and K. Alvelius, "The kinetic energy spectrum of the two-dimensional enstrophy turbulence cascade", Physics of fluids **12**, 945–947 (2000).

[132] V. Borue, "Inverse energy cascade in stationary two-dimensional homogeneous turbulence", Phys. Rev. Lett. **72**, 1475 (1994).

[133] A. Vallgren, "Infrared Reynolds number dependency of the two-dimensional inverse energy cascade", Journal of Fluid Mechanics **667**, 463–473 (2011).

[134] S. Y. Chen, R. E. Ecke, G. L. Eyink, M. Rivera, M. P. Wan, and Z. L. Xiao, "Physical mechanism of the two-dimensional inverse energy cascade", Phys. Rev. Lett. **96**, 084502 (2006).

[135] Z. Xiao, M. Wan, S. Chen, and G. Eyink, "Physical mechanism of the inverse energy cascade of two-dimensional turbulence: a numerical investigation", Journal of Fluid Mechanics **619**, 1–44 (2009).

[136] P. K. Newton, *The N-vortex problem: analytical techniques*, Vol. 145 (Springer-Verlag, New York, 2001).

[137] P. R. Spalart, *Vortex methods for separated flows*, NASA Ames Research Center, 1988.

[138] P. R. Spalart, *Direct numerical study of leading-edge contamination*, Advisory Group for Aerospace Research and Development (AGARD), 1989.

[139] R. Benzi, M. Colella, M. Briscolini, and P. Santangelo, "A simple point vortex model for two-dimensional decaying turbulence", Physics of Fluids A: Fluid Dynamics (1989-1993) **4**, 1036–1039 (1992).

[140] J. B. Weiss and J. C. McWilliams, "Temporal scaling behavior of decaying two-dimensional turbulence", Physics of Fluids A: Fluid Dynamics (1989-1993) **5**, 608–621 (1993).

[141] R. H. Kraichnan, "Statistical dynamics of two-dimensional flow", Journal of Fluid Mechanics **67**, 155–175 (1975).

[142] H. Aref, "Integrable, chaotic, and turbulent vortex motion in two-dimensional flows", Annual Review of Fluid Mechanics **15**, 345–389 (1983).

[143] G. L. Eyink and K. R. Sreenivasan, "Onsager and the theory of hydrodynamic turbulence", Rev. Mod. Phys. **78**, 87 (2006).

[144] E. A. Novikov, "Dynamics and statistics of a system of vortices", Zhurnal Eksperimentalnoi i Teoreticheskoi Fiziki **68**, 1868–1882 (1975).

[145] H. Aref, "Motion of three vortices", Physics of Fluids (1958-1988) **22**, 393–400 (1979).

[146] D. J. Griffiths and R. College, *Introduction to electrodynamics*, Vol. 3 (prentice Hall Upper Saddle River, NJ, 1999).

[147] L. J. Campbell and K. O'Neil, "Statistics of two-dimensional point vortices and high-energy vortex states", Journal of Statistical Physics **65**, 495 (1991).

[148] J. B. Weiss and J. C. McWilliams, "Nonergodicity of point vortices", Physics of Fluids A: Fluid Dynamics **3**, 835 (1991).

[149] H. Aref, P. Boyland, M. Stremler, and D. Vainchtein, "Turbulent statistical dynamics of a system of point vortices", in *Fundamental problematic issues in turbulence* (Springer, 1999), pp. 151–161.

[150] T. Kusumura, H. Takeuchi, and M. Tsubota, "Energy spectrum of the superfluid velocity made by quantized vortices in two-dimensional quantum turbulence", Journal of Low Temperature Physics **171**, 563–570 (2012).

[151] L. Onsager, "Statistical hydrodynamics", Nuovo Cimento Suppl. **6**, 279 (1949).

[152] G. Joyce and D. Montgomery, "Negative temperature states for the two-dimensional guiding-centre plasma", Journal of Plasma Physics **10**, 107–121 (1973).

[153] D. Montgomery and G. Joyce, "Statistical mechanics of "negative temperature" states", Phys. Fluids **17**, 1139 (1974).

[154] D. Montgomery, X. Shan, and W. H. Matthaeus, "Navier-Stokes relaxation to sinh-Poisson states at finite Reynolds numbers", Physics of Fluids A **5**, 2207–2216 (1993).

[155] J. Miller, "Statistical mechanics of Euler equations in two dimensions", Phys. Rev. Lett. **65**, 2137 (1990).

[156] R. Robert and J. Sommeria, "Statistical equilibrium states for two-dimensional flows", Journal of Fluid Mechanics **229**, 291 (1991).

[157] C. Pethic and H. Smith, *Bose-Einstein condensation in dilute atomic gases* (Cambridge University Press, Cambridge, UK, 2004).

[158] M. J. Davis, "Dynamics of Bose-Einstein condensation", PhD thesis (University of Oxford, Oxford, United Kingdom, 2001).

[159] E. P. Gross, "Structure of a quantized vortex in boson systems", Il Nuovo Cimento (1955-1965) **20**, 454–477 (1961).

[160] D. R. Tilley and J. Tilley, *Superfluidity and superconductivity* (CRC Press, 1990).

[161] W. Schoepe, "Fluctuations and stability of superfluid turbulence at milli-Kelvin temperatures", Phys. Rev. Lett. **92**, 095301 (2004).

[162] R. J. Donnelly, *Quantized vortices in helium II*, first (Cambridge University Press, Cambridge, UK, 1991).

[163] C. C. Bradley, C. A. Sackett, J. J. Tollett, and R. G. Hulet, "Evidence of Bose-Einstein condensation in an atomic gas with attractive interactions", Phys. Rev. Lett. **75**, 1687–1690 (1995).

[164] M. C. Tsatsos, P. E. Tavares, A. Cidrim, A. R. Fritsch, M. A. Caracanhas, F. E. A. dos Santos, C. F. Barenghi, and V. S. Bagnato, "Quantum turbulence in trapped atomic Bose-Einstein condensates ", Physics Reports **622**, 1–52 (2016).

[165] K. Henderson, C. Ryu, C. MacCormick, and M. Boshier, "Experimental demonstration of painting arbitrary and dynamic potentials for Bose-Einstein condensates", New Journal of Physics **11**, 043030 (2009).

[166] S. J. Rooney, P. B. Blakie, B. P. Anderson, and A. S. Bradley, "Suppression of kelvon-induced decay of quantized vortices in oblate Bose-Einstein condensates", Phys. Rev. A **84**, 023637 (2011).

[167] R. Desbuquois, L. Chomaz, T. Yefsah, J. Léonard, J. Beugnon, C. Weitenberg, and J. Dalibard, "Superfluid behaviour of a two-dimensional Bose gas", Nature Physics **8**, 645–648 (2012).

[168] T. Winiecki, B. Jackson, J. F. McCann, and C. S. Adams, "Vortex shedding and drag in dilute Bose-Einstein condensates", English, J. Phys. B: At. Mol. Opt. Phys. **33**, 4069–4078 (2000).

[169] B. Lautrup, *Physics of continuous matter: Exotic and everyday phenomena in the macroscopic world*, Second Edition (CRC press, Boca Raton, 2011).

[170] R. P. Feynman, "Application of quantum mechanics to liquid helium", Prog. Low Temp. Phys. **1**, 17 (1955).

[171] E. Lundh, "Multiply quantized vortices in trapped Bose-Einstein condensates", Phys. Rev. A **65**, 043604 (2002).

[172] J. A. M. Huhtamäki, M. Möttönen, and S. M. M. Virtanen, "Dynamically stable multiply quantized vortices in dilute Bose-Einstein condensates", Phys. Rev. A **74**, 063619 (2006).

[173] A. S. Bradley and B. P. Anderson, "Energy spectra of vortex distributions in two-dimensional quantum turbulence", Phys. Rev. X **2**, 041001 (2012).

[174] J. P. Boyd, *Chebyshev and Fourier spectral methods*, 2nd Edition (Dover, New York, 2000).

[175] L. M. Pismen, *Vortices in nonlinear fields*, 1st Edition (Oxford University Press, New York, 1999).

[176] L. Pismen, "Dissipative vortex dynamics and magnus force", in *Quantized vortex dynamics and superfluid turbulence* (Springer-Verlag, Berlin Heidelberg, 2001), pp. 290–296.

[177] A. L. Fetter, "Vortices in an Imperfect Bose gas. IV: Translational velocity", Phys. Rev. **151**, 100–104 (1966).

[178] R. J. Creswick and H. L. Morrison, "On the dynamics of quantum vortices", Physics Letters A **76**, 267–268 (1980).

[179] J. C. Neu, "Vortices in complex scalar fields", Physica D: Nonlinear Phenomena **43**, 385–406 (1990).

[180] F. Lund, "Defect dynamics for the nonlinear Schrödinger equation derived from a variational principle", Physics Letters A **159**, 245–251 (1991).

[181] K. Kawasaki, "Defect-phase dynamics for dissipative media with potential", Progress of Theoretical Physics Supplements **80**, 123–138 (1984).

[182] A. Lucas and P. Surówka, "Sound-induced vortex interactions in a zero-temperature two-dimensional superfluid", Phys. Rev. A **90**, 053617 (2014).

[183] M. D. Bustamante and S. Nazarenko, "Derivation of the Biot-Savart equation from the nonlinear Schrödinger equation", Phys. Rev. E **92**, 053019 (2015).

[184] O. Törnkvist and E. Schröder, "Vortex dynamics in dissipative systems", Phys. Rev. Lett. **78**, 1908 (1997).

[185] A. L. Fetter, "Vortices in an imperfect Bose gas. I: The condensate", Phys. Rev. **138**, A429–A437 (1965).

[186] R. Numasato, M. Tsubota, and V. S. L'vov, "Direct energy cascade in two-dimensional compressible quantum turbulence", Phys. Rev. A **81**, 063630 (2010).

[187] M. T. Reeves, B. P. Anderson, and A. S. Bradley, "Classical and quantum regimes of two-dimensional turbulence in trapped Bose-Einstein condensates", Phys. Rev. A **86**, 053621 (2012).

[188] M. T. Reeves, T. P. Billam, B. P. Anderson, and A. S. Bradley, "Inverse energy cascade in forced two-dimensional quantum turbulence", Phys. Rev. Lett. **110**, 104501 (2013).

[189] T. Simula, M. J. Davis, and K. Helmerson, "Emergence of order from turbulence in an isolated planar superfluid", Phys. Rev. Lett. **113**, 165302 (2014).

[190] W. F. Vinen, "Decay of superfluid turbulence at a very low temperature: the radiation of sound from a Kelvin wave on a quantized vortex", Phys. Rev. B **64**, 134520 (2001).

[191] C. A. Jones and P. H. Roberts, "Motions in a Bose condensate. IV: Axisymmetric solitary waves", Journal of Physics A: Mathematical and General **15**, 2599 (1982).

[192] C. A. Jones, S. J. Putterman, and P. H. Roberts, "Motions in a Bose condensate. V: Stability of solitary wave solutions of non-linear Schrodinger equations in two and three dimensions", Journal of Physics A: Mathematical and General **19**, 2991 (1986).

[193] N. G. Parker, A. J. Allen, C. F. Barenghi, and N. P. Proukakis, "Coherent cross talk and parametric driving of matter-wave vortices", Phys. Rev. A **86**, 013631 (2012).

[194] N. G. Berloff and P. H. Roberts, "Motions in a Bose condensate: X. New results on the stability of axisymmetric solitary waves of the Gross-Pitaevskii equation", Journal of Physics A: Mathematical and General **37**, 11333 (2004).

[195] A. J. Groszek, T. P. Simula, D. M. Paganin, and K. Helmerson, "Onsager vortex formation in Bose-Einstein condensates in two-dimensional power-law traps", Phys. Rev. A **93**, 043614 (2016).

[196] C. F. Barenghi, "Is the Reynolds number infinite in superfluid turbulence?", Physica D **237**, 2195 (2008).

[197] W. F. Vinen, "How is turbulent energy dissipated in a superfluid?", Journal of Physics: Condensed Matter **17**, S3231 (2005).

[198] F. Lund, "Response of a filamentary vortex to sound", Physics of Fluids A **1**, 1521–1531 (1989).

[199] V. E. Zakharov, V. S. L'vov, and G. Falkovich, *Kolmogorov spectra of turbulence I: wave turbulence* (Springer-Verlag, Berlin Heidelberg, 2012).

[200] S. Nazarenko and M. Onorato, "Wave turbulence and vortices in Bose-Einstein condensation", Physica D **219**, 1–12 (2006).

[201] S. Nazarenko and M. Onorato, "Freely decaying turbulence and Bose-Einstein condensation in Gross-Pitaevskii model", J. Low Temp. Phys. **146**, 31–46 (2007).

[202] D. Proment, S. Nazarenko, and M. Onorato, "Quantum turbulence cascades in the Gross-Pitaevskii model", Phys. Rev. A **80**, 051603 (2009).

[203] D. Proment, S. Nazarenko, and M. Onorato, "Sustained turbulence in the three-dimensional Gross-Pitaevskii model", Physica D: Nonlinear Phenomena **241**, Special Issue on Small Scale Turbulence, 304–314 (2012).

[204] R. H. Kraichnan, "Condensate turbulence in a weakly coupled boson gas", Phys. Rev. Lett. **18**, 202–206 (1967).

[205] M. J. Lighthill, "On sound generated aerodynamically. I. General theory", Proceedings of the Royal Society of London A: Mathematical, Physical and Engineering Sciences **211**, 564–587 (1952).

[206] M. J. Lighthill, "On sound generated aerodynamically. II: Turbulence as a source of sound", Proceedings of the Royal Society of London A: Mathematical, Physical and Engineering Sciences **222**, 1–32 (1954).

[207] M. S. Howe, *Theory of vortex sound*, Vol. 33 (Cambridge University Press, 2003).

[208] N. Proukakis, S. Gardiner, M. Davis, and M. Szymańska, *Quantum gases: Finite temperature and non-equilibrium dynamics*, Vol. 1 (World Scientific, 2013).

[209] P. B. Blakie, A. S. Bradley, M. J. Davis, R. J. Ballagh, and C. W. Gardiner, "Dynamics and statistical mechanics of ultra-cold Bose gases using c-field techniques", Adv. in Phys. **57**, 363–455 (2008).

[210] C. W. Gardiner, J. R. Anglin, and T. I. A. Fudge, "The stochastic Gross-Pitaevskii equation", J. Phys. B: At. Mol. Opt. Phys. **35**, 1555 (2002).

[211] C. W. Gardiner and M. J. Davis, "The stochastic Gross-Pitaevskii equation: II", J. Phys. B **36**, 4731 (2003).

[212] A. S. Bradley and C. W. Gardiner, arXiv:cond-mat/0602162.

[213] S. J. Rooney, "Implementation and applications of the stochastic projected Gross-Pitaevskii equation", PhD thesis (University of Otago, 2015).

[214] S. J. Rooney, A. J. Allen, U. Zülicke, N. P. Proukakis, and A. S. Bradley, "Reservoir interactions of a vortex in a trapped three-dimensional Bose-Einstein condensate", Phys. Rev. A **93**, 063603 (2016).

[215] L. D. Landau and E. M. Lifshitz, "Theory of elasticity, second edition: Volume 7 (Course of Theoretical Physics)", (1987).

[216] J. H. Kim, W. J. Kwon, and Y.-i. Shin, "Role of thermal friction in relaxation of turbulent Bose-Einstein condensates", ArXiv e-prints (2016).

[217] C. Huepe and M.-E. Brachet, "Scaling laws for vortical nucleation solutions in a model of superflow", Physica D: Nonlinear Phenomena **140**, 126–140 (2000).

[218] T. Frisch, Y. Pomeau, and S. Rica, "Transition to dissipation in a model of superflow", Phys. Rev. Lett. **69**, 1644–1647 (1992).

[219] J. S. Stießberger and W. Zwerger, "Critcal velocity of superfluid flow past large obstacles in Bose-Einstein condensates", Phys. Rev. A **62**, 061601 (2000).

[220] C. Nore, C. Huepe, and M. E. Brachet, "Subcritical dissipation in three-dimensional superflows", Phys. Rev. Lett. **84**, 2191–2194 (2000).

[221] W. J. Kwon, G. Moon, S. W. Seo, and Y.-i. Shin, "Critical velocity for vortex shedding in a Bose-Einstein condensate", Phys. Rev. A **91**, 053615 (2015).

[222] T. Aioi, T. Kadokura, T. Kishimoto, and H. Saito, "Controlled generation and manipulation of vortex dipoles in a Bose-Einstein condensate", Phys. Rev. X **1**, 021003 (2011).

[223] W. J. Kwon, S. W. Seo, and Y.-i. Shin, "Periodic shedding of vortex dipoles from a moving penetrable obstacle in a Bose-Einstein condensate", Phys. Rev. A **92**, 033613 (2015).

[224] P. G. Saffman, *Vortex dynamics* (Cambridge university press, 1992).

[225] T. Winiecki, J. F. McCann, and C. S. Adams, "Pressure drag in linear and nonlinear quantum fluids", Phys. Rev. Lett. **82**, 5186–5189 (1999).

[226] M. Abid, M. Brachet, J. Maurer, C. Nore, and P. Tabeling, "Experimental and numerical investigations of low-temperature superfluid turbulence", Eur. J. Mech. B-Fluid **17**, 665 (1998).

[227] N. Sasa, T. Kano, M. Machida, V. S. L'vov, O. Rudenko, and M. Tsubota, "Energy spectra of quantum turbulence: Large-scale simulation and modelling", **84**, 054525 (2011).

[228] M. Kobayashi and M. Tsubota, "Kolmogorov spectrum of superfluid turbulence: numerical analysis of the Gross-Pitaevskii equation with a small-scale dissipation", Phys. Rev. Lett. **94**, 065302 (2005).

[229] T. Araki, M. Tsubota, and S. K. Nemirovskii, "Energy spectrum of superfluid turbulence with no normal-fluid component", Phys. Rev. Lett. **89**, 145301 (2002).

[230] A. W. Baggaley, J. Laurie, and C. F. Barenghi, "Vortex-density fluctuations, energy spectra, and vortical regions in superfluid turbulence", Phys. Rev. Lett. **109**, 205304 (2012).

[231] P.-E. Roche, C. F. Barenghi, and E. Leveque, "Quantum turbulence at finite temperature: The two-fluids cascade", Europhysics Letters **87**, 54006 (2009).

[232] P.-E. Roche and C. F. Barenghi, "Vortex spectrum in superfluid turbulence: interpretation of a recent experiment", Europhysics Letters **81**, 36002 (2008).

[233] R. Hänninen, M. Tsubota, and W. F. Vinen, "Generation of turbulence by oscillating structures in superfluid helium at very low temperatures", Phys. Rev. B **75**, 064502 (2007).

[234] C. F. Barenghi, L. Skrbek, and K. R. Sreenivasan, "Introduction to quantum turbulence", Proceedings of the National Academy of Sciences **111**, 4647–4652 (2014).

[235] D. E. Zmeev, P. Walmsley, A. Golov, P. V. McClintock, S. N. Fisher, and W. Vinen, "Dissipation of quasiclassical turbulence in superfluid ^{4}He", Phys. Rev. Lett. **115**, 155303 (2015).

[236] G. Stagg, N. Parker, and C. Barenghi, "Ultra-quantum turbulence in a quenched homogeneous Bose gas", arXiv preprint arXiv:1607.03719 (2016).

[237] L. Onsager, "Introductory talk [on liquid helium]", in International conference of theoretical physics (Science Council of Japan, 1953), pp. 877–880.

[238] A. P. Finne, T. Araki, R. Blaauwgeers, V. B. Eltsov, N. B. Kopnin, M. Kruslus, L. Skrbek, M. Tsubota, and G. E. Volovik, "An Intrinsic Velocity-Independent Criterion for Superfluid Turbulence", Nature **424**, 1022 (2003).

[239] G. E. Volovik, "Classical and Quantum Regimes of Superfluid Turbulence", JETP Lett. **78**, 533 (2003).

[240] V. S. L'vov, L. Skrbek, and K. R. Sreenivasan, "Viscosity of liquid ^{4}He and quantum of circulation: Are they related?", Phys. Fluids **26**, 041703 (2014).

[241] N. G. Parker and C. S. Adams, "Emergence and decay of turbulence in stirred atomic Bose-Einstein condensates", Phys. Rev. Lett. **95**, 145301 (2005).

[242] T. L. Horng, C. H. Hsueh, S. W. Su, Y. M. Kao, and S. C. Gou, "Two-dimensional quantum turbulence in a nonuniform Bose-Einstein condensate", Phys. Rev. A **80**, 023618 (2009).

[243] R. Numasato and M. Tsubota, "Possibility of inverse energy cascade in two-dimensional quantum turbulence", J. Low Temp. Phys. **158**, 415–421 (2010).

[244] D. Kobyakov, A. Bezett, E. Lundh, M. Marklund, and V. Bychkov, "Turbulence in binary Bose-Einstein condensates generated by highly nonlinear Rayleigh-Taylor and Kelvin-Helmholtz instabilities", Phys. Rev. A **89**, 013631 (2014).

[245] A. C. White, B. P. Anderson, and V. S. Bagnato, "Vortices and turbulence in trapped atomic condensates", Proceedings of the National Academy of Sciences **111**, 4719–4726 (2014).

[246] A. Skaugen and L. Angheluta, "Vortex clustering and universal scaling laws in two-dimensional quantum turbulence", Phys. Rev. E **93**, 032106 (2016).

[247] P. Dmitruk and D. C. Montgomery, "Numerical study of the decay of enstrophy in a two-dimensional Navier-Stokes fluid in the limit of very small viscosities", Physics of Fluids (1994-present) **17**, 035114 (2005).

[248] P. M. Chesler, H. Liu, and A. Adams, "Holographic vortex liquids and superfluid turbulence", Science **341**, 368 (2013).

[249] A. White, C. Barenghi, and N. Proukakis, "Creation and characterization of vortex clusters in atomic Bose-Einstein condensates", Phys. Rev. A **86**, 013635 (2012).

[250] A. C. White, N. P. Proukakis, and C. F. Barenghi, "Topological stirring of two-dimensional atomic Bose-Einstein condensates", Journal of Physics: Conference Series **544**, 012021 (2014).

[251] R. Zamora-Zamora, O. Adame-Arana, and V. Romero-Rochin, "Macroscopic excitations in confined Bose-Einstein condensates, searching for quantum turbulence", Journal of Low Temperature Physics **180**, 109–125 (2015).

[252] H. Salman and D. Maestrini, "Long-range ordering of topological excitations in a two-dimensional superfluid far from equilibrium", Phys. Rev. A **94**, 043642 (2016).

[253] R. A. Smith, "Phase-transition behavior in a negative-temperature guiding-center plasma", Phys. Rev. Lett. **63**, 1479–1482 (1989).

[254] R. A. Smith and T. M. O'Niel, "Nonaxisymmetric thermal equilibria of a cylindrically bounded guiding-center plasma or discrete vortex system", Physics of Fluids B **2**, 2961–2975 (1990).

[255] R. H. Kraichnan and D. Montgomery, "Two-dimensional turbulence", Reports on Progress in Physics **43**, 547 (1980).

[256] A. L. Fetter, "Rotating trapped Bose-Einstein condensates", Rev. Mod. Phys. **81**, 647 (2009).

[257] A. L. Fetter and A. A. Svidzinsky, "Vortices in a trapped dilute Bose-Einstein condensate", J. Phys. B **13**, R135 (2001).

[258] M. Caracanhas, A. Fetter, S. Muniz, K. Magalhães, G. Roati, G. Bagnato, and V. Bagnato, "Self-similar wxpansion of the density profile in a turbulent Bose-Einstein condensate", J. Low Temp. Phys. **166**, 49 (2012).

[259] K. J. Thompson, G. G. Bagnato, G. D. Telles, M. A. Caracanhas, F. E. A. dos Santos, and V. S. Bagnato, "Evidence of power law behavior in the momentum distribution of a turbulent trapped Bose-Einstein condensate", Laser Physics Letters **11**, 015501 (2014).

[260] A. C. White, C. F. Barenghi, N. P. Proukakis, A. J. Youd, and D. H. Wacks, "Nonclassical velocity statistics in a turbulent atomic Bose-Einstein condensate", Phys. Rev. Lett. **104**, 075301 (2010).

[261] M. S. Paoletti, M. E. Fisher, K. R. Sreenivasan, and D. P. Lathrop, "Velocity statistics distinguish quantum turbulence from classical turbulence", Phys. Rev. Lett. **101**, 154501 (2008).

[262] I. A. Min, I. Mezic, and A. Leonard, "Lévy stable distributions for velocity and velocity difference in systems of vortex elements", Physics of Fluids **8**, 1169 (1996).

[263] J. B. Weiss, A. Provenzale, and J. C. McWilliams, "Lagrangian dynamics in high-dimensional point-vortex systems", Phys. Fluids **10**, 1929 (1998).

[264] H. Adachi and M. Tsubota, "Numerical study of velocity statistics in steady counterflow quantum turbulence", Phys. Rev. B **83**, 132503 (2011).

[265] A. W. Baggaley and C. F. Barenghi, "Quantum turbulent velocity statistics and quasiclassical limit", Phys. Rev. E **84**, 067301 (2011).

[266] D. Kobyakov, A. Bezett, E. Lundh, M. Marklund, and V. Bychkov, "Turbulence in binary Bose-Einstein condensates generated by highly nonlinear Rayleigh-Taylor and Kelvin-Helmholtz instabilities", Phys. Rev. A **89**, 013631 (2014).

[267] A. Recati, F. Zambelli, and S. Stringari, "Overcritical Rotation of a Trapped Bose-Einstein Condensate", Phys. Rev. Lett. **86**, 377 (2001).

[268] J. B. Kruskal, "On the shortest spanning subtree of a graph and the traveling salesman problem", Proceedings of the American Mathematical society **7**, 48–50 (1956).

[269] R. N. Valani, A. J. Groszek, and T. P. Simula, "Einstein-Bose condensation of Onsager vortices", arXiv preprint arXiv:1612.02930 (2016).

[270] A. W. Baggaley, C. F. Barenghi, A. Shukurov, and Y. A. Sergeev, "Coherent vortex structures in quantum turbulence", Europhys. Lett. **98**, 26002 (2012).

[271] D. Montgomery, W. H. Matthaeus, W. T. Stribling, D. Martinez, and S. Oughton, "Relaxation in two dimensions and the "sinh-Poisson" equation", Phys. Fluids A **4**, 3 (1992).

[272] R. A. Pasmanter, "On long-lived vortices in 2-D viscous flows, most probable states of inviscid 2-D flows and a soliton equation", Phys. Fluids **6**, 1236 (1994).

[273] W. H. Press, S. A. Teukolsky, W. T. Vetterling, and B. P. Flannery, *Numerical Recipes 3rd Edition: The Art of Scientific Computing* (Cambridge University Press, 2007).

[274] G. R. Dennis, J. J. Hope, and M. T. Johnsson, "XMDS2: Fast, scalable simulation of coupled stochastic partial differential equations", Comp. Phys. Comm. **184**, 201 (2013).

[275] C. H. K. Williamson, "Vortex dynamics in the cylinder wake", Annu. Rev. Fluid Mech. **28**, 477 (1996).

[276] T. Colonius, "Modelling artificial boundary conditions for compressible flow", Ann. Rev. Fluid Mech. **36**, 315–345 (2004).

[277] A. Mani, "Analysis and optimization of numerical sponge layers as a nonreflective boundary treatment", Journal of Computational Physics **231**, 704–716 (2012).

[278] J. Nordström, N. Nordin, and D. Henningson, "The fringe region technique and the Fourier method used in the direct numerical simulation of spatially evolving viscous flows", SIAM Journal on Scientific Computing **20**, 1365–1393 (1999).

[279] M. Tsubota, K. Kasamatsu, and M. Ueda, "Vortex lattice formation in a rotating Bose-Einstein condensate", Phys. Rev. A **65**, 023603 (2002).

[280] P. Saffman, *Vortex dynamics*, Cambridge Monographs on Mechanics (Cambridge University Press, 1995).

[281] B. Ahlborn, M. L. Seto, and B. R. Noack, "On drag, Strouhal number and vortex-street structure", Fluid Dynamics Research **30**, 379–399 (2002).

[282] A. Roshko, *On the drag and shedding frequency of two-dimensional bluff bodies*, tech. rep. 3169 (National Advisory Committee on Aeronautics (NACA), 1954).

[283] G. P. Bewley, M. S. Paoletti, K. R. Sreenivasan, and D. P. Lathrop, "Characterization of reconnecting vortices in superfluid helium", P Natl Acad Sci Usa **105**, 13707–13710 (2008).

[284] G. Tosi, F. M. Marchetti, D. Sanvitto, C. Antón, M. H. Szymanska, A. Berceanu, C. Tejedor, L. Marrucci, A. Lemaitre, J. Bloch, and L. Vina, "Onset and dynamics of vortex-antivortex pairs in polariton optical parametric oscillator superfluids", Phys. Rev. Lett. **107**, 036401 (2011).

[285] M. W. Zwierlein, J. R. Abo-Shaeer, A. Schirotzek, C. H. Schunck, and W. Ketterle, "Vortices and superfluidity in a strongly interacting Fermi gas", Nature **435**, 1047–1051 (2005).

[286] W. Schoepe, "Shedding of vortex rings from an oscillating sphere in superfluid ^{4}He below 0.5K", Journal of Low Temperature Physics **173**, 170–176 (2013).

[287] W. Schoepe, "Superfluid Reynolds number and the transition from potential flow to turbulence in superfluid ^{4}He at milli-Kelvin temperatures", JETP Letters **102**, 105–107 (2015).

[288] C. F. Barenghi, S. Hulton, and D. C. Samuels, "Polarization of superfluid turbulence", Phys. Rev. Lett. **89**, 275301 (2002).

[289] D. G. Dritschel, M. Lucia, and A. C. Poje, "Ergodicity and spectral cascades in point vortex flows on the sphere", Phys. Rev. E **91**, 063014 (2015).

[290] C. E. Leith, "Diffusion approximation for two-dimensional turbulence", Phys. Fluids **11**, 671 (1968).

[291] T. Y. Hou and J. Lowengrub, "Convergence of the point vortex method for the 3D Euler equations", Communications on Pure and Applied Mathematics **43**, 965–981 (1990).

[292] S. Schochet, "The point-vortex method for periodic weak solutions of the 2D Euler equations", Communications on pure and applied mathematics **49**, 911–965 (1996).

[293] I. B. Sedov, "Evolution of the energy spectrum of a system of vortices", Akademiia Nauk SSSR Izvestiia Mekhanika Zhidkosti i Gaza **12**, 43–48 (1976).

[294] E. D. Siggia and H. Aref, "Point-vortex simulation of the inverse energy cascade in two-dimensional turbulence", Physics of Fluids (1958-1988) **24**, 171–173 (1981).

[295] NVIDIA Corporation, *NVIDIA CUDA Programming Guide, Version 6.5*, 2014.

[296] M. Brachet, M. Meneguzzi, H. Politano, and P. Sulem, "The dynamics of freely decaying two-dimensional turbulence", Journal of Fluid Mechanics **194**, 333–349 (1988).

[297] J. R. Taylor, *An introduction to error analysis: The study of uncertainties in physical measurements*, Second (University Science Books, 1997).

[298] D. Boyer, "Critical behavior of vorticity in two-dimensional turbulence", Phys. Rev. E **60**, 6769–6775 (1999).

[299] A. Skaugen and L. Angheluta, "Origin of the inverse energy cascade in two-dimensional quantum turbulence", ArXiv e-prints (2016).

[300] R. H. Kraichnan, "Remarks on turbulence theory", Advances in Mathematics **16**, 305–331 (1975).

[301] C. Cichowlas, P. Bonaiti, F. Debbasch, and M. Brachet, "Effective dissipation and turbulence in spectrally truncated Euler flows", Phys. Rev. Lett. **95**, 264502 (2005).

[302] E. W. Streed, A. P. Chikkatur, T. L. Gustavson, M. Boyd, Y. Torii, D. Schneble, G. K. Campbell, D. E. Pritchard, and W. Ketterle, "Large atom number Bose-Einstein condensate machines", Review of Scientific Instruments **77**, 023106 (2006) 10.1063/1.2163977.

[303] J. Stenger, S. Inouye, M. R. Andrews, H.-J. Miesner, D. M. Stamper-Kurn, and W. Ketterle, "Strongly enhanced inelastic collisions in a Bose-Einstein condensate near Feshbach resonances", Phys. Rev. Lett. **82**, 2422–2425 (1999).